

**Development of Techniques for Cooling and Trapping
Polar Diatomic Molecules**

A Dissertation
Presented to the Faculty of the Graduate School
of
Yale University
in Candidacy for the Degree of
Doctor of Philosophy

by
David R. Glenn

Dissertation Director: Professor David DeMille

December 2009

UMI Number: 3395928

All rights reserved

INFORMATION TO ALL USERS

The quality of this reproduction is dependent upon the quality of the copy submitted.

In the unlikely event that the author did not send a complete manuscript and there are missing pages, these will be noted. Also, if material had to be removed, a note will indicate the deletion.



UMI 3395928

Copyright 2010 by ProQuest LLC.

All rights reserved. This edition of the work is protected against unauthorized copying under Title 17, United States Code.



ProQuest LLC
789 East Eisenhower Parkway
P.O. Box 1346
Ann Arbor, MI 48106-1346

Copyright © 2009 by David R. Glenn

All rights reserved.

For my parents

Contents

Table of Contents	iv
List of Figures	vi
Acknowledgements	ix
1 Introduction	1
1.1 Molecules in Modern Atomic Physics	1
1.2 Survey of Techniques for Cooling Molecules	2
1.2.1 Laser Cooling and Trapping of Atoms	2
1.2.2 Direct Cooling Methods	4
1.2.3 Assembly Methods	6
1.3 Applications	7
1.3.1 Many-body Physics	7
1.3.2 Quantum Information	8
1.3.3 Precision Measurement	9
1.3.4 Cold and Ultracold Chemistry	11
1.4 The Microwave Trap Experiment	12
2 Buffer-Gas Cooled Molecular Beams	17
2.1 Introduction to Buffer Gas Cooling	17
2.2 Molecule Selection	21
2.3 Experiment Setup	24
2.3.1 Cryogenic Beam Source	24

2.3.2	Detection Methods	25
2.4	Summary of SrO Measurements	31
2.4.1	SrO Ablation Yield and Beam Flux	31
2.5	Electrostatic Guiding	33
2.6	Development of a Hydrodynamic Beam	38
3	Microwave Trap Design	41
3.1	Introduction	41
3.2	Resonator Mode Structure	44
3.3	Trap Depth and Circular Polarization Requirement	49
3.3.1	Linear Polarization	51
3.3.2	Criterion for Non-Adiabaticity	53
3.3.3	Circular Polarization	54
3.3.4	General Elliptical Polarization	55
3.4	Mode Matching and Quasi-optical Design	59
3.4.1	Microwave Beam Profiler	59
3.4.2	Quasi-optical Elements	60
3.4.3	Quasi-optical Feed Design for a Near Semi-confocal Cavity	70
3.5	Cavity Coupling	71
3.5.1	Optimal Coupling and Sources of Loss	71
3.5.2	Single Aperture Coupling Measurements	77
3.5.3	Aperture Array Measurements	80
3.6	Thermal Considerations	86
3.6.1	Temperature Distribution Calculations	87
3.6.2	Ceramic Metallization and Thermal Contact Conductivity	88
3.6.3	Solder Selection	92
4	Investigation of Laser Cooling in SrF	94
4.1	Motivation: Slowing Hydrodynamic Beams	94
4.2	Quasi-cycling Transitions in SrF	95
4.2.1	Vibrational Structure	96
4.2.2	Rotational and Hyperfine Structure	98

4.2.3	Remixing Dark States	101
4.3	Experimental Apparatus	103
4.3.1	Cryostat and Vacuum Chamber	107
4.3.2	Laser Setup	109
4.3.3	Electro-Optic Modulators	112
4.4	Results: Demonstration of Cycling	113
4.4.1	Beam Flux Measurement for SrF	113
4.4.2	Rotational and Hyperfine Spectroscopy of SrF	114
4.4.3	Measurement of Vibrational Transition Strengths	116
4.4.4	Observation of Repumping by Enhanced Fluorescence	120
4.4.5	Observation of Beam Deflection by Radiative Force	121
4.5	Towards Laser Cooling and Microwave Trapping of SrF	125
5	Concluding Remarks	128
A	Drawings for HDL14 Cryostat	130
B	FM Signal Size	133
C	Noise in FM Spectroscopy	138
D	Electric Field in the Microwave Cavity	142
E	Aperture Array Transmission	144

List of Figures

1.1	Schematic of experimental setup for loading of the microwave trap	14
2.1	Helium buffer gas cell.	19
2.2	Comparison of in-cell absorption time traces for SrO, BaF and SrF in the hydrodynamic helium flow regime.	23
2.3	FM spectroscopy setup.	29
2.4	SrO forward velocity and beam flux data	33
2.5	Electrostatic guiding experiment	34
2.6	Guide fluorescence data	35
2.7	Demonstration of electrostatic guiding	37
2.8	Characterization of a hydrodynamic beam of BaF	39
3.1	Gaussian beam mode of the microwave trap cavity	46
3.2	Transmission spectrum for a minimally coupled cavity of length $L = 16.76$ cm.	48
3.3	Measured Q vs. cavity length	50
3.4	Dressed-state calculation, linear polarization	53
3.5	Dressed-state calculation, circular polarization	56
3.6	Dressed-state calculation, elliptical polarization	58
3.7	Design for quasi-optical feed using paired ellipsoidal focusing mirrors	62
3.8	Scalar feed horn	64
3.9	Dielectric lens	65
3.10	Ellipsoidal focussing mirror	66
3.11	Transmissive quasi-optical quarter wave plates	68
3.12	Final cavity feed design	69

3.13	Setup for measuring coupling efficiency and cavity Q for a semi-confocal cavity. . .	78
3.14	Cavity Q-factor and fraction of power transmitted into cavity as a function of coupling hole diameter	79
3.15	Setup for direct measurement of aperture array transmission	82
3.16	Aperture array transmission data	85
3.17	Finite element heat calculation for BeO substrate of 2.5 cm thickness	89
3.18	Setup for measuring thermal contact conductivities of metal-ceramic bonds.	90
3.19	Thermal contact conductivity measurement for vapor-deposited copper on BeO . . .	92
4.1	Calculated Franck-Condon factors and transition wavelengths for the X-A band in SrF	97
4.2	Rotational and hyperfine structure for the $ X, N = 0, 1\rangle$ and $ A, J = 1/2\rangle$ states of SrF .	100
4.3	Sideband frequency distribution chosen to excite all four hyperfine levels	102
4.4	Schematic of the SrF molecular beam apparatus	105
4.5	Cryostat for SrF beam source	108
4.6	Typical setup for the injection-locked diode lasers used in the SrF beam experiments	110
4.7	Beam flux measurement	115
4.8	Measured hyperfine transition frequencies for $ X, v = 0, N = 1, F\rangle \rightarrow A, v = 0, J = 1/2, F\rangle$.	117
4.9	Vibrational transition strength measurements.	119
4.10	Vibrational repumping and magnetic field remixing of dark magnetic sublevels . . .	122
4.11	Typical beam image from the CCD camera.	123
4.12	Beam deflection by radiative force.	124
A.1	Side section view of HDL14 cryostat.	131
A.2	Top and bottom views of HDL14 cryostat.	132
C.1	FM probe geometry	139
E.1	Aperture array geometry.	145

Acknowledgements

I gratefully acknowledge the contributions of numerous coworkers and friends, without whom this work would not have been possible. I am particularly indebted to Jessie Petricka, who was responsible for much of the early development of the buffer-gas cooled beam source, for his perseverance, generosity, and leadership in the challenging task of building up a new lab from an empty room. At the time we began this work, a new experiment was also being constructed to investigate parity violation related to the nuclear anapole moment in BaF molecules; I continue to remember fondly the sense of community and shared learning that I felt during these early years, working together with Jessie, as well as Dave Rahmlow and Dennis Murphree, our counterparts on the anapole experiment. I am also very grateful to Sid Cahn, research scientist and ERSF-director, for many years of enlightening digressions, wise advice, and kind willingness to utilize his extensive connections to secure liquid helium for us in times of need.

Of course, considerable thanks must also be extended to each of the other students and post-docs who have worked on the buffer-gas beam experiment, including Dan Farkas, John Barry, and Edward Shuman. Most of the results presented here are due in large part to their efforts, and I have learned a great deal from each of them. Likewise, I am much indebted to many other members of the DeMille group, past and present, for sharing their knowledge and expertise (and also the occasional hex-wrench or microwave signal generator). Without diminishing the contributions of others, I would like to extend particular thanks to Paul Hamilton, Amar Vutha, Nate Gilfoy, and Eric Hudson, in addition to those mentioned earlier, for numerous valuable conversations over the years; each of them has on numerous occasions asked me a question I couldn't immediately answer, or explained something I didn't understand about atomic or molecular physics, and I am grateful to them for it.

Finally, I would like to thank my advisor, Dave DeMille. His patient optimism, intellectual thoroughness, and extraordinary powers of explanation have been tremendously helpful for maintaining morale in the face of the null measurements, calculational setbacks and unexpected complications of experimental physics. It is difficult to imagine a more supportive environment for carrying out dissertation research than the one Dave has created in his group.

Abstract

Development of Techniques for Cooling and Trapping Polar Diatomic Molecules

David R. Glenn

2009

The study of ultracold dipolar molecules is an important emerging frontier in atomic physics. This thesis discusses the development of techniques for cooling diatomic molecules, focussing specifically on the idea of using a microwave frequency quasi-optical dipole trap for evaporative cooling. A prototype for such a trap has been designed, constructed, and tested. In order to load the microwave trap, a helium buffer gas cooled molecular beam source has been developed and characterized in a variety of flow regimes, ranging from the effusive (thermal mean velocity, moderate flux), to the deeply hydrodynamic (large forward velocity, high-flux, high collimation). We explain the development of this source in detail. In particular, we describe recent work towards demonstrating direct laser cooling of a hydrodynamic SrF molecular beam. We have identified a set of quasi-closed transitions which should enable more than 10^4 photon scattering events, sufficient to decelerate a hydrodynamic beam to the Doppler limit. We present experimental results demonstrating optical deflection of a SrF beam by radiative force using this scheme, in which each molecule scatters on the order of 150 photons, limited by its interaction time with the lasers.

Chapter 1

Introduction

1.1 Molecules in Modern Atomic Physics

Atomic physics has seen rapid and diverse growth during the past two decades. Significant advances in the cooling and trapping of atomic systems [1], have lead to the appearance of a whole sub-field concerned with the study of ultracold and condensed quantum gasses. The development of optical frequency combs [2], together with improved trapping and frequency-comparison technology, have given rise to a new generation of neutral atom [3] and single-ion [4] clocks with accuracy surpassing that of the Cs standard. Starting with Shor's discovery of a quantum algorithm for factoring large numbers in polynomial time [5], there has been an explosion of effort directed towards development of methods for the assembly and coherent manipulation of collections of qubits; both trapped ions [6][7]and neutral atoms with Rydberg excitations [8][9] show considerable promise as candidate systems in this respect. At the same time, precision measurements of atoms have advanced knowledge on a number of fronts, including searches for the electron dipole moment [10] and parity violation beyond the predictions of the standard model [11], and may soon allow laboratory tests of general relativity [12]

Remarkably, most of these accomplishments have been achieved using just a few atomic species: current atom cooling and trapping techniques are limited for the most part to alkali metals and the alkaline-earths. It is therefore unsurprising that one rapidly expanding frontier of the field is the search for new methods to cool and control more complex atoms, as well as simple *molecular*

systems [13]. Cold diatomic molecules in particular, while challenging to manipulate in certain respects, promise to yield distinct and interesting opportunities for study. Their internal rotational and vibrational structure gives rise to electric dipole transitions over a range of energies many orders of magnitude wider than those present in atoms. Furthermore, the large electric polarizability of a number of heteronuclear diatomic species enables them, when subjected to external electric fields, to interact at large distances through dipole-dipole interactions:

$$E_{dip-dip} = \frac{\vec{\mu}_1 \cdot \vec{\mu}_2 - 3(\hat{r} \cdot \vec{\mu}_1)(\hat{r} \cdot \vec{\mu}_2)}{r^3} \quad (1.1)$$

(Here, $\vec{\mu}_1$ and $\vec{\mu}_2$ are the dipole moments of the molecules, and \vec{r} is their separation.) These interactions are strong and anisotropic, making them qualitatively different from those governing the collective behavior of cold atoms, and suggesting a wide range of novel scientific and technical applications.

This thesis describes work towards the development and implementation of a new technique for trapping and cooling polar molecules using a microwave resonant cavity [14]. Such an approach should circumvent many of the limitations that have hitherto impeded the realization of samples of trapped, ultracold polar molecules. The present Chapter will provide a brief summary of the field of molecule cooling, including an outline of the current status of efforts in the community to produce ultracold molecular samples and the difficulties associated with them (section 1.2), as well as an overview of the various physics goals that one can hope to achieve (section 1.3). It will conclude with a description of our own technique and its advantages in this context (section 1.4).

1.2 Survey of Techniques for Cooling Molecules

1.2.1 Laser Cooling and Trapping of Atoms

Most of the recent progress in atomic physics can be traced to the realization of methods for exerting radiative forces on neutral atoms. By slightly detuning a narrow-band laser relative to an atomic transition, it is possible to create a situation whereby atoms of a particular velocity class in a thermal sample are Doppler shifted into resonance and preferentially excited. If they relax to the same initial state with high probability, a large number of photons can be scattered. Each

absorption event imparts a momentum kick $\hbar k$ in the direction of the laser beam; however, the average momentum transfer over many spontaneous emissions is zero because the direction of the emitted photon is random. The net result, for a red-detuned laser, is a velocity dependent force that opposes the motion of the atoms. Atomic beams may be decelerated either by sweeping the laser frequency through resonance with a range of velocities [15], or by continuously varying the atomic transition frequency itself through the application of spatially-dependent Zeeman shifts [16]. Alternatively, a sample of atoms in a vapor cell may be cooled by overlapping three pairs of counter-propagating laser beams to form an "optical molasses" [17]. Combining such a geometry with the 3D linear magnetic field gradient produced by quadrupole coils in the anti-Helmholtz configuration, one obtains the ubiquitous magneto-optical trap (MOT) [18]. This is a common starting point for many modern atomic physics experiments.

The other key enabling technique in atom cooling experiments since the mid 1990s has been forced evaporative cooling [19]. This procedure involves the confinement of atoms in a trap (magnetostatic or optical), in which they undergo a series of elastic collisions and arrive at thermal equilibrium. The atoms with the highest kinetic energy are then removed, either by decreasing the depth of the trapping potential or by preferentially inducing radio-frequency transitions to an untrapped state in atoms at the edge of the trap. When the remaining atoms rethermalize, their average energy is lower, and their density is increased because they occupy a smaller volume near the trap center. By repeating these steps many times, the total number of trapped atoms can be traded away for greatly increased phase space density. The use of evaporative cooling now allows atomic ensembles to be brought routinely to nanokelvin temperatures, and has enabled the observation of multiple quantum phases of matter including BEC[20], degenerate Fermi gas[21], and Mott-insulator[22].

Unfortunately, direct extension of these techniques for neutral atom cooling to molecules is made difficult by the complexity of molecular spectroscopic level structure. Standard laser cooling relies on the availability of a cycling transition, in which an atom is repeatedly excited and spontaneously emits to relax back to the same initial state. Such a procedure is not normally viable in molecules, which have a vibrational level structure that allows for relaxation to many spectrally distinct states. In general, the only way to scatter enough photons to obtain significant cooling is by applying a laser for each vibrational transition, which quickly becomes prohibitively complex in most cases. Despite

the practical difficulties involved, proposals have been made to use a series of repump lasers [23][24] or spectrally broad optical pulses [25] to close the loop by re-exciting from multiple vibrational states. In fact, a new method for establishing a quasi-closed set of laser cooling transitions in the SrF molecule is demonstrated in Chapter 4 of this thesis. Nevertheless, the conventional wisdom in the field has been that laser cooling is intractable in molecules, and that new methods must be found to cool from room temperature to the $\lesssim 1\text{mK}$ range.

Evaporative cooling is also more difficult to implement for molecules than for atoms. The challenge here is the impossibility of arranging a static electromagnetic field maximum in free space, combined with the fact that the ground state of an atom or molecule must always decrease in energy as the strength of the static field increases. Since the center of the static trap must always have a field minimum, only excited states (whose energies increase with increasing field strength) can be trapped and cooled. Inelastic collisions allow such excited atoms or molecules to scatter into the strong-field seeking ground state and hence to become ejected from the trap. Evaporative cooling can only be successful if the ratio of rates of thermalizing elastic collisions to loss-inducing inelastic collisions exceeds some minimum value. In some atomic species, this requirement can be satisfied and evaporative cooling may be achieved. The rotational structure of diatomic molecules, however, greatly increases the rate of inelastic collisions compared to that of atoms, making the prospects for evaporative cooling of molecules in static traps seem rather poor [26].

1.2.2 Direct Cooling Methods

As a result of these challenges, a number of new techniques have been developed for the cooling and trapping of molecules[13][27]. These may be grouped into two broad classes: (i.) those that directly cool molecules obtained from some thermal source, and (ii.) those in which molecules are assembled from pre-existing samples of cold atoms. Among the direct cooling methods, the most notable include buffer gas cooling [28], Stark slowing of supersonic beams [29], and selective guiding of the cold tail of a Boltzmann distribution [30]. These generally have the advantage of being independent of the level structure of the particular species being cooled, and have been employed to bring a wide range of species (CaH, NH, OH, CO, NO, PbO, NH₃) to temperatures of $\sim 1\text{-}100\text{ mK}$ in all degrees of freedom. Unfortunately, it appears that the significantly lower temperatures necessary for many of the applications described in section 1.3 below cannot be obtained by these

techniques without some new approach. This is because all of the cooling comes from thermalizing collisions with a cryogenic buffer gas, itself cooled to its practical limit either by refrigeration or supersonic expansion. In order to obtain lower temperatures, some other source of dissipation is required.

Buffer gas cooling involves bringing the molecules of interest into contact with a cold, non-reactive gas close to its boiling temperature¹ and allowing them to collisionally thermalize. Because the vapor pressure of the molecules at these temperatures is inevitably very small, collisions with the walls of the vessel effectively remove them from the sample. It is therefore necessary to trap the molecules before they reach the walls, or to extract them by entrainment in a beam of buffer gas atoms flowing out of the cell. Molecules can be introduced into the system by flowing a thermal beam into the cell, or by laser ablation of a solid precursor. The experiments described in this thesis depend for the most part on a cryogenic He buffer gas beam source, and a more detailed description of the process is given in Chapter 2.

The technique of **Stark deceleration** uses supersonic expansion from a nozzle, typically seeded in a heavy, inert carrier gas such as Xe, to cool the molecules in their translational and internal degrees of freedom. The result is a beam with a high mean velocity ($\sim 3 \times 10^2 - 10^3$ m/s) [33], and a low spread of forward kinetic energies (typically on the order of ~ 1 K). Rapidly switched, high voltage electrodes are then employed to decelerate a packet of molecules close to rest in the lab frame via the Stark effect. The electrodes are turned on as the synchronous bunch of low-field seeking molecules approaches, and off again after they have passed, causing them to climb a series of potential hills. Transverse focussing is achieved automatically, since the field minimum is always along the beam axis, midway between the electrodes. The end result after ~ 100 stages of deceleration is a packet of about 10^4 molecules traveling at a mean speed of roughly 20 m/s. (This corresponds to a translational temperature of 10s - 100s of mK, depending on the molecule.) High-field seeking states can also be decelerated using the technique of alternating gradient deceleration [34], although this tends to exhibit lower phase-space acceptance and is highly sensitive to details of the switching times.

Electrostatic **quadrupole filtering** uses DC Stark shifts to select the low-velocity tail of a Boltzmann-distributed effusive beam. The desired molecules are produced in a thermal source,

¹typically ^3He (0.5 K) [31], ^4He (4.2 K) [28], or Ne (15 K) [32]

typically either a room-temperature reservoir [35] or a helium buffer gas beam source [36]. They are allowed to flow out of the source through an aperture, next to which is situated the entrance to an electrostatic quadrupole guide. Weak-field seeking molecules of sufficiently low transverse kinetic energy are captured and funneled along the field minimum at the center of the guide, whereas helium buffer gas or contaminants from the oven are unguided and diverge in a cosine-distributed beam. If a bend is introduced into the guide, only molecules with sufficiently low forward kinetic energy will be able to reach the exit; by setting the radius of curvature of the bend, one can control the velocity cutoff beyond which molecules cannot be guided around the corner. This technique, in conjunction with a cryogenic source, has been demonstrated[36] to deliver fluxes of $\sim 7 \times 10^{10} \text{s}^{-1}$ deuterated ammonia (ND_3) molecules at a mean velocity of 65 m/s, corresponding to a temperature of approximately 4.0K.² If the beam is Boltzmann-distributed, the number N of molecules obtainable at low kinetic energies E_K should decrease quadratically, $N \propto E_K^2/k_B T$. (Note that this assumes no collisions with buffer gas in the vicinity of the cryogenic nozzle; if the hydrodynamic “boosting” effect described in Section 2.1 occurs, the low-velocity tail of the distribution will not be present.)

1.2.3 Assembly Methods

The only approach that has yet been demonstrated to produce molecules at sub-mK temperatures is that of direct assembly from laser-cooled atomic precursors. This allows the full power of the atom cooling techniques outlined above to be brought to bear, albeit at the expense of limiting the available molecular species to those derived from alkalis, and of significant experimental complexity. The starting point for such experiments is generally an atomic MOT, or a pair of overlapped MOTs for the creation of heteronuclear species. Molecules can then be formed either by photoassociation [37], or by sweeping a magnetic field through a Feshbach resonance [38]. Photoassociation uses an intense laser to excite colliding atoms from continuum states to a bound excited electronic state of the molecule. This then decays with some probability to a highly excited vibrational state in the ground electronic manifold, depending on the relevant Franck-Condon factors. Feshbach association, on the other hand, works by magnetically tuning the interaction potential of the colliding atoms such that their energy matches that of a bound state in a higher electronic manifold of the molecule, producing

²Note, however, that this high flux depended on the delivery of $10^{17} - 10^{18}$ molecules/s into the cell by a capillary gas-handling line, which may prove unsustainable over long times for most species due to the formation of ice-plugs in the line.

a resonance. If the field is swept so that the energy of the bound state is adiabatically lowered during the collision, a weakly bound molecule is formed. With both methods, it is desirable to quickly transfer the resulting molecule into a lower-lying vibrational state to avoid rapid collisional losses. It has been shown that a series of resonant optical pulses can be used to transfer photo-associated RbCs molecules to the vibrational ground state [39]; more recently, stimulated Raman adiabatic passage (STIRAP) has been used to accomplish the same goal with $^{40}\text{K}^{87}\text{Rb}$ Feshbach molecules [40].

1.3 Applications

There is considerable interest within the atomic physics community today in finding new ways to cool polar diatomic molecules (of species more general than the alkalis) to sub-mK temperatures. A wide range of applications for cold and ultracold molecules has been proposed over the past several years; an excellent summary can be found in the review paper of reference [41]. While an exhaustive survey is beyond the scope of this document, we will attempt to highlight some of the most interesting and relevant applications in the following sections.

1.3.1 Many-body Physics

One compelling reason to pursue new strategies for cooling polar molecules is related to the proven utility of ultracold atoms for investigating interesting condensed-matter systems. Dilute, ultracold atomic gasses and condensates are clean, tunable many-body systems, whose internal and translational degrees of freedom can be precisely controlled [42]. Molecule systems, by virtue of their dipolar interactions (recall equation 1.1) are a natural extension to this subfield. Unlike neutral atoms³, which usually interact by van der Waals potentials ($E_{vdW} \propto r^{-6}$) weak enough to be modeled with contact interactions, the electric dipole interactions of molecules are strong and anisotropic, analogous to those of spins in a solid. It has been predicted, for example, that a variety of novel quantum phases can be observed in systems of dipolar bosons in 2D optical lattices, including insulating checkerboard states (ordered patterns with well-defined atom numbers at each lattice

³One exception is the work of the Stuttgart group, which has realized a BEC of ^{52}Cr atoms [43] and used a Feshbach resonance to reduce the strength of the contact interaction so that dipolar interactions are of nearly equal strength [44]. Nevertheless, molecules offer the possibility of accessing the regime where dipolar effects are strongly dominant; compared to ^{52}Cr (magnetic moment $6 \mu_B$), a typical polar molecule with electric dipole moment $\mu = ea_0$ experiences interactions $\left(\frac{\omega_{dip}}{6\mu_B}\right)^2 = \frac{1}{36} \left(\frac{2}{a}\right)^2 = 2087$ times stronger than ^{52}Cr .

site) and supersolids (ordered states with large atom number fluctuations at each site and a nonzero global order parameter)[45][46][47]. Quantum magnetism may be simulated by trapping polar molecules of two different rotational states on a lattice, also resulting in a variety of interesting phases [48]. In the absence of a lattice, it was pointed out in reference [49] that quantum phase transitions (in this case between a crystal and 2D superfluid) can be induced using microwaves and static electric fields to control the intermolecular interaction potentials. Somewhat more esoterically, it has been shown that, for a rapidly rotated system of dipolar bosons with a filling factor (ratio of vortex number to particle number) $\nu = 3/2$, the ground state exhibits non-Abelian statistics[50].

1.3.2 Quantum Information

Quantum information applications require the ability to assemble and coherently entangle a collection of two-level quantum systems (“qubits”). In the circuit model of quantum computing [51], it is sufficient to be able to perform a pair of orthogonal Bloch-sphere rotations independently on each qubit, as well as two-qubit entangling operations that rotate the state of one qubit depending on the state of another. It has been shown that polar molecules trapped in an 1D optical lattice with unit-occupancy satisfy these requirements[52]. By applying a \hat{z} -directed linear electric field gradient [$\vec{E}(x) = (E_0 + xE_1)\hat{z}$] along the length of the array, each molecule experiences a slightly different relative Stark shift between its ground ($J=0, m=0$) and first excited ($J=1, m=0$) rotational states, allowing microwave pulses to spectrally resolve the individual molecules to perform single qubit operations. Furthermore, if the minimum field is large enough to fully polarize the molecules ($E_0 \gtrsim B_c/\mu$, for B_c the rotational constant), then adjacent sites interact with strong dipole-dipole interactions to create entanglement⁴. For the case of the KCs molecule considered in reference [52], the interaction energy due to dipole-dipole interactions with the adjacent lattice site is $h \delta\nu = d_{\text{eff}}/(\lambda_l/2)^3 \approx 30$ kHz (where d_{eff} is the effective dipole moment of the polarized molecule in the lab frame and $\lambda_l = 1\mu\text{m}$ is the lattice wavelength). Microwave pulses of duration $\tau \geq (2\pi \delta\nu)^{-1} \approx 50\mu\text{s}$ are required to resolve these shifts; for coherence lifetimes on the order of several seconds (limited by decoherence due to lattice-induced heating), this allows $\sim 10^5$ coherent entangling operations. State initialization in this system is automatic, since the molecules must already be in their rotational ground state to participate in the evaporative cooling step required to load the lattice. Readout

⁴These interactions are turned on continuously in this picture. However, selective entanglement can be generated by using the same refocussing techniques demonstrated in the early liquid-NMR quantum computing experiments.

is by state selective multiphoton ionization using pulsed lasers with resolution smaller than the rotational splitting $2B_e$.

Other proposals for quantum computing with polar molecules involve using their strong dipole interactions to couple them to superconducting microwave stripline resonators and superconducting qubits[53][54]. These ideas take advantage of the clean readout and gate control and convenient scalability of mesoscopic systems on the one hand, and the spectral stability and favorable decoherence properties of molecules compared to superconducting qubits on the other. Relatively deep (~ 1 K) traps can be fabricated by utilizing the high fields available at very small distances from the substrate, and the stripline itself can provide cavity-sideband cooling of its motion. One significant challenge of these proposals is loading of the trap; because the trap volumes must be very small to achieve strong coupling to the resonator, a new technique for producing high initial molecule densities from which to load them must be found.

1.3.3 Precision Measurement

Diatomic molecules are known to have favorable properties for several types of precision measurement. In most cases, such measurements amount to the determination of some spectroscopic frequency with high accuracy, and therefore benefit in a number of ways from the availability of samples at low temperatures. These include the reduction of Doppler broadening, as well as increased frequency resolution due to longer interaction times with probing fields, particularly if the molecules can be confined in a trap of some kind. Furthermore, because most diatomic species have rotational constants $B_e/k_B \sim 1$ K, room temperature and oven-generated thermal sources have their population spread out over a large number of rotational states. By cooling the internal degrees of freedom to collapse the Boltzmann distribution of rotational states, significant improvements in signal to noise can be obtained. It should be noted that the temperature requirements for realizing these benefits are not as stringent as those for most of the many-body physics and quantum information applications described above; high molecule densities in the sub-1K regime are sufficient in most cases. Experiments that could conceivably be improved using the properties of diatomic molecules include searches for the electric dipole moment (EDM) of the electron, measurements of nuclear spin-dependent parity violation, and time-variation of the proton/electron mass ratio, m_p/m_e .

In EDM experiments, external parallel electric and magnetic fields are switched between aligned and anti-aligned configurations to search for a possible Stark-induced energy shift due to an electric dipole moment in the direction of the electron spin. One considerable advantage of paramagnetic molecular systems in this context is the large enhancement of the effective electric field seen by the electron inside the molecule[55]. The enhancement factor is given by $E_{\text{eff}} = QP$, where $Q \sim 4 \cdot 10^{10}$ V/cm $\times \left[\frac{Z}{80}\right]^3$ (for Z the nuclear charge) is determined by relativistic effects and molecular structure, and P is the degree of polarization. Because the energy scale for polarizing molecules is usually that of the rotational constant B_e (which is typically several to several tens of GHz)⁵, it is relatively easy to obtain full polarization ($P \approx 1$) with laboratory-scale fields. By contrast, for typical paramagnetic atoms, the energy scale for polarization is the electronic transition energy (usually hundreds of THz) and the polarization factor at fields as high as ~ 100 kV/cm is only $P \approx 10^{-3}$. Details of molecular structure can also be of use in other ways; for example, in the PbO experiment, an Ω -doublet structure affords access to an additional set of symmetry-reversals that can be used to cancel some sources of systematic error. Two cold-beam based molecular EDM experiments are currently in development: one uses a cold, supersonic YbF beam [56], the other a hydrodynamic buffer-gas cooled beam of ThO [57] similar to the one described in Chapter 2 of this thesis.

Nuclear spin-dependent **parity violation** in atomic and molecular systems arises from two sources: intranuclear weak interactions that magnetically couple to the spin of orbiting electrons (the so-called "anapole moment"), and a vector electron, axial-vector nucleon ($V_e A_n$) coupling mediated by Z_0 -exchange. The former effect has been measured once, in atomic ^{133}Cs [11], the latter not at all. An experiment is currently underway at Yale [58] to measure both interactions in a range of nuclei, using their different dependence on atomic number⁶ to separate the two effects. The advantage of molecules in this context again arises from the existence closely-spaced rotational states of opposite parity. These can be Zeeman-shifted to near-degeneracy, where interference between the weak interaction and an applied RF electromagnetic excitation is expected to produce a measurable effect. The current version of the experiment uses a ^{137}BaF beam cooled to ~ 15 K by supersonic expansion from a pulsed valve. This may be upgraded to a high-flux beam from a hydrodynamic buffer gas source in the future.

⁵For the PbO experiment of reference [55], the scale is even smaller ($\sim 12\text{MHz}$) due to the Ω -doublet structure of the molecule.

⁶Anapole couplings scale as $A^{2/3}$, whereas the $V_e A_n$ is independent of atomic number.

It has been argued that diatomic molecules can also provide a highly sensitive probe for **time variations in the proton to electron mass ratio**. These proposals are somewhat unique in that they take explicit advantage of molecular vibrational structure. The idea is to look for m_p -dependent shifts in the vibrational structure of the molecule, relative to a reference clock based on an optical atomic transition that effectively holds m_e fixed. It can be shown[59] that the anharmonic shape of the internuclear vibrational potential results in m_p -dependence of the level spacing that is largest for excitations about halfway up the potential, and minimal near the ground state and the dissociation limit. Proposals have been made to drive two-photon optical Raman transitions between deeply- and moderately-bound states of Sr_2 [60], as well as to probe microwave transitions between a moderately-bound state of the ground electronic potential and a deeply-bound state of an excited electronic potential in Cs_2 [59]. Homonuclear molecules are preferred because their vibrational excitations are insensitive to stray fields and black-body induced shifts, affording longer interrogation times. Both proposed experiments rely on the production of ultracold samples to give very narrow spectral lines, the former in a magic-frequency optical lattice.

1.3.4 Cold and Ultracold Chemistry

Another area of considerable interest is the study of collisions and chemical reactions at cold and ultracold temperatures.⁷ In the cold-collision regime (typically ~ 1 mK - 1 K), molecules are usually in their rotational ground state, and are slow enough to confine in electric or magnetic traps. By aligning their dipoles in external fields and interrogating them with mono-energetic atomic or molecular beams (as from a Stark slower - see section 1.2.2), collision and reaction cross-sections may be measured with greatly improved precision [61]. Furthermore, there exists the possibility of actively controlling reactions using externally applied fields [62]. At ultracold temperatures, on the other hand, collisions are governed by one or a few partial waves. This gives rise to a number of potentially interesting quantum effects, including purely tunneling-driven reactions [63] and inelastic collision cross sections that vary over several orders of magnitude due to magnetic field induced resonances with rotational states [64]. One particularly intriguing prediction is that of

⁷Note that, rigorously speaking, the term "ultracold" should refer specifically to the situation where the collision is described by a single partial wave, i.e. where the centrifugal barrier for $L = 1$ exceeds the relative kinetic energy of the incoming particles. For polar molecules interacting via a dipole-dipole potential, this occurs at extremely low (possibly \sim pK) temperatures. The convention in the community, however is to use "ultracold" interchangeably with "sub-mK", which is the temperature regime where collisions between neutral atoms interacting with van der Waals $1/r^6$ potentials satisfy this criterion.

“field-linked states”, in which a pair of dipolar molecules is bound together in an effective potential well that forms at extremely long range ($\sim 10^3 - 10^4$ a.u.). [65]. A great deal has been written about cold and ultracold chemistry, of which the effects listed above are just a small example. The interested reader is referred to the review paper [41] and the references therein for a more comprehensive introduction to the subject.

1.4 The Microwave Trap Experiment

This thesis describes work we have done to develop tools for producing samples of ultracold polar molecules. Collisional cooling, either sympathetic or evaporative, appears to be the most general approach for obtaining temperatures much lower than ~ 1 mK. The problem of high inelastic collision rates described in section 1.2.1 very likely precludes the use of a traditional static electric or magnetic trap. Our solution [14] is to trap using a time-varying field, which is allowed to have a free-space maximum amplitude, and is therefore able to trap the molecules in their rotational ground state. The magnitude of the AC Stark shift increases as the frequency of the applied field approaches resonance, hence it is most natural to operate at microwave frequencies where the detuning can be made small and the trap correspondingly deep.⁸ Veldhoven *et. al.* recently reported an AC trap for ground state ND₃ molecules operating at kHz frequencies [66] which had a depth of approximately 5 mK, almost two orders of magnitude less than the projected value of 500 mK for our microwave frequency trap. The design of our trap is described in some detail in Chapter 3; briefly, it consists of an open Fabry-Perot type resonator with $Q \sim 5 \times 10^4$, operating with 2 kW of input power at a frequency of 18.1 GHz. The operating frequency was chosen to be near-resonant with the lowest rotational transition of strontium oxide (SrO), our initial test species. It must be emphasized, however, that the microwave trap should be applicable to any diatomic with a sufficiently large dipole moment - nothing about the principle of its operation is specific to SrO.

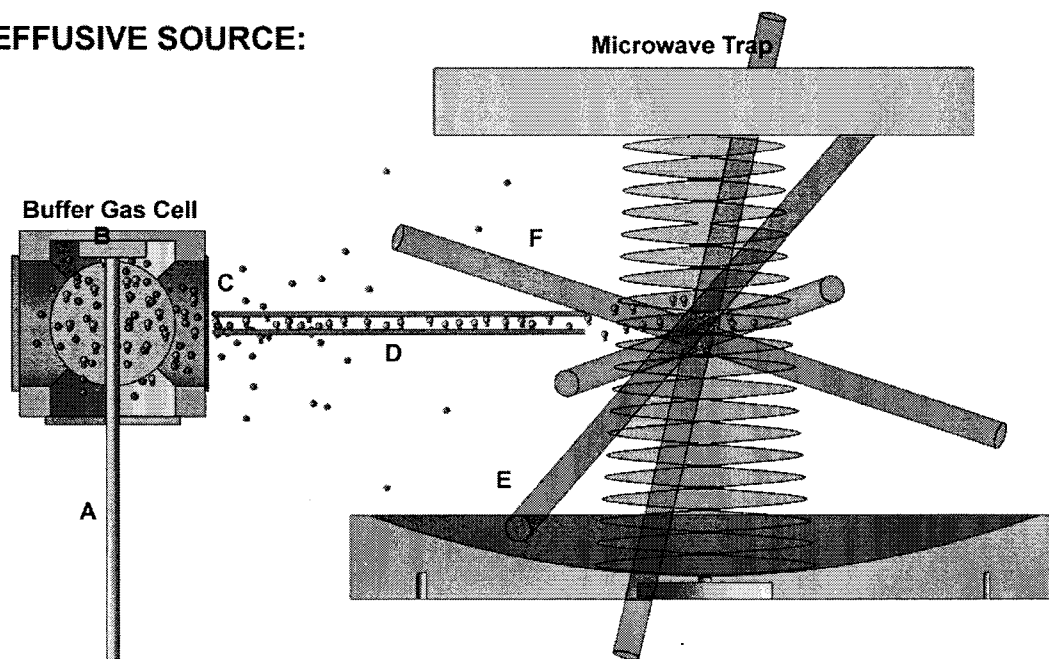
The ultimate goal of achieving a quantum-degenerate molecular gas requires (i) that the initial phase-space density of the trapped sample be sufficiently high to allow many thermalizing collisions over the trap lifetime, and (ii.) that the ratio of elastic to inelastic collisions remains favorable as

⁸Note that the lowest excited rotational level has an exceedingly long spontaneous emission lifetime (due to the small phase space associated with emission at long wavelengths) so that, unlike the case of the optical dipole trap, it is unnecessary to operate far off resonance to avoid heating by resonant scattering.

the sample is cooled to below the transition temperature. To satisfy the latter requirement, we note that two-body inelastic collisions should be eliminated by trapping in the rotational ground state. Losses should thus be dominated by background gas collisions, or three-body effects at high density. Furthermore, calculations for elastic collision cross sections during the evaporative cooling process seem relatively favorable. Because the trapped strong-field seeking states reside in the region of maximum field, they are electrically polarized. The resulting dipole-dipole interaction results in elastic collision sections (σ) that will increase as the temperature (T) of the molecules decreases ($\sigma \propto T^{-1/2}$) [26], so that collision rates (which scale as $\sim T^{1/2}$ for constant density) will not decrease as the sample cools. Thus, with sufficiently high initial density, it is essentially ensured that the trapped molecules can enter a regime of runaway evaporative cooling.

In order to obtain the required initial density for evaporation, our aim is to first load the trap using molecules pre-cooled by buffer gas cooling. As described in Chapter 2, a cryogenic buffer-gas beam source can be operated in two distinct flow regimes. When the helium buffer gas density in the source is sufficiently low to allow effusive flow, the resulting molecular beam temperature in all degrees of freedom (internal and translational) approaches 4.2 K, but the molecule flux is relatively low. On the other hand, if the helium density is turned up so as to give rise to hydrodynamic flow, the brightness of the molecular beam increases by several orders of magnitude, at the expense of much higher forward velocities. The estimated yield of the effusive source we have developed (roughly 2×10^6 molecules of SrO, our initial test species, trapped in a volume of $\sim 4 \text{ cm}^3$ at temperature $T \sim 500 \text{ mK}$) gives a density that is likely too small to initiate runaway evaporative cooling. One possible approach to solving this problem is by sympathetic cooling with alkali atoms, confined in an overlapping MOT, to bring the density above the required threshold. The geometry of the experiment has been designed to allow for this. Alternatively, we have recently demonstrated a new technique for applying radiative forces to the SrF molecule, which should ultimately afford the possibility of slowing and cooling a hydrodynamic beam to the Doppler limit $T_D = \frac{\hbar\gamma}{2k_B} = 0.17 \text{ mK}$. Such a source could conceivably allow the delivery of as many as $\sim 10^{10}$ molecules over the trap lifetime, and would place much less stringent requirements on the intra-cavity electric field strengths required for trapping. This is obviously a very attractive approach; the idea for laser-cooling of SrF and experiments to demonstrate the existence of a quasi-cycling transition in that system are presented in Chapter 4.

EFFUSIVE SOURCE:



HYDRODYNAMIC SOURCE:

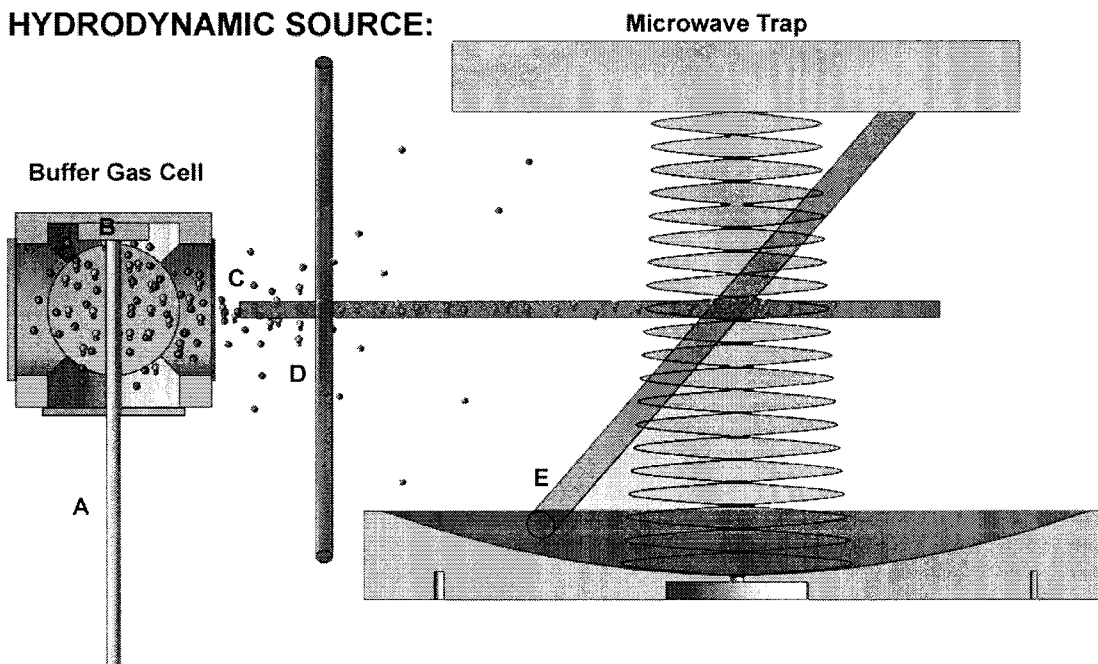


Figure 1.1: Schematic of experimental setup for loading of the microwave trap. Top panel shows an effusive beam source for SrO molecules; bottom panel shows a hydrodynamic source for SrF. A. Ablation laser beam. B. Solid molecular precursor. C. Extraction aperture. D. Electrostatic quadrupole guide for effusive source; transverse and longitudinal laser cooling beams for hydrodynamic source. E. Loading / detection laser beam. F. MOT beams used to trap atoms for sympathetic cooling for effusive source.

A schematic illustrating the trap loading scheme for each beam source is shown in figure 1.1. The process begins with the production of a molecular vapor by laser ablation of a solid target using a pulsed laser (A). The ablated molecules are pre-cooled by thermalization in helium buffer gas, held in thermal contact with a simple cryostat ($T \sim 4$ K). For sufficiently high helium density, the molecules are cooled to the equilibrium temperature in both their translational and internal degrees of freedom a small distance from the ablation point. Some fraction of the thermalized sample is then extracted from a hole (C) in the buffer gas cell to form a molecular beam. With gas flow in the effusive regime, the molecules exit at the temperature of the buffer gas in all degrees of freedom. However, the mean free path of the molecules must be greater than the hole diameter in order to avoid hydrodynamic boosting to the velocity of the lower-mass He atoms. This gives rise to an optimal extraction efficiency of $\sim 10^{-5}$ for a circular aperture, when the He density is such that the molecules thermalize in a length equal to the distance between the target and the aperture. In the hydrodynamic source, on the other hand, the helium density is maintained several orders of magnitude higher, in order to fully entrain the molecules before they diffuse to the cell walls. This affords extraction efficiencies on the order of 10% of the total ablation yield, but the initial kinetic energy of the molecules exiting the aperture is typically ~ 100 K or higher. In order to trap the molecules in a region of low background pressure, it is necessary to convey them away from the continuous He flow of the buffer gas source. For the effusive beam, an electrostatic quadrupole guide [35] is used to transport the weak-field seeking, rotationally excited states (primarily $|J = 1, m = 0\rangle$ for a rigid rotor such as SrO) in the molecular beam away from the buffer gas cell (D). For the hydrodynamic SrF source, transverse laser-cooling beams are applied to collimate the $|N = 1\rangle$ molecules in two dimensions, ideally producing a beam with divergence $v_{\text{Doppler}}/v_{\text{fwd}} \sim 10^{-3}$ radians. As the SrF molecules approach the trap, they are continuously decelerated by a frequency-chirped longitudinal cooling beam such that they reach the trapping region at forward velocities approaching the Doppler limit. Helium atoms escaping the cell (which are not affected by the electric quadrupole field or the transverse cooling beams) are pumped away before the molecules enter a differentially pumped trap region. This makes it possible to maintain ultra-high vacuum (UHV) conditions in the trap itself. Once the molecules enter the trap region, laser light (E) optically pumps them from the (rotationally excited) guided or collimated state to the rotational ground state for trapping. This dissipative mechanism allows continuous loading into the trap. For molecules from the effusive source, an initial stage of sympathetic cooling by collisions with alkali atoms trapped in an overlapping MOT (F) increases

the phase space density above the threshold for runaway evaporative cooling. The molecules are then evaporatively cooled by one of several standard techniques for ejecting fast-moving molecules, such as the RF knife method [19]).

Chapter 2

Buffer-Gas Cooled Molecular Beams

2.1 Introduction to Buffer Gas Cooling

Loading of the microwave trap requires a beam source capable of providing large fluxes of molecules at temperatures of $\sim 1\text{K}$ or less. As described in the previous chapter, a number of methods have been developed by various groups to produce samples of molecules in this temperature range. Arguably the most flexible and technically straightforward of these is buffer gas cooling.

The buffer gas technique proceeds from the insertion of the atoms or molecules to be cooled into a cell filled with a cold gas of inert atoms, with which they then thermalize by elastic collisions. The most common method of introducing the species of interest is by means of laser ablation of a solid precursor housed in the cell [67]. Some experiments have instead made use of capillary feed lines to convey gas from an exterior reservoir [36], or an entrance aperture in the buffer gas cell through which a beam from a nearby oven may be directed [68]. These methods have the advantage of producing high input fluxes, but are harder to operate for extended periods of time and require significantly more challenging thermal engineering. The choice of buffer gas is restricted to noble atoms with sufficiently high vapor pressure at the desired final temperature to allow thermalization to occur over a reasonably short distance. This effectively limits the possibilities¹ for cold beam

¹Some recent work in the Doyle group at Harvard has focussed on using Ne as a buffer gas for hydrodynamic beam sources [32], primarily on the grounds that the very low vapor pressure of Ne at 4K makes all surfaces in thermal contact with their liquid helium bath into highly efficient cryopumps. In most of our experiments however, we have been able to obtain sufficiently high pumping speeds with charcoal cryosorbs to obviate the problem of collisions with residual background helium. The technical difficulty of maintaining a $\sim 15\text{K}$ buffer gas cell in a 4K cryostat in order to obtain reasonable buffer gas densities, combined with the disadvantage of having a $\sim 15\text{K}$ final rotational temperature distribution in the molecular

sources to ^3He and ^4He , with the saturated vapor pressure curves shown in Figure 2.1. Although ^3He allows lower ultimate temperatures to be obtained, its high monetary cost precludes use in an open cell of the type needed to produce a beam. We have therefore chosen to use ^4He .

By working through the kinematics of hard-sphere elastic collisions between buffer gas atoms and the species of interest, it can be shown [69] that the rate of thermalization with respect to the number of buffer gas collisions is given by

$$\frac{dT_N}{dN} = \frac{-2Mm_B}{(M + m_B)^2}(T_N - T_B) \quad (2.1)$$

where T_N is the temperature of the species to be cooled (of mass M) after N collisions with buffer gas atoms (of mass m_B) at temperature T_B . The solution to this equation for initial temperature $T_{N=0}$ is then

$$T_N = T_B + (T_{N=0} - T_B) \exp\left(\frac{-2Mm_B}{(M + m_B)^2}N\right) \quad (2.2)$$

In our apparatus, laser ablation is used to introduce molecular species of mass $M \sim 100\text{amu}$ into the ^4He buffer gas ($m_B = 4\text{amu}$) cell, with a characteristic initial temperature on the order of $T_{N=0} \sim 1000\text{K}$ [28]. According to equation 2.2 then, approximately $N_{th} \sim 100$ collisions are required to thermalize the molecules to within 10% of the 4.2K buffer gas temperature. This sets the helium density needed for thermalization in a cell of a given size. Most of our beam development work has used the cubic cell of side length $D = 3\text{cm}$ shown in Figure 2.1. For typical molecule-helium collision cross sections of $\sigma_{M-\text{He}} \sim 10^{-14}\text{cm}^2$, and a desired thermalization length $L_{th} \sim 3\text{cm}$, the necessary helium density is approximately $n_{\text{He}} \approx \frac{N_{th}}{\sigma_{M-\text{He}}L_{th}} = 3 \times 10^{15}\text{cm}^{-3}$. (Here it is assumed that the molecules, with $M \gg m_B$ travel ballistically for most of the thermalization process, so that $L_{th} = N_{th}\lambda_{M-\text{He}}$, where $\lambda_{M-\text{He}}$ is the mean free path of the molecules in the buffer gas.)

In the standard picture of ablation into a cell filled with static buffer gas, the molecules leave the target ballistically and travel a distance L_{th} to thermalize, then diffuse outwards thereafter in a roughly spherical pattern. (This behavior has been seen in numerical simulations [69], and is consistent with optical absorption measurements made in the cell.) A circular aperture of diameter d_{ap} may be placed in one wall of the cell to allow the molecules to escape and form a beam, where

beam, seems to make Ne buffer gas less attractive than ^4He for our purposes.

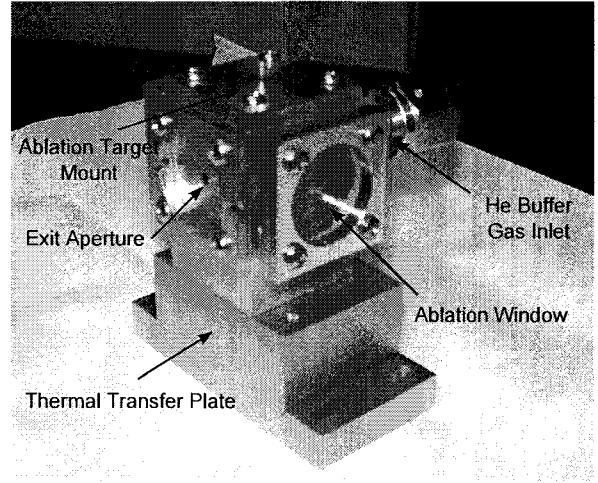
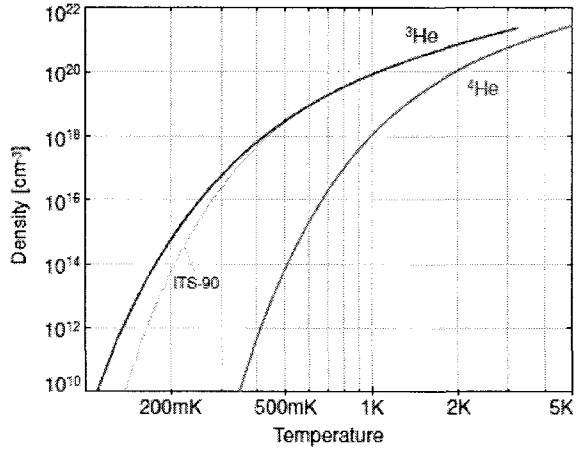


Figure 2.1: Helium buffer gas cell. **Left:** Saturated vapor density of helium as a function of temperature, obtained from [70]. Note that the 4K saturated density of ${}^4\text{He}$ exceeds the density required to thermalize in a $D = 3$ cm ($n_{\text{He}} \geq 3 \times 10^{15} \text{cm}^{-3}$) by about 5 orders of magnitude. **Right:** Photograph of the $D = 3$ cm cell used in our hydrodynamic beam experiments. Molecules are ablated from a solid target with a pulsed Nd:YAG laser that passes through the window on the side of the cell, and become entrained in helium entering through an inlet in the back face. Helium and molecules exit the cell through the $d_{\text{ap}} = 3$ mm diameter exit aperture.

$d_{\text{ap}} \lesssim \lambda_{M-\text{He}}$ is selected such that the molecules pass through the aperture effusively and thereby maintain a kinetic energy of $\sim 4\text{K}$ in all directions of motion. The optimal extraction efficiency η should be obtained if the characteristic size of the cell D is chosen to be equal to the thermalization length L_{th} , so that the molecules reach $\sim 4.2\text{K}$ as they arrive at the aperture. In this case, η is given by the ratio of the solid angle subtended by the aperture at the target to the solid angle into which the molecules expand. If we assume the molecules leave the target in a cosine distribution, with $\int \cos \theta d\Omega = 2\pi$, then

$$\eta = \frac{\pi d_{\text{ap}}^2 / 4}{2\pi L_{\text{th}}^2} \approx \frac{\lambda_{M-\text{He}}^2}{8(N_{\text{th}} \lambda_{M-\text{He}})^2} \approx 10^{-5} \quad (2.3)$$

Note again that $N_{\text{th}} \sim 100$. This estimate of the extraction efficiency for an effusive beam is independent of D or n_{He} ; it can, however, potentially be improved by as much as an order of magnitude by using a rectangular, slit-shaped aperture of dimensions $l_{\text{ap}} \times w_{\text{ap}}$, such that $l_{\text{ap}} \lesssim \lambda_{M-\text{He}}$ to ensure effusive flow, and $w_{\text{ap}} \sim 10 l_{\text{ap}}$. Otherwise, it is not possible to obtain significantly greater extraction with an effusive buffer gas beam source.

Increased molecule flux may, however, be obtained if the source is operated at higher buffer gas

density. When the density is increased (or, equivalently, the aperture diameter made larger for a fixed cell size) such that $d_{ap} \gg \lambda_{M-He}$, the molecules become entrained in the helium flow around the aperture and are more likely to exit the cell. This effect is clearly shown in the data of Section 2.4.1. The improved extraction efficiency is generally accompanied by an increase in the forward kinetic energy of the molecules forming the beam. In the vicinity of the aperture, molecules are struck from behind multiple times by the faster-moving helium atoms traveling out of the cell, with the result that their mean forward velocity is boosted to something approaching the helium velocity, v_{He} . Depending on the ratio of the aperture diameter to the helium-helium mean free path λ_{He-He} , the mean forward velocity of the helium exiting the aperture will be between its effusive and supersonic limits [71]:

$$\sqrt{\frac{8k_B T}{\pi m_{He}}} \leq v_{He} \leq \sqrt{2\gamma} \sqrt{\frac{2k_B T}{m_{He}}} \quad (2.4)$$

Here, $\gamma = C_P/C_V = 5/3$ for helium. At 4.2K, the helium velocity outside the aperture (and hence the mean molecule velocity) can range between 149m/s (for effusive He flow) to 241m/s (for fully supersonic He flow). For the molecules we typically use, with a mass exceeding that of helium by roughly a factor of ~ 25 , the resulting mean forward kinetic energy is between roughly $\sim 100K$ and $160K$.

Of particular experimental interest is the situation where the exit aperture of the buffer gas cell is made sufficiently large to allow all of the helium in the cell to be pumped out before the thermalized molecules have time to diffuse to the walls and stick. The characteristic timescale τ_{Pump} for emptying the cell of helium, and the time τ_{Diff} for molecules to diffuse through the buffer gas to reach the cell walls are given by [72]

$$\begin{aligned} \tau_{Pump} &= \frac{V}{C_{ap}} = \frac{4D^3}{\pi d_{ap}^2} \sqrt{\frac{2\pi m_{He}}{k_B T}} \\ \tau_{Diff} &= \frac{1}{\kappa_D} \left(\frac{D}{\pi}\right)^2 = \frac{16n_{He}\sigma_{M-He}}{3} \sqrt{\frac{\mu}{2k_B T}} \left(\frac{D}{\pi}\right)^2 \end{aligned} \quad (2.5)$$

Here, $\kappa_D = \frac{3}{16n_{He}\sigma_{M-He}} \sqrt{\frac{2k_B T}{\mu}}$ is the diffusion constant for the molecules in helium, with μ the re-

duced mass, and $C_{ap} = \frac{\pi d_{ap}^2}{4} \sqrt{\frac{k_B T}{2\pi m_{He}}}$ is the conductance of the aperture [73].² For our $D = 3\text{cm}$ cell, operating at a helium density $n_{He} \sim 5 \times 10^{16}\text{cm}^{-3}$, we therefore require an aperture diameter $d_{ap} > \left(\frac{3}{2}\pi^{3/2} \frac{D}{n_{He}\sigma_{M-He}} \sqrt{\frac{m_{He}+m_M}{m_M}}\right)^{1/2} \approx 2\text{mm}$ to obtain $\tau_{Pump} \ll \tau_{Diff}$ and thereby access the fully entrained regime. Beams formed in this way have been shown to extract as much as 40% of the single-shot ablation yield of a Yb target [74], and are furthermore extremely well-collimated, with 4K transverse velocity distributions $\Delta v_{Dopp} \sim 40\text{m/s}$ (FWHM) and mean forward velocities $v_z \sim 200\text{m/s}$. This makes them highly attractive for a number of molecular beam experiments, including the parity-violation experiment in BaF and electron EDM experiment with ThO being carried out in the DeMille group. We have therefore made some effort to develop and characterize these sources, as described in Section 2.6 and Chapter 4 of this thesis.

2.2 Molecule Selection

Compared to other methods for cold molecule production, buffer gas cooling is notable for its flexibility in terms of the wide range of molecular and atomic species to which it can be applied. Our cryogenic beam development work has largely focussed on three molecules: SrO, BaF, and SrF. We initially identified SrO as the molecule of choice for demonstrating microwave trapping, due to its large dipole moment ($\mu = 8.9$ Debye), laser diode-accessible optical transition wavelength ($\lambda = 786\text{nm}$ for the $|X, v = 0\rangle \rightarrow |A, v' = 3\rangle$ transition), and its rotational constant ($B_c = 10.14\text{GHz}$), which affords the possibility of acquiring significant power from DBS-band klystron amplifiers at microwave frequencies close to resonance with the $J = 0 \rightarrow J' = 1$ transition. For the experiments directed towards laser cooling of molecules described in Chapter 4, it was necessary to find species with highly diagonal Franck Condon factors to facilitate the scattering of large numbers of photons, and both BaF and SrF satisfy this requirement ($\beta_{0,0} = 0.98$ for SrF, and $\beta_{0,0} = 0.95$ for BaF). Both species also have relatively large dipole moments ($\mu = 3.5$ Debye for SrF and $\mu = 3.2$ Debye for BaF), and electronic transitions that can be excited with diode lasers. The existence of a metastable $A'^2\Delta$ state lying below the $A^2\Pi$ state in BaF effectively doubles the number of repump lasers required and therefore makes it less favorable than SrF for laser cooling; however, the fact that it was already being employed in another experiment in our group made it a useful test species for beam development

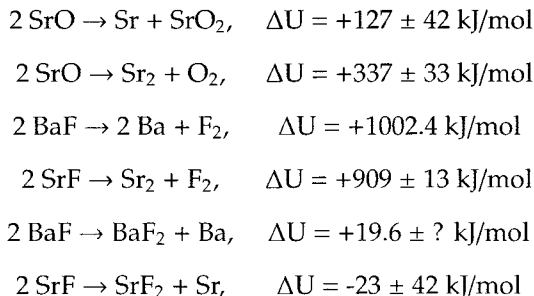
²In fact, this is the effusive conductance of the aperture; the conductance for deeply hydrodynamic flow may be somewhat higher. If anything, this would decrease the minimum required aperture diameter for full entrainment slightly.

until the appropriate lasers for SrF could be assembled.

Evaporative cooling in a microwave trap requires the molecular species under consideration to be stable against two-body chemical reactions with themselves. Relevant values from the literature for bond strengths in our molecules are summarized in the table below:

Bond	Bond Energy	Ref.
Sr - O	425.5 ± 16.7 kJ/mol	[75]
Sr - F	541.8 ± 6.7 kJ/mol	[75]
Ba - F	580.6 kJ/mol	[76]
Sr - O ₂	226 ± 25 kJ/mol	[77]
SrF - F	565 ± 42 kJ/mol	[78]
BaF - F	561 kJ/mol	[76]
Sr - Sr	15.5 ± 0.4 kJ/mol	[75]
O - O	498.36 ± 0.17 kJ/mol	[75]
F - F	158.78 kJ/mol	[75]

Estimated reaction energies are therefore as follows:



Thus, while SrO is unlikely to undergo 2-body chemical reactions in a trap, the situation is less clear with BaF and SrF. More accurate data for the BaF-F and SrF-F bond strengths may be required before proceeding with microwave trapping experiments with these species.

The results of calibrated fluorescence measurements for SrO at high helium flow rates may point to a potential problem in forming high flux hydrodynamic beams with that molecule. Using our $D = 3$ cm cell with an aperture diameter $d_{ap} = 3$ mm and helium densities $2 \times 10^{16} \text{ cm}^{-3} \leq n_{He} \leq 2 \times 10^{17}$, we have fairly consistently observed integrated SrO signal intensities some two orders of magnitude

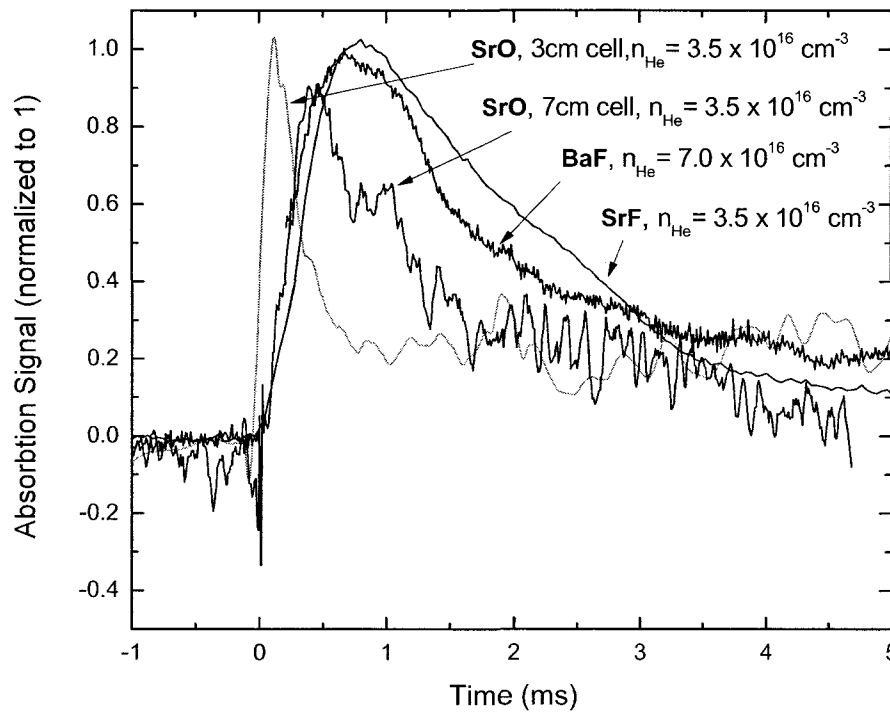


Figure 2.2: Comparison of in-cell absorption time traces for SrO, BaF and SrF in the hydrodynamic helium flow regime. The data were all obtained at different times using direct absorption spectroscopy. All data were collected in the $D = 3\text{cm}$ cell, except for the SrO trace labeled $D = 7\text{ cm}$. The data have been normalized such that the peak absorption is 1 in each case, in order to facilitate comparison the time characteristics of the traces. Several points were also removed from the $D = 7\text{ cm}$ SrO trace around $t = 0$ in order to eliminate a spike in the data due to electrical pickup from the Q-switch of the ablation laser. These data clearly show that the signal decay time for SrO in the $D = 3\text{cm}$ cell is much faster than for the other species, and also much faster than the decay time for SrO in the $D = 7\text{cm}$ cell. The cause for this effect is not known; our current hypothesis is that buffer gas flow properties of the small cell somehow promote chemical reactions between SrO and other ablation products (other molecules, clusters, dust) that are not present in BaF or SrF.

lower than would be expected for extraction efficiencies of ~ 0.05 and ablation yields $\sim 10^{12}$ per shot obtained under similar conditions with other species. This seems to be the result of some interaction between the chemical properties of SrO and buffer-gas dynamics associated with the $D = 3$ cm cell at high flow rates. Figure 2.2 shows characteristic absorption traces obtained at various times in the $D = 3$ cm cell for SrO, BaF and SrF, normalized such that the peak absorption is equal in each case. It is immediately evident that the rate for the SrO signal to decay inside the cell is much more rapid than for the other species. This decay time is also considerably shorter than the expected time for molecules to diffuse to the walls of the cell τ_{Diff} , or the time for all of the helium in the cell to leave via the aperture, τ_{Pump} , both of which are on the order of tens of ms at these helium densities. The current hypothesis is that the SrO molecules are undergoing chemical reactions with each other or with other ablation products in the vicinity of the target; this was the explanation proposed for a similar effect seen in experiments directed towards the trapping of VO in a buffer gas cell in the Doyle group at Harvard [79]. Somewhat surprisingly, this effect was *not* observed at similar buffer gas density in our $D = 7$ cm cell, as shown in Figure 2.2. This is difficult to understand, and presumably depends on the specific details of hydrodynamic helium flow in the two cells.

2.3 Experiment Setup

2.3.1 Cryogenic Beam Source

Most of our buffer gas cooled beam development work was carried out using a slightly modified version of the IR-Labs model HDL14 liquid helium cryostat. The cryogenic and vacuum apparatus for that beam source has been described extensively in [69]; a brief description of the key features is included here for completeness. The cryostat consists of a 8.5ℓ liquid nitrogen bath and a 36.4ℓ liquid helium vessel, with a 14 inch diameter cold plate. Mechanical drawings of the cryostat and cold plate are in Appendix A. A high-purity aluminum shield extends from the nitrogen vessel to cover the 4K components of the cryostat and protect them from room temperature black-body radiation.³ The vacuum chamber housing the cryostat is of cylindrical cross section (outer diameter OD = 16 inches), with an ISO-500 bottom flange, and an o-ring seal to the cryostat at the top. A series of 6" CF viewports provide optical access at the height of the cold plate. In order to be able

³Recall that the radiative heat load due black-body emission scales as ΔT^4 . The inclusion of a shield at 77K has the advantage of transferring most of the radiative load due to the ~ 298 K interior surface of the vacuum chamber to the vessel containing liquid nitrogen, which has both a higher heat of evaporation and a lower monetary cost than liquid helium. [80]

to handle the high helium gas load of the beam source, vacuum was originally obtained using a large diffusion pump (Edwards HT16, pumping speed $S \approx 7200\ell/s$ for helium) mounted directly to the bottom of the chamber. (Protection from back-streamed pump oil and high temperature black-body photons was provided by a set of water-cooled baffles.) When it was recognized that charcoal cryosorbs [81] could be used to make high-capacity helium pumps with comparable or better pumping speed, the diffusion pump was eliminated and a bottom flange installed with a long rectangular window (of dimensions $10.5'' \times 1.5''$) for observing the molecular beam at various points.

The buffer gas cell is mounted to the cold surface of the cryostat via an intermediate transfer plate which allows some flexibility in positioning.⁴ Most of the SrO measurements described in [69] were made with a relatively large, cubic brass cell of dimension $D = 7\text{cm}$; more recent beam work has primarily used the $D = 3\text{cm}$ copper cell shown in Figure 2.1. Helium gas is supplied to the cell through a copper tube that is thermally anchored to both the 77K and 4K vessels. The temperature of the cell and various other cold surfaces is monitored using diode thermometers (Lakeshore Cryogenics DT-670). Molecules are introduced into the cell through ablation of a solid target by a pulsed Nd:YAG laser (Quantel Big Sky CFR200), using 30mJ pulses at 1064nm, focussed onto the target by a $f = 50\text{cm}$ achromatic doublet lens.

2.3.2 Detection Methods

The detection of small numbers of diatomic molecules is made challenging, compared to typical experiments with alkali atoms, by the absence of cycling transitions. Typically, only a single photon can be absorbed or emitted before the internal state of the molecule is changed. We have employed several methods of detection during the development of the buffer gas beam source, including direct absorption of an optical probe, the collection of laser-induced fluorescence, and absorptive detection using a frequency-modulated laser. A brief description of each approach is included below, along with a discussion of its advantages and potential drawbacks in this context.

For calibration of ablation yields and measurements of the molecule density inside the buffer gas cell, straightforward **absorption** measurements are usually sufficient. A weak probe beam,

⁴It was found that maintaining a good mechanical surface quality at the interfaces between the cell, transfer plate and cryostat was crucial for holding the cell temperature close to 4K. The application of a very thin layer of Apiezon-N cryogenic vacuum grease was also useful in this regard.

tuned to a particular molecular ro-vibronic transition, is passed through the cell and detected using a photodiode, and the attenuation due to absorption by the molecules is measured. For SrO measurements, the probe was provided by an external cavity diode (ECD) laser in the Littman configuration (Sacher Lasertechnik TEC500), locked to a stabilized optical cavity and typically tuned to the $|X, v = 0, J = 2\rangle \rightarrow |A, v = 3, J = 3\rangle$ transition. (Some effort was made to develop a "ratchet-lock" technique whereby the laser could be scanned tens of GHz to access multiple rotational lines while remaining locked; see [69] for details.) For SrF, the laser setup described in Chapter 4 was used instead.

In absorption measurements, when the probe is tuned to resonance, the fractional power attenuation is given by $\Delta P/P = 1 - \exp(-n_M \sigma_D \Delta z) \approx n_M \sigma_D \Delta z$ (the final approximation being for the case of small optical depth), where n_M is the molecule density, σ_D the Doppler-broadened absorption cross section, and Δz the optical path length through the molecules [82]. Typical in-cell absorption signals observed for SrO were on the order of $\sim 2 - 5\%$, depending on the target used, ablation beam parameters, and the position of the probe in the cell; for BaF and SrF, signals of $10 - 40\%$ were fairly usual. The practical limit on the sensitivity of these direct absorption measurements is set by laser amplitude noise, and is about $\sim 3 \times 10^{-3}$ for a single measurement, detected within a 30kHz bandwidth. The noise arises mainly from mechanical vibrations in the cryostat, which are coupled to the optical intensity by etalon effects due to imperfectly anti-reflection coated windows. It is improved to some extent by the use of a balanced detection setup, where a second probe beam of equal intensity is passed through all of the same optical surfaces except buffer gas cell, and the detected signal subtracted from the main probe to eliminate common-mode noise. Performing this procedure with the New Focus Nirvana auto-balanced detector improves the sensitivity to somewhat better than $\sim 10^{-3}$. Beyond ease of implementation, the chief advantages of absorptive detection are simplicity of calibration (assuming that the strength of the probed transition is well known, as it is in all three of our cases), and the ability to obtain spatial resolution by translating the probe beam through the region of interest. This allows for the distribution of molecules in the cell to be mapped out, and would in principle provide the ability to measure the spatial characteristics of the beam if signals were sufficiently large. The latter application requires the use of the FM technique described below for molecules; however, it should be possible in direct absorption with, for instance, the Yb beams developed by the Doyle group at Harvard.

For the detection of the molecular beam itself, we have relied largely on **laser induced fluorescence (LIF)**. Here, a probe tuned to resonance with a molecular transition intersects the beam at a fixed point and the resulting fluorescence is detected with a photomultiplier tube (PMT). This approach has the advantage of being able to detect very small numbers of molecules; ideally, the minimum observable signal is determined by shot noise in the dark current at the PMT photocathode. Photons are collected using a lens (typically an achromatic doublet) positioned close to the detection point. The maximum solid angle over which light may be collected without resorting to more elaborate optics is about $0.04 \times 4\pi$ steradians (using a $f/1$ lens for fluorescence collection), although this can be increased by a factor of two by placing a mirror of the same focal length on the opposite side of the detection point. The measured signal is then directly proportional to the number of photons collected, multiplied by the gain of the PMT and its quantum efficiency at the detection wavelength.

The chief technical challenge with LIF detection is to collect only photons emitted by the molecules. For SrO, interference filters may be used to block much of the 786nm background light from the probe laser (tuned to the $|X, v = 0, J = 2\rangle \rightarrow |A, v = 3, J = 3\rangle$ transition) scattered off the vacuum windows and interior surfaces of the chamber, while still admitting fluorescence emitted from $|A, v = 3, J = 3\rangle \rightarrow |X, v = 1, J\rangle$ at 828nm. (PMT efficiency at emission wavelengths further to the red is sufficiently poor that they need not be considered.) This approach cannot be used with BaF and SrF, however, which have strongly diagonal Franck-Condon factors and therefore emit negligible fluorescence at wavelengths other than that of the excitation. In these cases, the only solution is to use Brewster-angled or AR coated windows, to align the probe carefully, and to try to minimize the solid angle over which the detector can collect reflections of scattered light off interior surfaces. Stray light from the intense plume of highly excited material inside the cell immediately following the ablation event can also be a issue, particularly if it causes the PMT to become saturated over the ~ 5 ms timescale during which the molecule signal can be detected. The use of an aperture to spatially filter detected light, as well as gating off the high-voltage supply to PMT dynodes during ablation, can help to solve this problem. The other obvious drawback of LIF detection is that it does not admit changes in the position of the probe once the optics have been aligned and the cryostat cooled down, precluding the possibility of studying spatial variations in molecule density.

In order to enhance the sensitivity of our absorptive detection, we have made use of **frequency modulation (FM) spectroscopy** [83]. Radio frequency sidebands at $\Omega = 2\pi \times 100\text{MHz}$ are inscribed onto the absorption probe using an electro-optic modulator (EOM) (Thorlabs EO-PM-R-C1), and it is then passed through the sample and directed onto a high-bandwidth amplified photodiode (Thorlabs PDA10A). Homodyne mixing is used to extract the component of the photodiode signal at the modulation frequency. In general, the modulation depth is chosen to be $M \sim 1.4$ radians, which gives approximately equal power in the fundamental and each of the first-order sidebands at $\pm\Omega$. The sidebands are exactly out of phase so that, in the absence of absorption by the molecules, the beat signal between the $+\Omega$ sideband and the fundamental is exactly canceled by that between the $-\Omega$ sideband and the fundamental. If the probe is tuned such that one sideband is preferentially absorbed, however, the cancelation is incomplete and a signal is detected. For electric field amplitude coefficients β_0 , β_1 , and β_2 in the fundamental, first-, and second-order sidebands respectively (normalized such that $\beta_0^2 + 2\beta_1^2 + 2\beta_2^2 = 1$, and assuming that the modulation depth is sufficiently low to prevent significant power from going into higher order sidebands), it can be shown (see calculation in Appendix B) that the FM signal component in phase with the modulation waveform is proportional to $S_{FM} \propto P_0 2\delta(\beta_0\beta_1 + \beta_1\beta_2)$. Here, P_0 is the laser power impinging on the detector, and 2δ is the fractional power absorption due to the molecules. (The out of phase component of the signal measures the optical dispersion induced by interaction with the molecules.) Figure 2.3 shows a schematic of the RF detection circuit and the optical components used for our FM spectroscopy setup.

The sensitivity of the FM spectroscopy setup is ideally limited by detector noise. We normally operate with sideband intensities given by $\beta_0 = 0.59$, $\beta_1 = 0.54$, and $\beta_2 = 0.19$, so that for unit absorption ($2\delta = 1$), the effective power in the FM signal is $(\beta_0\beta_1 + \beta_1\beta_2)P_0 = 0.42 P_0$. For a typical probe beam power⁵ on the order of $P_0 \sim 3 \text{ mW}$, this gives an effective FM signal power at unit

⁵It is somewhat remarkable that we are able to operate at these high probe powers without bleaching the transition. For molecules traveling at $\sim 150 \text{ m/s}$ through a $\sim 3 \text{ mm}$ diameter probe beam, the transit time linewidth is approximately $\gamma_T \approx 2\pi \times 50\text{kHz}$. The $v = 0 \rightarrow v' = 1$ transitions in BaF and SrF have line strengths comparable to that of the $5^2S_{1/2} \rightarrow 5^2P_{3/2}$ transition in ^{85}Rb ($\gamma_{\text{Rb}} = 2\pi \times 5.98\text{MHz}$), for which the saturation intensity is $I_{\text{sat}} = 1.64 \text{ mW/cm}^2$ [1]. (The $v = 0 \rightarrow v' = 3$ transition in SrO is about two orders of magnitude weaker, and should have correspondingly lower saturation intensity.) We would therefore expect to excite each BaF or SrF molecule once before it passes through the beam with a probe intensity of $\gamma_T/\gamma_{\text{Rb}}I_{\text{sat}} \approx 14\mu\text{W/cm}^2$. With our $\sim 3 \text{ mm}$ diameter beam, the saturation power should be about $P_{\text{sat}} = \frac{\pi}{2}I_{\text{sat}}w^2 \approx 2\mu\text{W}$. Even allowing for several photons to be scattered per molecule due to the relatively diagonal Franck-Condon factors, we would still expect to see bleaching at powers no more than an order of magnitude higher than this. Nevertheless, we observe no bleaching even with $\geq 1 \text{ mW}$ of power in our probe beam; the FM signal size varies linearly with power. The only plausible explanation for this observation is that background helium atoms or other ablation products in the beam are colliding with the molecules over length scales less than 3 mm . This is surprising, given that our vacuum is typically measured to be better

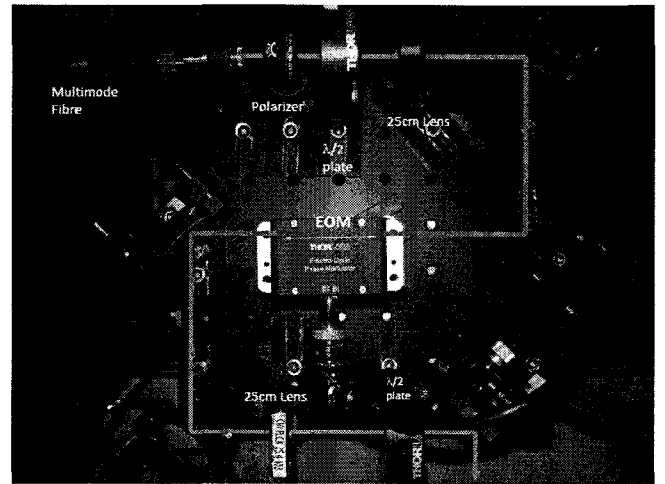
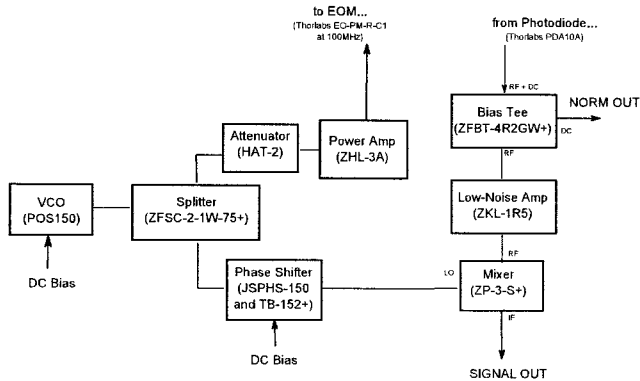


Figure 2.3: FM Spectroscopy Setup. **Left:** Radio frequency (RF) components for homodyne measurement of the FM signal. An oscillator generates $\sim 10\text{dBm}$ of RF power at 100 MHz, which is split between the EOM drive channel and the local oscillator (LO) input of a mixer. (A VCO should, in principle, suffice for this purpose, although we used the Agilent 8257D signal generator to guarantee very low phase noise for our measurements.) A variable phase shifter is inserted into the reference channel to compensate for phase delays in cables to and from the EOM and photodiode. The EOM drive is amplified so as to produce a modulation depth $M \approx 1.4$ in the optical probe beam. The light from the probe is detected by a high-bandwidth photodiode and the signal is fed back into the radio frequency (RF) port of the mixer, where the 100 MHz component is mixed down to DC. (The mixer output is low-pass filtered before digitization to remove the component at 200MHz.) The DC component of the photodiode signal is also read off from a bias tee, in order to normalize for fluctuations in laser power. **Right:** Optical path for the FM probe beam. The polarization of the input beam from a multimode fiber is purified using a linear polarizer, then rotated to coincide with the fast axis of the EOM crystal. The light is focussed through the crystal with a 1:1 telescope consisting of two 25 cm focal length lenses. The crystal produces 100 MHz sidebands in the spectrum of the probe beam. The polarization of the probe is then rotated to the desired axis and the beam is passed through the sample.

absorption of $S \sim 1.2$ mW. (This is the expected raw signal size, without dividing by the 3 mW signal from the DC channel of the bias-tee for power normalization.) The specified noise equivalent power (NEP) for the Thorlabs PDA10A diode is 5.5×10^{-11} W/ $\sqrt{\text{Hz}}$, for a total noise power in our $B = 30$ kHz detection bandwidth (chosen to allow time resolution $T_{res} \approx (\pi B)^{-1} \approx 0.01$ ms, much finer than the ~ 5 ms duration of our signals) of $N = 9.5 \times 10^{-6}$ mW. Thus, the expected maximum sensitivity is on the order of $N/S \sim 8 \times 10^{-6}$. (By comparison, the shot-noise on our 3 mW probe beam is given by $\delta P / \sqrt{B} = \sqrt{P \frac{hc}{\lambda}} = 2.8 \times 10^{-11}$ W/ $\sqrt{\text{Hz}}$; for a $1 \mu\text{W}$ beam, it is 5.0×10^{-13} W/ $\sqrt{\text{Hz}}$.) In fact, we have normally observed higher than specified noise levels in the diode power spectrum when illuminated, which increase linearly with intensity roughly as $\text{NEP} \sim 6.7 \times 10^{-10}$ W/ $\sqrt{\text{Hz}}/\text{mW}$ at the frequencies of interest. This noise is highly sensitive to beam pointing, which suggests it may be due to slight spatial separation of the frequency components of the probe. It effectively limits the maximum sensitivity of our measurements to $N/S \sim 3 \times 10^{-4}$ in a single ablation shot. Efforts made to reduce the noise in the FM setup are detailed in Appendix C.

Frequency modulation spectroscopy therefore gives at least a factor of 3 better sensitivity than could be obtained even with balanced absorption detection, and has the added advantage of requiring the translation of only a single probe beam for measurements of spatial density variations. It has proven extremely useful for beam characterization purposes, where signals tend to be small until the necessary optimizations can be made. It does have the drawback that signal sizes can be somewhat difficult to calibrate for molecule density measurements, primarily due to the variability of the phase delay between the FM signal and homodyne reference with respect to even relatively small changes (on the order of a few cm) in optical path length.⁶ Furthermore, the FM technique requires the sideband spacing to be chosen such that only a single sideband be absorbed; for a sufficiently well-resolved molecular spectrum, this just requires the spacing to be greater than the Doppler linewidth, $\Omega > \Delta\omega_D$, where $\omega_D \sim 2\pi \times 40\text{MHz}$ for our species of interest at 4K. However, the hyperfine structure of SrF is of the same order as the $\Omega = 2\pi \times 100\text{MHz}$ sideband frequency we have chosen, which again complicates the determination of molecule number from measured signal size if more than one sideband is being absorbed.

than 10^{-7} Torr, although that measurement is made on a gauge located far away from the molecular beam and is therefore not sensitive to local helium density.

⁶A reliable calibration would require having a known absorber in the beam path with exactly the same geometry as used to make the measurement. Practically, our best calibrations were made by measuring the known decrease in reflection from an optical cavity as it was scanned through resonance. These were made with a completely different beam path, and therefore required the relative phase to be adjusted for the actual molecular beam measurement. It is inconvenient, though not impossible, to account for this change with accurate measurements of the optical path length.

2.4 Summary of SrO Measurements

2.4.1 SrO Ablation Yield and Beam Flux

Early development of the buffer gas beam source focussed primarily on the production of effusive beams of SrO in the original $D = 7$ cm cell, and much of this work is already described in some detail in [69]. Typical ablation yields for our SrO targets were characterized both in a room-temperature setup and in a closed buffer gas cell at 4K. For these measurements, the helium density in the cell was varied such that the thermalization length L_{th} was approximately equal to the distance between the target and the probe beam, hence maximizing the absorption signal. (If the thermalization length is not equal to the probe distance, then the probe does not pass through the center of the roughly spherical distribution of diffusing thermalized molecules, and the absorption signal is consequently reduced.) A buffer gas density of approximately $n_{He} \sim 5 \times 10^{15} \text{cm}^{-3}$ was required to achieve this condition for our probe geometry. Modeling the diffusing molecules as a sphere of constant density gives $n_{SrO} = \frac{N_{v,J}}{4/3\pi(L_{th}/2)^3}$; for an optical absorption length of L_{th} (equal to the diameter of the sphere of diffusing molecules), the expected signal is then $\Delta P/P = \frac{6N_{v,J}}{\pi L_{th}^2} \sigma_D$, with $N_{v,J}$ the number of ablated molecules in the probed state and σ_D the Doppler-broadened cross section. The Doppler cross-section for $|X, v, J\rangle \rightarrow |A, v', J' = J + 1\rangle$ is given by [84]:

$$\sigma_D = \frac{\sqrt{\pi} \lambda^2 2J' + 1 \gamma_p}{2 \ 2\pi 2J + 1 \ \Gamma_D} \quad (2.6)$$

Here, the partial linewidth of the transition is given by $\gamma_p = \frac{1}{\tau_A} \beta_{v,v'} \frac{J+1}{2J+3}$, and the Doppler width is $\Gamma_D = \frac{2\pi}{\lambda} \sqrt{\frac{2k_B T}{m_{SrO}}}$. Using an excited state lifetime $\tau_A \approx 270$ ns (see below) and temperature $T = 300$ K, this gives $\sigma_D = 5 \times 10^{-13} \text{cm}^2$ for the $J=8 \rightarrow J'=9$ transition used in the room-temperature measurement. The measured signal was divided by the fractional Boltzmann population ~ 0.025 for the $J=8$ state at 300K to obtain a total ablation yield of about 2×10^{12} molecules. Similar measurements performed for SrO, BaF, and SrF in closed or effusively-flowing cells at 4K are all consistent with characteristic yields on the order of $\sim 10^{12}$ or higher.⁷ In-cell absorption measurements of this type, combined with the diffusion model of equation 2.6, also allow the SrO-He collision cross section at $T \sim 4$ K to be estimated, $\sigma_{SrO-He} = 5 \pm 3 \times 10^{-15} \text{cm}^2$.

⁷It is perhaps worthy of note that, for a $D = 3$ cm cell with high buffer gas throughput (producing hydrodynamic helium flow), the measured SrO yields are $\leq 10^{-11}$ total molecules; this may be further evidence for clustering of SrO at high buffer gas densities.

The decay lifetime of the $A^1\Sigma$ state of SrO was measured by sending a rapidly switched⁸ probe beam through the cell and observing the exponential decay of the resulting fluorescence, giving the value of $\tau_A = 270 \pm 20$ ns used to calculate the absorption cross section used in the yield measurements.

Rotational spectroscopy was carried out for a series of $|X^1\Sigma, v = 0, J\rangle \rightarrow |A^1\Sigma, v' = 1, J' = J + 1\rangle$ transitions in SrO, and the measured frequencies were found to be in good agreement with those of [85].

Measurements of near-effusive SrO beams were made using LIF spectroscopy, with light-collection optics set up to detect molecules immediately outside the cell aperture. An optical probe locked to a stabilized Fabry-Perot cavity was directed into the detection region at a right angle to the molecular beam, and its frequency scanned over the $|X^2\Sigma, v = 0, J = 2\rangle \rightarrow |A^2\Sigma, v = 3, J = 3\rangle$ transition to determine the transverse Doppler width. Similarly, a probe nearly parallel to the molecular beam was reflected off a mirror mounted on the front of the buffer gas cell and thereby passed through the molecules in both the forward and reverse directions, allowing the longitudinal Doppler width and the mean forward velocity (determined from the frequency difference between the fluorescence lines due to the co-propagating and counter-propagating beams) to be measured. Finally, the transverse probe was scanned over a series of rotational lines and their relative amplitudes were compared to extract the rotational temperature of the molecules. For sufficiently low buffer gas flow rates (corresponding to $n_{He} \lesssim 3 \times 10^{16} \text{cm}^{-3}$), the temperatures measured in all degrees of freedom were consistent with the $\sim 4\text{-}6\text{K}$ temperature of the $D = 7$ cm cell.

Interestingly, even for relatively modest buffer gas densities, $n_{He} \lesssim 5 \times 10^{15} \text{cm}^{-3}$, the measured forward velocity of the beam was already considerably higher than the expected 4K SrO effusive mean velocity of $\bar{v} = \sqrt{\frac{8k_B T}{\pi m_{\text{SrO}}}} = 28.5$ m/s. The forward velocity, as well as beam flux, are shown as a function of buffer gas density, in Figure 2.4. (Molecule flux numbers were estimated by using calibrated collection optics and a previous measurement of the PMT quantum efficiency; see [69] for details.) Even for the smallest detectable number molecules in the beam, the forward velocity was roughly a factor of two above the effusive limit. At the same time, the observed molecule number

⁸The switching was performed by tightly focusing the 786nm beam through an acousto-optic modulator (NEOS N23110) and using the first diffracted order to probe the molecules. The RF supply to the AOM was switched at 100 kHz; the rise time of the first order output was specified to be ~ 20 ns. A fast avalanche photodiode (Advanced Photonix SD 197-70-72-661) with 14 MHz bandwidth (and hence rise time ~ 11 ns) was used to detect the fluorescence.

for a fixed aperture diameter increased rapidly with in-cell buffer gas density. This is consistent with the picture of a small number of SrO-He collisions in the vicinity of the aperture causing a significant boost in the molecule velocity, outlined in Section 2.1 and discussed in detail in [86]. These data were among the first indications that it might be favorable for a variety of molecular beam experiments to operate in the high buffer gas density, large aperture, entrainment regime $\tau_{\text{Pump}} \ll \tau_{\text{Diff}}$. This was the primary motivation for switching to the small, $D = 3$ cm cell.

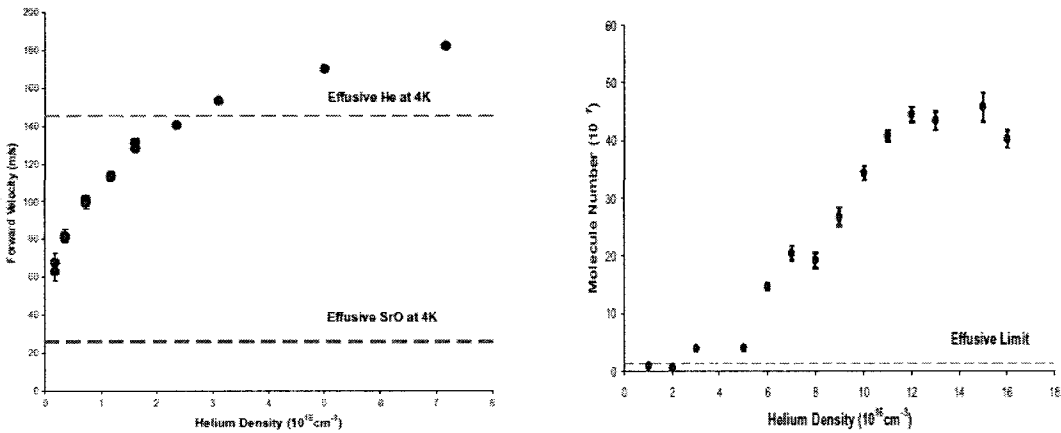


Figure 2.4: SrO forward velocity and beam flux data, measured by LIF immediately outside a $d_{\text{ap}} = 3$ mm orifice on the front face of the $D = 7$ cm cell. (Figure modified from [69]). **Left:** Forward velocity as a function of in-cell helium density. Even for the smallest detectable flux, the SrO molecules are boosted well above the 4K effusive velocity limit by collisions with He atoms in the vicinity of the aperture. For sufficiently high buffer gas density, they approach 200 m/s. **Right:** Molecule number vs. helium density. For densities $n_{\text{He}} \gtrsim 3 \times 10^{15} \text{ cm}^{-3}$ the observed flux greatly exceeds that predicted by the model of simple diffusion inside the cell, providing further evidence of entrainment in the bulk helium flow.

2.5 Electrostatic Guiding

We have demonstrated electrostatic guiding of a hydrodynamic beam of SrO molecules. Transverse confinement was provided by the quadrupole potential generated by four guide rods with alternating positive and negative voltages $\pm V_0$, which takes the form

$$V(r, \theta) = V_0 r^2 \cos(2\theta) \quad (2.7)$$

The resulting electric field has magnitude $|\vec{E}| = 2V_0 r/R^2$, where r is the distance from the axis of the

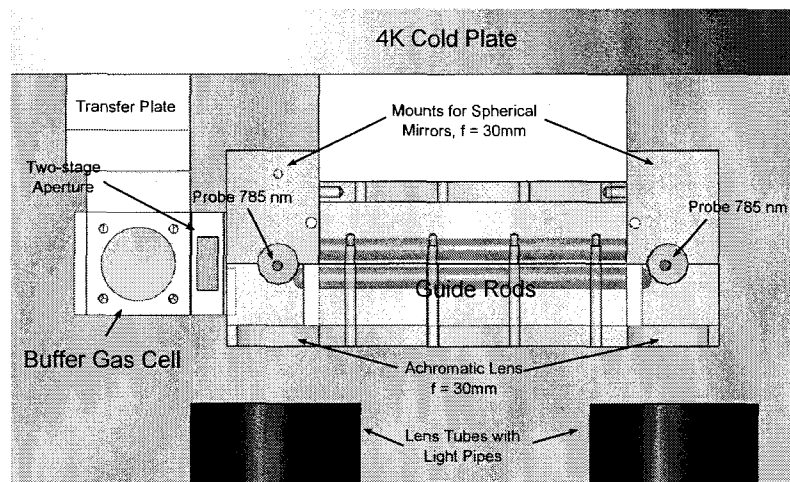


Figure 2.5: Electrostatic guiding experiment. SrO molecules are produced by ablation in the $D = 3$ cm cell at a buffer gas density $n_{\text{He}} \approx 2.6 \times 10^{16} \text{cm}^{-3}$, and flow out the $d_{\text{ap}} = 3$ mm aperture in the front face of the cell at an estimated average velocity $v_z \sim 150$ m/s. (Note that for the data actually shown in Figure 2.7, the two stage aperture was *not* used; the cell was moved forward to be adjacent to the guide mount, so that the orifice was roughly 2cm from the start of the guides.) The electrostatic guide, with rods of radius $R = 0.32$ cm, provides transverse confinement over a distance $L_G = 11$ cm. LIF probe beams and light collection optics are placed before and after the guide to measure the increase in beam flux at the end of the guide as a function of the voltage applied to the rods.

guide and $R = 0.32$ cm is the radius of the guide rods. (Note that, in order to create the quadrupole field, the surface of each rod must also be located a distance R away from the axis.) At low fields, the thermally populated excited rotational states $|J \geq 1, m = 0\rangle$ experience a Stark shift that causes their energy to increase with increasing field, and hence a radial force directed towards the axis of the guide. A calculation of the expected Stark shifts, obtained by numerically diagonalizing the molecular Hamiltonian, $H = B_e J(J + 1) - \vec{d} \cdot \vec{E}$, is shown in Figure 2.7.

The experiment was carried out using the setup depicted in Figure 2.5. A hydrodynamic SrO beam was produced in the $D = 3$ cm cell with an aperture diameter $d_{\text{ap}} = 3$ mm and a helium input flow of 15 sccm, corresponding to a buffer gas density of $n_{\text{He}} \approx 2.6 \times 10^{16} \text{cm}^{-3}$. The quadrupole guide, with rods of radius $R = 0.32$ cm and length $L_G = 11$ cm, was mounted in a copper box thermally linked to the cold plate of the cryostat, the interior surfaces of which were covered with charcoal for cryopumping.⁹ The entrance to the guide was located approximately 2 cm downstream from the cell orifice. Fluorescence collection optics were set up before and after the guide, and a

⁹In hindsight, the box surrounding the guide was likely a mistake, as the probability for helium to stick to the charcoal surface on any given wall collision is significantly less than unity [87]. The box has the effect of preventing helium from leaving the vicinity of the guide, and may therefore actually increase the local helium background pressure. A better approach would have been to use the charcoal aperture plates described in Section 2.6.

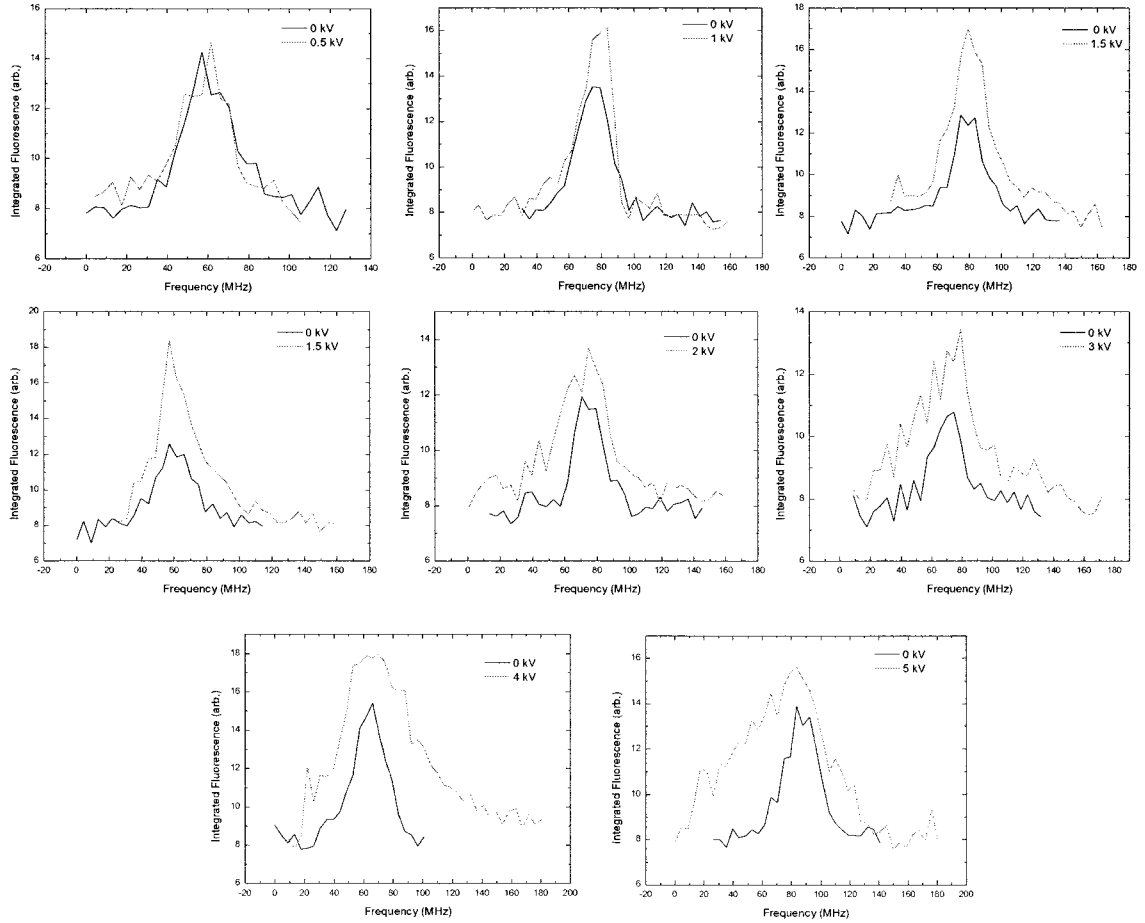
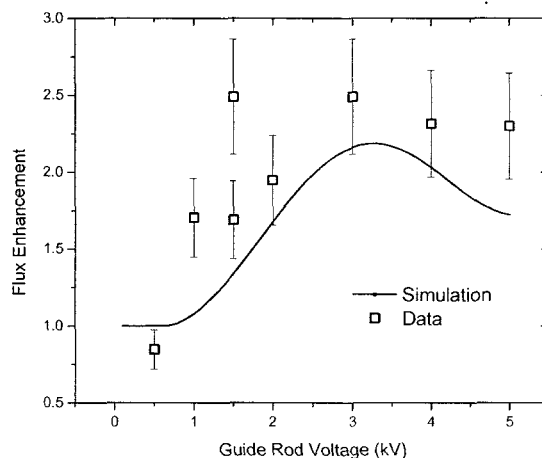
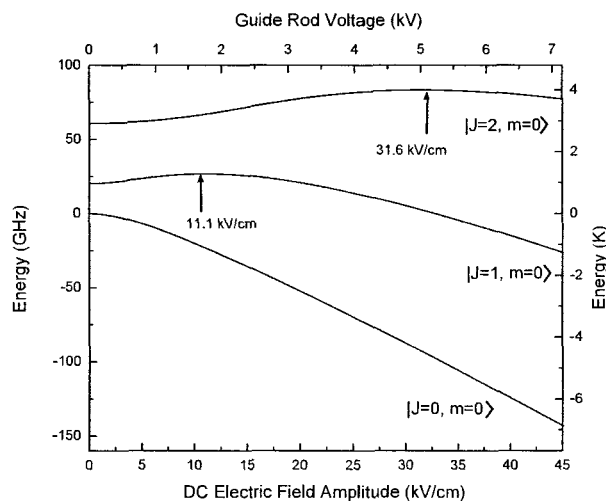


Figure 2.6: End-of-guide fluorescence data. Each panel shows the collected fluorescence as a function of laser frequency for a fixed voltage applied to the electrostatic guide. The data were collected by first switching the guide voltage off and scanning the probe laser through resonance to obtain a normalization signal, then setting it to the desired voltage and repeating the scan; each panel therefore shows the corresponding zero-voltage scan in addition to the data at the voltage of interest. (These data were all collected over the course of a few hours and the vertical axes in each graph have the same scale. It is worthwhile to note that the magnitude of the frequency-integrated normalization signal varies by 10% or more between scans due to short-term variability in ablation yield.) The frequency scans were carried out in steps of 4.4 MHz. Every data point corresponds to the sum of 10 ablation shots collected at a given frequency; the fluorescence integration time was 5 ms for each shot, and 1 ms of data was taken before the ablation laser fired for background subtraction. The frequency-integrated fluorescence signal with the guide voltage on was divided by the integrated signal at zero voltage to determine the flux enhancement factors shown in Figure 2.7. (Each panel here corresponds to one point in that graph.)

probe beam tuned to the $|X^2\Sigma, v = 0, J = 1\rangle \rightarrow |A^2\Sigma, v' = 3, J' = 2\rangle$ transition introduced at each side. In order to maximize the light collection efficiency, a spherical mirror of focal length $f = 30\text{mm}$ was introduced above the beam to match the $f = 30\text{mm}$ achromatic doublets below, thereby increasing the collected solid angle to about $\Omega/4\pi \approx 0.08$. Acrylic light pipes of 7/8" diameter were used to carry the light to the bottom of the cryostat, where it was detected by a PMT (Hamamatsu R5900U).

Measurements were performed by first detecting the molecule flux at the second PMT with the guide voltage turned off, then switching it on and repeating the observation. The laser frequency was swept over the $J = 2 \rightarrow J' = 3$ resonance in steps of about 4.4 MHz, with 10 ablation shots averaged per step. Typical fluorescence data are depicted in Figure 2.6. The frequency-integrated signal for the guided beam was divided by the integrated unguided signal to obtain a flux enhancement factor, shown in the data of Figure 2.7. (Integration over frequency was necessary because the guide changes the transverse Doppler width of the output beam.) Displayed in the same figure is the result of a numerical calculation of the expected flux enhancement for molecules in the $J = 2$ state. The calculation was carried out for a guide-aperture separation of 2cm, assuming initial transverse and rotational temperatures of 4K and an initial mean forward velocity of 150m/s (corresponding to the measured value shown in Figure 2.4 for $n_{\text{He}} \approx 2.6 \times 10^{16}\text{cm}^{-3}$). The molecule trajectories were integrated using a force field derived from the Stark shifts of Figure 2.5, and a symplectic PEFRL algorithm [88] with a $10\mu\text{m}$ step size. Approximately 10^5 trajectories were run for each value of the guide voltage. The calculation assigned each molecule randomly to one of the five magnetic sublevels for $J = 2$; as expected, significant flux enhancement was seen only for the population with $m_J = 0$. Note that, as the voltage exceeds the threshold at which the derivative of the potential changes sign for a given rotational state at the edge of the guide ($V_0 = E_{\text{max}}R/2 = 5.06\text{ kV}$ for $J = 2$), the guided fraction in that state begins to decrease, as the guide entrance aperture is effectively becoming smaller. The data agree reasonably well with the simulation, although the error bars are large due to both poor signal to noise in the detection and significant ($\sim 10 - 20\%$) shot-to-shot variability in ablation yields. We briefly attempted similar measurements with a guide of length $L_G = 30\text{ cm}$, but were not able to detect a signal at the output. Collisions with background helium gas are the suspected cause for poor guiding efficiency in this case; the experiment could probably be repeated with greater success using the charcoal plate skimmers described in Section 2.6.



0

Figure 2.7: Demonstration of electrostatic guiding. **Top:** Calculated DC Stark shifts for $J=0, 1,$ and 2 ; $m = 0$ states of SrO. (Stark shifts for $m_j \neq 0$ decrease monotonically with increasing field; these states are not guided.) Molecules in the excited rotational states (with $m_j = 0$) are attracted to low field for electric field amplitudes less than some value E_{max} , at which the derivative of the potential changes sign. This occurs at $E = 11.1$ kV/cm for $J=1$, and $E = 31.6$ kV/cm for $J=2$. The top axis shows the voltage required to produce a given field at the surface of the rods, $r = R$. **Bottom:** Measurement of the increase in molecule number detected at the end of the guide as a function of the voltage applied to the rods. The solid line is a numerical simulation carried out for our guide geometry and molecules in the $J = 2$ state. (Equal populations were assigned to all magnetic sublevels m_j and the "detected" fractions summed to obtain the calculated enhancement shown.) Note that the uncertainty in the measurements is quite large, due to the small detected fluorescence signals and large shot-to-shot variability in the ablation yield. The error bars were estimated assuming 10% uncertainty both in each guide measurement and the preceding normalization measurement; this may in fact be an underestimate.

2.6 Development of a Hydrodynamic Beam

Limited optical access to the interior of the cryostat makes it an impractical environment for carrying out many of the experiments one might wish to do with the buffer gas beam source. We have therefore spent considerable effort to optimize the brightness of our beam, with the goal of delivering cold molecules to an adjoining room-temperature vacuum apparatus. Much of our early work towards this objective was carried out with BaF instead of SrO, due to its apparently superior ablation properties (c.f. Section 2.2), its greater electric dipole transition strength (excited state lifetime $\tau \approx 24$ ns and Franck Condon Factor $\beta_{0,0} = 0.95$ for the $|X^2\Sigma, v = 0\rangle \rightarrow |A^2\Pi_{1/2}, v = 0\rangle$ transition in BaF, compared to $\tau \approx 270$ ns and $\beta_{0,3} = 0.11$ for the $|X^1\Sigma, v = 0\rangle \rightarrow |A^1\Sigma, v = 3\rangle$ transition in SrO), and its relevance to the molecular parity violation experiment being pursued in the DeMille group. We typically used the $D = 3$ cm cell, an aperture diameter of $d_{ap} = 3$ mm and high helium input rate of ≥ 50 sccm (corresponding to in-cell density of about $n_{He} \geq 9 \times 10^{16} \text{cm}^{-3}$), in order to access the strong-entrainment regime. The effects of varying ablation parameters, including pulse energy and tightness of focus were investigated, as well as the relative positions of the ablation target and buffer gas feed line to the cell.

The spatial characteristics of the molecular beam were measured using FM absorption spectroscopy, with 100 MHz modulation sidebands on a 859 nm probe beam accessing the $|X^2\Sigma, v = 0\rangle \rightarrow |A^2\Pi_{1/2}, v = 0\rangle$ transition in BaF. Figure 2.8 illustrates typical data for the transverse beam profile and attenuation as a function of distance from the cell. The first panel shows a vertical profile of the beam, taken at a distance of 2.5 cm from the front face of the cell, with a helium flow rate of 70 sccm (buffer gas density $n_{He} \approx 1.2 \times 10^{17} \text{cm}^{-3}$), fit to a gaussian lineshape of FWHM 12 mm. This corresponds to a ratio of horizontal to longitudinal velocities of approximately 6, assuming a FWHM ~ 3 mm at the aperture. It is somewhat less than the optimum ratio of ~ 11.5 , for BaF with a 4K Doppler distribution of FWHM $\Delta v_{Dopp} = \sqrt{\frac{2k_B T}{m_{BaF}}} \approx 34$ m/s and mean boosted forward velocity $v_z \sim 200$ m/s, but is nevertheless considerably better collimation than would be possible in a standard supersonic beam expansion [71]. The second panel of Figure 2.8 shows the attenuation of a BaF beam from a cell with a helium flow rate of 50 sccm (buffer gas density $n_{He} \approx 9 \times 10^{16} \text{cm}^{-3}$). It is fit to a curve of the form C/z , for C the fit parameter and z the distance from the cell in cm. (The molecule density is expected to decrease as $\sim 1/z^2$, but the absorption probe integrates over density along its length.) We note that the signal decreases faster than the expected $1/z$ dependence, which

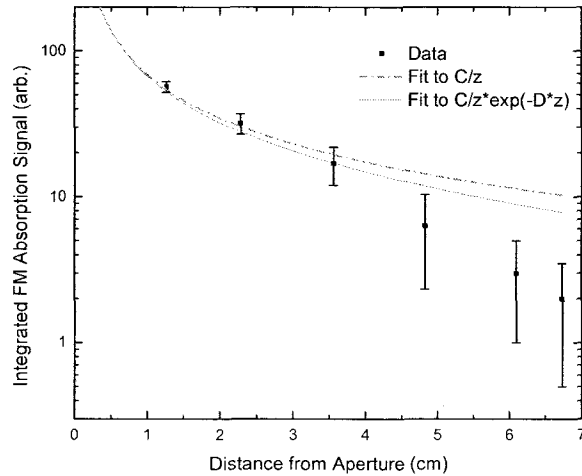
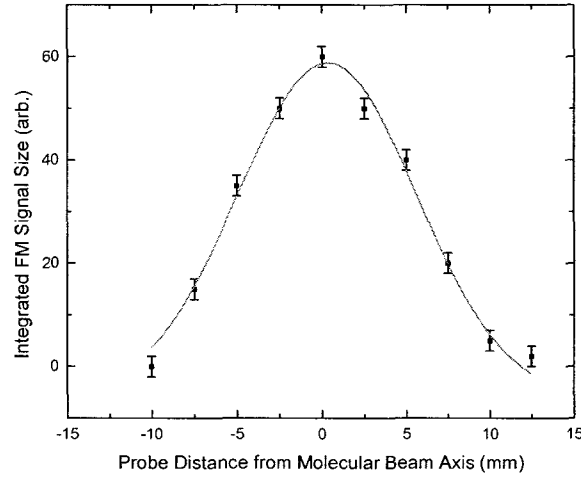


Figure 2.8: Characterization of a hydrodynamic beam of BaF. **Top:** Transverse beam profile measured with FM absorption spectroscopy at a distance of 2.5 cm from the $d_{ap} = 3$ mm aperture. The buffer gas density in the cell was $n_{He} \approx 1.2 \times 10^{17} \text{cm}^{-3}$. The gaussian fit to the beam profile gives a FWHM of 12 mm, corresponding to ratio of longitudinal to transverse velocity of ~ 6 . **Bottom:** Measurement of beam attenuation as a function of distance from the buffer gas cell. The in-cell helium density in this case was $n_{He} \approx 9 \times 10^{16} \text{cm}^{-3}$. The data is fit to curves of the form C/z and $Cz^{-1}e^{-Dz}$, for z the distance to the aperture. It can be seen that the attenuation is more rapid than expected ($\sim C/z$) for a freely propagating molecular beam, likely due to collisions with background helium gas or helium other ablation products in the beam itself. Interestingly, these data also decrease more rapidly than the fit to a simple exponential decay (and in fact fit well with a curve of the form $Cz^{-1}e^{-Dz^2}$, not shown), which may be consistent with a gradual degradation of the ablation target as the probe beam was moved progressively further from the cell.

is attributed to collisions either with background helium gas, or with other material in the beam. Interestingly, the data also decrease more rapidly with distance than a fit to $Cz^{-1}e^{-Dz}$ that would be expected for constant background gas density. It seems unlikely that the rate of collisions increases with distance from the cell; a more plausible explanation in this case may be that the ablation yield decreased over time for these measurements due to degradation of the target as the probe beam was moved progressively further from the cell.

In order to address the problem of background helium collisions, a series of charcoal cryosorption plates were constructed and placed in front of the cell. Apertures of varying diameter were drilled into the plates along the beam axis to allow for the molecules to pass through. The plates were made from 1/8" thick copper, to which a layer of activated coconut charcoal was attached using thermally conductive epoxy (Arctic Silver Thermal Adhesive). Helium atoms from the buffer gas cell striking the charcoal surface were adsorbed with high probability; those bouncing off were deflected away from the beam and eventually pumped away by other charcoal-covered surfaces in the cryostat. Our most successful configuration had one charcoal plate with a 1.25 cm diameter aperture at a distance of 6 cm from the cell, and a second plate with a 2.5 cm aperture at a distance of 7.5 cm from the cell, followed by a 1.25 cm aperture in the wall of the cryostat 77K shield at a distance of 10 cm from the cell. Using this setup, we were able to detect SrF molecules with FM spectroscopy outside the cryostat in an external vacuum chamber, at a total distance of ~20 cm from the cell. This was the limit of our hydrodynamic beam development with the 37L cryostat; shortly thereafter we switched to the 1L cryostat described in Chapter 4. With the arrangement shown in Figure 4.4, we now routinely see large SrF molecular fluorescence signals at distances up to 36 cm from the beam source. We have not yet performed a calibrated measurement to determine the absolute number of molecules delivered by the beam at a given distance from the cell, although this will likely be necessary before moving on to microwave trapping experiments.

Chapter 3

Microwave Trap Design

3.1 Introduction

The principal novel feature of the molecular cooling scheme outlined in Chapter 1 is the microwave trap. This device is a direct analogue of the optical dipole traps now in wide use in atom trapping and BEC experiments [89][90][91], and it shares several of their attractive features. In particular, it allows for the trapping of molecules in their ground angular momentum state, which is necessarily strong-field seeking. (Recall that Earnshaw's theorem precludes the possibility of setting up a DC field maximum in free space.) This is essential for studying collisional cooling in polar molecular systems, where the ratio of inelastic to elastic collision rates is less favorable than for alkali atoms [26]. Moreover, it potentially affords a significantly deeper confining potential than optical traps by taking advantage of Stark shifts associated with molecular *rotational* (rather than electronic) excitations, which are very long lived and hence allow large fields to be applied at small detunings without the risk of heating due to photon scattering.¹ Finally, because the wavelengths associated with microwave frequencies are on the order of 1cm, the trap volume should be large enough to allow efficient loading from a molecular beam source.

The ultimate goal of the microwave trap is to enable collisional cooling of polar diatomic

¹In a standing-wave dipole trap, the scattering (heating) force due to spontaneous emission is given by $F_{sp} = \frac{\hbar k s_0 \gamma / 2}{1 + s_0 + (2\delta/\gamma)^2}$, and the dipole (trapping) force by $F_{dip} = \frac{2\hbar k \delta s_0 \sin(2kz)}{1 + 4s_0 \cos^2(kz) + (2\delta/\gamma)^2}$, for $\hbar k$ the photon momentum, $s_0 = 2|\Omega|^2/\gamma^2$ the saturation parameter at Rabi frequency Ω , γ the transition linewidth, and δ the laser detuning.[1]. Optical dipole traps operate in the limit $\Omega \ll \delta$, where $F_{sp} \propto 1/\delta^2$ and $F_{dip} \propto 1/\delta$. For the microwave trap tuned close to a molecular rotational transition, γ is so small that $\Omega \gtrsim \delta$ becomes viable.

molecules of arbitrary species, in order to bridge the gap between the temperatures achievable by current direct-cooling methods (typically ~ 100 s of mK to a few K) and the ultra-cold regime. This is facilitated on the one hand by the capacity for trapping in the rotational ground state and thereby strongly suppressing inelastic collision rates, and on the other by the enhancement of elastic collisions due to polarization of the molecular dipoles at the trapping field maximum. Collisional cooling can take two possible forms: (i) forced evaporation, in which the trapping potential is repeatedly lowered to remove the molecules with the highest kinetic energy, and those remaining collide with each other and thermalize to a lower mean temperature; and (ii) sympathetic cooling, where the molecules are made to collide elastically and thermalize with a much lower-temperature sample of MOT-cooled alkali atoms. In both cases, it is highly advantageous to have a large ratio of elastic rate to inverse trap lifetime. The elastic scattering cross section can be determined by semi-classical methods [92], with the following result:

$$\sigma \approx C \frac{1}{4\pi\epsilon_0} \frac{\langle\mu\rangle^2}{\hbar v} \quad (3.1)$$

Here, C is a numerical prefactor, originally estimated in [14] by adapting the result of a calculation using Kajita's Fourier technique [93] as $C = \frac{40\pi\sqrt{2}}{3}$. A more recent Eikonal calculation by Cavagnero and Bohn [92] for the full anisotropic dipole-dipole potential (c.f. equation 1.1), when averaged over all angles of incidence, gives $C = \frac{8\pi}{3}$. The result of equation 3.1 is expected to be valid when the collision involves contributions from many partial waves, which should be true down to temperatures $T \gtrsim 3 \times 10^{-14} \text{K}$ (again, see [14]). Using $C = \frac{8\pi}{3}$, and substituting current values for the expected trap depth $T = \frac{1}{2}mv^2 = 0.3\text{K}$ and $\langle\mu\rangle \approx 6.9$ Debye gives $\sigma \sim 5.5 \times 10^{-10} \text{cm}^2$, an extremely large cross section. Likewise, the elastic Cs-SrO cross section due to dipole interactions may be approximated using the Cs polarizability[94] $\alpha_0 = 6.61 \times 10^{-39} \text{C m}^2/\text{V}$ to obtain an rms dipole moment $\langle\mu\rangle_{\text{Cs}} = \alpha_0 E_0 / \sqrt{2} = 3.2 \times 10^{-33} \text{C m}$ for $E_0 = 6.8 \text{ kV/cm}$. Substituting this value for one power of the dipole moment in 3.1 and using $T = 0.3\text{K}$ gives $\sigma_{\text{Cs-SrO}}^{(\text{elastic})} \approx 7.5 \times 10^{-14} \text{cm}^2$. For typical Cs MOT densities of about $n \sim 10^{12}/\text{cm}^3$ [39], and assuming a relative velocity of ~ 7 m/s (corresponding to a SrO temperature on the order of ~ 300 mK), the mean time for Cs-SrO collisions is $1/(n \sigma v) \sim 0.02\text{s}$. This should be sufficient to allow for significant sympathetic cooling for vacuum-limited trap lifetimes on the order of a few seconds.²

²Note that this estimate for the mean time for Cs-SrO collisions assumes that the molecules spend all of their time in contact with the atoms. In reality, the volume occupied by atoms in a typical MOT is on the order of $\sim 10^{-3} \text{cm}^3$, compared

We have designed and constructed prototypes for a microwave trap consisting of an open, near semi-confocal resonator with copper mirrors. The open geometry was chosen to maximize optical access, in order to allow for a MOT of Rubidium or Cesium atoms to be superposed over the molecular trap. This facilitates the study of alkali-molecule collisions and should potentially enable an initial step of sympathetic cooling to increase the phase-space density of the molecules to a level favorable for evaporative cooling [19]. The decision to use a near semi-confocal cavity design was motivated mainly by ease of fabrication; we have elected to couple power into the cavity through an array of subwavelength apertures (as described in Section 3.5.3 below), the production of which is simplified considerably with the use of a plane mirror. Finally, copper was chosen for the mirror material in order to obtain the largest possible peak electric field in the cavity, despite some initial consideration given to the possibility of constructing the mirrors from superconducting niobium. The obvious advantage of niobium is the improvement in cavity quality factor Q afforded by its high conductivity: Taking the reported Q of a state-of-the-art niobium cavity cooled to temperature $T = 0.8$ K ($Q \sim 3 \times 10^8$ for a $TEM_{0,0,9}$ mode at $f = 51.1$ GHz) [95] and scaling³ to our geometry (a $TEM_{0,0,20}$ mode at 18.1 GHz) would give $Q \sim 6.7 \times 10^9$. However, the relevant figure of merit for determining the maximum electric field is the product of the Q -factor and input power, $E_{max} \propto QP_{in}$. For a copper cavity, it should be possible to obtain a Q of $\sim 10^5$ with an input power of ~ 2 kW, so $QP_{in} \sim 2 \times 10^8$ W. To do as well with a niobium cavity, it would be necessary to dissipate roughly $P_{in} \sim 30$ mW of input power, which is a difficult technical challenge at sub-Kelvin temperatures [96]. Furthermore, the need to maintain very low heat loads for the superconducting cavity would likely be incompatible with the insertion of MOT beams. Thus, a high-power, room-temperature copper cavity was chosen as the preferred design.

The operating frequency of our microwave trap is 18.1 GHz, selected to be as close as possible to the $J=0 \rightarrow J=1$ rotational transition in SrO (at 20.3 GHz) while still remaining within the DBS frequency band where high-powered klystron amplifiers are available. At least two such amplifiers have been identified with maximum output powers on the order of 2kW (Xicom XTKD-2000DBS and CPI K3D64A), and most of the cavity design and prototype work described here was done with this figure in mind. The resulting nominal trap depth for SrO molecules is roughly 1.0 K.

to the total microwave trap volume of $\sim 5\text{cm}^3$. If the molecules sample the entire trap volume equally, then, the prospects for sympathetic cooling therefore become considerably poorer.

³Note that this scaling is subject to the reasonable assumption that loss is dominated by imperfections in the mirror and stray magnetic fields, rather than $R_{BCS} \propto \omega^{1.7}$.

Unfortunately, it was recognized late in the design process that, for our microwave frequency and polarization purity, a multi-photon resonance occurs in the trap which limits its effective depth to 0.5 K, at an input power of 500 W. (This is described in detail in Section 3.3.4.) In principle, this would reduce the fraction of molecules captured from the Boltzmann tail of an effusive SrO beam by roughly a factor of 5 compared to the full 2 kW trap. However, more recent developments make it seem likely that the beam source for loading our trap will, in any case, ultimately be the laser-cooled SrF beam described in Chapter 4. This source is expected to have a significantly lower forward kinetic energy (potentially as small as the Doppler temperature, $T_D = \frac{h\gamma}{2k_B} = 0.17$ mK, for $\gamma = 2\pi \times 7$ MHz the $X^2\Sigma \rightarrow A^2\Pi$ transition frequency in SrF), which should obviate the problem. Furthermore, the multi-photon resonance at half the maximum trapping field is not necessarily general to all molecular species, and the thermal management lessons learned for the 2kW input power design may still be applicable to future trap designs.

The balance of this chapter is devoted to describing the development of the microwave trap initially set out in Reference [14]. Section 3.2 gives a brief review of the mode structure and other generic features of Fabry-Perot type resonators. In Section 3.3, a calculation for the AC-Stark shifts experienced by the trapped molecules is shown for various electric field polarizations, and the form of the confining potential is determined. Sections 3.4-3.5 describe the quasi-optical feed and sub-wavelength aperture coupling scheme designed to transfer microwave power into the cavity with near unit efficiency. The thermal design of the cavity coupling mirror, which consists of a thin copper layer mounted on a slab of thermally-conductive ceramic is outlined in Section 3.6.

3.2 Resonator Mode Structure

The mode structure of open Fabry-Perot type resonators has been studied extensively since the 1960s, and is well described in a variety of standard textbooks [97][98][99]. An early numerical calculation using successive Huygens integrals to compute the (scalar) electric field at one mirror due to illumination by the other showed that the eigenmodes for typical cavity geometries look very much like low transverse-order Gaussian beam modes [100]. These modes will be such that the shape of the phase front exactly matches the radius of curvature of each mirror at its surface. The form of such a Gaussian mode for a cylindrically symmetric cavity is given by

$$\begin{aligned}
E_{pm}(r, \phi, z) = & \left[\frac{2p!}{\pi(p+m)!} \right]^{1/2} \frac{1}{w(z)} \left[\frac{\sqrt{2}r}{w(z)} \right]^m L_{pm} \left(\frac{2r^2}{w^2(z)} \right) \\
& \cdot \exp \left[\frac{-r^2}{w^2(z)} - ikz - \frac{i\pi r^2}{\lambda R(z)} + i(2p+m+1)\Phi_0(z) \right] \exp(im\phi)
\end{aligned} \tag{3.2}$$

Here, L_{pm} is the Laguerre polynomial of order (p,m) ; $w(z) = w_0 \left[1 + \left(\frac{\lambda z}{\pi w_0^2} \right)^2 \right]^{1/2}$ is the beam radius as a function of z , for w_0 the minimum radius in the $z=0$ "waist" plane; $R(z) = z + \frac{(\pi w_0^2/\lambda)^2}{z}$ is the phase-front radius of curvature as a function of z ; and $\Phi_0 = \tan^{-1} \left(\frac{\lambda z}{\pi w_0^2} \right)$ is the so-called "Guoy" phase. Such a mode is completely characterized by its wavenumber k , transverse excitation indices (p,m) , and the complex q -parameter defined as $\frac{1}{q(z)} = \frac{1}{R(z)} + \frac{i\lambda}{\pi w^2(z)}$. For a cavity of length L and concave mirrors with radii of curvature R_1 and R_2 (where the sign of R is positive for a center of curvature to the left of the mirror), there is a unique solution for the set of (p,m) modes that satisfy $R(z_1) = R_1$ and $R(z_2) = R_2$, with $z=0$ inside the cavity and $z_2 - z_1 = L$. See Siegman [97], section 19.1 for the most general form of this solution; the solution relevant to our cavity is given in equations 3.4-3.5 below. The resonant frequencies of the cavity can be determined from equation 3.2 by requiring that the phase evolution associated with a round trip be a multiple of 2π . This gives

$$kL - (2p+m+1) \left[\tan^{-1} \left(\frac{\lambda z_2}{\pi w_0^2} \right) - \tan^{-1} \left(\frac{\lambda z_1}{\pi w_0^2} \right) \right] = N\pi \tag{3.3}$$

The cavity for the microwave trap is formed from a plane mirror ($R_1 \rightarrow \infty$) and a concave parabolic mirror of focal length $f=17.65$ cm, separated by a distance $L = 16.8$ cm along the cavity axis. (A spherical mirror of the same focal length would have radius of curvature $R_2 = 35.30$ cm. The two should be equivalent in the paraxial limit; the parabolic shape was chosen to reduce spherical aberration by exactly matching the form of the Gaussian wavefronts far off-axis.) The molecules are accumulated in the 9th antinode from the flat mirror surface, close to the center of the cavity, so as to maximize optical access for probing them and superposing a MOT over the trap. Figure 3.1 shows a schematic view of the cavity, as well as the original mechanical drawing for the curved mirror.

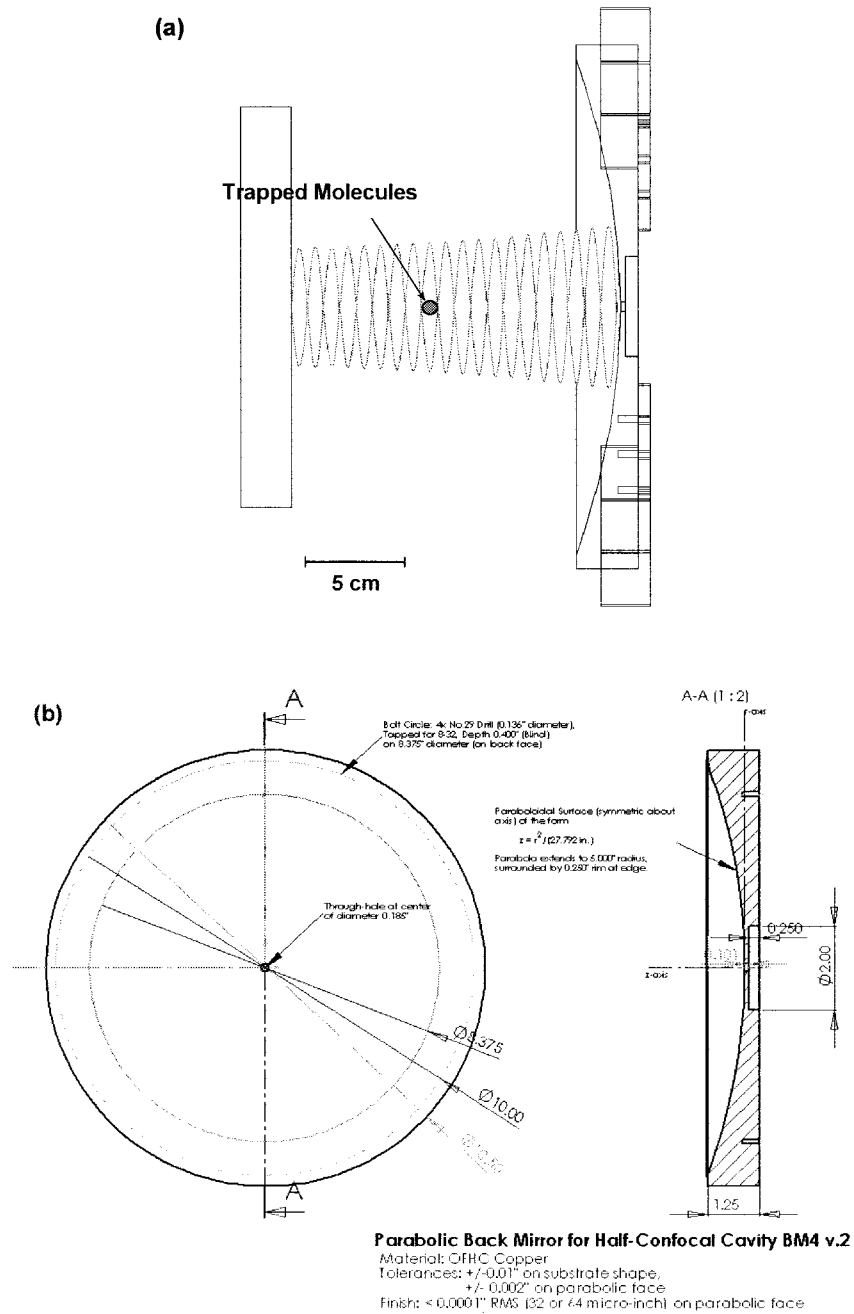


Figure 3.1: Gaussian beam mode of the microwave trap cavity. (a) To-scale cross section of the cavity, with the $1/e^2$ envelope of the $TEM_{0,0,20}$ trap mode drawn in. The molecules are confined in the 9th antinode from the plane mirror. (In fact, it is likely that molecules will be loaded into adjacent antinodes as well; however, this is the position at which the atomic MOT will overlap the cavity mode for sympathetic cooling.) (b) Mechanical drawing for the parabolic cavity mirror, showing all relevant dimensions. The focal length of the paraboloid is $f = 17.65 \text{ cm} = 6.95''$, and the mirror diameter is $25.4 \text{ cm} = 10.0''$.

For a half-symmetric resonator, the beam waist must be in the plane of the flat mirror ($z_1 = 0$), and it can be shown that the beam spot sizes are given by [97]:

$$w_0^2 = w_1^2 = \frac{L\lambda}{\pi} \sqrt{\frac{R}{L} - 1} \quad \text{and} \quad w_2^2 = \frac{L\lambda}{\pi} \sqrt{\frac{R^2}{L(R-L)}} \quad (3.4)$$

Then, for $R = 35.3$ cm and $L = 16.8$ cm, the spot sizes are $w_0 = 3.05$ cm at the beam waist and at $w_2 = 4.21$ cm at the surface of the curved mirror. The resonant frequencies for this resonator can be derived from equation 3.3 as

$$f = \frac{c}{2L} \left[N + \frac{(2p + m + 1)}{\pi} \tan^{-1} \left(\sqrt{\frac{L}{R-L}} \right) \right] \quad (3.5)$$

Figure 3.2 shows a typical transmission spectrum for the microwave trap cavity. The data were collected using the setup described in section 3.5.3, with minimal input coupling. (This means that the linewidth is dominated by loss mechanisms other than mirror transmission, and is therefore unaffected by further decreasing the coupling.) The free spectral range is observed to be $\Delta f_{FSR} = 894.5$ MHz, corresponding to a cavity length of $L \approx \frac{c}{2\Delta f_{FSR}} = 16.76$ cm. The longitudinal mode number for the peak at $f_0 \approx 18.1$ GHz is $N = 20$. Note that the transverse excitations between the main peaks are strongly suppressed, indicating good mode-matching of the input power. The inset figure shows a higher-resolution scan taken in the vicinity of the 18.1 GHz resonance. Fitting to a Lorentzian lineshape gives a FWHM width of $\Gamma = 210.4$ kHz, corresponding to a cavity $Q = \frac{f_0}{\Gamma} = 8.61 \times 10^4$. This can be related to the mode number N and round-trip intra-cavity loss, $\Sigma\alpha_{int}$, by $Q = \frac{2\pi N}{\Sigma\alpha_{int}}$ [101].

Note that if the operating length L is tuned slightly such that $L_{conf} = 17.65$ cm, the semi-confocal condition $R = 2L$ is obtained. In this situation, and assuming the excitation is azimuthally symmetric such that $m = 0$, the resonant frequencies are given by $f_{conf} = \frac{c}{2L} \left[\frac{(2p+1)}{4} + N \right]$. The mode structure of the cavity is now considerably simplified, as half of all transverse excitations (parameterized by p) are degenerate with the longitudinal modes N . This (and the fully confocal analogue in symmetric resonators) is a common operating condition for optical cavities, because it greatly simplifies alignment of the input beam. When the cavity is tuned to the correct length, all input power that overlaps any of the resonant transverse modes can be coupled in. This is, in fact, an

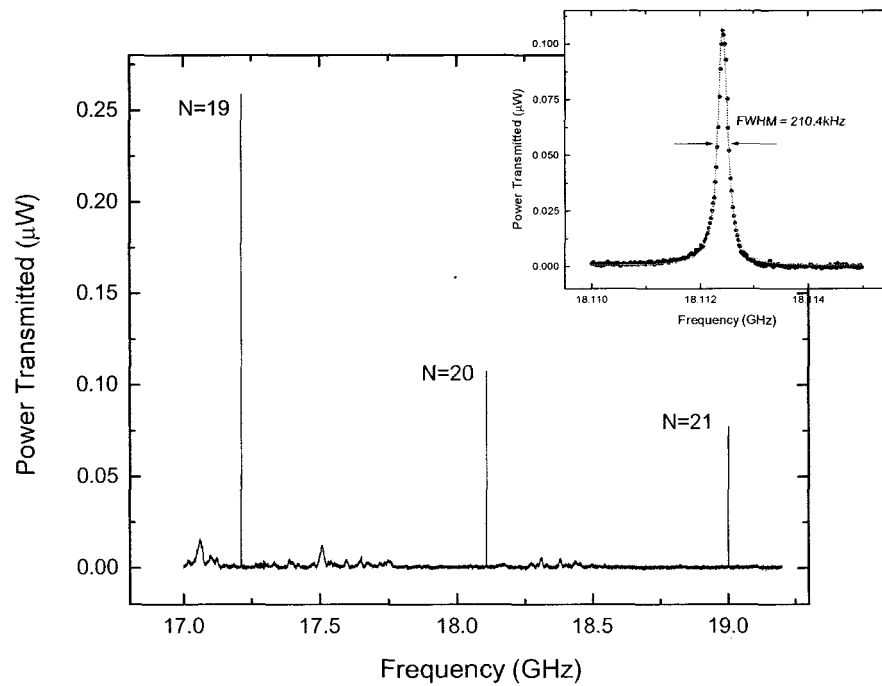


Figure 3.2: Transmission spectrum for a minimally coupled cavity of length $L = 16.76\text{cm}$. The sharp peaks correspond to longitudinal modes $N = 19, 20$ and 21 . Transverse excitations at frequencies between these modes are suppressed due to good input mode matching. The inset shows a high-resolution scan around the $f \sim 18.1\text{GHz}$ peak, which has been fit to a Lorentzian of linewidth $\Delta f_{FWHM} = 210.4\text{ kHz}$. This gives $Q = 8.61 \times 10^4$.

undesirable situation for the microwave trap cavity, where the goal is to direct all of the input power into the fundamental $p = 0$ mode in order to maximize the trapping field. Furthermore, because the ratio of the mirror diameter to the beam spot size of the microwave cavity is considerably smaller than for most optical cavities, diffractive losses increase rapidly with transverse mode number, and the Q of the cavity is diminished. Figure 3.3 shows a series of Q measurements taken as a function of cavity length for several different mirror combinations. The length of each cavity was varied by moving the curved mirror using a stack of 3 Thorlabs PT-1 micrometer-adjusted translation stages, while the excitation frequency was held fixed at 18.1 GHz. The angular alignment of the curved mirror was tweaked to maximize the Q at each length. In general, the Q is expected to increase linearly with length until diffractive losses (in the $p = 0$ mode) begin to dominate. The key feature to notice here, however, is the sharp decrease in the observed Q at the half-confocal condition (corresponding to $N = 21$), presumably due to coupling of power into the higher order transverse modes. In order to avoid this difficulty, it was decided to operate the cavity at $N = 20$ for the implementation of the microwave trap.

3.3 Trap Depth and Circular Polarization Requirement

The basic principle of the microwave trap is to use electric-field induced AC Stark shifts to create a confining potential for polar molecules. For a microwave frequency tuned to the red of the lowest rotational transition $\hbar < 2B_e$, the energy of the rotational ground state ($J = 0$) will necessarily decrease with increasing electric field. To calculate the depth of the trapping potential non-perturbatively in the regime of strong fields ($\mu E_0 \gtrsim B_e$), we use the formalism of dressed states [102]. In this picture, the quantized electric field is represented by a coherent state, and the mean number of photons \bar{N} in the cavity is large enough that it is not changed appreciably by a small number n of absorption or emission events: $n \ll \sqrt{\bar{N}}$. Defining the zero of the electric-field energy so as to consider only these transition-induced deviations from the mean photon number, and noting that the $^1\Sigma$ electronic ground state of the SrO molecule has the rotational structure of a rigid rotor, we can write the Hamiltonian of the system as $H = H_0 + H_{St}$, where

$$H_0 = B_e \mathbf{J}^2 + \hbar\omega(\hat{N} - \bar{N}) \quad (3.6)$$

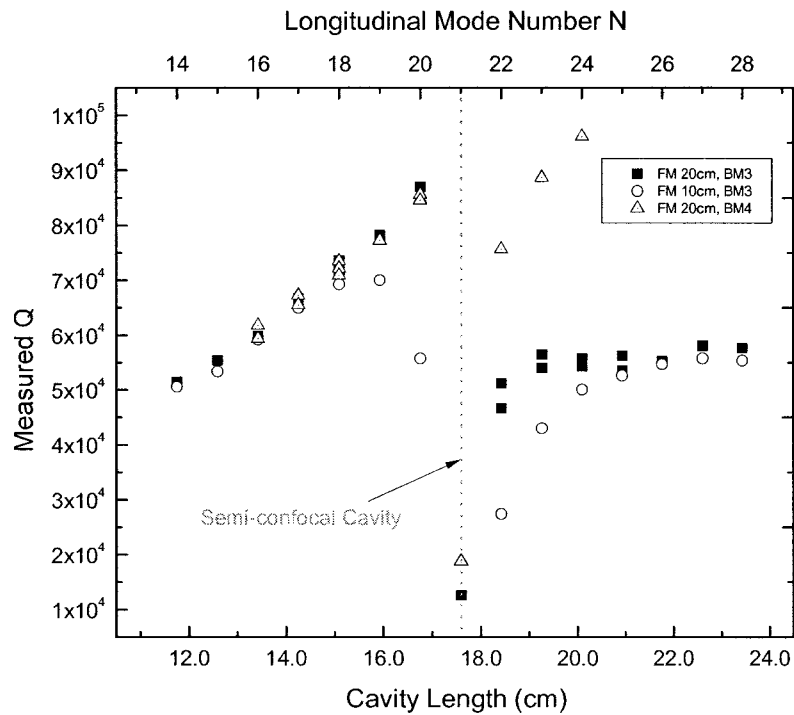


Figure 3.3: Measured Q vs. Cavity Length. Several mirror combinations were used to investigate diffractive loss. FM 10 cm and FM 20 cm are square plane mirrors of area $(10 \text{ cm})^2$ and $(20 \text{ cm})^2$ respectively. BM4 is the parabolic mirror depicted in figure 3.1; BM3 is a parabolic mirror of the same focal length, $f = 17.65 \text{ cm}$, but with a diameter of only 19.8 cm and coarser surface quality specification. The cavity Q is seen to drop sharply at the confocal length ($L = 17.6 \text{ cm}$) due to the excitation of many transverse modes which are simultaneously resonant and which experience higher diffraction loss than the fundamental.

Here, $\hat{N} = a^\dagger a$ is the photon number operator, $\omega = 2\pi \times 18.1$ GHz is the microwave field frequency, and $B_e = 10.14$ GHz is the rotational constant of SrO. The mean photon number for a coherent state is related to E_0 , the classical electric field amplitude, by $\bar{N} = \frac{E_0^2 \epsilon_0 V}{2 \hbar \omega}$. Using $\sqrt{\bar{N} \pm n} \approx \sqrt{\bar{N}}$, molecule-field interaction is then described by the Stark Hamiltonian,

$$H_{St} = -\boldsymbol{\mu} \cdot \mathbf{E} = -\mu \left(\frac{\hbar \omega}{2 \epsilon_0 V} \right) [(\mathbf{n} \cdot \boldsymbol{\epsilon}^*) a^\dagger + (\mathbf{n} \cdot \boldsymbol{\epsilon}) a], \quad (3.7)$$

for a^\dagger and a photon creation and annihilation operators, \mathbf{n} an operator unit vector pointing along the internuclear axis, $\boldsymbol{\epsilon}$ a complex (c-number) unit vector defining the electric field polarization, and $\mu = 8.9$ Debye = 4.48 MHz \cdot (V/cm) $^{-1}$ the dipole moment of SrO. Writing the combined molecule-field eigenstates in the basis $|J, m, n\rangle$, the matrix elements are given by

$$\begin{aligned} \langle J', m', n' | H_0 | J, m, n \rangle &= B_e J(J+1) + n \hbar \omega \\ \langle J', m', n' | H_{St} | J, m, n \rangle &= \frac{\mu E_0}{2} [\langle J', m' | \mathbf{n} \cdot \boldsymbol{\epsilon} | J, m \rangle \delta_{n', n-1} + \langle J', m' | \mathbf{n} \cdot \boldsymbol{\epsilon}^* | J, m \rangle \delta_{n', n+1}] \end{aligned} \quad (3.8)$$

Note that this will yield an energy structure periodic in n . Numerical calculations to diagonalize this Hamiltonian can now be performed on a finite Hilbert space $0 \leq J \leq J_{max}$ and $-n_{max} \leq n \leq n_{max}$. Their convergence can be determined by verifying their periodicity in n , as well as by checking that the results remain the same when the number of states set by J_{max} and n_{max} is increased.

3.3.1 Linear Polarization

Consider first the case of a linearly polarized electric field in the cavity, $\boldsymbol{\epsilon} = \hat{z}$. The matrix elements of Equation 3.8 can then be calculated explicitly as

$$\begin{aligned}
\langle J', m' | \mathbf{n} \cdot \boldsymbol{\epsilon} | J, m \rangle &= \langle J', m' | \mathbf{n} \cdot \boldsymbol{\epsilon}^* | J, m \rangle = \int Y_j^{m'*} \cos \theta Y_j^m d\Omega \\
&= \left[\frac{J+1}{\sqrt{2J+1}\sqrt{2J+3}} \delta_{J', J+1} + \frac{J}{\sqrt{2J-1}\sqrt{2J+1}} \delta_{J', J-1} \right] \delta_{m', m}
\end{aligned} \tag{3.9}$$

We are interested primarily in the energy shifts of the $|J = 0, m = 0, n = 0\rangle$ trapped state, and therefore need to consider only the subspace $\{|J, m = 0, n\rangle\}$ with $\text{mod}(|J + n|, 2) = 0$ that is connected to it through this interaction. Figure 3.4 shows the calculated AC Stark shifts for states in this manifold with $J_{\text{max}} = 5$ and $n_{\text{max}} = 20$, for a linearly polarized trapping field at frequency $f = 18.1$ GHz. Approximately one fifth of the calculational subspace is shown in the left panel; as expected, the energy structure for each rotational state is repeated in steps separated by 36.2 GHz, or two photon energy units, along the vertical axis. (A computation on the full Hilbert space would yield repetitions every 18.1GHz. We have included only half of the possible photon number states $|n\rangle$, however, the others being unable to interact with the $|0, 0, 0\rangle$ state of interest.) The vertical (energy) axis of the plot is labeled both in GHz and in units of the rotational constant of SrO, $B_e/h = 10.14$ GHz; similarly, the horizontal axis is labeled in kV/cm as well as in units of the dipole interaction energy divided by the rotational constant, $\mu \cdot E/B_e$, for $\mu = 8.9$ Debye. The advantage of expressing the shifts in terms of the rotational constant is generality, since the shapes of the curves will be the same for all rigid-rotor molecules when expressed in these units. The right panel of the figure focusses on a single period of the energy structure, showing just one line for each zero-field J state. Here, we clearly see that the $|0, 0, 0\rangle$ state initially repels from $|1, 0, -1\rangle$ and decreases in energy. (Note that these state labels apply rigorously only at zero field; as the electric field grows, the states become increasingly mixed. Nevertheless, we will continue to use the zero field labels to refer to the states which connect adiabatically to them for convenience.) It then undergoes interactions with other states as the field is increased further, manifested in a series of avoided crossings. Physically, these are brought about as the field-dressed molecular levels come into multi-photon resonance at particular values of the electric field strength. In particular, the interaction with the $|2, 0, -4\rangle$ state is quite strong (on the order of ~ 70 MHz), and will lead to state-changing excitations when the trapped molecule traverses this part of the trap.

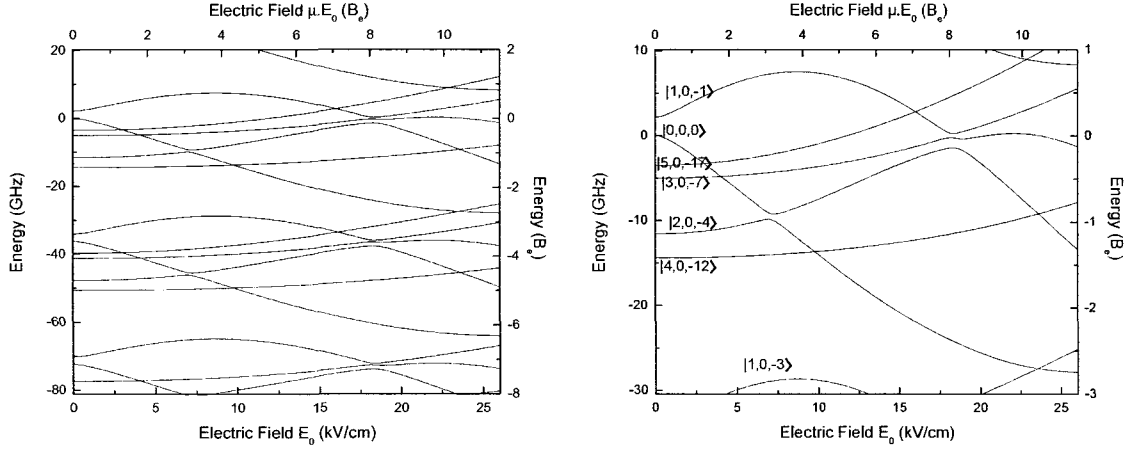


Figure 3.4: Dressed-state calculation for the energies of rotational levels up to $J_{max} = 5$ in a linearly-polarized ($\epsilon = \hat{z}$) AC electric field at frequency $f = 18.1$ GHz. The left panel shows several periods of the energy structure, each of which corresponds to a change of the mean cavity photon number n by ± 2 . The calculation is performed for photon numbers up to $n_{max} = 20$, hence the figure shows approximately one fifth of all of the included states. The right panel focusses specifically on one period immediately surrounding the nominal $|J=0, m=0, n=0\rangle$ state. This state undergoes a series of avoided crossings as it is shifted into multi-photon resonance with other rotational levels.

3.3.2 Criterion for Non-Adiabaticity

It is important to consider the scale of these crossings compared to the rate at which the molecule moves through them as it orbits within the trap. Adiabatic traversal corresponds to a multi-photon absorption or emission event which rotationally excites the molecule and thereby significantly reduces the effective trap depth. The probability of non-adiabatic passage is given by Zener [103] as

$$P_{non-adiabatic} = e^{-2\pi\gamma}, \quad \text{for} \quad \gamma = \frac{2\pi}{h} \frac{U_{12}^2}{\left| \frac{d}{dt}(U_1 - U_2) \right|} \quad (3.10)$$

Here, U_1 and U_2 are the energies of the two states, and U_{12} is the strength of the interaction between them. The minimum energy splitting at the avoided crossing is approximately $2 U_{12}$. In order for the splitting to be small enough to allow non-adiabatic traversals with high probability, we require

$$U_{12}^2 \ll \frac{h \left| \frac{d}{dt}(U_1 - U_2) \right|}{(2\pi)^2} \quad (3.11)$$

Strictly speaking, the parameter γ should be calculated for each crossing independently to

account for variations in the local slopes $\frac{d}{dt}(U_1 - U_2)$. Nevertheless, it is possible to use typical values for our trap parameters to estimate the approximate size of splitting required to allow non-adiabatic traversals. Write $\frac{d}{dt}(U_1 - U_2) = \frac{d(U_1 - U_2)}{dE} \cdot \frac{dE}{dx} \cdot \frac{dx}{dt}$. Now, the spatial variation of the electric field is slowest in the radial direction of the Gaussian beam profile, $E(x) \approx E_{peak} \exp(-\frac{x^2}{w_0^2})$. Taking the spatial derivative and eliminating x in favor of $E(x)$ gives

$$\frac{dE(x)}{dx} = E_{peak} \left(\frac{-2x \exp\left(-\frac{x^2}{w_0^2}\right)}{w_0^2} \right) = \frac{-2E(x)}{w_0} \sqrt{\ln\left(\frac{E_{peak}}{E(x)}\right)}$$

Now choose a typical value for the field, say $E(x) = E_{peak}/2$, so that $\frac{dE}{dx} = -\sqrt{\ln(2)} \frac{E_{peak}}{w_0}$. Note that, in the absence of avoided crossings, $\frac{dU}{dE}$ would saturate to $\mu/2$ at electric field strengths sufficiently large to fully mix the rotational states. (This is shown in Section 3.3.3 below.) It is therefore reasonable to estimate that $\frac{d(U_1 - U_2)}{dE} \sim \mu$. Finally, we can write $\frac{dx}{dt} = v_{SrO}$, the characteristic velocity of trapped SrO molecules with ~ 4 K of kinetic energy. Equation 3.11 thus becomes

$$U_{12}^2 \ll (8.78 \times 10^{-3})(\mu E_{peak}) \left(\frac{h v_{SrO}}{w_0} \right) \quad (3.12)$$

Substituting $\mu E_{peak} \sim (4.48 \frac{\text{GHz}}{\text{kV/cm}}) \times (12.2 \text{ kV/cm})$ and $\frac{v_{SrO}}{w_0} \sim \frac{25.3 \text{ m/s}}{0.031 \text{ m}}$ (in units of $h = 1$) gives $U_{12} \ll 631$ kHz. Thus, the maximum allowed splitting to avoid adiabatic passage to more rotationally excited states is on the order of ~ 1.2 MHz (or $\sim 10^{-4} B_e$) - too small to observe on the scale of Figure 3.4. When the calculation is repeated on a finer grid in the vicinity of each crossing, it is found that the interactions with the states that connect to zero-field eigenstates $|3, 0, -7\rangle$, $|4, 0, -12\rangle$, and $|5, 0, -17\rangle$ (of strengths $2U_{12} \sim 34.7$ kHz, 368 Hz, and < 1 Hz respectively), are sufficiently weak for non-adiabaticity. The avoided crossing with the $|2, 0, -4\rangle$ state, however, is approximately $2U_{12} \sim 690$ MHz and necessarily leads to a reduction in the effective depth of a linearly-polarized microwave trap for SrO molecules.

3.3.3 Circular Polarization

The difficulty can be resolved, in principle, by using a circularly-polarized field. Consider, for instance, the case of $\epsilon = \hat{\sigma}^+ = (\hat{x} + i\hat{y})/\sqrt{2}$. Here, the absorption of a photon is accompanied by a change in the angular momentum projection of $\Delta m = +1$, and emission of a photon results in $\Delta m = -1$. The subspace of states connected to the trapped $|J = 0, m = 0, n = 0\rangle$ state is therefore defined

by $\{|J, m, n = m\rangle\}$ with $\text{mod}(|J + n|, 2) = 0$. This guarantees that resonant multi-photon transitions to a final state $|J', m', n'\rangle$ are impossible, because $n' = m'$ and $m' \leq J'$ necessarily implies $n' \leq J'$, but the energy difference $U(J') - U(J = 0) \geq B_e J'(J'+1)$ at any electric field value. Since the photons are red-detuned from the lowest transition, $\hbar\omega < 2B_e$, we know that $n'\hbar\omega < 2J'B_e \leq U(J') - U(J = 0)$ (due to $2J \leq J(J+1)$ for $J \geq 1$). The complicated structure seen in Figure 3.4 is thus eliminated, and the $J=0$ state decreases monotonically in energy with increasing field. The analytic form of the off-diagonal matrix elements from Equation 3.8 is now given by

$$\begin{aligned}
\langle J', m' | \mathbf{n} \cdot \boldsymbol{\epsilon} | J, m \rangle &= \langle J', m' | \mathbf{n} \cdot \boldsymbol{\epsilon}^* | J, m \rangle \\
&= \frac{1}{\sqrt{2}} \int \gamma_p^{m'^*} \sin \theta e^{i\phi} \gamma_j^m d\Omega \\
&= \frac{1}{\sqrt{2}} \left[\frac{\sqrt{J-m-1} \sqrt{J-m}}{\sqrt{2J-1} \sqrt{2J+1}} \delta_{J', J-1} + \frac{\sqrt{J+m+1} \sqrt{J+m+2}}{\sqrt{2J+1} \sqrt{2J+3}} \delta_{J', J+1} \right] \delta_{m', m+1} .
\end{aligned} \tag{3.13}$$

The results of a matrix diagonalization calculation performed for a circularly polarized field at 18.1 GHz, with $J_{max} = 10$ and $n_{max} = 20$, are shown in Figure 3.5. As expected, the avoided crossings of the linearly polarized case are absent. The energy of the trapped state decreases with increasing field and, for field strengths $E_0 \gtrsim \frac{B_e}{\mu}$, does so linearly with a slope approximately $\sim \mu/2$. The maximum attainable trap depth for a peak electric field of 12.2 kV/cm (see Section 3.5.1 for details) is seen to be 21.1 GHz, or approximately 1.0 K.

3.3.4 General Elliptical Polarization

One additional complication arises in considering the polarization requirement for the microwave trap, in that it is not possible to produce the ideal circular state assumed in Section 3.3.3. Real microwave antennas invariably produce fields with some polarization component of the opposite handedness (termed "cross-polarization"), which has the effect of restoring some of the multi-photon interactions seen in the linear polarization calculation. Intuitively, it can be seen that the strength of a particular multi-photon interaction should be suppressed relative to the linear case by a factor roughly equal to the fraction of the electric field amplitude in the wrong polarization, raised to the power of the number of wrong-handed photons required to connect the angular momenta

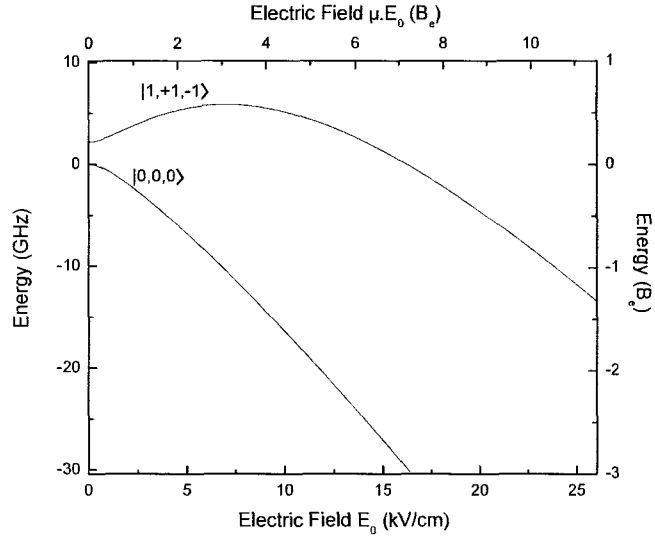


Figure 3.5: Dressed-state calculation for the energies of rotational levels up to $J_{max} = 10$ in a circularly-polarized ($\epsilon = \hat{\sigma}^-$) AC electric field at frequency $f = 18.1\text{GHz}$. The maximum photon number for states used in the calculation is $n_{max} = 20$. Note that the avoided crossings seen in Figure 3.4 are eliminated and the energy of the $|0,0,0\rangle$ trapped state decreases monotonically.

of the $|J', m', n'\rangle$ final state to the $|0,0,0\rangle$ trapped state. For example, if the electric field is such that a six-photon resonance exists between the trapped state and $|J = 2, m = 2, n = -6\rangle$, then four of the photons must be σ^+ and two σ^- to provide the correct angular momentum transfer, and the resonance is suppressed by the square of fractional field amplitude in the σ^- polarization.

The foregoing is, of course, a qualitative argument, and it is necessary to repeat the AC Stark shift calculation for a general elliptically-polarized field to determine the polarization purity required for the microwave trap. This is numerically more challenging than the previous calculations due to the larger number of states that must be included; the subspace connected to $|J = 0, m = 0, n = 0\rangle$ now includes all $\{|J, m, n\rangle\}$ such that $\text{mod}(|J + m|, 2) = 0$ and $\text{mod}(|J + n|, 2) = 0$. If we define the polarization vector as $\epsilon = A \hat{\sigma}^+ + B \hat{\sigma}^-$ (with $|A|^2 + |B|^2 = 1$), then the molecular off-diagonal matrix

elements from Equation 3.8 may be written as

$$\begin{aligned}
\langle J', m' | \mathbf{n} \cdot \boldsymbol{\epsilon} | J, m \rangle &= \frac{A}{\sqrt{2}} \int Y_j^{m'*} \sin \theta e^{i\phi} Y_j^m d\Omega + \frac{B}{\sqrt{2}} \int Y_j^{m'*} \sin \theta e^{-i\phi} Y_j^m d\Omega \\
&= \frac{A}{\sqrt{2}} \left[\frac{\sqrt{J-m-1} \sqrt{J-m}}{\sqrt{2J-1} \sqrt{2J+1}} \delta_{J', J-1} + \frac{\sqrt{J+m+1} \sqrt{J+m+2}}{\sqrt{2J+1} \sqrt{2J+3}} \delta_{J', J+1} \right] \delta_{m', m+1} \\
&\quad + \frac{B}{\sqrt{2}} \left[\frac{\sqrt{J+m-1} \sqrt{J+m}}{\sqrt{2J-1} \sqrt{2J+1}} \delta_{J', J-1} + \frac{\sqrt{J-m+1} \sqrt{J-m+2}}{\sqrt{2J+1} \sqrt{2J+3}} \delta_{J', J+1} \right] \delta_{m', m-1}
\end{aligned} \tag{3.14}$$

$$\begin{aligned}
\langle J', m' | \mathbf{n} \cdot \boldsymbol{\epsilon}^* | J, m \rangle &= \frac{A^*}{\sqrt{2}} \int Y_j^{m'*} \sin \theta e^{-i\phi} Y_j^m d\Omega + \frac{B^*}{\sqrt{2}} \int Y_j^{m'*} \sin \theta e^{i\phi} Y_j^m d\Omega \\
&= \frac{A^*}{\sqrt{2}} \left[\frac{\sqrt{J+m-1} \sqrt{J+m}}{\sqrt{2J-1} \sqrt{2J+1}} \delta_{J', J-1} + \frac{\sqrt{J-m+1} \sqrt{J-m+2}}{\sqrt{2J+1} \sqrt{2J+3}} \delta_{J', J+1} \right] \delta_{m', m-1} \\
&\quad + \frac{B^*}{\sqrt{2}} \left[\frac{\sqrt{J-m-1} \sqrt{J-m}}{\sqrt{2J-1} \sqrt{2J+1}} \delta_{J', J-1} + \frac{\sqrt{J+m+1} \sqrt{J+m+2}}{\sqrt{2J+1} \sqrt{2J+3}} \delta_{J', J+1} \right] \delta_{m', m+1}
\end{aligned} \tag{3.15}$$

It can be shown that the above matrix elements reproduce the expected behavior of the linearly- and circularly- polarized fields with $A = B = 1/\sqrt{2}$ for the former, and $A = 1, B = 0$ for the latter. Figure 3.6 shows the AC Stark shifts calculated for a field at $f = 18.1$ GHz and with polarization vector defined by $A = 0.995$ and $B = 0.0995$. This corresponds to a cross-polarization specification of -20dB for the source antenna, roughly equivalent to that of our current polarizer and feed horn (see Section 3.4.3 for details). The calculation includes all magnetic sublevels that can potentially connect with the $|0, 0, 0\rangle$ state, $m = \{-J, -J+2, \dots, J-2, J\}$. The trapped state interacts most strongly with the $m = +J$ states, as expected for predominantly σ^+ polarization. In particular, the size of the avoided crossing with the $|J = 2, m = +2, n = -4\rangle$ state is now about $2U_{12} \sim 91$ MHz, which is still several orders of magnitude larger than the non-adiabatic traversal criterion given by Equation 3.11. Repeating the calculation for purer polarizations shows that the size of the crossing decreases by an order of magnitude for every 20dB reduction in cross-polarization. This is reasonable, since the interaction involves 3 σ^+ photons and 1 σ^- photon; the strength of the crossing is therefore linear in the B component of the polarization. Unfortunately, this means that fulfillment of the non-adiabatic criterion requires a cross-polarization of -60dB or better, which is very difficult to achieve. This has the practical effect of reducing the useful microwave trap depth to 9.9 GHz (or 0.48 K) at a maximum field of 6.8 kV/cm for SrO.⁴

⁴It is interesting to note that a deeper effective confining potential can be obtained by operating the trap at a *larger*

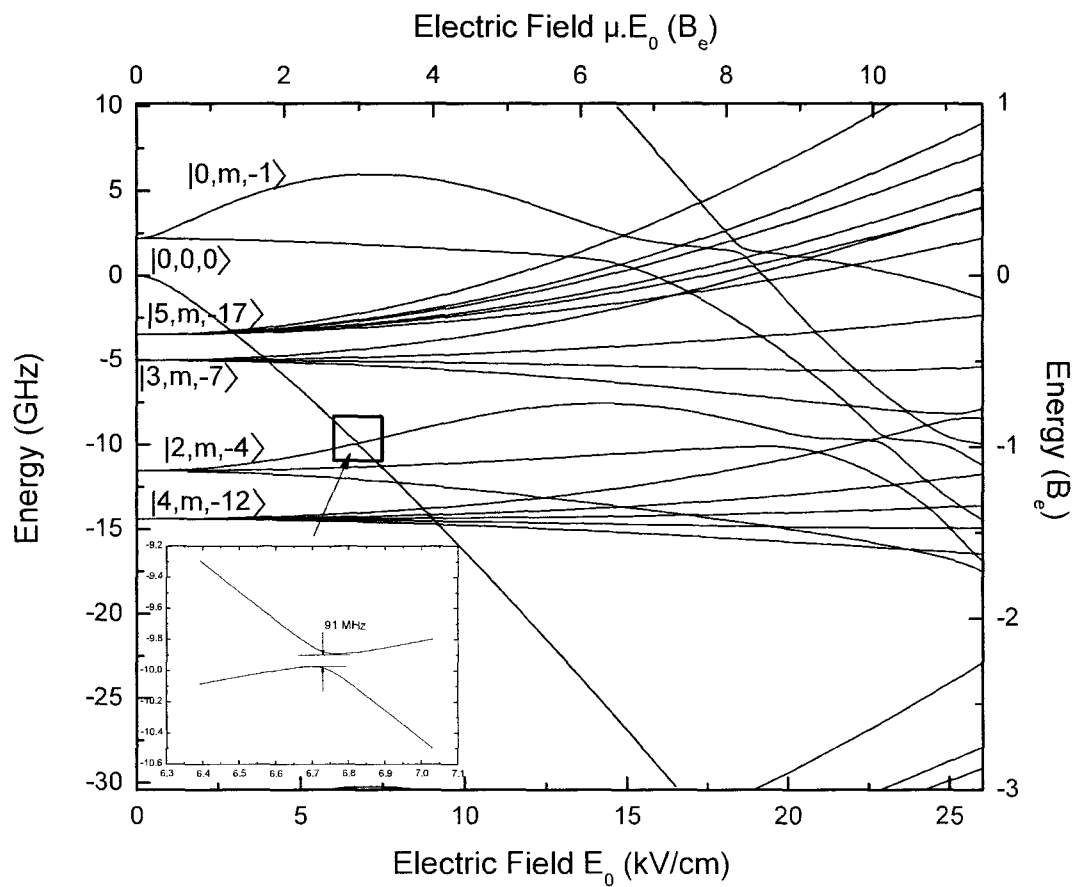


Figure 3.6: Dressed-state calculation for an elliptically polarized field with -20dB cross-polarization. Although the 4-photon interaction with the $|J = 2\rangle$ state is reduced by an order of magnitude compared to the linearly-polarized case, it is still too large to satisfy the criterion for non-adiabatic transit.

3.4 Mode Matching and Quasi-optical Design

Efficient transfer of input power into the Gaussian TEM_{00} trap mode requires a high degree of spatial overlap with the excitation field. The power coupling coefficient between two unit-normalized Gaussian beam modes Ψ_1 and Ψ_2 is given by (see, for example, [104])

$$K_{12} = \left| \int \int \Psi_1^* \Psi_2 dS \right|^2 \quad (3.16)$$

This suggests that the best way to excite the cavity mode of interest is with an externally-launched Gaussian beam of the the same complex q-parameter. While excitation by, for instance, an internal dipole or half-wave antenna is also possible, the radiation patterns of these sources are likely to have significant overlap with many higher-order cavity modes, resulting in inefficient coupling to the TEM_{00} trap mode. Fortunately an extensive literature exists on the generation and manipulation of Gaussian “quasi-optical” beams in the microwave and mm-wave regime, for applications in radio astronomy, remote sensing, and communications [99] [105]. The present section describes the development of a quasi-optical beam source to excite the TEM_{00} trap mode of our cavity with nearly unit efficiency. Note that power from this source can be coupled into the cavity by a partially-transmitting mirror, in direct analogy to the multi-layer dielectric mirrors used in optical cavities. This can be achieved by perforating the mirror with an array of sub-wavelength apertures, as described below in Section 3.5.

3.4.1 Microwave Beam Profiler

In order to facilitate rapid measurements of quasi-optical beam parameters, an automated beam-profiler was constructed. It consisted of a pyramidal horn antenna (ATM, Inc 62-440-6), mounted on a belt-driven 2D translation stage (Arrick Robotics X-18) with 18” travel in the horizontal direction and 8” in the vertical. Stepper motors were used to control the motion in each direction, with nominal resolution of 0.005” and accuracy of 0.02” over the full range of translation. (Empirically, it was found that errors tended to accumulate for step sizes less than ~ 0.08 ”, but this may have

detuning from the $J = 0 \rightarrow J = 1$ resonance. In particular, if we select f to be slightly smaller than $6B_c/4 = 15.21$ GHz, then the $|j = 2, m = +2, n = -4\rangle$ state is shifted to $U \approx 6B_c - 4f \geq 0$, and does not have a crossing with trapped state. At $f = 15$ GHz, for instance, the only multi-photon interactions at achievable field strengths are with $|j = 4, m, n = -14\rangle$ at $E \sim 6$ kV/cm, and with $|j = 3, m, n = -9\rangle$ at $E \sim 9$ kV/cm; however, these are of sufficiently high order that the interaction strength should satisfy the non-adiabaticity requirement. The first crossing that fails to meet this condition is with $|j = 1, m, n = -3\rangle$, but this does not occur until $E \sim 14$ kV/cm, which exceeds our maximum field. Thus, the full ~ 20 GHz trap depth can be recovered.

been a result of rounding errors in the calibration of the control software. This was sufficient for the present application, in any case.) Control of the motor driver was by RS-232 interface, using NI Labview drivers from third-party vendor TEM Consulting. Power collected by the antenna was transmitted through a waveguide-coax transition and a 15 cm length of cable to a calibrated diode detector (Rohde & Schwartz NRP-Z23), which was in turn read by the computer via a USB interface. It was found that repeatable measurements could only be obtained if the detector was mounted on the moving stage with the horn, in order to avoid curvature-dependent changes in the transmission of the coaxial cable.

The spatial resolution of the beam profiler is inversely related the angular acceptance of the gain horn. A rough estimate of the resolution of a given horn can be obtained by comparing its angular beam width to the divergence angle of a Gaussian beam with some waist parameter w_0 ,

$$w_0 = \frac{\lambda \sqrt{\ln 2}}{\sqrt{2}\pi \tan(\theta/2)} \quad (3.17)$$

where λ is the microwave wavelength and θ is the full 3dB angle of the antenna field pattern. Our wavelength is $\lambda = 1.66$ cm and, for the horn used, the E-plane beam width is specified to be 55.3° . This gives an estimated spatial resolution of ~ 0.6 cm. Most scans consisted of approximately 1000 points, typically over an area of about $10 \text{ cm} \times 10 \text{ cm}$ (depending on the beam diameter in the plane being scanned), and required on the order of 5 minutes to complete. Full characterization of a Gaussian beam to accurately determine the position of its waist generally required scans in ~ 10 planes, with the profiler being moved manually between each measurement. The entire process typically took several hours.

3.4.2 Quasi-optical Elements

Because the final microwave trap design requires very high input power, some effort was made to develop an efficient quasi-optical feed system. See Figure 3.7 for an example of one proposed feed system design consisting of a scalar horn and a pair of ellipsoidal focussing mirrors. The basic goal of such a system is to transform the beam produced by a horn antenna into the mode supported by the cavity, with the correct (circular) polarization. Some combination of focussing and polarization-changing elements is used to effect this transformation. The modes of interest are

fairly well described by Gaussian beams, so the formalism of 2×2 ray transfer matrices (or "ABDC matrices") can be employed. The matrices for standard focussing elements can be found in many textbooks (see, for example Yariv [98] chapter 6). Recall that for a transfer matrix with elements $M_{11} = A$, $M_{12} = B$, $M_{21} = C$, and $M_{22} = D$, the q -parameter of an incident Gaussian beam is transformed according to $q_{out} = \frac{Aq_m + B}{Cq_m + D}$, where q is related to the diameter w and radius of curvature R in a given plane by $\frac{1}{q} = \frac{1}{R} + \frac{i\lambda}{\pi w^2}$. Some simple algebra can be performed to eliminate q -parameters in favor of the initial and final beam diameter and radius of curvature, yielding the following useful formulas:

$$\begin{aligned} R_f &= \frac{\pi^2 w_i^4 (AR_i + B)^2 + \lambda^2 R_i^2 B^2}{\pi^2 w_i^4 (AR_i + B)(CR_i + D) + \lambda^2 R_i^2 BD} \\ w_f^2 &= \frac{\pi^2 w_i^4 (AR_i + B)^2 + \lambda^2 R_i^2 B^2}{\pi^2 R_i^2 w_i^2} \end{aligned} \tag{3.18}$$

The final microwave feed setup (described in section 3.4.3) is actually relatively simple, consisting only of a specially-engineered horn antenna and a waveguide-based polarization rotator. Earlier design iterations involved a variety of quasi-optical elements, however, and these will be enumerated and briefly described here for completeness.

Corrugated Feed Horn: A common approach for generating relatively symmetric, linearly polarized gaussian beams at microwave and millimeter-wave frequencies is the corrugated horn antenna [99]. (Although smooth-walled conical horns can be used in principle, their ellipticity and cross-polarization properties are often less favorable.) The interior of the corrugated horn is inscribed with cylindrically-symmetric grooves of periodicity less than a wavelength, and depth $\lambda/4$. This has the effect of creating an infinite reactance at the walls of the horn, and thereby concentrating the field close to the axis. Such a structure supports the so-called hybrid EH_{1m} modes, which have more commonly been used to describe light propagation in hollow dielectric waveguides [106]. In particular, the hybrid EH_{11} mode has $\mathbf{E}(r) = J_0\left(\frac{u_{01}r}{a}\right)\hat{z}$, for linearly polarized excitation in the \hat{z} direction. (Here, a is the horn aperture radius and $u_{01} = 2.4048$ is the first zero of J_0). This mode has linear polarization and an azimuthally symmetric radiation pattern, and can be shown to overlap with a TEM_{00} Gaussian beam mode of diameter $w = 0.644a$ with an efficiency $K \sim 0.979$ [107]. We

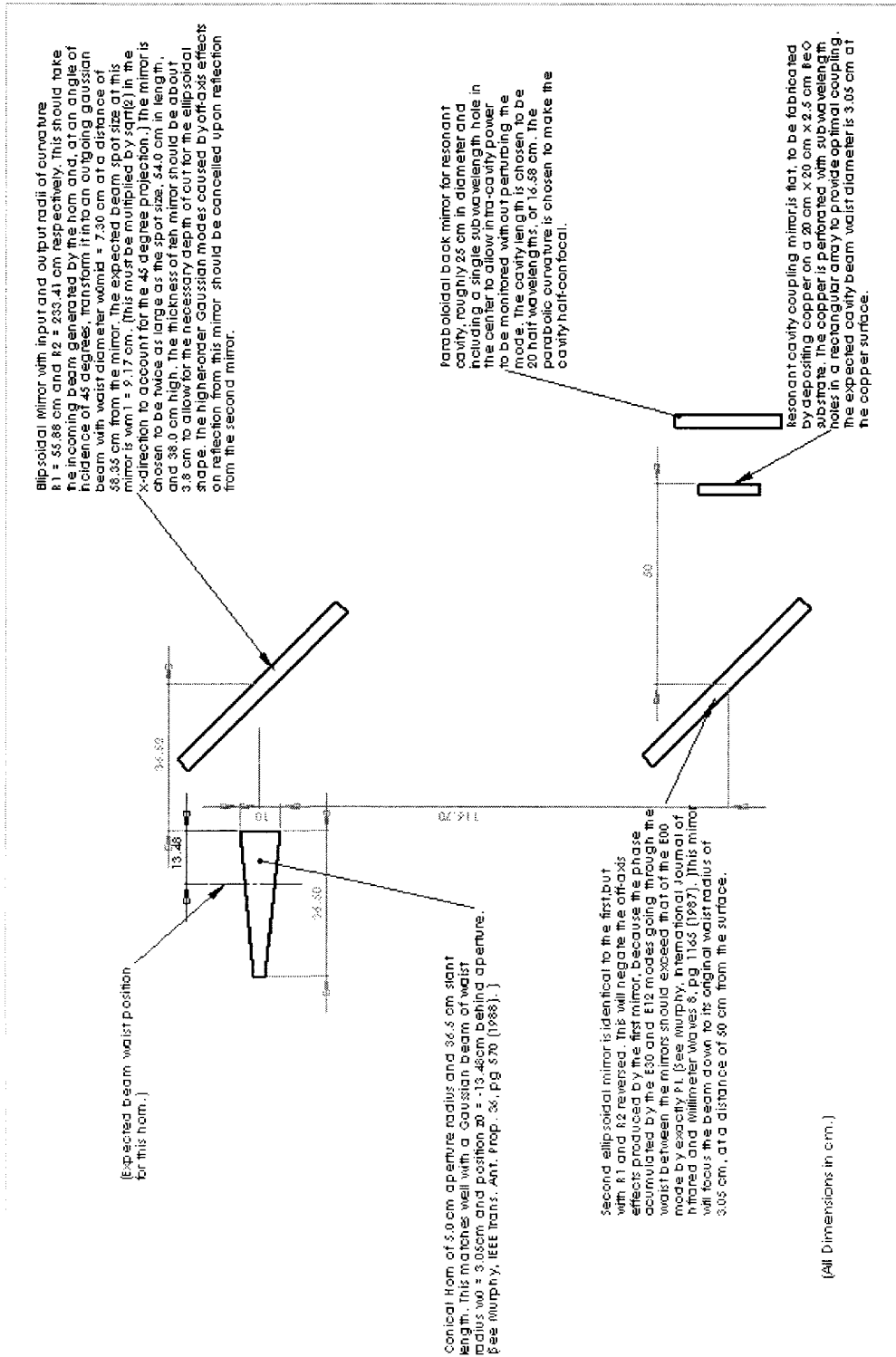


Figure 3.7: Design for Quasi-Optical Feed Using Paired Ellipsoidal Focusing Mirrors

have used two corrugated horns in our quasi-optical beam development, (purchased from Thomas Keating Instruments), both designed to operate at 18.1 GHz. The first outputs a mode that is well-approximated by a Gaussian beam of waist diameter $w_0 = 2.03$ cm in a plane approximately 2 cm behind the aperture. The second was specially designed to produce a waist very close to the aperture plane; its field there has approximately $K = 0.988$ overlap with a Gaussian beam waist of $w_0 = 3.05$ cm. A mechanical drawing of the newer horn is shown in Figure 3.8.

Dielectric Lens: As in conventional optics, lenses are arguably the simplest quasi-optical focussing devices to design and fabricate. The relatively long wavelengths associated with microwave radiation mean that numerical machining methods can be used to produce aspheric shapes with relative ease, and also allow for much more relaxed surface quality tolerances than in the optical domain. The tradeoff is that microwave lenses tend to become quite large and thick, and power absorption in the dielectric can become an issue. Relatively low loss, machinable materials such as Teflon and Rexolite are therefore preferred. We constructed and tested a single-surface Rexolite (index $n = 1.59$, loss tangent $\delta = 4 \times 10^{-4}$ at 13 GHz [108]) lens of diameter $d = 30$ cm and focal length $f = 21$ cm. (See Figure 3.9.) The curved face is hyperboloidal, this being the best form for collimating waves originating at its focus [99]. (In fact, a bi-hyperbolic shape would be preferred for focussing back down into the cavity mode, but this design was easier to construct and performed adequately for testing purposes.) The on-axis thickness of the lens is $t_c = 6.4$ cm, giving an absorbed power fraction of $\alpha t_c = \frac{2\pi n \tan \delta}{\lambda} t_c = 0.015$. This is reasonable for low to moderate incident powers, but for $P_{in} = 2$ kW, then $\alpha t_c = 30$ W, which cannot easily be dissipated in the dielectric. An even more serious problem arises from Fresnel reflections at the dielectric surface. For normal incidence, the reflection coefficient is $R = \left(\frac{n-1}{n+1}\right)^2 = 0.052$; for 2 kW incident power, this is over 100 W at each surface! No known dielectric exists with index of refraction $n = \sqrt{n_{Rexolite}} = 1.26$ at GHz frequencies, so anti-reflection coatings would be difficult to fabricate. It is possible in principle to produce a layer of the appropriate index by machining grooves with sub-wavelength periodicity into the surface of the lens (see the discussion of waveplates below for details), but doing so would necessarily introduce birefringence. For these reasons, it was ultimately decided that dielectric lenses are not suitable for our high-power quasi-optical mode matching application.

Ellipsoidal Mirror: As an alternative to lenses, off-axis reflectors are sometimes employed as low-loss quasi-optical focussing elements. The concave surface of an ellipsoidal mirror is described by

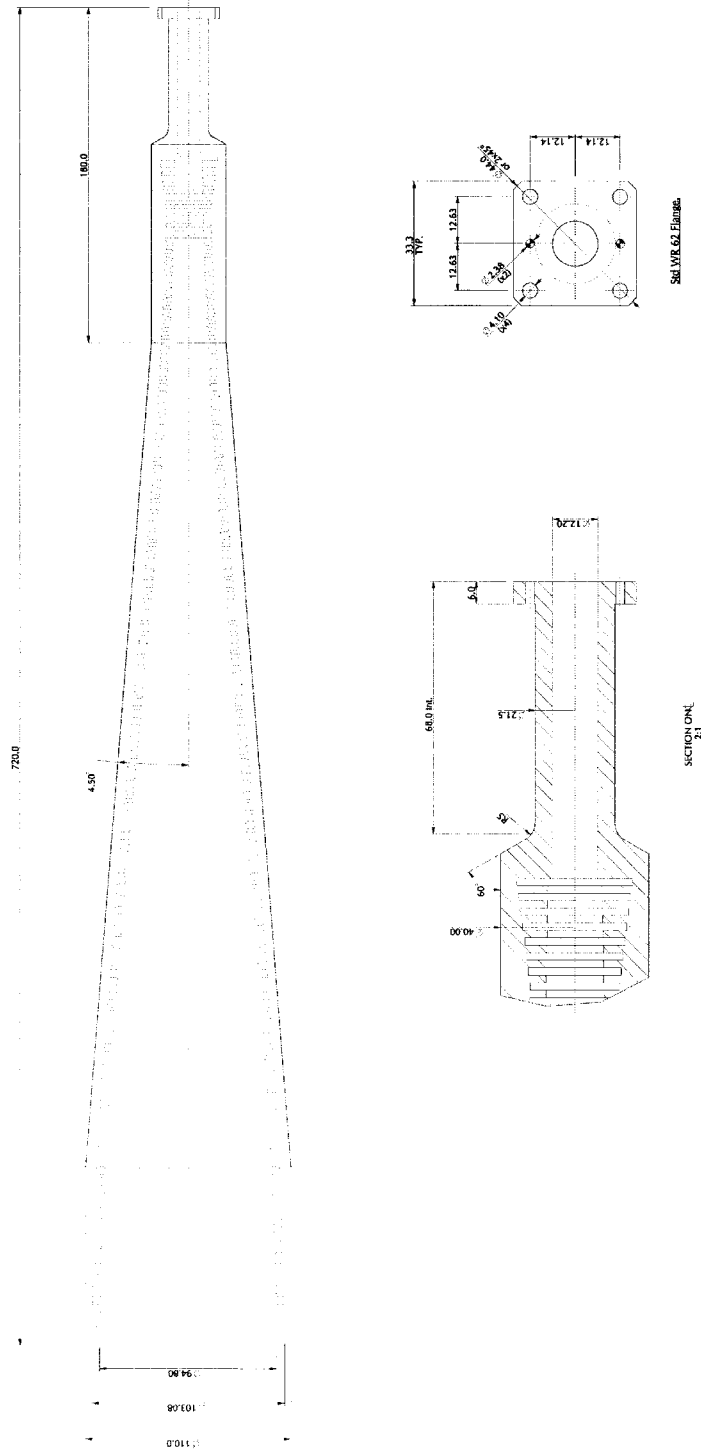


Figure 3.8: Mechanical drawing of one of our scalar horns, designed by Richard Wylde of Thomas Keating Instruments. Its output is nominally a Gaussian beam of diameter $w_0 = 3.05$ cm, with the waist located about in the aperture plane.

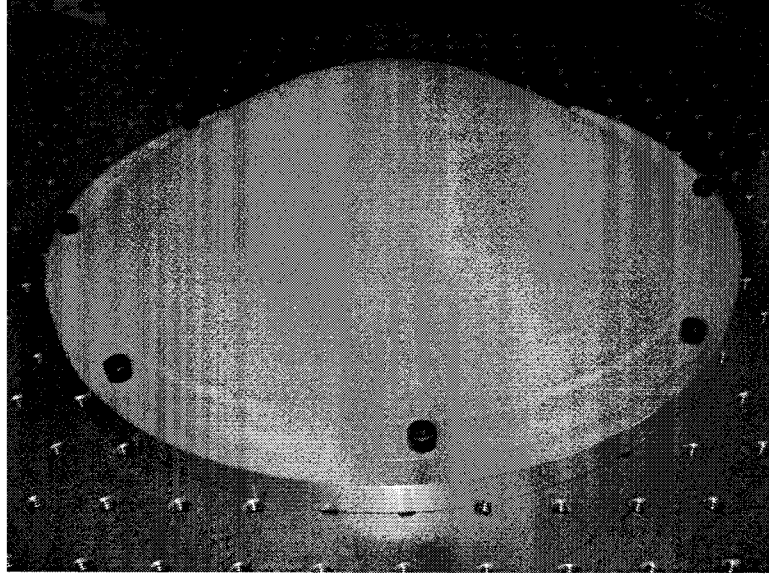


Figure 3.9: Dielectric lens. Fabricated from Rexolite, with an aperture diameter $d=30$ cm and on-axis thickness of 6.4 cm. The hyperbolic surface gives a focal length of $f=21$ cm.

an ellipse rotated about its major axis, $\frac{x^2+y^2}{b^2} + \frac{z^2}{a^2} = 1$, where $2a$ is the length of the major axis. The ellipse is defined by two foci on the major axis F_1 and F_2 , such that for any point P on the ellipse, the lengths R_1 of $\overline{F_1P}$ and R_2 of $\overline{F_2P}$ satisfy $R_1 + R_2 = 2a$. An incident TEM_{00} Gaussian beam mode passing through F_1 and having a radius of curvature R_1 when it strikes the surface of the mirror will be transformed into an outgoing beam of radius R_2 that passes through F_2 . The focal length of the mirror is therefore given by $f = \left(\frac{1}{R_1} + \frac{1}{R_2}\right)^{-1}$. By further specifying the angle $2\theta_i$ between the incident and reflected beams, the shape of the mirror is fully determined.

The chief drawbacks of the ellipsoidal mirror lie in (i.) the amplitude distortion associated with off-axis reflection, as well as (ii.) spatially-dependent cross-polarization effects caused by the locally varying normal vector of the reflector. Both effects are considered in a paper by Murphy [109]. In the first case, the distortion is described by expansion of the incoming beam at the mirror surface in terms of the Gaussian mode functions of the outgoing beam. It is shown that, to lowest order in w_m/f , the reflected field is given by

$$E_r = C(E_{00} + \frac{U}{2}[\sqrt{3}E_{30} + E_{12}]), \quad \text{for } U = \frac{w_m \tan \theta_i}{2\sqrt{2}f} \quad (3.19)$$

where w_m is the size of the Gaussian beam at the mirror surface and C is a normalization constant.

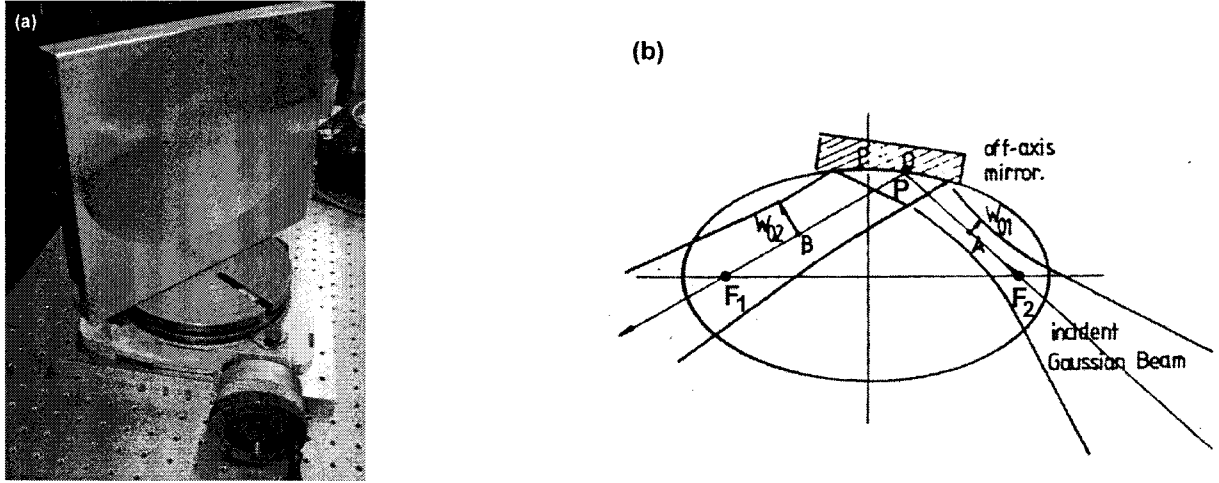


Figure 3.10: Ellipsoidal Focussing Mirror. (a) Photograph of the mirror constructed with $f = 19.2$ cm and 20 cm diameter aperture in the vertical direction. (b) Ellipsoidal mirror geometry. The incoming Gaussian beam that passes through F_1 with radius of curvature R_1 (equal to the length of F_1P) is transformed into the outgoing beam through F_2 with radius of curvature R_2 . Figure is from [109].

The total power lost to the TEM_{30} and TEM_{21} modes is therefore $K_{30} + K_{12} = \frac{w_m^2 \tan^2 \theta_i}{8f^2}$. Interestingly, analysis of the power converted to the orthogonal polarization for a linearly-polarized input beam yields the same result, $K_{XP} = \frac{w_m^2 \tan^2 \theta_i}{8f^2}$. Murphy points out that both of these effects can be largely eliminated by the appropriate use of a two-mirror feed system of the type shown in Figure 3.7.

We have constructed an ellipsoidal mirror of focal length $f = 19.2$ cm for an angle of incidence $\theta_i = 45^\circ$, with $R_1 = 44.5$ cm and $R_2 = 33.9$ cm (see Figure 3.10) and used it to feed a variety of prototype microwave cavity designs. The mode distortion and cross-polarization loss associated with this mirror are each on the order of $K \sim 0.015$. While this was sufficient for testing purposes, the polarization impurity would be a significant problem for the final trap design. A two-mirror feed system was considered briefly to overcome this problem, but the solution described in Section 3.4.3 was ultimately deemed simpler to implement.

Quasi-optical Quarter Wave Plates: The ability to machine dielectric materials with sub-wavelength features affords the possibility of manufacturing birefringent structures for microwave beams. One approach is to take advantage of so-called "form birefringence", by cutting sub-wavelength grooves of a particular orientation into a dielectric solid. The resulting average dielectric constants parallel and perpendicular to the grooves have been calculated to second order in the groove-periodicity to

wavelength ratio Λ/λ using effective medium theory [110]:

$$\begin{aligned}
\epsilon_{\parallel}^{(0)} &= r\epsilon_2 + (1-r)\epsilon_1 & \epsilon_{\parallel}^{(2)} &= \epsilon_{\parallel}^{(0)} \left[1 + \frac{\pi^2}{3} \left(\frac{\Lambda}{\lambda} \right)^2 r^2 (1-r)^2 \frac{(\epsilon_2 - \epsilon_1)^2}{\epsilon_0 \epsilon_{\parallel}^{(0)}} \right] \\
\epsilon_{\perp}^{(0)} &= \frac{\epsilon_1 \epsilon_2}{r\epsilon_1 + (1-r)\epsilon_2} & \epsilon_{\perp}^{(2)} &= \epsilon_{\perp}^{(0)} \left[1 + \frac{\pi^2}{3} \left(\frac{\Lambda}{\lambda} \right)^2 r^2 (1-r)^2 (\epsilon_2 - \epsilon_1)^2 \frac{\epsilon_{\parallel}^{(0)}}{\epsilon_0} \left(\frac{\epsilon_{\perp}^{(0)}}{\epsilon_1 \epsilon_2} \right)^2 \right]
\end{aligned} \tag{3.20}$$

where ϵ_0 is the permittivity of free space, $\epsilon_2 \simeq \epsilon_0$ is the dielectric constant of air, ϵ_1 is the dielectric constant of the material, and $r\Lambda$ is the width of each groove. By cutting the grooves to the appropriate depth, it is possible to arrange the desired phase delay of one polarization relative to the other.

Birefringence can also be obtained by constructing a series of thin metal strips, such that the incident beam sees an array of parallel-plate waveguides along one polarization axis. If the metal strips are separated by dielectric spacers of refractive index ϵ and thickness a , the effective indices of refraction for beam polarizations parallel and perpendicular to the metal surfaces are given by [111]:

$$\epsilon_{\parallel} = \epsilon - \left(\frac{\lambda}{2a} \right)^2 \quad \text{and} \quad \epsilon_{\perp} = \epsilon \tag{3.21}$$

(Here, λ is the free-space wavelength.) Once again, the desired polarization rotation can then be achieved by fixing the depth of the structure to give the appropriate phase delay. Goldsmith [99] points out that the normal-incidence reflection coefficient, $R = \left| \frac{\sqrt{\epsilon_j} - 1}{\sqrt{\epsilon_j} + 1} \right|^2$ can be made equal for the two polarizations $j = \{\parallel, \perp\}$ if the condition $\epsilon_{\parallel} = 1/\epsilon_{\perp}$ is satisfied. This is equivalent to requiring $\frac{\lambda}{2a} = \sqrt{\frac{\epsilon-1}{\epsilon}}$.

We have investigated the performance of quasi-optical quarter wave plates (QWPs) constructed using both of the techniques described above. A grooved dielectric QWP (shown in Figure 3.11a) was made from Delrin ($\epsilon_r = 3.7$) using a groove periodicity $\Lambda = 0.318$ cm, with groove widths $r\Lambda = 0.159$ cm. The device was actually constructed as two $\lambda/8$ -plates, each with grooves of depth $d_1 = 0.368$ cm inscribed on both sides of a solid Delrin core of thickness $d_2 = 0.93$ cm. Thus, the incoming microwave beam encountered a series of grooved and solid layers of thicknesses in the

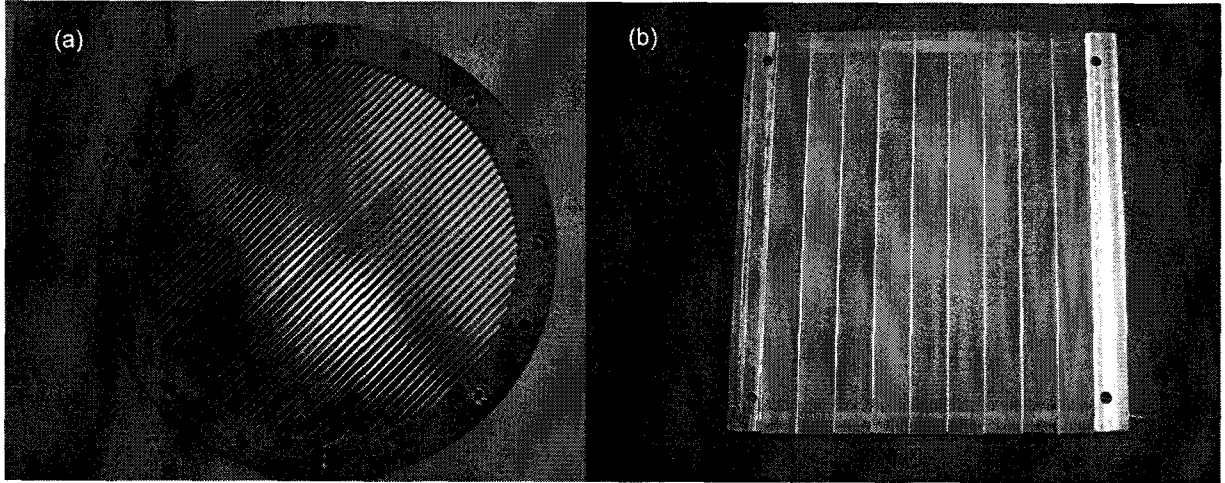


Figure 3.11: Transmissive quasi-optical quarter wave plates. (a) Form birefringent wave plate made from black Delrin with groove period $\Lambda = 0.318$ cm, groove width $r\Lambda = 0.159$ cm, and groove depths $d_1 = 0.368$ cm. (b) Waveguide quarter wave plate made from 0.08 cm thick aluminum fins and Rexolite spacers of width $a = 1.06$ cm. The depth of the waveguides into the page is $L = 2.04$ cm.

ratio $d_1 : d_2 : 2d_1 : d_2 : d_1$, which acted as a multi-layer dielectric stack and served to reduce the polarization-averaged reflection from the front face to $R \sim 0.005$ (calculated). Unfortunately, this device did not display the desired polarization rotation properties. It was realized after testing that black Delrin is filled with carbon particles which change its electrical properties; the dielectric constant ($\epsilon_r = 3.7$) used in the design is a generic value for Delrin and may not reflect this fact. The parallel-plate waveguide QWP shown in Figure 3.11b was constructed using 0.08 cm thick aluminum fins, spaced by $a = 1.06$ cm Rexolite ($\epsilon_r = 2.53$) sheets. This satisfies the equal-reflection condition defined above. The depth of the waveguides was chosen to be $L = 2.04$ cm in order to obtain a quarter-wave rotation. Testing showed that the cross-polarization of the output was approximately -8dB, which is insufficient for the polarization-purity requirements of the microwave trap. Some deliberation was given to the choice of either fabricating another waveguide device with higher machining tolerances or switching to a reflective QWP of the Martin Puplett type [105], the latter being harder to construct but free of potential power absorption problems when operating the beam at full power. Ultimately, it was decided to adopt a waveguide-based polarization rotator instead.

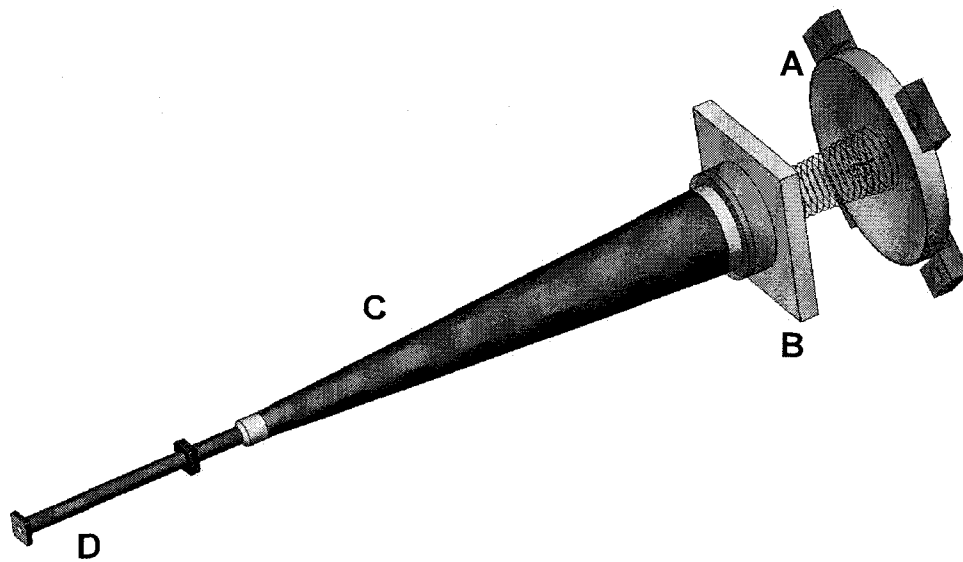


Figure 3.12: Final cavity feed design. The trap consists of a half-symmetric resonator [A] operating at frequency 18.1 GHz with a longitudinal mode number of $p=20$. Power is coupled into the resonator through the flat mirror [B], consisting of a $10\mu\text{m}$ layer of copper deposited onto the surface of a $20\text{ cm} \times 20\text{ cm} \times 2.5\text{ cm}$ beryllia (BeO) substrate. A fused silica vacuum window of thickness 0.95 cm, together with a 1.38 cm thick Teflon slab, functions as a good anti-reflection coating for the BeO. Power is delivered to the cavity by a corrugated feed horn antenna [C], which produces a TEM_{00} Gaussian beam mode of waist radius $w_0 = 2.92\text{ cm}$ exactly at the horn aperture. The measured field pattern of the horn gives $>99\%$ overlap with the cavity mode. The gain horn is in turn fed by a waveguide squashed-plate polarizer [D], which generates circular polarization with $\sim 20\text{dB}$ purity from a linearly polarized TE_{10} waveguide mode.

3.4.3 Quasi-optical Feed Design for a Near Semi-confocal Cavity

The final design for transmitted power into the microwave trap is shown in Figure 3.12. The realization that a corrugated scalar horn could be fabricated with an effective beam waist in its aperture plane afforded considerable simplification of the feed system. (Most horn antennas produce a mode with an effective waist located well behind the aperture.) The new scalar horn is specified to produce a Gaussian beam with waist parameter $w_0 = 3.05$ cm, equal to that of the desired cavity mode. Although the horn aperture plane is offset from the cavity mode waist by a distance equal to the combined thickness of the BeO mirror substrate, the vacuum chamber window, and an anti-reflection layer of Teflon ($\frac{t_{\text{BeO}}}{n_{\text{BeO}}} + \frac{t_{\text{glass}}}{n_{\text{glass}}} + \frac{t_{\text{Teflon}}}{n_{\text{Teflon}}} = 2.41$ cm), the fractional power loss due to imperfect mode overlap can be calculated using standard Gaussian beam propagation formulas:

$$\alpha_{\text{Mode}} = 1 - \frac{4}{\left(\frac{w_{0h}}{w_{0c}} + \frac{w_{0c}}{w_{0h}}\right)^2 + \left(\frac{\lambda \Delta z}{\pi w_{0h} w_{0c}}\right)^2} = 7.3 \times 10^{-3} \quad (3.22)$$

Here, $w_{0c} = 3.05$ cm is the Gaussian waist parameter of the cavity mode, $w_{0h} = 2.92$ cm is the beam waist parameter of the horn output measured using the beam profiler, $\lambda = 1.656$ cm is the microwave wavelength, and $\Delta z = 2.41$ cm is the distance between the aperture plane and the cavity mirror surface, divided by the refractive indices of the intervening materials.

Efficient cavity excitation also requires the minimization of reflections from the back surface of the BeO mirror substrate due to index mismatch ($n_{\text{BeO}} = 2.62$). The thickness of the fused silica vacuum chamber window ($n_{\text{FusedSilica}} = 1.98$) can be chosen to reduce reflections to as little as $R = 0.04$, but considerable further improvement is realized with the addition of a layer of Teflon ($n_{\text{Teflon}} = 1.43$) between the horn and the window. In particular, for Teflon thickness $t_{\text{Teflon}} = 1.38 \pm 0.03$ cm and window thickness $t_{\text{FusedSilica}} = 0.95 \pm 0.03$ cm, the combined normal-incidence reflection coefficient at 18.1GHz is found to be $R \lesssim 4 \times 10^{-3}$. Power absorption in each dielectric material can be estimated using loss tangents $\delta_{\text{BeO}} = 2 \times 10^{-3}$, $\delta_{\text{FusedSilica}} = 2 \times 10^{-3}$, and $\delta_{\text{Teflon}} = 2 \times 10^{-4}$, using $\alpha_{\text{abs}} = \frac{2\pi}{\lambda} \sum_j n_j t_j \tan \delta_j = 0.066$, for $j = \{\text{BeO, Fused Silica, Teflon}\}$. Note that about three quarters of this power is absorbed in the BeO substrate, which will be water cooled. Finally, the total power lost coupling into the cavity is given by:

$$\alpha_{\text{Tot}} = \alpha_{\text{Mode}} + R + \alpha_{\text{abs}} = \mathbf{0.077} \quad (3.23)$$

Circular polarization is achieved in the cavity feed design by the use of a custom-made squashed plate polarizer at the input of the scalar horn. This device is essentially a rectangular (WR-62) to circular waveguide transition that uses precisely designed indentations to create a circularly-polarized field at the output. It has the advantage of being able to operate at higher input power levels than conventional ortho-mode transducers, which contain a delicate iris, or devices relying on dielectric materials to provide birefringence. Our squashed plate polarizer is specified to give -25dB cross-polarization over a 270 MHz bandwidth and -20dB cross-polarization over 900 MHz bandwidth around the nominal 18.1GHz operating frequency. Polarization measurements of the horn output show -22dB over ~50 MHz about 18.08 GHz, and -18dB over ~100 MHz bandwidth. (The original design was reportedly hampered by a bug in the HFSS design software.)

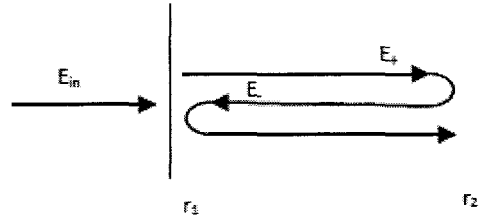
3.5 Cavity Coupling

Having a high degree of spatial overlap between the quasi-optical feed and the cavity mode is a necessary but not sufficient condition for maximizing the standing wave electric field in the microwave resonator; it is also required that the fractional transmission through the mirror be tuned to the correct value. This can be understood in direct analogy to the requirement for impedance matching at discontinuities in transmission line systems in order to minimize reflections. While it is obviously optimal to couple all of the incident power into the resonator, our minimum design requirement was set by the limit on the amount of microwave power that could safely be reflected back to the amplifier. (Unfortunately, circulators cannot be obtained for our wavelength and power level short of a very costly custom design.) The Xicom XTKD-2000DBS and CPI K3D64A amplifiers are both specified to enter shutdown (without damage to the klystron, according to sales engineers) at a load VSWR of 2.0, corresponding to a power reflection coefficient of approximately 0.1. Our goal, then, was to find a coupling mirror design with power transmission > 0.9 , which did not reduce the cavity Q to below half of its nominal minimally-coupled value.

3.5.1 Optimal Coupling and Sources of Loss

In order to obtain the deepest possible trap, it is desirable to tune the degree of coupling between the external power source and the cavity mode so as to maximize the intra-cavity electric field. This can be accomplished by setting the coupling equal to the sum of all other losses associated with

the mode being excited. To see why this is true, consider the case of a plane wave impinging on a plane-parallel resonator. (The following argument is similar to those presented by Grachev *et. al.* [112] and Siegman [97], among others.) Denote the incoming plane wave $\tilde{E}_{in} = E_{in}e^{i(kx-\omega t)}$, and the right- and left- going traveling wave components of the intra-cavity field as \tilde{E}_+ and \tilde{E}_- respectively, for $\tilde{E}_{\pm} = E_{\pm}e^{\pm i(kx-\omega t)}$.



Now, let r_1 and r_2 be the field reflection coefficients for the left and right mirrors. Then $r_1 = 1 - \sqrt{1 - \gamma_{\sigma}^2 - \gamma_{coup}^2 - \gamma_d^2}$ and $r_2 = 1 - \sqrt{1 - \gamma_{\sigma}^2 - \gamma_{ap}^2 - \gamma_d^2}$, where γ_{σ} is the loss at each mirror due to the finite resistivity of copper, γ_d is the diffractive loss at each mirror, γ_{ap} is the loss through the output coupling hole in mirror 2, and γ_{coup} is the input coupling coefficient at mirror 1. The standing wave field amplitude in the cavity is then given by $E_0 = E_+ + E_-$, where

$$E_+ = \gamma_{coup}(1 + r_2 r_1 + r_2^2 r_1^2 + \dots) = \frac{\gamma_{coup}}{1 - r_1 r_2} = \frac{\gamma_{coup}}{1 - \sqrt{1 - \gamma_{\sigma}^2 - \gamma_{coup}^2 - \gamma_d^2} \sqrt{1 - \gamma_{\sigma}^2 - \gamma_{ap}^2 - \gamma_d^2}}$$

Finally, noting that $E_- = r_2 E_+$, and expanding in each of the small loss parameters,

$$\begin{aligned}
\frac{E_0}{E_{in}} &= \frac{\gamma_{coup}(1+r_2)}{1-r_1r_2} \\
&= \frac{\gamma_{coup}(1+\sqrt{1-\gamma_\sigma^2-\gamma_{ap}^2-\gamma_d^2})}{1-\sqrt{1-\gamma_\sigma^2-\gamma_{coup}^2-\gamma_d^2}\sqrt{1-\gamma_\sigma^2-\gamma_{ap}^2-\gamma_d^2}} \\
&\approx \frac{\gamma_{coup}(1+(1-\frac{\gamma_\sigma^2}{2}-\frac{\gamma_{ap}^2}{2}-\frac{\gamma_d^2}{2}))}{1-(1-\frac{2\gamma_\sigma^2}{2}-\frac{\gamma_{coup}^2}{2}-\frac{\gamma_{ap}^2}{2}-\frac{2\gamma_d^2}{2})} \\
&= 4\sqrt{\alpha_{coup}}\frac{1-\alpha_\sigma-\alpha_{ap}-\alpha_d}{2\alpha_\sigma+\alpha_{coup}+\alpha_{ap}+2\alpha_d}
\end{aligned} \tag{3.24}$$

where $\alpha_j = \gamma_j^2$ are the loss coefficients expressed in terms of power, rather than electric field. Clearly E_0 is maximized in the above expression when $\alpha_{coup} = 2\alpha_\sigma + \alpha_{ap} + 2\alpha_d = \Sigma\alpha_{cav}$. The practical signature of optimal coupling, then, is that the observed Q-factor of the cavity is reduced by a factor of 2 compared to the value at very low coupling. Note also that, although the foregoing argument was presented in terms of parallel mirrors and plane waves, it applies equally well to the Gaussian modes of our semi-confocal cavity.

Relatively simple estimates can be made for the loss mechanisms mentioned above. For our cavity, the curvature of the paraboloidal mirror is sufficiently large on the scale of a wavelength that the local geometry for reflection is reasonably approximated by a plane wave impinging on a flat mirror; in this case, the resistive loss per reflection is given by [113]:

$$\alpha_\sigma = 4\sqrt{\pi f \epsilon_0 \rho} = 3.68 \times 10^{-4} \tag{3.25}$$

where $f = 18.1$ GHz is the microwave frequency, $\epsilon_0 = \frac{10^{-9}}{36\pi} \frac{s}{\Omega \cdot m}$ is the permittivity of free space, and $\rho = 1.68 \times 10^{-9} \Omega \cdot m$ is the resistivity of copper at room temperature. This establishes a fundamental limit for the Q-factor of the cavity for a given mirror material; apart from cooling the mirrors to reduce their resistivity, it is impossible to obtain a linewidth smaller than the one set by this mechanism. Part of the goal in engineering the cavity, then, is to ensure that the losses due to all other processes are smaller.

Diffraction losses may be estimated by calculating the fraction of the Gaussian $TEM_{0,0,N}$ mode

that extends past the finite mirror radius:

$$\alpha_{diff} = \left| \frac{\int_{r=r_0}^{\infty} \exp\left(\frac{-r^2}{w^2}\right)}{\int_{r=0}^{\infty} \exp\left(\frac{-r^2}{w^2}\right)} \right|^2 = \exp\left(\frac{-2r_0^2}{w^2}\right) = 2.1 \times 10^{-5} \quad (3.26)$$

where $r_0 = 10$ cm is the mirror radius and $w = w_0 = 3.05$ cm for the flat mirror, or $r_0 = 12.5$ cm and $w = \sqrt{2}w_0 = 4.31$ cm for the curved mirror. The value for α_{diff} given above is for the curved mirror; obviously the loss will be considerably smaller at the flat mirror. Two parenthetical comments should be made, however, regarding this estimate for diffractive loss. First, as is pointed out by Siegman ([97], section 19.5) and others, the actual modes of a semi-confocal resonator with finite mirror diameters differ from the ideal Gaussian modes of an infinite-mirror resonator, in that the actual field modes become distorted near the mirror edges in such a way as to minimize spillover. This results in lower expected diffractive loss than the estimate above suggests - see Siegman and Weinstein [114] for more detailed discussions of diffractive loss for real modes of symmetric resonators. Second, and of perhaps greater practical relevance, it should be noted that the observed diffractive losses associated with the flat mirror in our setup were actually *larger* than expected. Early versions of the test cavity used a 15cm \times 15 cm square flat mirror, which should give a diffractive loss of less 4×10^{-6} according to the estimate above, significantly less than the resistive loss of the copper. In fact, we observed a systematic improvement in the Q of the cavity for flat mirrors of up to 20 cm \times 20 cm. (Further increasing the size of the mirror made no detectable difference.) The reason for this apparent discrepancy is unclear; one possibility is that the input coupling hole pattern has the effect of redistributing the field pattern in the vicinity of the mirror in such a way as to increase the amplitude far from the cavity axis. In any case, operating with mirrors of 20 cm diameter is apparently sufficient to ensure that diffraction is insignificant compared to resistive loss in the cavity mirrors.

The loss associated with the small output coupling aperture at the center of the paraboloidal mirror is also somewhat difficult to calculate, even neglecting the distortion of the field mode caused by its presence. (For numerical calculations of the eigenmode distortion caused by introducing on-axis apertures into a non-symmetric cavity, see [115].) If we restrict our description of the problem to Gaussian cavity modes, then, for a thin mirror, Bethe's theory for diffraction by a sub-wavelength aperture (see section 3.5.2 below) could in principle be employed; for the present case, however, the aperture has a finite thickness that is comparable to its diameter, and corrections to Bethe's

small-aperture polarizability are required [116] [117]. Following Levy [116],

$$m = C_H R^3 H_t, \quad \text{for} \quad C_H = -2 \left[\frac{-4}{3} \exp \frac{-2\pi A_m t}{\lambda_{cm}} \sqrt{1 - \left(\frac{\lambda_{cm}}{\lambda} \right)^2} \right]$$

Here, m is the effective magnetic moment of the magnetic dipole in the plane of the aperture that models the aperture field, $R = 0.23$ cm is the aperture radius, $t=0.25$ cm is the mirror thickness, $\lambda = 1.656$ cm is the microwave wavelength, $\lambda_{cm} = 3.412 \times R = 0.80$ cm is the cutoff wavelength for the H_{11} mode inside the aperture, $A_m t = 1.0064t + 0.0819R$ is a numerical correction factor determined by McDonald [117], and H_t is the tangential magnetic field of the cavity mode at the mirror surface. Then, for P_{in} the power in the gaussian mode generating H_t , and η_0 the impedance of free space, one finds the power transmission of the aperture to be

$$\alpha_{ap} = \frac{4\pi^3}{3\lambda^4} \eta_0 \frac{|m|^2}{P_{in}} = 5.7 \times 10^{-6} \quad (3.27)$$

A somewhat crude direct transmission measurement was performed on an early prototype mirror with a similar aperture diameter and thickness by measuring the attenuation in a free-space gaussian beam between two gain horns when the mirror was interposed between them. (See Section 3.5.3 for details about how such a measurement can be performed.) In that case, the measured result agreed with the predictions of this theory to within about 20%, consistent with the uncertainty in the measurement.

Other possible line-broadening mechanisms considered in addition to those enumerated in Equation 3.24 included the accumulation of phase errors due to surface imperfections in the cavity mirrors, as well as distributed absorptive loss due to water vapor in the air-filled prototype cavity. (The latter effect would not, of course, be an issue in the final UHV microwave trap geometry, but could lead to the observation of misleadingly low Q values during testing.) Goldsmith ([99], section 5.8.4) points out that phase errors in a reflector antenna system lead to gain reduction of $G/G_0 = 1 - \left(\frac{4\pi\epsilon_{rms}}{\lambda} \right)^2$, where ϵ_{rms} is the RMS amplitude of a sinusoidal perturbation on the reflector surface, and suggests that losses in a quasi-optical reflector system should be of the same order. Our cavity mirrors are specified to be flat to 10^{-4} inches, so $\epsilon_{RMS}/\lambda \sim 1.5 \times 10^{-4}$, giving an associated loss $\alpha_{phase} \sim 3.7 \times 10^{-6}$. Finally, the attenuation of the circulating cavity power due to absorption by water vapor can be estimated using the data of Becker and Autler [118]. They found that the

highest absorption in the wavelength range investigated (0.7 cm to 1.7 cm) occurred at $\lambda = 1.33$ cm, and was roughly equal to 0.024 dB/km per g/m^3 . Conservatively assuming this level of attenuation at our wavelength and 100% relative humidity (corresponding to a water density of 23 g/m^3 in air at 298 K), one finds an attenuation per round trip through the cavity of $\alpha_{abs} = 4.2 \times 10^{-5}$. To verify that power loss due to absorption by water vapor should not be an important effect, the resonance width of a cavity with nominal $Q \sim 4 \times 10^4$ (corresponding to a round-trip loss of 2.3×10^{-4}) was measured in a dry-nitrogen environment, and no change was observed in the spectrum.

A summary of the various loss mechanisms and their expected magnitudes is shown below:

Loss Mechanism	Symbol	Round-Trip Power Loss
Copper Finite Resistance	$2\alpha_\sigma$	7.36×10^{-4}
Diffraction	$\alpha_{diff1} + \alpha_{diff2}$	5.2×10^{-8}
Surface Roughness Phase Error	$2\alpha_{phase}$	7.4×10^{-6}
Output Coupling Aperture	α_{ap}	5.7×10^{-6}
Absorption by Water Vapour	α_{abs}	4.2×10^{-5}
Sum	$\Sigma\alpha_{int}$	7.91×10^{-4}

The expected Q-factor of the cavity can now be calculated using ([97], section 11.4) (or maybe ref to eq. above...):

$$Q = \frac{2\pi q}{\Sigma\alpha_{int} + \alpha_{coup}} \quad (3.28)$$

where $q = 20$ is the longitudinal mode number. For a minimally-coupled cavity, $\alpha_{coup} \rightarrow 0$, this gives $Q \sim 1.55 \times 10^5$. In practice, we have not observed minimally-coupled Q-factors higher than $Q \sim 9 \times 10^4$. (See Section 3.5.3 for details.) This is presumably due to finite copper resistivity somewhat worse than the nominal value, as might be expected if a surface oxide layer is allowed to form at the mirror surface. Thus, to obtain the maximum possible intra-cavity electric field, an input coupling of $\alpha_{coup} = \frac{2\pi q}{\Sigma\alpha_{int,observed}} = \frac{40\pi}{9 \times 10^4} = 1.40 \times 10^{-3}$ is required. (Note from Equation 3.24, however, that $\frac{E_0}{E_{in}} \propto \frac{\sqrt{\alpha_{coup}}}{\Sigma\alpha_{int} + \alpha_{coup}}$ is a rather slowly varying function - one still obtains $\sim 99.8\%$ of the maximum electric field even if α_{coup} differs from the optimal value by as much as 10%.) Using the optimally-coupled Q of 4.5×10^4 , the expected peak field in the cavity is found (see calculation in Appendix D) to be **12.2 kV/cm**.

3.5.2 Single Aperture Coupling Measurements

Perhaps the simplest way to couple power into the microwave trap is by the use of a single sub-wavelength aperture located on the cavity axis. Small aperture coupling is a fairly standard technique for controlling the transmission of power from a waveguide mode into a closed resonator, and much has been written on calculating the effective impedance of such a system. (See, for example Marcuvitz [119].) The general theory for diffraction by a sub-wavelength aperture in a conducting plane, worked out by Bethe [120] and summarized by Jackson [121], shows that the aperture may be modeled as the sum of an electric dipole oscillating perpendicular to the plane and a magnetic dipole parallel to the plane. The effective dipole moments for a circular aperture are given by Jackson as

$$\mathbf{p}_{\text{eff}} = -\frac{4\epsilon_0 R^3}{3} \mathbf{E}_0, \quad \mathbf{m}_{\text{eff}} = \frac{8R^3}{3} \mathbf{H}_0 \quad (3.29)$$

where R is the aperture radius and \mathbf{E}_0 and \mathbf{B}_0 are the (perpendicular) electric and (parallel) magnetic fields of the incident radiation, respectively.

On the basis of results described in the literature, it was not expected that a single-aperture coupling scheme would be sufficient to simultaneously satisfy our requirements of high cavity Q and near-unit coupling efficiency into the $\text{TEM}_{0,0,N}$ mode. While high Q factors may be obtained by making the aperture very small, the overlap between the dipole pattern of the aperture and the desired resonator mode is expected to be poor in this case, resulting in low power coupling. A brief series of measurements was undertaken using the setup sketched schematically in Figure 3.13 to verify this for our near semi-confocal resonator.

A series of apertures of increasing diameter were drilled into an OFHC copper plate of dimensions $20 \text{ cm} \times 20 \text{ cm} \times 0.65 \text{ cm}$ that formed the flat mirror of the cavity, and the resonance width and maximum power transmitted into the cavity on resonance were measured for each. The aperture was excited through a short section of waveguide mounted directly to the back of the mirror. Reflected power was monitored at the reverse-coupled port of a -20dB directional coupler (Pasternack PE 2206-20) inserted between the source and the SMA-waveguide transition. Alternatively, power transmitted through the cavity could be monitored via a 0.45 cm diameter hole located at the center of the curved mirror, using a standard WR-62 format 10dB pyramidal gain horn (purchased from

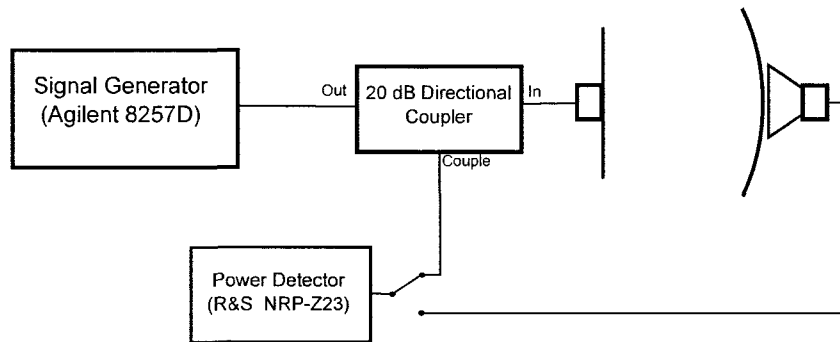


Figure 3.13: Setup for measuring coupling efficiency and cavity Q for a semi-confocal cavity.

ATM inc.) to collect the transmitted radiation. (Note that the output coupling aperture was of smaller diameter than any input coupling aperture investigated, and should not have significantly affected the cavity Q ; see section 3.5.1 for details.) The cavity length was adjusted such that the $TEM_{0,0,20}$ mode was resonant at 18.095 ± 0.005 GHz. Frequency-dependent reflections from coaxial and waveguide elements between the source and the cavity were eliminated by measuring the reflection spectrum while the cavity was loaded with ~ 20 dB of absorbing foam and subtracting the result from the later cavity resonance measurements.

Figure 3.14 summarizes the cavity Q -factors and coupling values measured as a function of aperture diameter. Note that at diameters large enough to transmit an appreciable fraction of power into the cavity, the observed Q -factors are much lower than half the value at minimal coupling. The reason for this high loss at increased coupling is somewhat unclear. Goldsmith [99] points out that, for apertures small enough to give optimal α_{coup} for typical cavities, the power tends to be radiated into a large solid angle, leading to significant insertion loss. A simple calculation was performed to check this hypothesis by calculating the overlap of an idealized (uniform) aperture field with the higher-order Gauss-Laguerre modes of the cavity. The process of radiation out of the cavity by the aperture should be equivalent to coupling to high-order modes that have field distributions concentrated far from the cavity axis and which therefore show correspondingly high diffractive

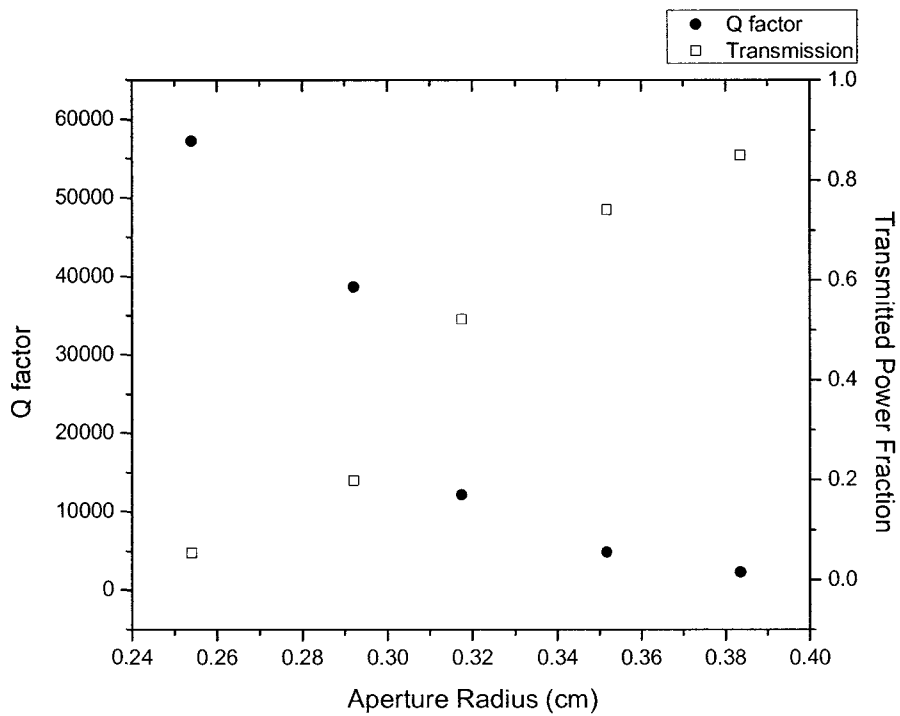


Figure 3.14: Cavity Q-factor and fraction of power transmitted into cavity as a function of coupling hole diameter. It is expected that the transmission should approach unity when the coupling is large enough to reduce the Q to half of its minimally-coupled value. In fact, the Q at power transmission $T \geq 0.2$ is much less than half of the minimally-coupled value, indicating that the coupling aperture has significantly distorted the mode shape by this point.

loss. Unfortunately, it was not possible to account for the observed power loss using this model - even for relatively high-loss modes with large linewidths, their finite detuning from the $TEM_{0,0,N}$ mode when the cavity is tuned away from the semiconfocal condition makes it hard to couple much power into them. Furthermore, one would probably expect to see a broad transmission feature around the main $TEM_{0,0,N}$ peak in the reflection spectrum if this explanation were correct, and no such feature is observed. A more likely explanation for the observed effect is that, as the aperture diameter is increased to the point where $\alpha_{coup} \sim \Sigma\alpha_{cav}$, the eigenmodes are significantly perturbed such that the field distribution is no longer well described by individual Gaussian modes; this hypothesis may be supported by the observation that the frequency of the main resonance shifts to the red by ~ 10 MHz as the aperture size is increased. In any case, it is clear from the data of Figure 3.14 that a different approach to feeding power into the cavity must be found in order to achieve the goals of high coupling and low loss required for the microwave trap.

3.5.3 Aperture Array Measurements

A more promising approach for coupling power into the microwave trap mode is to perforate the cavity input mirror with an array of sub-wavelength apertures. This should enable the field distribution of the incident radiation to be approximately preserved, and thereby to be matched to the $TEM_{0,0,N}$ mode of the cavity. At the same time, adjustment of the density and diameter of the apertures allows the transmission α_{coup} to be tuned to the optimal value. An estimate for the power transmitted through a square array of circular apertures with radius a and spacing d can be made by summing the individual Bethe dipole fields (Equation 3.29) for a plane-wave excitation. The calculation is summarized in Appendix E, and gives the result

$$\alpha_{coup} = \left(\frac{8\pi a^3}{3\lambda d^2} \right)^2 \quad (3.30)$$

This simple summation gives an idea of the expected scaling of the aperture array transmission, although it does not take into account either the possibility of finite mirror thickness, or the mutual coupling between magnetic dipoles in the array. (The latter effect is considered in [122], and is numerically found to affect the effective dipole moment of each aperture by less than 10% for our typical array parameters of aperture spacing $d = 0.51$ cm and diameter $0.1 \text{ cm} \lesssim 2a \lesssim 0.2 \text{ cm}$.) A more sophisticated approach to the problem of transmission through perforated conducting

plates is put forth in a series of papers by Chen ([123] [124] [125]), in which the free space fields are expanded in a basis of Floquet modes at multiples of the array periodicity, and their overlap integrals with in-aperture fields described by sums of cylindrical waveguide modes are calculated. This “method of moments” [126] is encoded in a freely-downloadable software package from the microwave group at the University of Pavia [127]. Somewhat reasonable agreement (usually at the ~50% level) was obtained between calculations using this software and transmission measurements made on our early test mirrors. In general, however, the software limited the maximum number of modes in the calculation to less than was apparently required for numerical convergence with our sub-wavelength apertures. Furthermore, the ceramic substrate in our final cavity design alters the transmission properties of the array in a way that the software does not take into account.

A series of measurements was therefore undertaken to determine the correct multi-aperture grid pattern for optimal input coupling, using the scaling of Equation 3.30 as a general guide. The initial test mirrors for the semi-confocal cavity geometry were made using single-sided copper printed-circuit prototyping boards (Injectorall Electronics PC7-T). The boards consisted of a 30 cm \times 30 cm square substrate (FR-4 glass-epoxy laminate [128] of thickness 1.6 mm, onto which a 1oz./ft² \approx 35 μ m copper layer had been deposited. Because the printed circuit board (PCB) substrates were much thinner than a wavelength (thickness $\sim \lambda/10$), it was expected that finite refractive index effects on the aperture array transmission should be small, and that the mirror should approximate an ideal thin, perforated metal screen. The array was created by drilling holes into the substrate on a 2-axis numerical mill. In most cases, the full 30 cm \times 30 cm substrate area was used to form the mirror, although it was empirically determined that there was no appreciable increase in diffractive loss for mirrors as small as 20 cm \times 20 cm.

A second set of mirrors was fabricated to investigate changes in transmission through the aperture array in the presence of a ceramic substrate of finite refractive index. Aluminum oxide (Al₂O₃) substrates were used (dielectric constant $\epsilon_r = 9.8$ at 1 MHz) instead of Beryllium Oxide (BeO, $\epsilon_r = 6.76$ at 1 MHz) because of the cost and difficulty of working with the latter material. Square, 20cm \times 20cm \times 0.64cm substrates of 99.8% pure Al₂O₃ were purchased from Stratamet Advanced Materials Corporation and ground to 2.5 μ m flatness by Ron Kehl Engineering. A thin layer of copper (1 μ m thickness) was then vapor deposited on one surface over a 500 \AA Chromium adhesion layer. Optical lithography was used to etch away copper so as to form the desired aperture array,

and the remaining copper was electroplated up to $10\mu\text{m}$ total thickness. All steps of the deposition and lithography process were performed by IJ Research, Inc. An additional $20\text{ cm} \times 20\text{ cm} \times 1.91\text{ cm}$ slab of Al_2O_3 was purchased and was clamped against each mirror substrate during transmission measurements in order to reproduce the full 2.5 cm design thickness of ceramic. (This approach was more cost-effective than fabricating each test mirror on a 2.5 cm thick substrate.)

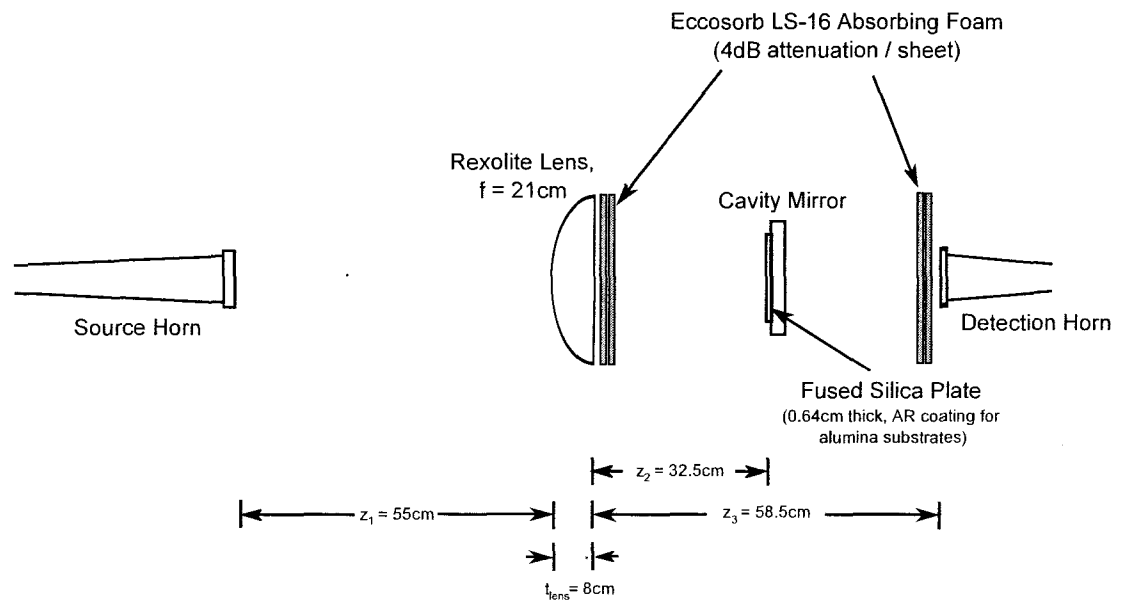


Figure 3.15: Setup for Direct Measurement of Aperture Array Transmission

Two different techniques were used for measuring the transmission through a given aperture array. For arrays with relatively high transmission coefficients ($\alpha_{\text{comp}} \gtrsim 10^{-3}$), the transmitted power was measured directly between two gain horns, as illustrated in Figure 3.15. The rexolite dielectric lens of Section 3.4.2 was used to produce a beam waist at the mirror, and, for the Al_2O_3 mirrors, a fused silica plate of 0.64 cm thickness formed an antireflection (AR) coating at the surface of the ceramic. Even with the glass AR coating, etalon effects between the lens and mirror and between the mirror and detection horn were noticeable; to further mitigate the problem, 2 sheets of absorbing foam (Eccosorb LS-16, attenuation -4 dB per sheet) were introduced between each pair of surfaces, and the mirror was translated several centimeters along the beam axis to enable averaging over any

remaining fringes.

Aperture arrays with sufficiently low transmission coefficients ($\alpha_{coup} \lesssim 5 \times 10^{-3}$) were most conveniently measured using a setup similar to that shown in Figure 3.5.1. In this case, however, the cavity was excited by the scalar feed horn with squashed-plate polarizer, and a 0.63 cm fused silica plate was again placed between horn and mirror to form an AR coating for the ceramic mirrors. Because the squashed-plate polarizer acts as a quarter wave plate, power reflected through the cavity must make two additional passes through the horn before returning to the waveguide transition with the appropriate polarization. This meant that line-widths observed in reflection tended to be lower than those seen in transmission (presumably due to the increased ohmic loss in the horn), and the latter were used to calculate the total cavity Q value when the two were significantly different. Before any set of transmission measurements was taken, the intrinsic cavity line-width was measured using a mirror with very low coupling to establish $\Sigma\alpha_{int}$. (The typical dimensions of the minimal-coupling array were aperture diameter $2a = 0.10$ cm and spacing $d = 1.02$ cm. Further decreasing the coupling by using smaller or more widely spaced apertures reduced the transmission signal, but had no effect on the cavity line-width.) The coupling parameter of each mirror could then be extracted from the associated Q value as

$$\alpha_{coup} = 2\pi q \left(\frac{1}{Q} - \frac{1}{Q_0} \right),$$

for Q_0 the minimum coupling quality factor. One drawback of this approach is that Q_0 is generally only reproducible to within a few percent of its nominal value for a given cavity geometry (ie. length and mirror angle alignment), probably due to mechanical instabilities in the cavity and/or in the coaxial cables that carry power from the source and to the detector. This means that the lower limit on coupling coefficients that can be reliably measured is roughly $\alpha_{coup,min} \gtrsim \Sigma\alpha_{int} \sim 10^{-4}$. One additional issue with these measurements was the at times surprisingly strong dependence of the cavity line-width on small changes in the resonant frequency. For some coupling mirrors and cavity geometries, tuning the cavity length so as to move the resonant frequency by ~ 20 MHz could cause the observed Q to change (repeatably) by as much as 30%. It is unclear what causes this strong frequency dependence; the most likely explanation would seem to be coincidental degeneracy of some high order transverse mode, although sharp resonance features associated with the transmission properties of the subwavelength hole array may also be a possibility (see, eg.

[129] [130] [131]). Care was taken to perform all measurements for a given series of aperture arrays at the same resonance frequency, to within a few MHz.

Figure 3.16 shows results from a series of aperture array transmission measurements, in which the aperture spacing was fixed at $d = 0.51$ cm and the aperture diameter was varied. The top panel shows a plot of the measured aperture array coupling parameter α_{coup} as a function of aperture diameter, for both PCB and Al_2O_3 mirrors. The data were taken at longitudinal mode number $q = 20$ for a resonant frequency of 18.080 ± 0.003 GHz. As expected from Equation 3.30, the coupling varies as the sixth power of the diameter. The difference in slopes is the result of the finite refractive index of the ceramic substrates. The bottom panel shows the coupling parameter and fractional power transmission (the latter measured in reflection) for a series of Al_2O_3 aperture arrays, at the same mode number and frequency. Note in particular the points at aperture diameter $2a = 0.14$ cm. This mirror shows coupling $\alpha_{coup} = 1.60 \times 10^{-3}$ and fractional power transmission ~ 0.94 , which is sufficient to satisfy our design requirements. There is, however, one noteworthy caveat: while this aperture array could be used to fabricate a cavity with an Al_2O_3 mirror substrate, the refractive index of BeO is significantly different and would likely result in somewhat different coupling. Some effort was made to determine the dependence of α_{coup} on the refractive index of the substrate by fabricating fused silica mirrors ($\epsilon_r = 3.92$ at 18.1 GHz, as measured using the method of [132]). Unfortunately, only two such mirrors were made, and their transmission characteristics (summarized in the table below for longitudinal mode number $q = 20$ at a resonant frequency of 18.080 ± 0.003 GHz) were almost the same. If anything, the coupling for the smaller aperture size seems to be larger, suggesting some uncontrolled parameter or error in fabrication.

Fused Quartz Mirror Transmission Properties at $f = 18.080$ GHz					
Mirror	$2a$ (cm)	d (cm)	Q [Transmission]	α_{coup}	Power Transmitted T [Reflection]
Fused Quartz #1	0.17	0.51	46136	2.72×10^{-3}	73%
Fused Quartz #2	0.11	0.51	43399	2.90×10^{-3}	82%

Clearly, before attempting to fabricate the final BeO mirror substrate for the 2 kW resonator, it would be desirable to repeat the measurements of Figure 3.16 with several substrates of a different refractive index. This would ideally be BeO, of course, but it may still be possible to extract the desired dependence of α_{coup} on ϵ_r with fused silica; the latter material has the advantage of being

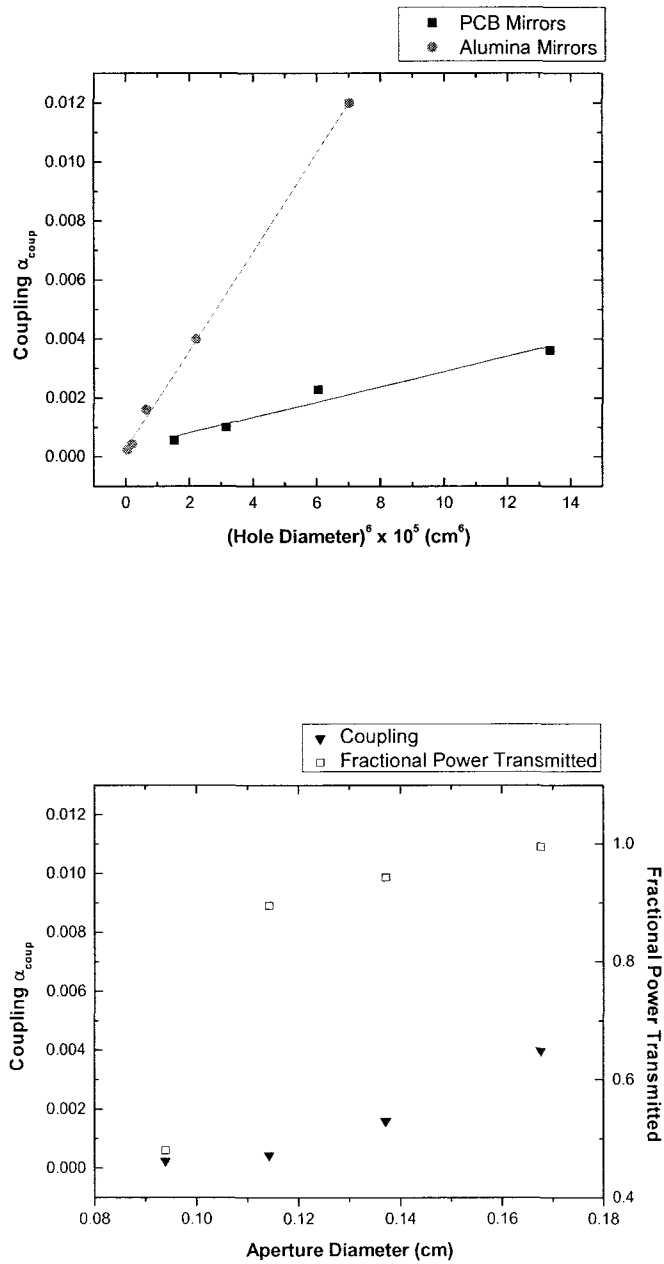


Figure 3.16: Aperture array transmission data. The top panel shows measured coupling parameter as a function of aperture diameter; the expected a^6 dependence is evident. The slope of each line is determined by the dielectric constant of the substrate. In the bottom panel, coupling parameter α_{coup} and power transmission coefficient T are plotted against aperture diameter for an Al_2O_3 substrate. The points at aperture diameter $2a = 0.14\text{cm}$ has $\alpha_{coup} = 1.60 \times 10^{-3}$ and $T \sim 0.94$, which meets our design requirements.

less expensive and much easier to work with. In the meantime, the measurements made for Al_2O_3 mirrors should be sufficient to allow the construction of a low-powered (~ 100 W) microwave trap for use with slow SrF molecular beams.

3.6 Thermal Considerations

Providing adequate heat dissipation is an important consideration in the design of the microwave trap. As pointed out in Section 3.5.1, resistive losses in the copper mirrors are expected to be by far the dominant form of line-broadening in the cavity. Almost all of the nominal ~ 2 kW input power, then, will ultimately go into ohmic heating of the mirrors. This power must be rapidly dissipated to prevent an excessive increase in mirror temperature, both to avoid outgassing in the UHV environment, and to ensure that the cavity Q is not compromised due to elevated resistance of the copper. Water cooling is therefore a necessary element of the trap design.

The situation is further complicated by the fact that the input coupling scheme investigated in Section 3.5.3 requires the diameter of the apertures in the array be less than the thickness of the mirror, $2a \lesssim t_{\text{Cu}}$; increasing the thickness of the copper beyond this value will result in exponential attenuation of the transmission. This restricts the mirror thickness to $t_{\text{Cu}} \lesssim 1\text{mm}$.⁵ Furthermore, the coupling aperture array must be unobstructed to allow the input power to reach the trap, precluding the attachment of water-cooling pipes anywhere except at the edges of the coupling mirror. Unfortunately, it is not possible to efficiently dissipate ~ 1 kW of heat through a 1 mm thick copper sheet at a distance of ~ 10 cm without developing unacceptably high temperatures at the mirror center.

It was therefore decided to mount the coupling mirror onto a slab of thermally-conductive ceramic (which should still be transparent to the incoming microwaves) in order to carry away the heat. Several such ceramic materials of varying dielectric constant ϵ_r and bulk thermal conductivity κ were considered, including Aluminum Oxide [Al_2O_3 , $\epsilon_r = 9.8$, $\kappa = 31\text{W}/(\text{K m})$ for AM998 grade from Stratamet], Aluminum Nitride [AlN , $\epsilon_r = 8.7$, $\kappa = 180\text{ W}/(\text{K m})$ for sintered Ceralloy 1370DP from Ceradyne], and Beryllium Oxide [BeO , $\epsilon_r = 6.67$, $\kappa = 285\text{ W}/(\text{K m})$ for isostatically-pressed

⁵It should be noted in passing that the *minimum* thickness of the mirror is set by the skin depth of copper at a frequency of $f = 18.1$ GHz, $\delta_s = \sqrt{\frac{1}{\pi f \mu_0 \sigma}} = 0.49\mu\text{m}$, where $\sigma = 5.813 \times 10^7$ S/m is the conductivity of copper [133]. We typically use a lower limit of $t_{\text{Cu}} \geq 10\mu\text{m}$ to ensure that no power is transmitted in the absence of coupling apertures.

Thermalox 995 from Brush-Wellman]. Alumina is comparatively inexpensive and therefore useful for lower-power prototypes, but its thermal conductivity is insufficient for use in the 2kW cavity. Conversely, Beryllia is obviously the best material from the point of view of thermal conductivity, but is also the most expensive and is difficult to work with due to its toxicity when inhaled. The thermal properties of Aluminum Nitride are also sufficient, but it is potentially even more costly than Beryllia for substrates of the size we require. None of the three ceramics has a clear advantage in terms of the matching of its thermal expansion coefficient to that of copper. (The room-temperature expansion coefficient for copper is $\alpha_{Cu} \sim 16 \times 10^{-6}/K$, whereas the ceramics have $\alpha_{Al_2O_3} \sim 7.9 \times 10^{-6}/K$, $\alpha_{BeO} \sim 9.0 \times 10^{-6}/K$, and $\alpha_{AlN} \sim 6.2 \times 10^{-6}/K$.) According to these criteria, it was determined that the substrate for the final cavity coupling mirror should be made from BeO; prototypes and a possible low-power cavity mirror for use with our SrF beam (see Chapter 4) are fabricated using Al_2O_3 .

Note that cooling of the curved mirror is considerably simpler, since there is no requirement for coupling microwave power through it over a large surface area. (The output coupling aperture on the cavity axis is only ~ 0.4 cm in diameter.) It can therefore be made entirely from copper, which simplifies the machining of the curved surface considerably, and can have water cooling pipes brazed directly to its back face. The short thermal path length to the cooled surface guarantees a temperature increase of no more than a few $^{\circ}C$.

3.6.1 Temperature Distribution Calculations

The maximum temperature of the input coupling mirror can be determined by solving the heat equation in three dimensions. Due to the cylindrical symmetry of the heating by the Gaussian cavity mode, an analytical solution is most easily obtained for a mirror of circular cross section, where the radial solutions are Bessel functions. Specifically, one can solve Laplace's equation for the temperature $u(r, \theta, z)$ over the mirror volume:

$$\frac{1}{r} \partial_r (r \partial_r u) + \frac{1}{r^2} \partial_{\theta}^2 u + \partial_z^2 u = 0 \quad (3.31)$$

The solution is subject to the boundary conditions $u(r = R, \theta, z) = T_0$, together with $\partial_z u|_{z=0} = \alpha(r)$ and $\partial_z u|_{z=L} = 0$. Here, R is the mirror radius, T_0 is the fixed temperature of the water cooling lines wrapped around the lateral surface, L is the thickness of the ceramic substrate, and $\alpha(r) =$

$\frac{2P_{circ}}{\kappa\pi w_0^2} \exp(-2\frac{r^2}{w_0^2})$ is the spatial distribution of the heating due to the Gaussian cavity mode. (Note that this formulation does not account for possible discontinuities at the ceramic-metal interfaces on the front and lateral surfaces of the mirror. These lead to finite temperature steps at the boundaries, as described in Section 3.6.2.) The problem can be broken up into two separate parts, each with one inhomogeneous boundary condition, which can then be solved by separation of variables and summed to give the final temperature distribution. This is a standard procedure described in many textbooks [134] and is not reproduced here. Calculations were performed for mirrors of various thicknesses and radii; results for the maximum temperature at the center of a $L = 2.5$ cm thick mirror for each ceramic are summarized in the table below.

Maximum Temperature $T(r = 0)$ for P=1kW Heating, with $T_0 = 20^\circ\text{C}$			
Mirror Radius	Al ₂ O ₃ [$\kappa = 31\text{W}/(\text{K m})$]	AlN [$\kappa = 180\text{W}/(\text{K m})$]	BeO [$\kappa = 285\text{W}/(\text{K m})$]
R = 10.0cm	537.2 °C	109.1 °C	76.3 °C
R = 14.1cm	607.2 °C	121.1 °C	83.9 °C

Note that the mirror substrate for the final cavity design is a square of side length 20 cm; the actual maximum temperature should be somewhere between those calculated for round substrates of $R = 10$ cm and $R = 10\sqrt{2}\text{cm} = 14.1$ cm shown above.

A series of numerical temperature distribution calculations were also performed for several more complicated geometries during the design process, using the finite element package FEMLAB and a relaxation-type algorithm written in C. Figure 3.17 shows a the output of a FEMLAB calculation for a BeO substrate of 2.5 cm thickness. The maximum temperature of 77.3°C matches well with the results of the analytical calculation above.

3.6.2 Ceramic Metallization and Thermal Contact Conductivity

Fabrication of the microwave cavity input coupler requires metallization of the main 20 cm × 20 cm mirror surface of the ceramic substrate, as well as the four lateral 20 cm × 2.5 cm surfaces that are to be water-cooled. The ceramic-metal bond should be both thermally conductive and robust against thermal cycling, and a number of standard metallization techniques were considered. The bonding technology of choice for many high power microwave applications is known as Direct-Bond Copper (DBC) [135]. It involves the formation of a eutectic bond between the ceramic substrate and copper

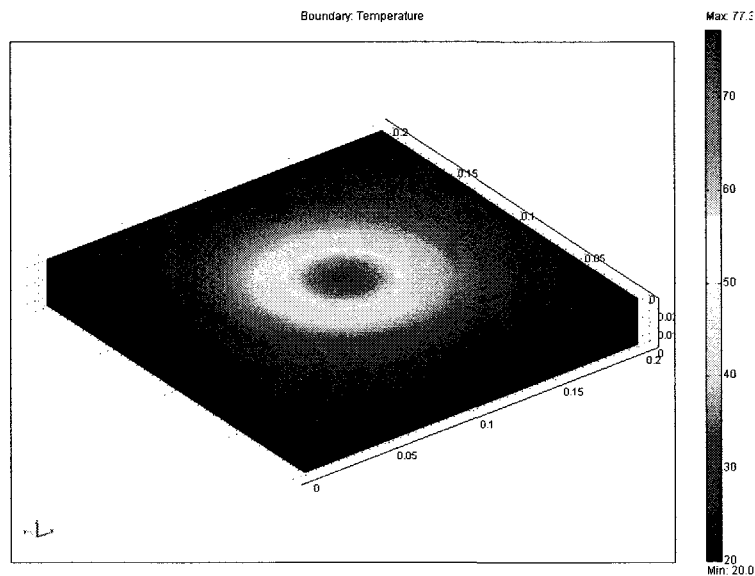


Figure 3.17: Finite element calculation of temperature distribution for a BeO substrate of 2.5 cm thickness, with 1kW of power impinging in a Gaussian beam of waist parameter $w_0 = 3.05$ cm. The peak temperature at the center of the mirror is about 77.3°C.

oxide at 1070°C, and generally results in very high thermal conductivity between the metal and substrate. Unfortunately, it was determined through conversations with engineers at companies specializing in the metallization of BeO (notably Stellar Industries and Zentrix) that DBC is not a viable approach for our design. The problem arises due to the narrow range of temperatures over which the eutectic can form (1065°C-1083°C [136]); vendors are typically equipped to metallize substrates on the order of ~ 10 cm \times 10 cm \times 0.1 cm, and are unable to obtain sufficient temperature uniformity for an object with the large thermal mass and physical size of our mirror. Other standard metallization techniques include thick film coatings, high temperature refractory-metal deposition, and direct vapor deposition of copper over a thin refractory adhesion layer (for matching to the ceramic lattice). Thick films generally involve the formation of a glassy layer of poor thermal conductivity and were not considered. Both vapor deposition techniques, however, were seen as potentially viable.

Imperfect lattice-matching across a ceramic-metal bond leads to a reduction in heat flow, which is often described in terms of a finite "thermal contact conductivity". Practically, this results in a discontinuity in the temperature distribution at the interface between the two materials. In order to measure the contact conductivities associated with the available bonding technologies, a number of

5 cm × 5 cm × 0.58 cm BeO test substrates were purchased from Brush-Wellman, and metallized in various ways. In particular, we obtained a 1 μm thick refractory molybdenum-manganese (Mo-Mn) coating and a 1 μm refractory molybdenum-tungsten (Mo-W) test part (both from Omley Industries), as well as a series of parts with 1 μm copper vapor-deposited over a 500 Å tungsten adhesion layer, with the copper thickness then increased to 10 μm by electroplating (4 parts total, all fabricated by Thinfilms, Inc.). The Mo-Mn metallization was not successful due to the inability of the metal to properly wet the ceramic surface; the other coatings appeared fairly homogenous and were without obvious blisters or voids.

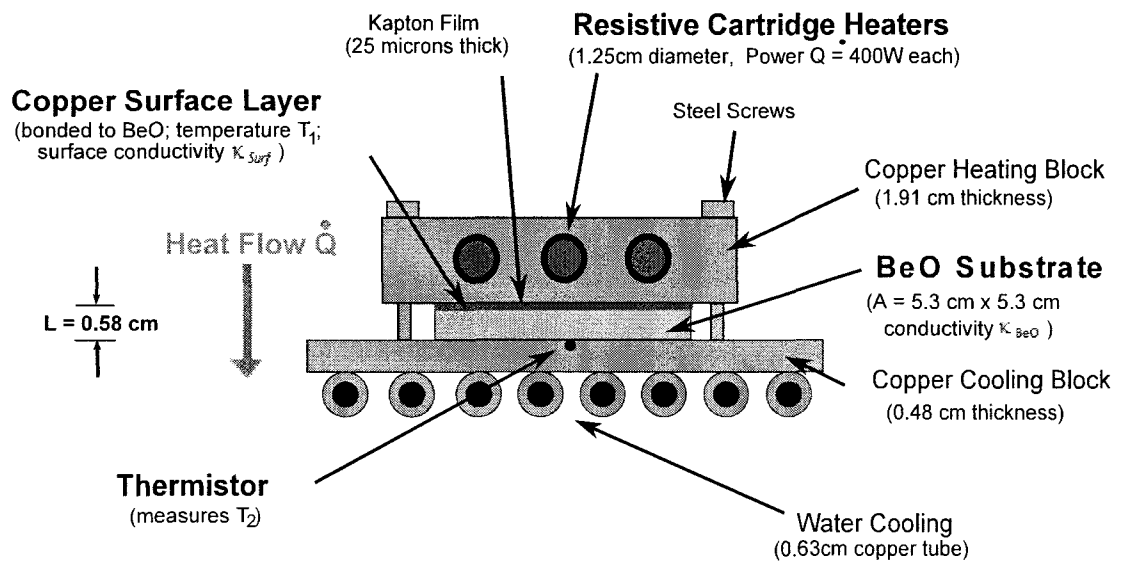


Figure 3.18: Setup for measuring thermal contact conductivities of metal-ceramic bonds.

After some trial and error, it was determined that the setup shown in Figure 3.18 provided a fairly repeatable method for thermal contact conductivity measurements. (For similar experiments, see [137] [138].) A temperature gradient was applied across the ceramic-metal interface of interest via two copper transfer plates. The 7.5 cm × 7.5 cm × 1.9 cm top plate was heated with three resistive cartridge heaters (Omega Engineering CSH-302400/120V), each of which can provide up to 400 W of power. Heat was extracted from the 12.5 cm × 12.5 cm × 0.48 cm bottom plate with a series of 1/4"

copper tubes, through which 13°C chilled water was flowed continuously. The metallized upper surface of the substrate was electrically insulated from the top plate with a 25μm layer of kapton film. The entire assembly was clamped together with steel 8-32 screws⁶, and wrapped in several layers of fiberglass insulation. A thin coat of silver-loaded thermal paste (Arctic Silver 5) was applied to the bottom surface of the ceramic, the temperature (T_2) of which was monitored with a glass bead type thermistor (Omega Engineering 1PT100KN1510-RTD). In order to determine the temperature drop across the metal-ceramic interface, the temperature of the bonded copper layer (T_1) was found by measuring its resistance. A four-terminal measurement was made, in which a known DC current was applied using a 5V supply and a 2.5Ω series resistor. The resulting voltage across the copper layer was read using a low-noise pre-amp (SRS model SR560) with a 1 Hz low-pass filter, and the resistance was used to determine the temperature of the metal. Because the current distribution over the surface was not uniform, it was necessary to calibrate the observed resistance as a function of temperature before using it to make the thermal conductivity measurement. (It varied linearly, but the effective cross-sectional area of the conductor was not known *a priori*). Comparing the temperatures in the metal film and at the bottom of the substrate for a known heat flow rate gives the contact resistance associated with the metal-ceramic bond:

$$T_1 - T_2 = \left(\frac{1}{\kappa_{surf}} + \frac{L}{\kappa_{BeO}} \right) \frac{\dot{Q}}{A} \quad (3.32)$$

where $L = 0.58$ cm is the thickness of the substrate, $A = 5.3$ cm \times 5.3 cm is its area, and $\kappa_{BeO} = 285$ W/(K m) is its bulk thermal conductivity. Figure 3.19 shows the measured temperature difference across the substrate and bond for the vapor-deposited copper layer, $\Delta T = T_1 - T_2$, at heat flow rates \dot{Q} between 40 W and 1200 W. A linear fit gives the slope $\left(\frac{1}{\kappa_{surf}A} + \frac{L}{\kappa_{BeO}A} \right) = 0.0115 \pm 0.0004$ W/K. (Note that the last three data points, for $\dot{Q} \gtrsim 800$ W, deviate significantly from the expected linear behavior, presumably due to imperfect thermal isolation of the system at high temperatures. These points are therefore excluded from the fit.) Subtracting the known thermal conductance of the substrate yields a final measured thermal contact conductivity of $\kappa_{surf}^{Cu} = 8.8 \times 10^4$ W/(Km²) for the vapor-deposited / electroplated copper. A similar measurement for the Mo-W coating (not shown) gives

⁶Note that the steel screws are not included in the thermal conductivity calculation of equation 3.32. Even assuming perfect thermal contact between the screws and the copper, and taking a high estimate for the bulk conductivity of steel, $\kappa_{Steel} \approx 43$ W/Km, the resulting conductance through the screws is $4 \times \frac{\kappa_{Steel}(\pi d_{screw}^2 L)}{L} \approx 0.8$ W/K, for $d_{screw} = 6$ mm the screw diameter and $L = 0.58$ cm the thermal path length. This is a factor of 100 lower than the conductance through the sample, ~ 87 W/K, equal to one over slope of the fit in Figure 3.19.

$\kappa_{surf}^{Mo-W} = 8.3 \times 10^3 \text{W}/(\text{Km}^2)$. The former bonding process is therefore clearly the superior choice for both the reflective surface and the water-cooling braze joints on the lateral surfaces of the cavity mirror. For $\dot{Q} = 1\text{kW}$ of heat flow, the measured contact conductivity for the copper-ceramic bond gives rise to a temperature step of $\Delta T_{bond} \sim 8^\circ\text{C}$ across the boundary, which should be acceptable for our design.

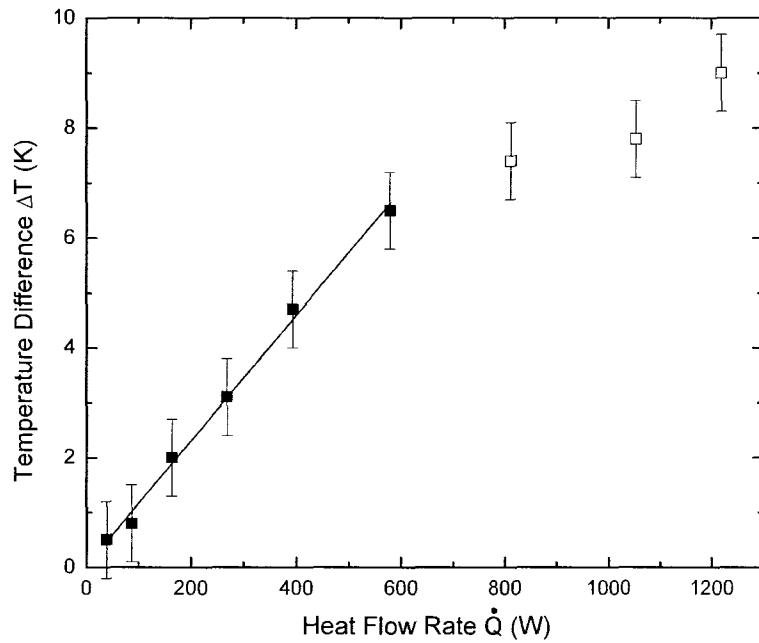


Figure 3.19: Measured thermal contact conductivity of the BeO - copper bond for the vapor-deposited substrate. A linear fit to the data gives the slope $\left(\frac{1}{\kappa_{surf}A} + \frac{L}{\kappa_{BeO}A}\right) = 0.0115 \pm 0.0004 \text{ W/K}$. The points at $\dot{Q} \geq 800 \text{ W}$ deviate from a straight line due to imperfect thermal isolation, and are not included in the fit. Multiplying by the area $A = (5.3\text{cm})^2$ and subtracting the known conductance of the substrate, $\frac{L}{\kappa_{BeO}} = 2.03 \times 10^{-5} \frac{\text{Km}^2}{\text{W}}$ gives a the surface contact resistance of the bond, $\frac{1}{\kappa_{surf}} = 1.14 \times 10^{-5} \frac{\text{Km}^2}{\text{W}}$.

3.6.3 Solder Selection

The input mirror will be cooled by flowing water through channels in a set of rectangular copper blocks affixed to its edges. The blocks are to be connected via 1/2" VCR fittings and flexible bellows to an external chilled water circulator. They must be attached to the metallized lateral surfaces

of the mirror substrate in such a way as to maximize thermal conductivity. This is probably best achieved by vacuum brazing, which has the attractive feature of not requiring solder flux that might contaminate the UHV environment of the molecule trapping experiment if not properly cleaned. Some consideration has been given to the choice of an appropriate solder for the brazing process, such that the following conditions are satisfied: (i) the vapor pressure of all constituents of the solder should be low ($\lesssim 10^{-9}$ Torr) at temperatures up to $\sim 200^\circ\text{C}$ for UHV bake-out; (ii) it should not contain lead which, when heated, tends to form porous brazes that can trap water and are bad for vacuum; and (iii) its melting temperature should be low enough that copper does not delaminate from the surface of the substrate upon heating. We have tested a number of different solders by attempting to braze small copper blocks (generally about $4\text{ cm} \times 1\text{ cm} \times 1\text{ cm}$) to our copper-coated BeO substrates (described in section 3.6.2) in a vacuum furnace. It was found empirically that the substrates can be thermally cycled up to about $\sim 200^\circ\text{C}$ without differential-expansion induced delamination, as long as the heating and cooling are sufficiently slow (~ 6 hours in each direction). The solder we ultimately selected is a 60% Sn - 40% Bi mixture (Alloy 281-338 from Indium Corporation of America), with a liquidus temperature of 170°C . This solder satisfies the criteria listed above, and forms a strong mechanical bond between the copper bar and the test substrate.

Chapter 4

Investigation of Laser Cooling in SrF

4.1 Motivation: Slowing Hydrodynamic Beams

The brightness of hydrodynamic buffer gas beam sources makes them very attractive in a variety of applications. For loading the microwave trap, however, the high forward kinetic energy of the hydrodynamically-boosted molecules renders the source effectively unusable, unless a means can be found for efficiently slowing them. We have considered several possible approaches to this problem, including beam slowing using a "two-stage" aperture or secondary buffer gas cell [74], billiard-like collisions between crossed molecular beams [139], and continuous deceleration by adiabatic population transfer in a spatially modulated electric field [140]. Unfortunately, none of the techniques investigated combines the efficiency and ease of implementation needed to justify changing from an effusive source.

Rather surprisingly, one plausible method of hydrodynamic beam deceleration appears to be the extension of atomic laser-cooling techniques to diatomic molecules that possess favorable level structure for establishing a so-called "quasi-cycling" set of transitions. This approach obviously lacks the generality of the others mentioned above; nevertheless, it is in principle applicable to a fairly wide range of molecular species (including ground state TiO, TiS, CaF, BaF, and SrF, as well as metastable FeC, ZrO, HfO, ThO and SeO [41], and a range of hydrides [24]) with quite different properties than the heteronuclear alkalis, which are the only other current candidates for cooling to quantum degeneracy. This chapter describes work we have done to demonstrate the existence

of a set of quasi-cycling transitions in strontium fluoride (SrF).

4.2 Quasi-cycling Transitions in SrF

It has been recognized for some time that there exists a class of molecules which could, in principle, be amenable to laser cooling. In order to scatter enough photons to obtain appreciable phase-space compression, it is necessary to find a species that undergoes decays to undesired vibrational and rotational sublevels relatively infrequently. Practically, the key requirement is that the molecular vibrational potential curves for the ground and lowest excited electronic states should be very similar to each other as a function of internuclear distance. This gives rise to vibrational wavefunctions with significant overlap in the two electronic manifolds, and hence to highly diagonal Franck-Condon matrices. Molecules excited from $|X, v = 0\rangle$ to $|A, v' = 0\rangle$ then decay with high probability $P_{0,0}$ back to the vibrational ground state, or with much lower likelihood $P_{0,1}, P_{0,2}, \dots$ to the states $|X, v = 1\rangle, |X, v = 2\rangle, \dots$, etc. For a typical molecule of interest with a mass $m \sim 100$ amu and an initial velocity $v \sim 200$ m/s in a hydrodynamic buffer gas beam, the number of photon scattering events required to bring it close to rest is $N_{scatt} = \frac{mv}{\hbar k} \sim 5 \times 10^4$, assuming an optical transition at $\lambda = 1 \mu\text{m}$. The number of vibrational repump lasers needed to scatter this many photons is then given by the lowest n such that $1/(1 - \sum_{k=1}^n P_{0,k}) \gtrsim N_{scatt}$. For example, if the molecule of interest had $P_{0,0} = 0.9$ and $P_{0,v+1}/P_{0,v} = 0.1$ for all other v , then a total of five lasers (tuned to $|A, v' = 0\rangle \leftarrow |X, v\rangle$ for $v = 1 \dots 5$) would be required. This is obviously technically challenging, but feasible in principle. It is interesting, by comparison, to note that producing ultracold polar alkali molecules typically requires 6 or more lasers.

In addition to repumping vibrational decays, it is also necessary to create a closed cycle for rotational states. It was recently pointed out by Jun Ye and coworkers[141], however, that this is easily accomplished by choosing a ground state with $J = 1$ and exciting to $J' = 0$. Then, due to angular momentum and parity selection rules, the only possible decays are back to the starting rotational level. Furthermore, it is important to consider the possibility of metastable electronic states to which the excited molecules could potentially decay to disrupt the cycle. An example of this is the $A'^2\Delta$ state in BaF [142] that lies beneath the $A^2\Pi$ state and decays only very slowly to the $X^2\Sigma$; this effectively doubles the number of repump lasers required and makes BaF a considerably less

attractive test species than it would be otherwise. Finally, because of the large number of photons that must be scattered to produce an appreciable momentum change in a molecule, it is useful to select a species with a relatively short excited state lifetime (preferably ≤ 10 s of ns) to minimize the distance over which the cooling laser beams must be applied.

The test species we have considered that best satisfies the requirements outlined above is SrF. It has favorable Franck-Condon factors which should allow the necessary number of photons to be scattered with only 2 repump lasers, and all required optical transitions are at convenient wavelengths (i.e. accessible by diode lasers). The angular momentum structure of the ground state is tractable, and the excited state has a lifetime of ~ 24 ns [143], allowing many photons to be scattered over a relatively short distance. The following sections describe calculations and measurements performed to demonstrate the suitability of SrF for laser cooling.

4.2.1 Vibrational Structure

Franck-Condon factors have been calculated numerically for the X-A band of vibrational transitions in SrF to verify its suitability as a candidate for laser cooling. The internuclear potentials for each electronic state were approximated by Morse potentials¹ [145] of the form

$$U(r) = D_e(1 - e^{\beta(r-r_e)})^2 \quad (4.1)$$

where r_e is the mean internuclear separation and D_e the dissociation energy. Molecular constants obtained from references [146] and [145] for the $X^2\Sigma$ and $A^2\Pi$ states are as follows:

	T_e (cm ⁻¹)	B_e (cm ⁻¹)	ω_e (cm ⁻¹)	$\omega_e x_e$ (cm ⁻¹)
$X^2\Sigma$	0	0.2505346	501.96496	2.2046
$A^2\Pi$	15072.0872	0.25359	509.5406	2.2361

These are related to the Morse parameters according to $D_e = \frac{\omega_e^2}{4\omega_e x_e}$, $\beta_e = \left(\frac{\pi\mu c\omega_e^2}{\hbar D_e}\right)^{1/2}$, and $r_e = \left(\frac{\hbar}{4\pi c\mu B_e}\right)^{1/2}$. (Here, c is the speed of light and μ is the reduced mass of SrF.) The vibrational wavefunctions were calculated using a two-step symplectic integrator [147]. The Franck-Condon factors

¹We have chosen Morse potentials due to the limited available spectroscopic data on vibrational states of SrF, particularly in the $A^2\Pi_{1/2}$ electronic manifold. While it is, in principle, possible to use more accurate potential functions that incorporate higher order Dunham coefficients, the Morse potential is expected to suffice for the low-lying vibrational states of interest here. Empirically, Franck-Condon calculations performed for BaF using RKR potentials (see [144] and references contained therein) differed by less than 0.01 overall for $v < 5$.

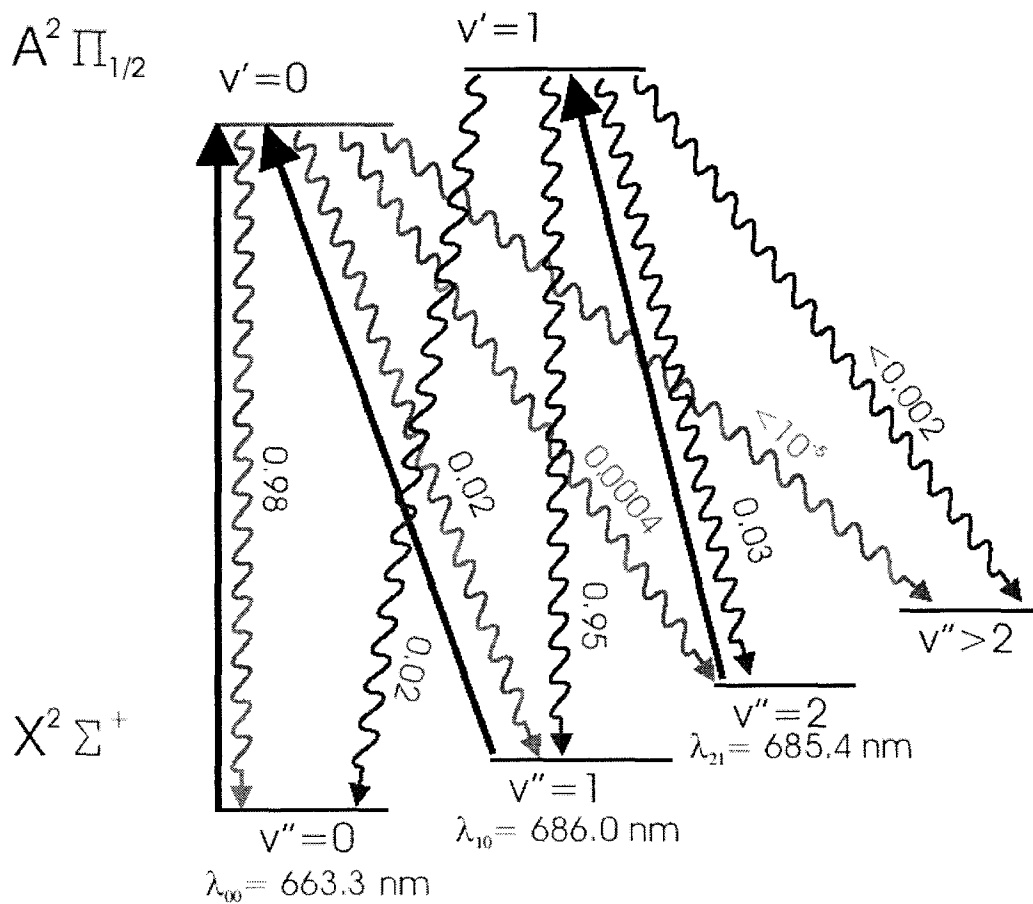


Figure 4.1: Calculated Franck-Condon factors and transition wavelengths for the X-A band in SrF. The resulting branching ratios suggest that it should be possible to scatter nearly 10^5 photons using only three lasers. Solid black arrows indicate transitions induced by the pump and repump beams; wavy arrows depict possible spontaneous emission processes and their respective branching ratios. Note that the required excitation wavelengths (663.3nm, 686.0nm, and 685.4nm) can all be produced with inexpensive diode lasers.

obtained by numerically evaluating the resulting wavefunction overlap integrals are summarized below:

	A(v'=0)	A(v'=1)	A(v'=2)	A(v'=3)	A(v'=4)	A(v'=5)
X(v=0)	0.982	0.0182	3.05×10^{-5}	3.12×10^{-8}	1.33×10^{-11}	6.97×10^{-14}
X(v=1)	0.0178	0.946	0.0360	8.97×10^{-5}	1.29×10^{-7}	7.78×10^{-11}
X(v=2)	4.01×10^{-4}	0.0345	0.911	0.0534	1.76×10^{-4}	3.34×10^{-7}
X(v=3)	1.05×10^{-5}	0.00117	0.0501	0.878	0.0704	2.87×10^{-4}
X(v=4)	3.13×10^{-7}	4.12×10^{-5}	0.00227	0.0646	0.846	0.0870
X(v=5)	1.03×10^{-8}	1.54×10^{-6}	1.00×10^{-4}	0.00368	0.0780	0.814

These results suggest that three lasers should be sufficient to scatter nearly $\sim 10^5$ photons and thus to cool SrF to the Doppler limit. Our repumping scheme, along with the relevant Franck-Condon factors and optical wavelengths calculated from the spectroscopic constants given above, is outlined in Figure 4.1. The required wavelengths for the main pump, $\lambda_{00} = 663.3$ nm, and the two repump beams $\lambda_{10} = 686.0$ nm and $\lambda_{21} = 685.4$ nm, are all conveniently accessible with diode lasers. Note that we have elected to repump $|X, v = 2\rangle$ to $|A, v = 1\rangle$, instead of to $|A, v = 0\rangle$ directly, because the latter transition at 710.0nm is more difficult to reach with current diode technology; this still returns the molecule to the cooling cycle with high probability.

4.2.2 Rotational and Hyperfine Structure

One potential complication in the re-pumping scheme for SrF arises from the existence of resolved hyperfine structure due to the unpaired spin of ^{19}F . For the $X^2\Sigma$ electronic ground state, the projection of the electron orbital angular momentum on the internuclear axis is zero and spin-rotation interactions become dominant; this situation is best described using the Hund's case (b) basis [145]. The effective angular momentum Hamiltonian is given by [148]

$$H = B\mathbf{N}^2 + \gamma\mathbf{N} \cdot \mathbf{S} + H_{hfs}, \quad \text{for} \quad H_{hfs} = b\mathbf{I} \cdot \mathbf{S} + c(\mathbf{I} \cdot \hat{\mathbf{z}})(\mathbf{S} \cdot \hat{\mathbf{z}}) + C_I \mathbf{I} \cdot \mathbf{N} \quad (4.2)$$

The spin-rotation and hyperfine interaction parameters for the $v = 0$ state were measured in reference [149] using laser-rf double resonance spectroscopy, and are given by $\gamma = 74.79485\text{MHz}$, $b = 97.0834\text{MHz}$, $c = 30.268\text{MHz}$, and $C_I = 0.00230\text{MHz}$. The Hamiltonian matrix is block-diagonal in

the Hund's case (b) basis $\{|(N, S = 1/2), I = 1/2, F, m_F\rangle\}$, with the term that couples electron spin and nuclear spin via the internuclear axis (parameterized by c) causing mixing between the $J = (N \pm 1/2)$ states for $F = N$ [150]. It can be diagonalized analytically [151] to give the following energies $E_{N,J,F}$:

$$\begin{aligned}
E_{N,N+1/2,N+1} &= \frac{\gamma + C_I}{2} \times N + \frac{b}{4} + \frac{c}{4(2N+3)} \\
E_{N,N+1/2,N} &= -\frac{\gamma + C_I + b}{4} + \frac{1}{4}[(2N+1)^2(\gamma - C_I)^2 - 2(\gamma + C_I)(2b+c) + (2b+c)^2 + 4C_I\gamma]^{1/2} \\
E_{N,N-1/2,N} &= -\frac{\gamma + C_I + b}{4} - \frac{1}{4}[(2N+1)^2(\gamma - C_I)^2 - 2(\gamma + C_I)(2b+c) + (2b+c)^2 + 4C_I\gamma]^{1/2} \\
E_{N,N-1/2,N-1} &= -\frac{\gamma + C_I}{2} \times (N+1) + \frac{b}{4} - \frac{c}{4(2N-1)}
\end{aligned} \tag{4.3}$$

A level diagram showing frequency splittings for the two lowest rotational states is given in figure 4.2.2. By exciting transitions from the odd-parity $|X^2\Sigma^+, N = 1\rangle$ ground states to the even-parity $|A^2\Pi_{1/2}, J = 1/2\rangle$, it is guaranteed that all decays will be back to the same initial rotational level. This is due to the fact that the $|X^2\Sigma^+, N = 2\rangle$ states are even parity, and transitions to all higher N states are forbidden by angular momentum selection rules. Hyperfine mixing between the $|X^2\Sigma^+, N = 1, F = 2\rangle$ and the $|X^2\Sigma^+, N = 3, F = 2\rangle$ states could, in principle lead to decays outside of the cycling states, but this mixing is expected to be of order $\sim \left(\frac{|H_{hf}|}{10B_e}\right)^2 = \left(\frac{200\text{MHz}}{75.1\text{GHz}}\right)^2 = 7 \times 10^{-6}$; likewise hyperfine mixing in the excited state Λ -doublet between $|A^2\Pi_{1/2}, J = 1/2, F = 1^+\rangle$ and $|A^2\Pi_{1/2}, J = 1/2, F = 1^-\rangle$ could lead to decays to $|X^2\Sigma, N = 2, J = 3/2, F\rangle$, but the hyperfine splitting in the $A^2\Pi$ state is unresolved, so the mixing must be less than $\sim \left(\frac{\gamma_0}{\Delta E_\Lambda}\right)^2 = \left(\frac{7\text{MHz}}{7\text{GHz}}\right)^2 = 10^{-6}$, where $\Delta E_\Lambda = 7\text{GHz}$ is the excited state Λ -doublet splitting [152]. Similar estimates show that realistic stray electric fields of less than $\sim 5\text{V/cm}$ and our applied magnetic fields of ~ 10 gauss give acceptably small mixing with states outside the cycling transition, for a dipole moment 3.5 Debye, and the ground electronic state magnetic moment of $1 \mu_B$ (with g-factors of order unity in the ground state, and zero in the excited electronic state).

Because the hyperfine splitting is unresolved in the $|A^2\Pi_{1/2}, J = 1/2\rangle$ states, it is possible for decays to populate all four ground-state hyperfine levels. It is thus necessary to re-excite from each of them with a separate laser frequency. Fortunately, this task is simplified by a coincidence of

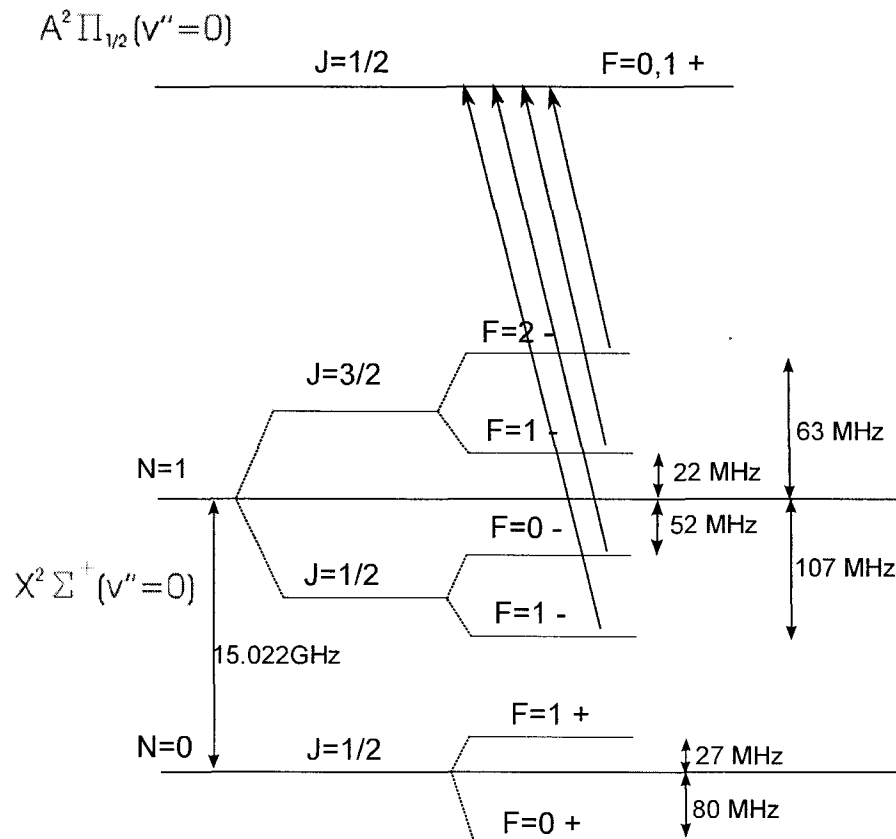


Figure 4.2: Rotational and hyperfine structure for the $|X, N = 0, 1\rangle$ and $|A, J = 1/2\rangle$ states of SrF. Splittings were calculated using the spectroscopic constants given in Section 4.2.2. Solid arrows denote transitions that must be excited in order to close the quasi-cycling transition. Note that the even parity of the $|X, N = 0\rangle$ and $|X, N = 2\rangle$ states precludes decays from the $|A, J = 1/2\rangle$ states to lowest order.

the level structure which makes all four hyperfine states accessible to a single phase-modulation sideband spectrum. Recall that for modulation depth M and angular frequency Ω , the resulting signal is given by [84]

$$e^{i(\omega t + M \sin \Omega t)} = e^{i\omega t} \sum_{n=-\infty}^{\infty} J_n(M) e^{in\Omega t} \quad (4.4)$$

It can be shown that for a modulation index $M = 2.6$ radians, the power in the first and second order sidebands (at frequencies $\pm\Omega$ and $\pm 2\Omega$ relative to the fundamental, respectively) is approximately equal and constitutes about 86% of the total power. Figure 4.2.2 depicts the sideband frequencies generated by phase-modulating the pump laser at this modulation depth ($M = 2.6$ radians), at a frequency of 41.4MHz, and shifting the fundamental by about ~ 8 MHz to the red of the $N = 1$ frequency from figure 4.2.2. This results in a spectrum for which the laser frequencies are detuned from each of the $|J = 3/2, F\rangle$ and $|J = 1/2, F = 1\rangle$ hyperfine transitions by about ~ 1.5 natural linewidths ($\gamma_0 = 7$ MHz), which is close to the optimal condition for laser cooling in atomic systems. The transition from $|J = 1/2, F = 0\rangle$ in the figure is resonant and will not be efficiently cooled; however this state has the lowest multiplicity (one magnetic sublevel out of a total of 12) and is therefore sampled relatively infrequently by the cycling molecules.

4.2.3 Remixing Dark States

One potential drawback of cycling on a $J \rightarrow J-1$ transition is the inevitability of optical pumping into dark Zeeman sublevels of the ground angular momentum state. In the simple case of a $J = 1 \rightarrow J = 0$ transition, for example, only one ground state sublevel is accessible to a fixed laser polarization, and the other two are dark. In their recent TiO laser cooling paper, Ye and coworkers [141] propose to solve the problem by utilizing the large Stark shifts associated with the Λ -doublet in the $^3\Delta_1$ ground state of that molecule, periodically applying a rapidly-switched electric field to non-adiabatically remix the dark sublevels. While SrF does not possess comparable doublet structure, it does have a large ground state magnetic moment ($1\mu_B$), opening the possibility of direct remixing using a magnetic field.

The use of a static magnetic field for the destabilization of dark states has been demonstrated in trapped ion systems [153]. A discussion of magnetic field remixing, along with the equivalent technique of remixing by laser polarization modulation, is found in a recent paper by Berkeland and

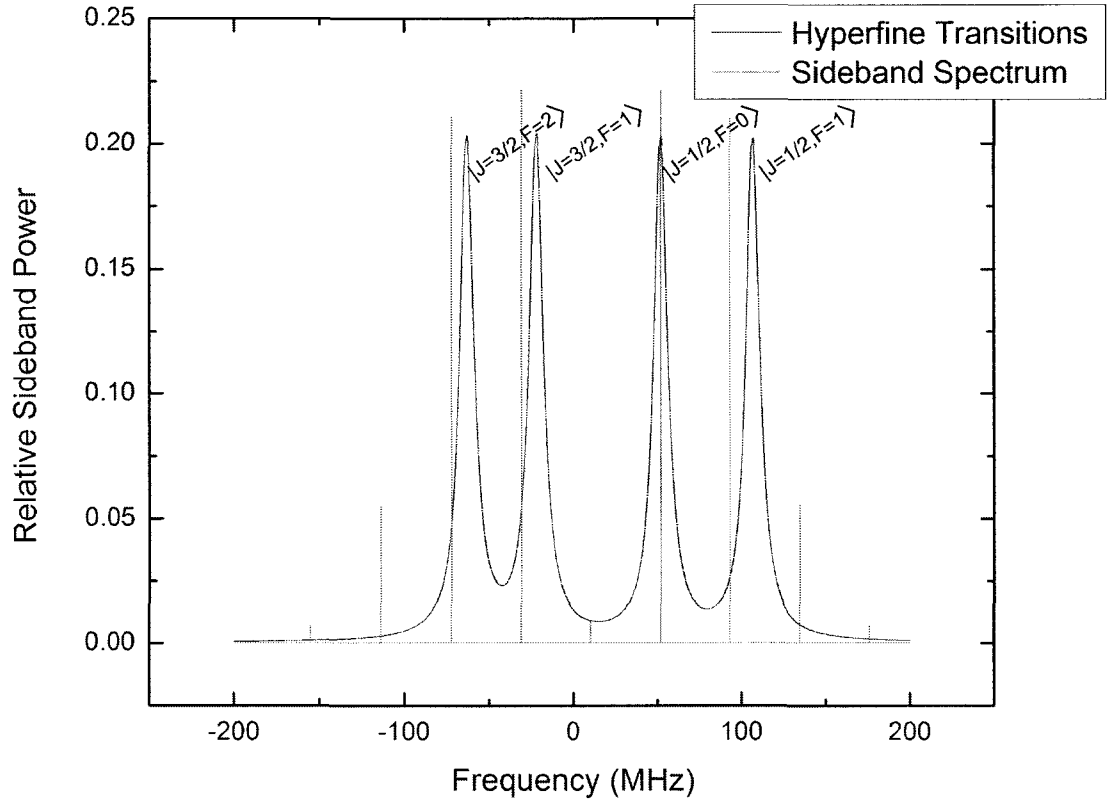


Figure 4.3: Sideband frequency distribution chosen to excite all four hyperfine levels. Spectral components of the laser are shown as red vertical lines; the molecular hyperfine transitions are depicted as Lorentzian lineshapes of full width $\gamma \approx \sqrt{2}\gamma_0 = 10\text{MHz}$, corresponding to a saturation parameter $I/I_{\text{sat}} = 1$. The vertical axis indicates the relative power in each sideband (normalized to 1). The amplitude of the hyperfine peaks is arbitrary. For the sideband parameters chosen (frequency $f = 41.4\text{MHz}$, modulation depth $M = 2.6$ radians), the detunings of each laser line relative to the nearest hyperfine transition were: -9.2MHz for $|J = 3/2, F = 2\rangle$, -8.8MHz for $|J = 3/2, F = 1\rangle$, 0MHz for $|J = 1/2, F = 0\rangle$, and -13.6MHz for $|J = 1/2, F = 1\rangle$. Thus, for each transition except the one from $|J = 1/2, F = 0\rangle$, the laser is red-detuned from the transition by $\delta \sim -1.5\gamma_0$, which should be favorable for laser cooling. The $|J = 1/2, F = 1\rangle$ transition is resonant, and should be efficiently repumped without heating.

Boshier [154]. There, a density-matrix approach is used to calculate the steady-state spontaneous emission rate for several simple 2-level and 3-level systems, as a function of magnetic field strength and laser polarization (relative to the magnetic field axis). Our system, which includes a total of 16 magnetic sublevels and laser excitations at 4 separate frequencies, is significantly more complex to calculate. Nevertheless, the qualitative conclusions made by Berkeland and Boshier can be extended to the case of SrF. In particular, it is expected that the optimal magnetic-field strength for maximizing photon scattering rates is such as to produce a Zeeman shift $\delta \sim \Omega/2$, where Ω is the resonant Rabi frequency. If the magnetic field is much weaker than this, the induced precession out of dark sublevels will be unnecessarily slow; if it is much stronger, some sublevels will be tuned out of resonance with the laser field and the excitation rate will decrease. Furthermore, the numerical simulations show that, for a $J = 1 \rightarrow J = 0$ transition, the excited state population is maximized for a laser polarized at an angle $\theta_{BE} = \arccos(1/\sqrt{3})$ to the magnetic field. While the optimal angle will likely be different for a more complex set of transitions, it is clear that the polarization must have some component in the direction of the magnetic field, but must not be exactly parallel. (To see this, consider again the case of $J = 1 \rightarrow J = 0$, for a magnetic field pointed in the \hat{z} direction. If the laser is also polarized in \hat{z} , then transitions can only be excited from the $m_z = 0$ state and $m_z = \pm 1$ remain dark. If the laser is polarized perpendicular to the magnetic field, say in \hat{x} , then a rotating superposition of the $m_z = \pm 1$ states is bright, but the $m_z = 0$ state is always dark. Only if the polarization is such as to excite transitions from a superposition of all three Zeeman sublevels does the rotation destabilize all dark states.) Our setup for one-dimensional transverse cooling of a SrF beam therefore includes two independently-adjustable pairs of orthogonal magnetic field coils to allow for the optimization both of the strength of the remixing field and of its direction relative to the laser polarization.

4.3 Experimental Apparatus

A new molecular beam apparatus has been constructed for demonstrating quasi-cycling transitions in a hydrodynamic beam of SrF, as illustrated in the schematic of Figure 4.4. The source consists of a cubic helium buffer gas cell of side length 3 cm, held in thermal contact with the cold plate of a liquid helium cryostat. Molecules are introduced into the cell via ablation of a solid precursor using a pulsed Nd:YAG laser (Quantel Big Sky Ultra-50), with pulse energies of up to 50 mJ and

duration ~ 7 ns. The laser fires at a maximum repetition rate of 20 Hz, although it has been found empirically that ablating faster than 1Hz results in a significant decrease (by a factor of ~ 2 or more) in the molecule yield.² The ablation beam is expanded to a diameter of ~ 1 cm using a telescope, then focussed onto the target with an achromatic doublet lens of focal length $f = 30$ cm. The focussing lens is placed on a translating mount to adjust the focal plane and thereby maximize the ablation yield. The observed SrF signal is generally greatest when the ablation laser is focussed tightly at the surface of the target and fired at the full 50 mJ pulse energy. The ablation target was prepared by pressing SrF powder into a disc of 13 mm diameter and 4 mm thickness, using a 9 ton hydraulic press. Helium buffer gas is supplied continuously to the cell via a mass flow controller (MKS model M100B00122CR1BV) at a typical rate of 5 - 30 sccm. Upon ablation, the SrF molecules become entrained in the helium flow and exit the cell through a 3 mm diameter aperture in the front face.

Outside the cell, the SrF beam is collimated slightly by a 6mm diameter aperture in a charcoal-covered copper plate approximately 2.5cm downstream; it then traverses a series of larger openings in the 4K shield and 77K shield to exit the cryostat. Background helium gas is pumped away by cryosorption due to the activated coconut charcoal (Spectrum Chemicals C1221) that covers the collimating plate and all other interior surfaces of the 4K shield. The shield is constructed from plates of 1/8"-thick OFHC copper; its temperature is monitored with a diode thermometer and does not exceed ~ 4.5 K. (Note that one exception to this is the front face of the shield, which has charcoal on the its exterior surface and hence a high emissivity. This face typically reaches ~ 7 K. The purpose of the charcoal here is to reduce the helium density in the volume immediately outside the cell.) Charcoal is affixed to the copper plates using silver-loaded epoxy (Arctic Silver Thermal Adhesive). The total surface area of charcoal is approximately 1000cm^2 . We have verified that it is possible to run for at least 5 hours (and possibly considerably longer) at a helium input rate of 30sccm without saturating the charcoal cryopumps.

The room temperature vacuum chamber consists of a pair of KF-40 crosses, through which the beam passes to be optically manipulated and interrogated. Approximately 17.5cm downstream from the buffer gas cell exit aperture, a second collimation slit has been placed to limit the transverse

²The decrease in yield at even moderate ablation rates is rather surprising, and has not been observed for the ablation of other molecular targets including SrO, BaF, and ThO in similar geometries. Given the slow timescale involved, it is conjectured that the problem is due to some thermal process unique to our SrF targets, but no careful investigation has been performed to date.

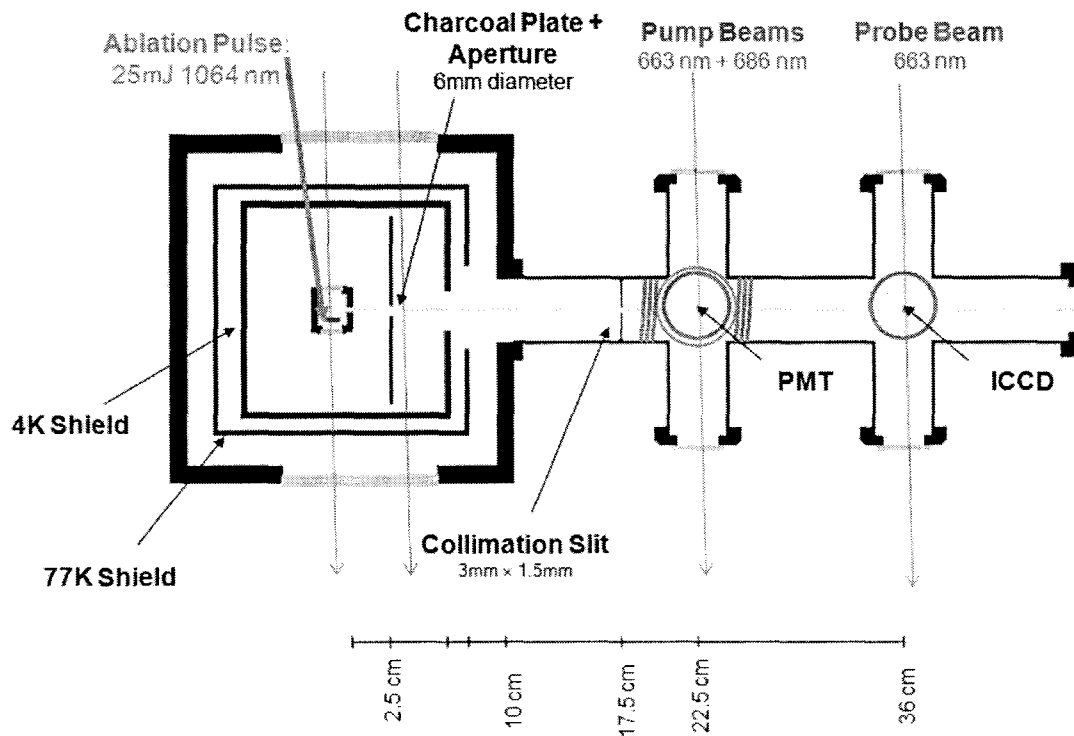


Figure 4.4: Schematic of the SrF molecular beam apparatus. Molecules are produced by ablation in a helium buffer gas cell and become entrained in hydrodynamic helium flow through the exit aperture. Excess background helium is pumped away by activated coconut charcoal cryosorbs. Optical access is provided for probe beams through the cell and through the beam inside the cryostat. The molecular beam is collimated at a distance of 17.5cm from the aperture to a Doppler width of $\Gamma_D \approx 10\text{MHz}$. Pump and repump beams can be used to induce quasi-cycling transitions in the molecules at a distance of 22.5cm from the aperture, and magnetic field coils are used to provide mixing of Zeeman sublevels. Fluorescence from the molecules is collected with a $f = 30\text{mm}$ achromatic doublet lens and detected by a photomultiplier. The molecules can then be probed and imaged again at a distance of 36cm from the aperture, using an intensified CCD camera.

Doppler velocity spread of the beam to roughly the natural linewidth of the X-A transition in SrF.³ The height of the slit was selected to ensure that all transmitted molecules traverse the ~2mm diameter laser beams. Molecules reach the center of the first cross at a distance of ~22.5 cm from the cell exit, where they interact with the 663.3nm pump and 686.0nm repump beams, tuned to the $|X, v = 0\rangle \rightarrow |A, v' = 0\rangle$ and $|X, v = 1\rangle \rightarrow |A, v' = 0\rangle$ transitions respectively. For most experiments, the optical beams are fully overlapped using a dichroic mirror. The second vibrational repump, when introduced into the apparatus, will be inserted here as well. Anti-reflection (AR) coated or Brewster-angled windows are used in order to reduce scatter, as well as to minimize optical power loss for beam deflection and transverse cooling measurements. Laser-induced fluorescence (LIF) from the molecules is collected by a $f = 30\text{mm}$, $d = 25\text{mm}$ achromatic doublet and transmitted through a 7/8" diameter acrylic light pipe to an overhead photomultiplier tube (PMT) (Hamamatsu R3896). The interior of the chamber has been lined with black antistatic foam to reduce scattered light backgrounds reaching the PMT; this is a significant issue because the diagonal FC-factors of SrF generally make it necessary to excite and detect fluorescence on the same optical transition. It has been determined empirically that outgassing from the foam is not sufficient to attenuate the molecular beam. Two pairs of field coils are wrapped around the exterior of the KF-40 tube to allow for magnetic remixing of the dark Zeeman sublevels. The horizontal coils (axis parallel to the molecular beam) consist of 28 turns each at a radius $r = 20\text{mm}$ and separation $2z = 60\text{mm}$; the vertical coils have 26 turns each at $r = 30\text{mm}$ and $2z = 75\text{mm}$. Both pairs of coils provide a relatively homogenous magnetic field of $B \sim 10\text{gauss}$ at the intersection of the laser and molecular beams for an applied current $I = 3\text{A}$.

For state-depletion and radiative-force deflection measurements, it is desirable to probe the molecules some time after they have interacted with the main pump beams. This facility is provided by a second cross, centered at a point approximately 36cm downstream from the beam source. Probe light at 663.3nm (and in some cases also 686nm) intersects the molecular beam here, and the resulting fluorescence is imaged (1:1 imaging ratio) by a pair of $f = 40\text{mm}$, $d = 25\text{mm}$ achromatic doublets onto the photocathode of an intensified CCD camera (Princeton Instruments PI-MAX2). The camera consists of a 1024×1024 array of $12.8\mu\text{m}$ square pixels, which provide information

³The full width of the slit (3 mm) plus that of the cell exit aperture (3 mm) limits the maximum angle to $\frac{6\text{mm}}{175\text{mm}} = 0.034 \text{ rad.}$; for a mean forward velocity of ~200 m/s, this ensures the maximum transverse velocity spread is $\Delta v_T \lesssim 6.9\text{m/s}$, corresponding to a FWHM Doppler width of $\Gamma_D/2\pi \approx 10.3 \text{ MHz}$. The natural linewidth of the transition is $\gamma_0/2\pi \sim 7 \text{ MHz}$.

about both the net molecule flux and the spatial distribution of the beam. Finally, one additional AR-coated window is located on-axis at the end of the second cross to allow for the insertion a counter-propagating laser to probe the forward velocity of the beam. The entire room-temperature vacuum assembly is pumped with a 60L/s turbomolecular pump (Pfeiffer TMU071P) attached to the second cross to a pressure of $\lesssim 10^{-6}$; this is found to be necessary for maximizing the detected molecular beam flux.

4.3.1 Cryostat and Vacuum Chamber

The SrF hydrodynamic beam experiments described in this chapter were all performed using a new cryogenic apparatus, based around an IR-Labs model HDL-5 liquid helium dewar.⁴ This cryostat was originally developed to serve as part of a new source for the BaF parity-violation experiment in the DeMille group, which is also expected to benefit significantly from a high-flux hydrodynamic beam. The helium (nitrogen) vessel has a volume of 1.2 ℓ (0.8 ℓ), and the total thermal mass of the cryostat is relatively small, allowing for cooldown times from room-temperature to 4K on the order of 2 hours. The warm-up time is also very fast, typically about 4-5 hours when ~ 100 Torr of He gas is admitted to facilitate convective heat transfer from the outer vacuum chamber walls. This has proven extremely advantageous for rapid prototyping of the beam geometry; the ability to break vacuum, make modifications, then cool down again and run every day (as compared to once or twice per week with the cryogenic apparatus described in Chapter 2) cannot be overstated. An isometric cutaway view of the cryostat is shown in Figure 4.5. The external vacuum chamber (not shown) consists of a single length of 8" outer diameter square aluminum tube, with top and bottom flanges attached by exterior welds. The helium gas fill line is made of thin-walled stainless steel tube, and is thermally anchored to both the 77K and 4K surfaces. Rectangular windows (4.5" \times 1") have been used on the exterior chamber, and afford considerable optical access for probing both inside the cell and in the molecular beam region. Matching rectangular apertures have been cut into both the 77K and 4K shields. The combination of helium gas flow and radiative heating via the windows give rise to a thermal load of approximately ~ 1 W, allowing for run-times on the order of an hour (for liquid ^4He density $\rho = 124.7$ g/ ℓ and latent heat of vaporization $H = 20.75$ J/g [80], corresponding to a boil-off rate of 1.38 $\ell/\text{W}^{-1}\text{hour}^{-1}$) before the helium vessel must be refilled.

⁴This cryostat was designed and assembled by Yale undergraduate Christopher Yale and graduate student Peter Orth. Full technical details can be found in [155].

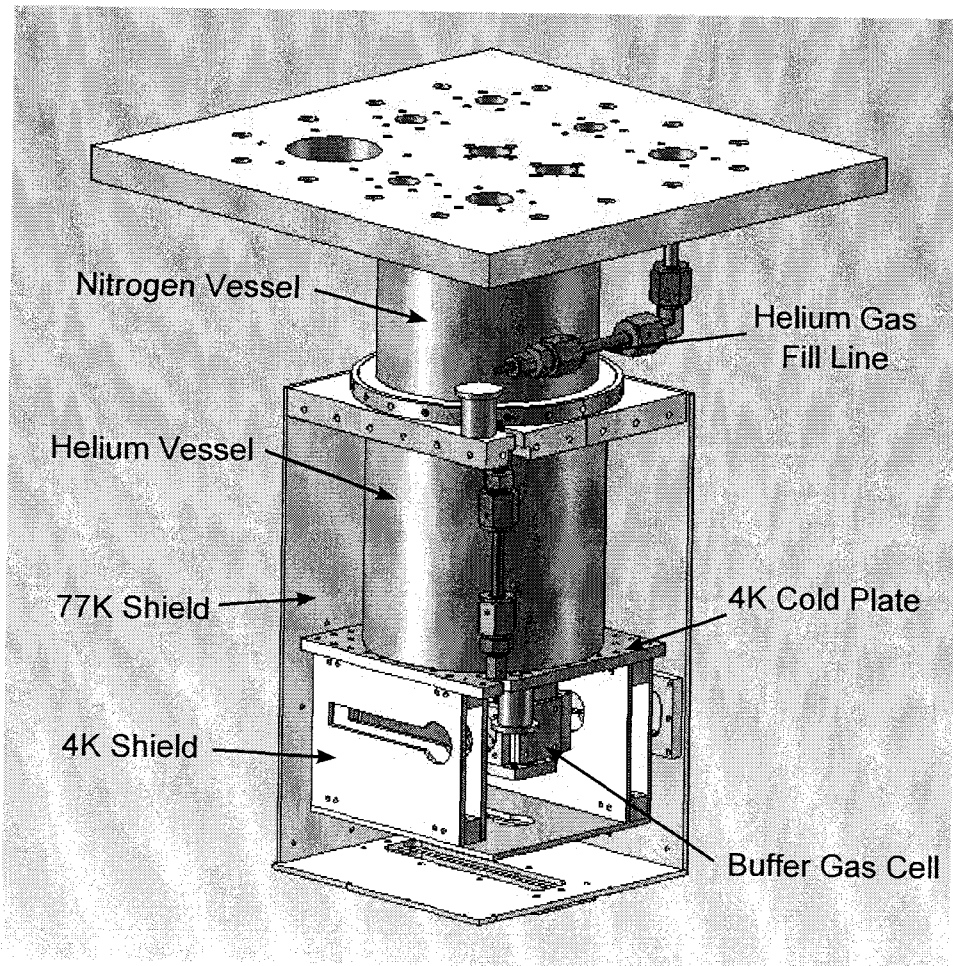


Figure 4.5: Cryostat for SrF beam source. Figure modified from [155].

4.3.2 Laser Setup

A system of diode lasers has been assembled to demonstrate the quasi-cycling transition in SrF. The requirements for frequency stability and power are largely determined by the ultimate goal of performing laser cooling on the molecular beam, and are similar to those for comparable experiments in alkali atomic systems. The X-A electronic transition of interest has a natural linewidth of $\gamma_0 \approx 2\pi \times 7$ MHz; branching ratios associated with angular momentum matrix elements of different hyperfine transitions vary, but are typically on the order of $\beta_{R,R'} = \left| \langle A^2 \Pi; J = 1/2, F, m_F | \mu \cdot E | X^2 \Sigma; N = 1, F, m_F \rangle \right|^2 \sim 1/4$ to $1/3$, giving rise to a saturation intensity for each hyperfine transition of about $I_{sat} = \frac{\pi \hbar c \gamma_{eff}}{3 \lambda^2} \sim 10$ mW/cm². (Here, $\gamma_{eff} = \gamma_0 \beta_{R,R'} \beta_{V,V'}$ is the effective linewidth for a given hyperfine transition, where $\beta_{V,V'} \approx 1$ for diagonal vibronic matrix elements. The subscript R is used as shorthand for angular momentum quantum numbers N, J, F , and m_F .) To obtain this intensity in each of the four frequency sidebands at a modulation depth $M = 2.6$ radians requires a total intensity of roughly $I_{sat} = 50$ mW/cm²; for a gaussian beam of FWHM diameter⁵ $w \approx 2$ mm, the total power needed to saturate all of the transitions is then $P_{sat} = \frac{\pi}{2} I_{sat} w^2 \sim 3$ mW. For many applications it is desirable to exceed the saturation intensity in the main pump beam by a factor of 10 or more, necessitating a total power of approximately 30mW. Note that although the line strengths for the $|X, v = 1\rangle$ to $|A, v' = 0\rangle$ transitions are considerably weaker, the power requirement for the repump beam is no more stringent than for the pump. For a vibrational branching ratio β_V , and assuming equal power in the pump and repump beams, a given molecule decays to $|X, v = 1\rangle$ roughly every β_V pumping cycles, then remains there on average for β_V times the duration of one cycle before being repumped. If the repump transition could be deeply saturated, the total number of photons scattered over many pump-repump cycles would thus be increased only by a factor of 2.

Efficient laser cooling typically requires that the optical frequency be stably tuned to the red of the transition by approximately one linewidth [156]. For the SrF transition linewidth $2\pi \times \gamma = 7$ MHz, it is expected that frequency stability on the order of $\lesssim 1$ MHz should be adequate. This relatively modest requirement is satisfied (or nearly so) in our setup by locking the external cavity diode lasers (ECDs) to a stabilized He-Ne reference via a transfer cavity (Coherent 33-2486-000). The cavity length is scanned successively through resonance with both lasers at a rate of approximately 10 Hz, and the frequency separation of the resulting peaks is read into an analog-to-digital converter

⁵Measured using a CCD camera (Mightex MCE-BO13-U) consisting of a 512×512 array of $5\mu\text{m}$ pixels.

(DAC) via a photodiode (Thorlabs PDA36A). A software-driven feedback loop with a bandwidth of a few Hz controls the external cavity length of the diode laser by setting the voltage across a piezo-electric transducer (PZT) attached to the diffraction grating. The intrinsic stability of our home-built ECD lasers is such that even this slow feedback loop holds the frequency fixed to about ± 2 MHz over many minutes.⁶ (This is roughly the same as the long-term stability of the HeNe.) This has been adequate for all measurements performed to date; it may be necessary to upgrade to a higher-bandwidth analog or digital servo-lock for future laser cooling experiments.

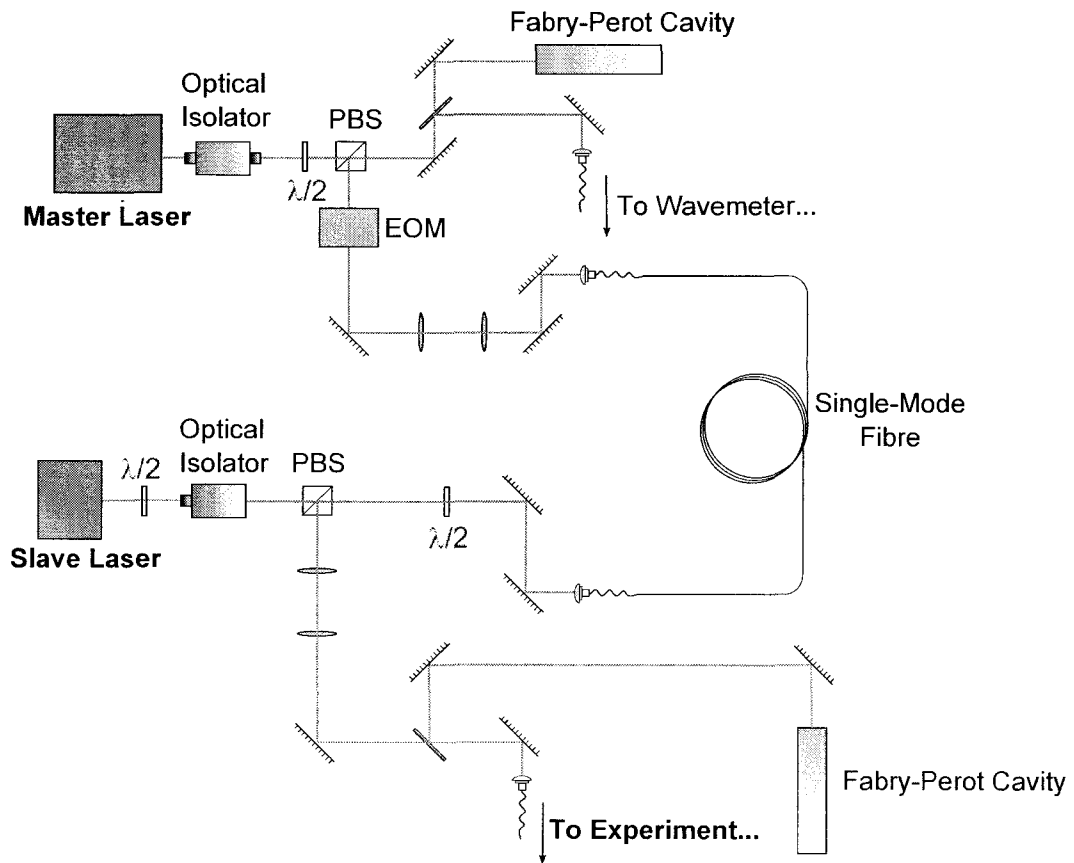


Figure 4.6: Typical setup for the injection-locked diode lasers used in the SrF beam experiments. Not shown is a frequency-stabilized HeNe laser for locking the (top) Fabry-Perot cavity, to which the master laser is locked in turn.

In order to obtain the desired intensities in the pump and repump beams, a series of injection-

⁶The frequency stability of the software lock is estimated by monitoring the magnitude of the error signal.

locked, high power diode lasers has been implemented. A typical beamline is illustrated in Figure 4.6. Light from a narrow linewidth ECD travels through an electro-optic modulator (EOM) that inscribes the sidebands required to access all four hyperfine transitions, and is then passed through a single mode optical fiber to seed a high power (~ 100 mW) slave diode. A fraction of the beam from the master oscillator is initially split off and sent to a wavemeter (HP 86120B) for frequency determination, as well as to the Fabry Perot transfer cavity (Coherent 33-2486-000, FSR = 750 MHz) used in the servo-lock. Both lasers are protected from feedback with optical isolators; the master uses a 2-stage isolator (Conoptics Model 716) that provides >55 dB extinction in the reverse direction, while the slave has a single-stage, >34 dB isolator (OFR IO-3-665-HP). The output polarizer of the slave isolator is replaced with a polarizing beamsplitter (PBS), which directs the outgoing beam through another single-mode fiber to the experiment. Telescopes are used to improve mode matching into each optical fiber. A fraction of the slave output is split off and sent to a home-built optical cavity (quartz-tube based confocal cavity, FSR = 750 MHz, constructed by John Barry) to monitor the stability of the injection lock. One advantage of using a single-mode fiber between the two lasers is that the slight polarization-leakage of the slave diode output through the PBS is return-coupled through the fiber and can be used to facilitate precise spatial mode-matching.

The full laser system used for the experiments described in Section 4.4 consists of the following oscillators: (i) a Toptica DL-100 ECD at 663 nm (Toptica temperature controller and current supply electronics), driving a slave diode that provides the main pump beam (~ 50 mW delivered to the experiment); (ii) a home-built Littrow-configuration ECD⁷ at 686nm driving two slaves, one of which provides the the main repump beam (~ 60 mW at the experiment), the other a high-powered repump used in the probe region to measure vibrational state depletion (~ 50 mW); (iii) a home-built Littrow ECD at 663 nm that provides the main probe beam (~ 20 mW); and (iv) another home-built Littrow ECD at 663nm used as an auxiliary probe for different rotational lines or the $|X, v = 1\rangle \rightarrow |A, v' = 1\rangle$ vibrational transition. In principle, all lasers except the last one are operated at a fixed frequency and do not need to be tuned on a day-to-day basis.

⁷All home-built ECDs were constructed by graduate student John Barry. All but one utilize temperature-control and current supply electronics designed by post-doc Daniel Farkas and constructed by John Barry. (The other laser uses a Vescent D2-105 laser control module.) All home-built ECDs and slave lasers at 663 nm were built using the Mitsubishi ML101J27 diode; those at 686 nm were built with Hitachi Optnex HL6750M6 diodes. Documentation for these lasers and electronics can be found in a report written by Dan.

4.3.3 Electro-Optic Modulators

One additional noteworthy aspect of the laser setup is the use of a series of home-built EOMs for effecting the required phase modulation. These have been constructed using lithium tantalate (LiTaO₃) crystals of dimensions 3.2 mm × 3.2 mm × 40 mm, purchased from Almaz Optics. The crystals are Y-cut (as needed for phase modulation) and come with gold electrodes deposited onto two of the rectangular faces. The square faces are AR-coated for 700-1000 nm and specified to 20-10 scratch-dig tolerance. We require a phase-modulation depth of at least $M = 2.6$ radians to obtain the desired sideband pattern; the dependence of modulation depth on applied voltage is generally parameterized in terms of V_π , the peak voltage required to obtain a π phase shift. For light passing through a crystal with optical path-length L and a distance d between the electrodes, the induced phase shift ϕ for an applied voltage V is given [157] by $\phi = \beta VL/d$. Here, $\beta = r_{33}\pi n^3/\lambda = 1.62 \times 10^{-3}\text{V}^{-1}$, for $r_{33} = 33$ pm/V the electro-optic coefficient of LiTaO₃, $n = 2.18$ its refractive index, and $\lambda = 663$ nm the optical wavelength. For a crystal of our dimensions, this gives $V_\pi = 157.1$ V. To drive such a high voltage directly at 41MHz would be a significant technical challenge, and we have therefore constructed a resonant RLC circuit to amplify the applied voltage.

The EOM tank circuit consists primarily of an inductor selected to match the intrinsic capacitance of the crystal ($C = \frac{\epsilon_r \epsilon_0 A}{d} \approx 15$ pF, for $\epsilon_r = 43$ the RF dielectric constant of LiTaO₃, $A = 40$ mm × 3.2 mm the area of the electrodes, and $d = 3.2$ mm the separation between them) in order to obtain the correct resonant frequency, as well as a transformer for matching to the 50Ω impedance of the input line. Components were soldered to a custom-made printed circuit board (fabricated by ExpressPCB inc.), onto which the crystal is mounted directly with electrically-conductive epoxy (Epoxies Etc., silver-filled epoxy resin 40-3900). The measured capacitance of the circuit is ~20pF (slightly higher than the crystal alone due to stray capacitance at contacts and in printed circuit board leads), necessitating an inductance of $L = 0.75$ μH to obtain a resonant frequency $f_0 = \frac{1}{2\pi\sqrt{LC}} = 41$ MHz. Our best results were observed with a hand-wound inductor of $N \sim 35$ turns wrapped around a 1/8" diameter teflon rod. It would, in principle, be advantageous to use a variable inductor in order to adjust the resonant frequency and thereby tune the EOM sidebands while maintaining a high Q for the circuit. Several such inductors (most notably the 7M2-102 and SLOT-TEN-1-01 models from Coilcraft Inc.) were investigated, but it was found that they degraded the circuit Q, presumably due to saturation of the adjustable ferrite cores at high power and/or frequency. The transformer

selected was a 1:16 impedance ratio unbalanced model with a 2 W maximum power specification (RFMD model XFA-0101-16UH). It was expected that this should give maximum power coupling for a resistive load of $R \approx 3.1\Omega$, and a 10Ω cermet potentiometer was therefore included in the circuit trim the resistance to this value. This proved unnecessary, however, as the finite resistance of the inductor at high frequency was large enough that shorting the leads of the potentiometer gave the best impedance match. Reflected power measurements using an RF network analyzer (HP 8712C) showed a Q of 21 and a power reflection coefficient on resonance of $R = -18.1\text{dB}$. This suggested that the peak input voltage required to produce a π -phase shift should be reduced to $V_{\pi}/Q = 7.9$ V, equivalent to a power input of 0.6 W. In fact, the power required to obtain the desired phase shift of 2.6 radians is somewhat greater than 1W, indicating a voltage drop somewhere in the circuit other than across the crystal (likely in one of the other reactive components) when operating at high power.

4.4 Results: Demonstration of Cycling

4.4.1 Beam Flux Measurement for SrF

During the development of the cryogenic apparatus described in Section 4.3.1, a series of measurements were performed to determine the approximate ablation yield and hydrodynamic beam flux for SrF. A weak, linearly polarized probe beam was tuned to one of the $|X^2\Sigma, v = 0; N = 1\rangle \rightarrow |A^2\Pi, v' = 0, J' = 1/2\rangle$ hyperfine transitions while the target was ablated at a helium buffer gas inflow rate of 20sccm. The rotational line was identified by measuring the optical frequency on a wavemeter (HP 86120B) with an accuracy of a few GHz; however, the laser was unlocked, making identification of hyperfine structure difficult at this stage. The probe beam was passed through the buffer gas cell or through the beam immediately beyond the exit aperture, and the absorbed power was monitored on a photodiode (Thorlabs PDA36A). Figure 4.7 shows typical absorption traces in each case. The out-of-cell trace can be used to make a rough estimate of the flux of molecules in the beam populating the probed rotational state. The Doppler-broadened absorption cross section for a probe laser with linewidth narrower than the transition of interest is given by [84]:

$$\sigma_D = \frac{\sqrt{\pi}}{2} \frac{\lambda^2}{2\pi} \frac{2F' + 1}{2F + 1} \frac{\gamma_{\text{partial}}}{\Gamma_{\text{Dop}}} = 2.14 \times 10^{-11} \text{cm}^2 \quad (4.5)$$

Here, $\Gamma_{Dop} = \frac{2\pi}{\lambda} \sqrt{\frac{2k_B T}{m_{SrF}}} = 2\pi \times 37.6$ MHz is the 4 K Doppler width, and $\gamma_{partial} = \frac{1}{\tau} \beta_{V,V'} \beta_{R,R'} \sim 2\pi \times 1.3$ MHz, where $\tau = 24$ ns is the state lifetime, $\beta_{V,V'} \approx 1$ is the Franck Condon factor for the transition, and $\beta_{R,R'}$ is the square of an unknown angular momentum matrix element that will be estimated here as $\beta_{R,R'} \sim 0.2$. Likewise, F and F' are each taken to be 1. (The rotational matrix element is uncertain because the hyperfine structure was not resolved; this could conceivably lead to an error of roughly a factor of 2-3 in the final result.) In the limit of small absorption, the signal size is given by $S = 1 - e^{-n\sigma_D L} \approx n\sigma_D L$, for n the density of absorbers and L the optical path length. The total number of absorbing molecules is now given by $N_{mol} = \frac{A}{\sigma} \int \frac{dS}{dt} dt$, for $A = \frac{\pi w_0^2}{4} = 0.031$ cm² the area of the probe laser intersecting the molecules. Integrating the absorption trace in Figure 4.7 gives $N_{mol} \sim 8.5 \times 10^9$ molecules in the probed state. The total number of molecules in all hyperfine states of the $N = 1$ level of the electronic ground state could be several times higher, owing to the uncertainty in the effective angular momentum matrix elements for unresolved transitions and the fact that only one or two of the hyperfine transitions were probed.

4.4.2 Rotational and Hyperfine Spectroscopy of SrF

The spectroscopic constants tabulated in Section 4.4.3 have been used to locate a variety of transitions, including the main pump and repump frequencies and several others of interest. The calculated transition frequencies are summarized in the following table:

Initial State	Final State	Frequency
$ X^2\Sigma, v = 0, N = 1\rangle$	$ A^2\Pi, v' = 0, J' = 1/2+\rangle$	451954GHz
$ X^2\Sigma, v = 1, N = 1\rangle$	$ A^2\Pi, v' = 0, J' = 1/2+\rangle$	437037GHz
$ X^2\Sigma, v = 1, N = 1\rangle$	$ A^2\Pi, v' = 1, J' = 1/2+\rangle$	452179GHz
$ X^2\Sigma, v = 0, N = 1\rangle$	$ A^2\Pi, v' = 0, J' = 3/2+\rangle$	451977GHz
$ X^2\Sigma, v = 0, N = 0\rangle$	$ A^2\Pi, v' = 0, J' = 1/2+\rangle$	451969GHz

In each case, wavemeter readings have agreed with the calculated transition frequency to within about ~1GHz. (This is roughly the specified accuracy of the wavemeter.) Measurements have also been made to verify our knowledge of the hyperfine structure presented in Section 4.2.2. A very weak, linearly polarized probe beam (peak intensity $I_0 = 0.05$ mW/cm², approximately equivalent to $I_{sat}/200$ for a single hyperfine transition) was directed through the first KF cross in Figure 4.4,

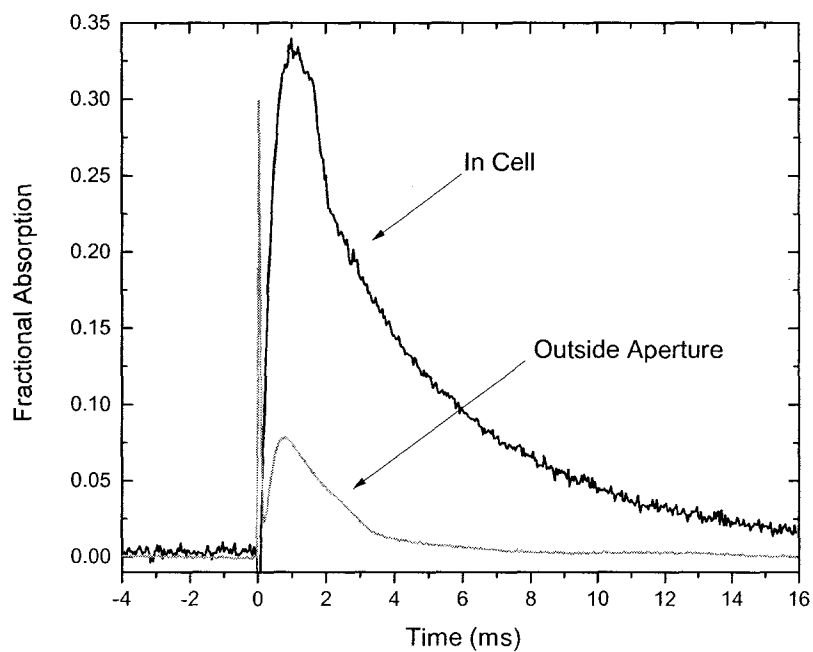


Figure 4.7: Beam flux measurement. Fractional absorption data for probe beams directed through the buffer gas cell and immediately outside the aperture to measure SrF ablation yield. Integration of the beam absorption signal shows that the number of molecules per beam pulse in the probed $|X, v = 0, N = 1, F\rangle$ state is $N_{\text{mol}} \sim 8.5 \times 10^9$. The sharp spike at $t = 0$ is due to electrical pickup from the Q-switch of the ablation laser. These data were collected by John Barry and Christopher Yale.

and the resulting fluorescence collected by the overhead PMT. The collimation slit ensured that the transverse Doppler width of the molecular beam was $\lesssim 10$ MHz. The probe frequency was scanned over the $|X^2\Sigma, v = 0, N = 1, J, F\rangle \rightarrow |A^2\Pi, v' = 0, J' = 1/2\rangle$ hyperfine transitions by tuning the PZT-controlled diffraction grating angle of the ECD; part of the beam was split off and sent to one of our home-built quartz tube optical cavities, the length of which had been adjusted to create a re-entrant mode [158] with FSR = 46.9 MHz. (The FSR of the cavity was first determined by writing sidebands onto the laser using RF modulation of the drive current; the RF frequency was increased until the difference between the fundamental and the first order sideband observed in the cavity spectrum equaled exactly one FSR.) This provided regular frequency markers to calibrate the measured hyperfine transition frequencies.

The resulting data are shown in Figure 4.8. Two pairs of peaks corresponding to the electron spin-rotation doublets are visible, each one split by hyperfine interactions. Qualitatively, the transition from the $|N = 1, J = 1/2, F = 0\rangle$ initial state is weakest, as is expected given its lower multiplicity and therefore its smaller thermal population compared to the other hyperfine states. The other lines are, somewhat surprisingly, of roughly equal strength; this may be due to some coincidence of averaging over different initial-state Zeeman sublevels, since the Earth's magnetic field was not nulled for the measurement. A sum of four Lorentzian lineshapes was fitted to the measured spectrum, and the resulting splittings relative to the $|N = 1, J = 3/2, F = 2\rangle$ line are summarized below:

Hyperfine State	Expected Frequency	Fitted Frequency	Difference
$ J = 3/2, F = 2\rangle$	0 MHz	-1.3 MHz	-1.3 MHz
$ J = 3/2, F = 1\rangle$	41 MHz	34.1 MHz	-6.9 MHz
$ J = 1/2, F = 0\rangle$	115 MHz	121.5 MHz	+6.5 MHz
$ J = 1/2, F = 1\rangle$	170 MHz	171.7 MHz	+1.7 MHz

Thus, the observed hyperfine splittings were in relatively good agreement with theory. The recorded deviations, on the order of a natural linewidth $\gamma_0 = 7$ MHz or less, may be due to thermal fluctuations in the cavity length.

4.4.3 Measurement of Vibrational Transition Strengths

In order to test the calculated vibrational branching ratios given in Section 4.2.1, the relative absorption line-strengths of the $|X, v = 1\rangle \rightarrow |A, v' = 1\rangle$ and $|X, v = 1\rangle \rightarrow |A, v' = 0\rangle$ transitions

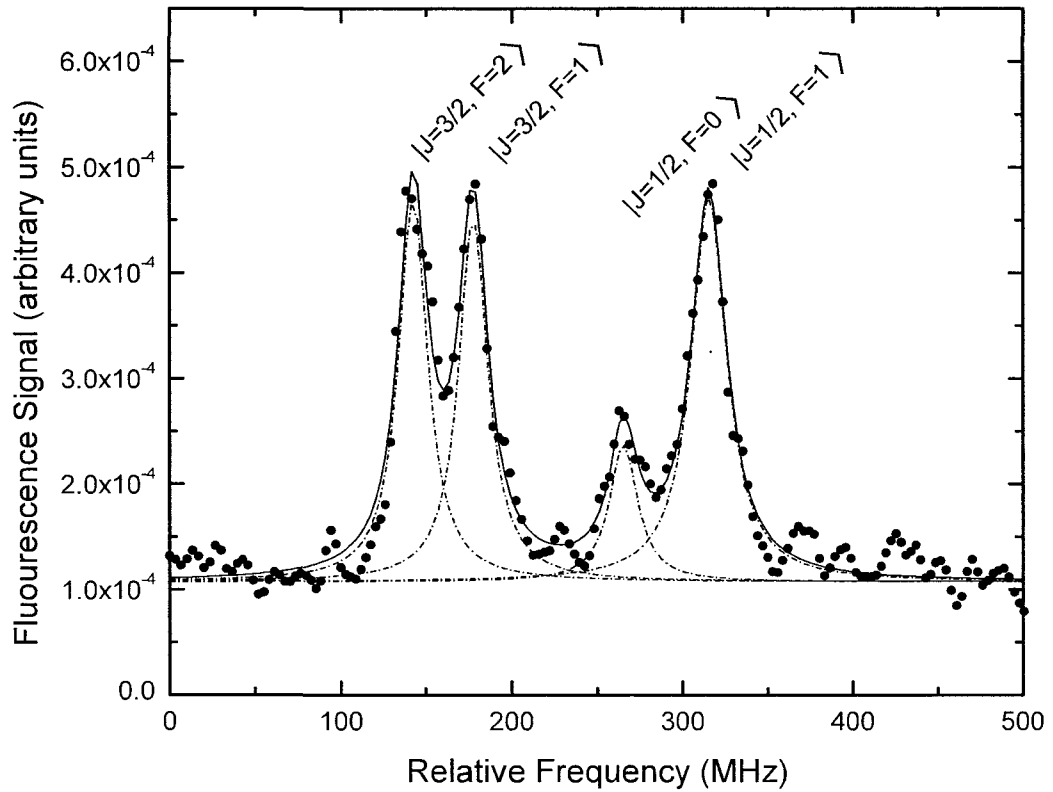


Figure 4.8: Measured hyperfine transition frequencies for $|X, v = 0, N = 1, F\rangle \rightarrow |A, v = 0, J = 1/2, F\rangle$. The data were obtained by sending a weak probe ($I/I_{sat} = 5 \times 10^{-3}$) through the beam at a distance of 22.5 cm from the source, using an optical cavity of FSR = 46.9 MHz for frequency calibration, and detecting the resulting fluorescence with a PMT. Black dots are measured points; the solid line depicts a fit to a sum of 4 Lorentzian lineshapes, each of which are shown individually by the dashed lines. The measured frequency splittings were -1.3 MHz, 34.1 MHz, 121.5 MHz, and 171.7 MHz relative to the expected position of the $|J = 3/2, F = 2\rangle$ peak. These are all within one natural linewidth of the expected splittings.

were measured in the buffer gas cell. Because of the weakness of the latter transition, FM spectroscopy was used to make the measurements. Sidebands at 100 MHz were inscribed onto the main probe beam (of intensity $I = 22 \text{ mW/cm}^2$) with a modulation depth $M \sim 1.4$, corresponding to approximately equal power in the fundamental and first-order sidebands, using an EOM (Thorlabs EO-PM-R-C1). A second probe (intensity $I = 22 \text{ mW/cm}^2$) without sidebands was simultaneously directed through the cell in order to account for shot-to-shot variations in the ablation yield. For both measurements, the secondary probe was tuned to the stronger $|X, v = 0\rangle \rightarrow |A, v' = 0\rangle$ transition.⁸ Typical time traces for both the FM probe and the direct absorption signals are shown in Figure 4.9. The measured peak FM spectroscopy signal was normalized both by the direct absorption from the secondary probe, and by the DC component of the signal from the diode (Thorlabs PDA10A) used to detect the FM beam.⁹ The peak direct absorption signal sizes were each scaled by one over the relevant calculated Franck-Condon factor ($\beta_{0,0} = 0.98$ for the $v = 0 \rightarrow v' = 0$ transition, $\beta_{1,1} = 0.95$ for the $v = 1 \rightarrow v' = 1$ transition) to account for the small difference in line strengths before they were used to normalize the FM signals.

For each measurement, the FM signal was maximized with respect to both the frequency of the fundamental (by finely adjusting grating position in the ECD) and the relative phase between local oscillator and the detected FM absorption signal. The former optimization likely resulted in the fundamental being tuned close to the transitions from the two $J = 3/2$ hyperfine levels in the ground state. However, the fact that the laser frequency was not locked at the time, combined with the difficulty of resolving individual hyperfine transitions (due to the 38 MHz Doppler width of SrF at 4 K), likely limits the accuracy of the measurement. Four independent measurements of the $|X, v = 1\rangle \rightarrow |A, v' = 1\rangle$ FM absorption signal and three measurements of the $|X, v = 1\rangle \rightarrow |A, v' = 0\rangle$ were recorded, and the ratios of each pair were calculated. The mean FM signal ratio was found to be $S_{v=1 \rightarrow v'=1}/S_{v=1 \rightarrow v'=0} = 43.5 \pm 5$. The uncertainty here is given as the standard deviation of the calculated ratios over all combinations of measurements, and reflects the variability in measured signals. If we make the conservative assumption that the calculated value for the $v = 1 \rightarrow v' = 1$ branching ratio, $\beta_{1,1} = 0.946$, is correct to within 5%, then the measured branching ratio for the $v = 1 \rightarrow v' = 0$ transition becomes $\beta_{1,0} = 0.946/43.5 = 0.022 \pm 0.003$. This result is in reasonably good

⁸Note that this normalization assumes that the thermal population of vibrational states is constant from shot to shot, which has not been explicitly verified.

⁹The DC and 100 MHz signals from the detector were split using a bias-tee (Minicircuits ZFBT-4R2GW+); the FM signal is normalized by the DC signal in order to account for variations in laser intensity between measurements.

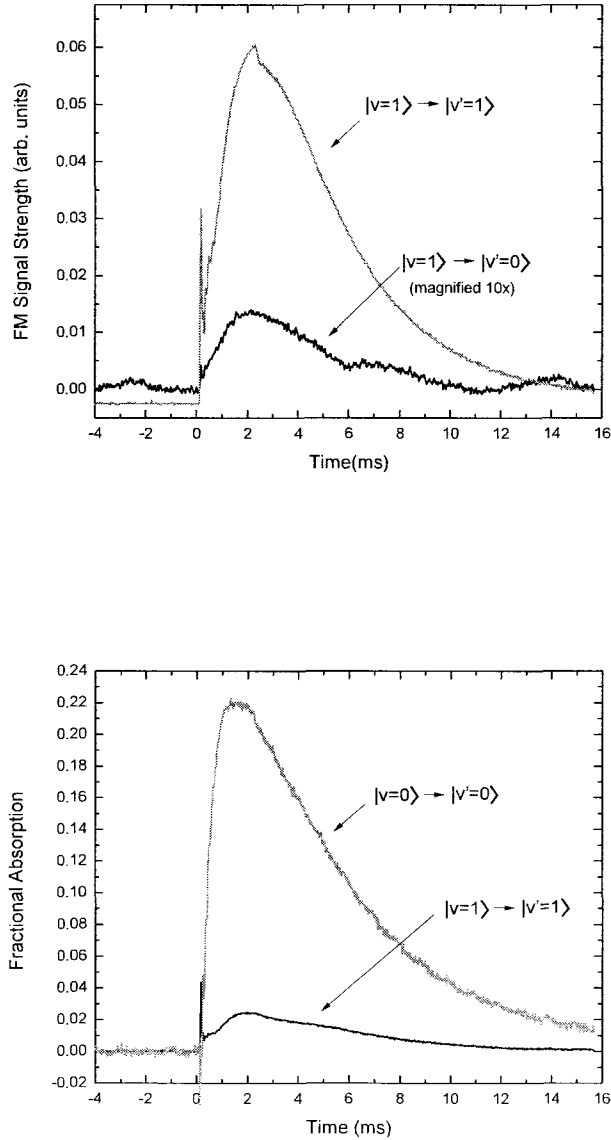


Figure 4.9: Vibrational transition strength measurements. **Top panel:** Time traces from FM spectroscopy on the $v = 1 \rightarrow v' = 1$ and $v = 1 \rightarrow v' = 0$ transitions in the buffer gas cell. The latter trace has been multiplied by a factor of 10 for visibility. When properly normalized, these data indicate a ratio of Franck Condon factors of $\beta_{1,0}/\beta_{1,1} = 43.5 \pm 5$. The two traces were collected at different times during the run. **Bottom panel:** Direct absorption data for $v = 0 \rightarrow v' = 0$ transition collected simultaneously with each of the traces above, used to normalize the FM signals for shot-to-shot variations in ablation yield. Also shown is a direct absorption trace (collected at a different time) for the $v = 1 \rightarrow v' = 1$ transition, which can be used to estimate the vibrational temperature of the molecules at about $T_{vib} \sim 360$ K.

agreement with the calculations presented in Section 4.2.1.

It is interesting to note in passing that the secondary (direct absorption) probe can be tuned to the $v = 1 \rightarrow v' = 1$ and thereby used to obtain a rough estimate of the vibrational temperature of the molecules. The expected ratio for Boltzmann-distributed molecules at temperature T is given by

$$\frac{S_{v=0 \rightarrow v=0}}{S_{v=1 \rightarrow v=1}} = \frac{0.98 \exp\left[\frac{-1/2\omega_e}{k_B T}\right]}{0.95 \exp\left[\frac{-3/2\omega_e}{k_B T}\right]} \quad (4.6)$$

A typical pair of traces for direct absorption on $v = 0 \rightarrow v' = 0$ and $v = 1 \rightarrow v' = 1$ in the bottom panel of Figure 4.9. (Note that these are taken at different times during the run, and hence do not take into account shot-to-shot variations in ablation yield, which could be ~ 20 - 30% .) Solving for the observed ratio of ~ 7.1 gives a vibrational temperature $T_{vib} \sim 360$ K. This is consistent with the often-made claim that buffer gas collisions do not efficiently cool vibrational excitations. It is also somewhat encouraging from the point of view of being able to spectroscopically locate the $v = 2 \rightarrow v = 1$ transition when the second vibrational repump is added to the experiment; that transition is weak to begin with, and its initial state population is strongly suppressed at low temperatures. Of course, a more systematic study covering more vibrational lines, preferably performed outside the cell, would be necessary to draw any general conclusions about buffer gas cooling of molecular vibrations.

4.4.4 Observation of Repumping by Enhanced Fluorescence

Direct evidence for the scattering of multiple photons by SrF has been obtained by observing an increase in the fluorescence collected from the molecular beam coinciding with the addition of a magnetic field and vibrational repump. As shown in Figure 4.4, the collimated molecular beam was made to interact with a strong pump beam ($I \approx 200$ mW/cm² in each sideband) in the first KF cross, and a fraction of the resulting fluorescence was collected by a $f = 30$ mm achromatic doublet lens and detected with a PMT. Frequency sidebands were inscribed in the pump beam using an EOM, as described in Section 4.2.2, at a frequency $f = 42.0$ MHz and modulation depth $M \approx 2.6$ radians. (In practice, the sideband frequency can be varied by several MHz without appreciably changing the fluorescence amplitude. This is likely due to the large power broadening in the pump beams with $I/I_{sat} \sim 20$ in each sideband.) In order to maximize the length of interaction, the pump beam

was retro-reflected back and forth through the vacuum chamber with partially overlapping beam spots approximately 8 times. This allowed for a total interaction length $L_{int} \approx 2\text{cm}$. Fluorescence was initially collected with the current to the magnetic field coils turned off; when it was switched on and tuned such that the angle between the net field and the laser polarization was optimal, the observed fluorescence increased by a factor of 1.8. The magnitude of the magnetic field produced by each coil for an input current of 3A was measured with a gauss-meter (FW Bell 4048) to be about 10 gauss. The increase in fluorescence is due to the re-mixing of dark Zeeman sublevels, allowing for multiple photons to be scattered before each molecule is eventually pumped into the $v = 1$ vibrational state. Note that the Earth's magnetic field of ~ 0.5 gauss likely provides some remixing, albeit at a considerably lower rate, allowing molecules to scatter more than one photon on average even with the coils switched off. Finally, the addition of a vibrational repump beam with 42 MHz sidebands ($I \approx 240\text{mW/cm}^2$ in each sideband) produced a further increase in the detected fluorescence to approximately 10.0 times the initial signal. The only plausible explanation for this observation is that molecules were being successfully repumped back from the $v = 1$ vibrational state into the main cycling transition; as seen in Section 4.4.3, the thermal population of the first excited vibrational state is too small to account for this large increase in signal. Typical time traces for the fluorescence signals with and without the remixing field and repump beam are shown in Figure 4.10.

4.4.5 Observation of Beam Deflection by Radiative Force

We have demonstrated the manipulation of SrF molecules by radiative force in a beam deflection experiment. Molecules passing through the first KF cross of Figure 4.4 were acted upon by the combination of a pump beam at 663.3 nm and a vibrational repump at 686.0 nm, as well a ~ 10 gauss magnetic field for the mixing of Zeeman sublevels. Sidebands were written onto both the pump and repump beams with EOMs at frequency $f = 42$ MHz and modulation depth $M = 2.6$. The intensities of the beams were $I_{\text{pump}} \approx 200 \text{ mW/cm}^2$ and $I_{\text{repump}} \approx 240 \text{ mW/cm}^2$ respectively, in each sideband. (Thus, $I/I_{\text{sat}} \sim 20$ for the pump and $I/I_{\text{sat}} \sim 0.5$ for the repump.) The laser beams were overlapped on a dichroic mirror and directed into the KF cross. Instead of retro-reflecting the beams back through the chamber as in Section 4.4.4, a ring consisting of four mirrors was constructed to direct the beams around the outside of the vacuum chamber, such that they impinged on the molecules from only

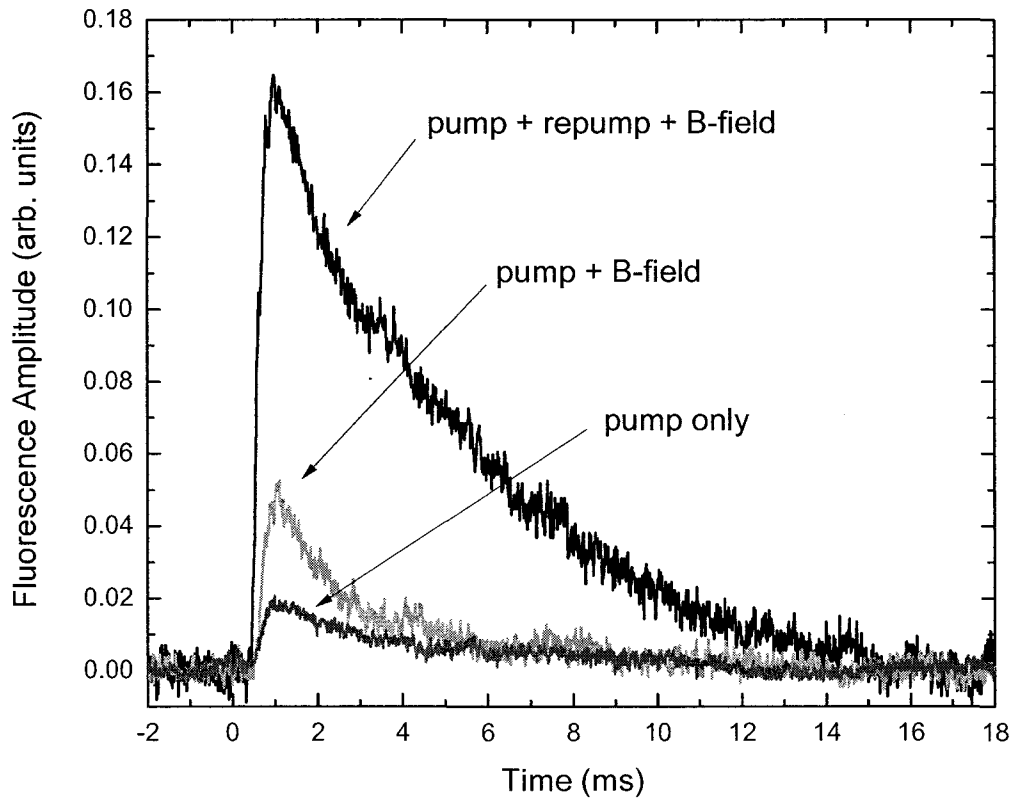


Figure 4.10: Vibrational repumping and magnetic field remixing of dark magnetic sublevels. The data shown are time traces of fluorescence detected by the PMT over the first laser interaction region at a distance of 22.5 cm from the beam source. The smallest trace shows fluorescence produced by molecules when pumped by a laser ($I/I_{sat} \approx 20$) tuned to the $|X, v = 0, N = 1, F\rangle \rightarrow |A, v' = 0, J' = 1/2, F'\rangle$ transition, with sidebands inscribed by an EOM to access all hyperfine transitions. When a magnetic field of about 10 gauss is added to remix the Zeeman sublevels, the fluorescence increases by a factor of 1.8. When a vibrational repump beam ($I/I_{sat} \approx 0.5$), also with the appropriate sidebands, is added to repump on the $|X, v = 1, N = 1, F\rangle \rightarrow |A, v' = 0, J' = 1/2, F'\rangle$ transition, the total fluorescence is increased by a factor 10.0 compared to the original signal.

one direction. A total of 8 passes with partially overlapping beam spots through this ring were arranged, for an interaction length $L_{int} \approx 2$ cm. Laser alignment and magnetic field strength were tweaked to maximize the fluorescence signal detected in the PMT above the first KF cross.

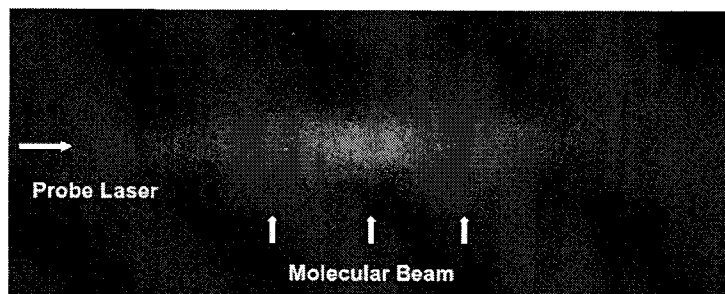


Figure 4.11: Typical beam image from the CCD camera.

After traversing this interaction zone, the molecules were allowed to travel about 13 cm further downstream, where they were interrogated by a second probe beam ($I_{\text{pump}} \approx 80$ mW/cm²) at 663.3 nm. Fluorescence light from this beam was imaged by a pair of 40 mm achromatic doublets onto the photocathode of an ICCD camera. The camera was gated on the Q-switch of the ablation laser, and set for an exposure time of 5 ms. The exposure was chosen as a tradeoff between being long enough to detect most of the molecules in the molecular beam pulse (as can be seen from the time traces of Figure 4.10), but sufficiently short to minimize background from scattered probe light. A typical fluorescence image is shown in Figure 4.11. Images of this type were integrated column-wise, and the resulting molecular beam profiles fit to gaussian curves. As the vibrational pump and repump beams were switched on and off, the deflection of the molecular beam was measured as a displacement of the center of the gaussian fit. Typical deflection data are illustrated in Figure 4.12.

The largest observed molecular beam deflections were on the order of 46 camera pixels, corresponding to a shift in the center of the detected fluorescence distribution of about 0.6 mm. (This conversion assumes 1:1 imaging and 12.8 μm pixels for the Princeton PI-MAX2 camera. It has been approximately verified by rough calibration performed with a LED moved systematically under the collection optics¹⁰.) The deflection angle is therefore $\theta_{def} = \tan^{-1}(0.6 \text{ mm}/135 \text{ mm}) = 4.4 \times 10^{-3}$ radians. For a forward beam velocity¹¹ of $v_z = 200$ m/s, the average number of photon recoils experienced by each molecule is given by $N_\gamma = \frac{m_{\text{SrF}} v_z \tan(\theta_{def})}{\hbar k} = 158$. This is a clear indication that the

¹⁰This calibration was carried out by John Barry.

¹¹Measured for the SrF beam by Edward Shuman subsequent to the collection of this data.

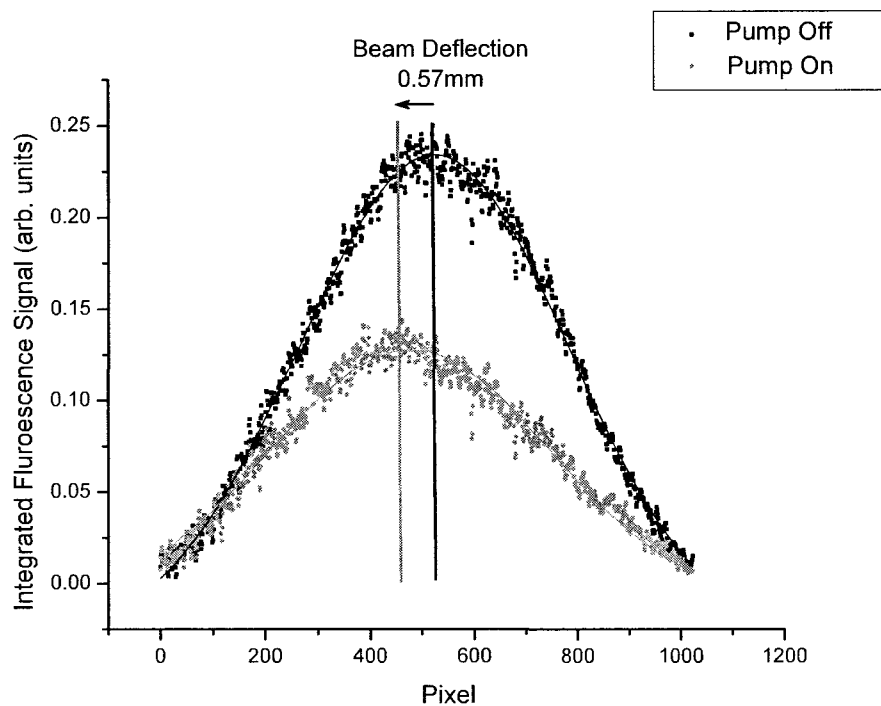


Figure 4.12: Beam deflection by radiative force. Data points are column-wise sums of fluorescence intensities detected by the CCD camera above the probe region, 36 cm downstream from the buffer gas source. The beam profiles are fit to gaussian curves (solid lines). When the pump and repump lasers are turned on and caused to interact with the molecules at a distance of 22.5 cm from the source, a deflection of the molecular beam by up to 0.6 mm is observed. For a forward beam velocity of ~ 200 m/s, this corresponds to an average of 158 photons scattered per molecule. The photon scattering rate is $\Gamma_{scatt.} \approx 1.6 \times 10^6 \text{s}^{-1}$. When the pump and repump lasers are turned on with approximately equal power in each beam, the fluorescence signal decreases by a factor of 2, because the molecules spend roughly half their time in the $v = 1$ state.

vibrational repump is successfully transferring molecules back into the cycling transition; no more than ~50 photons could be scattered on average according to the observed vibrational branching ratios. In the data of Figure 4.12, it can be seen that the total number of molecules detected on the $v = 0 \rightarrow v' = 0$ transition in the deflected beam decreases by approximately a factor of 2 compared to the undeflected case. This is consistent with the molecules being distributed evenly over the two vibrational levels in the ground state, as expected for roughly equal power in the pump and repump beams. Subsequent measurements have shown that, if a strong repump beam is added before the probe beam in the second KF cross, all molecules are pumped back to $v = 0$ and the original signal size is almost entirely recovered.

For an interaction length of about 2 cm and a mean forward velocity $v_z = 200$ m/s, the molecules interact with the deflection lasers over a period of approximately 100 μ s. This indicates an average photon scattering rate of $\Gamma_{scatt.} \approx 1.6 \times 10^6 \text{s}^{-1}$. In the limit of deeply saturated optical transitions and rapid magnetic field re-mixing, it is expected that the population should be distributed equally over all ground and excited state hyperfine levels while interacting with the laser. In our system, the multiplicity of the Zeeman sublevels in the excited electronic state is 4; in the two vibrational states of the ground electronic manifold, it is 24. Thus, the molecules should spend roughly 4/28 of their time in the excited hyperfine states, and the expected scattering rate is $\Gamma_{expected} = \gamma_0/7 = 6.3 \times 10^6 \text{s}^{-1}$. It is unclear why the observed rate is lower by almost a factor of 4; though our repump beam has a saturation parameter of somewhat less than one, this should only make a difference of approximately a factor of 2 in the scattering rate compared to the deeply saturated case. The problem may arise from sub-optimal magnetic field remixing, or occasional collisions with background helium atoms or other ablation products that remove the molecules from the cycling transition before they scatter the maximum number of photons. An investigation is currently underway to determine the cause of this apparent discrepancy.

4.5 Towards Laser Cooling and Microwave Trapping of SrF

As of this writing, all necessary components have been obtained to attempt one-dimensional transverse cooling of SrF. The expected maximum capture velocity for an optical molasses with saturation parameter $I/I_{sat} = 1$ and detuning $\delta \sim -\gamma_0$ is approximately $v_C = \gamma_0/k \approx 4.6 \text{m/s}$ [1]. Cooling from this

velocity to the Doppler limit requires a net number of photon recoils equal to $N_\gamma = \frac{mv_z}{\hbar k} \approx 820$. This is easily attainable with a single vibrational repump. Assuming that operating with a saturation parameter of one¹² roughly halves the photon scattering rate compared to the deeply saturated case described in Section 4.4.5, we can expect $\Gamma_{scatt.} \approx \sim 0.8 \times 10^6 \text{s}^{-1}$. For a molecular beam with mean forward velocity $v_z = 200 \text{ m/s}$, then, an interaction length $L_{int} \approx 20 \text{ cm}$ is required. (This could be reduced by a factor of 2-4 if the expected scattering rate can be obtained in future deflection experiments.) We have constructed a new vacuum component to replace the first KF cross in Figure 4.4, which is able to accommodate windows of length 15cm parallel to the beam axis on all four sides. Custom-made 15cm long Brewster-angled windows, as well as high-reflectivity mirrors ($R \approx 0.999$) have been obtained to allow the pump and repump beams to be reflected through the interaction region many times. It is expected that these components will be assembled and transverse cooling demonstrated in the near future; further extension to transverse cooling in two dimensions should then simply be a matter of increasing the number of injection-locked slave diode lasers for generating the necessary beams.

Longitudinal deceleration of the collimated SrF beam appears feasible, but will likely be technically challenging. It is, in principle, possible to sweep the frequency of a longitudinal pump beam in order to remain in resonance with a packet of decelerating molecules. To bring a molecule to rest from an initial velocity of $v_z = 200 \text{ m/s}$ requires $N_\gamma = \approx 3.6 \times 10^4$ photon recoils, necessitating the addition of the second vibrational repump. The task of spectroscopically locating the $v = 2 \rightarrow v' = 1$ transition may prove difficult, owing to the low thermal population of that initial state. Furthermore, again assuming a photon scattering rate of $\Gamma_{scatt.} \approx \sim 0.8 \times 10^6 \text{s}^{-1}$, the expected stopping length is $L_{stop} = \frac{mv_z^2}{2\hbar k \Gamma_{scatt.}} \approx 4.4 \text{ m}$. This is obviously somewhat inconvenient, though not technically impossible. Other methods have been considered for longitudinal deceleration which might allow for a shorter stopping distance, including the use of stimulated radiative forces [159], and Zeeman deceleration with permanent magnets.

The ultimate goal of confining molecules in a microwave trap becomes significantly simpler if the beam can be decelerated in this way. Consider the trap described in Chapter 3, driven with 20 W

¹²Laser cooling requires operation in the $I/I_{sat} \sim 1$ regime, so that the laser linewidth is not power broadened. This is necessary to ensure that the molecules in a particular velocity class scatter photons preferentially from the blue-shifted laser that opposes their motion; if the large intensities $I/I_{sat} \sim 20$ employed in the deflection experiments of Section 4.4.5 were used in this case, the molecules would scatter photons from the red-shifted and blue-shifted lasers at nearly equal rates, inhibiting cooling.

of input power. The peak electric field obtainable scales as the square of the power, and is therefore $E \sim 1.2$ kV/cm for $P_{in} = 20$ W (c.f. Section 3.3.3). For SrF, with a dipole moment of $\mu = 3.5$ Debye and rotational constant $B_e/h = 7.51$ GHz, this gives $\mu \cdot E \approx 0.28B_e$. Comparing to Figure 3.5, we see that the resulting trap depth for the $|X^2\Sigma, v = 0, N = 0\rangle$ states is approximately $U = 0.03B_e \approx 10.5$ mK. This is more than sufficient to capture SrF molecules that have been decelerated to the Doppler limit $T_D = \frac{\hbar\gamma_0}{2k_B} = 168$ μ K. At these relatively low fields, the multi-photon transitions described in Section 3.3.4 are no longer an issue, and the requirement of high circular polarization purity is relaxed. Furthermore, with only 20 W of drive power, heat dissipation becomes considerably easier, and Al₂O₃ mirrors should be adequate. Some minor effort may be required to re-design the input coupling aperture array for an operating frequency close to the 15GHz rotational transition frequency of SrF, but this is expected to be fairly straightforward; given that the aperture array transmission is expected to scale as the square of the frequency, and that the peak field varies slowly with input coupling (c.f. Section 3.5.1), it is possible that the existing design will not require modification.

Chapter 5

Concluding Remarks

This thesis has described the development of techniques which should ultimately enable the demonstration of ultracold samples of polar diatomic molecules. Evaporative cooling in a microwave frequency dipole trap is expected to provide a general means for cooling molecules from the cold (\sim several hundred mK) regime to the temperatures and densities required to achieve quantum degeneracy. We have therefore designed and constructed prototypes for a microwave trap that can produce a confining potential of $U \sim 0.5$ K for the SrO molecule. (The depth is limited to some extent by microwave multi-photon resonances within the trap. By changing the operating frequency from 18.1 GHz to 15 GHz, it could be increased to $U \sim 1.0$ K.) Practical difficulties in obtaining a sufficiently high flux of cold molecules from an effusive helium buffer gas beam source, together with challenges in the construction of prototype cavity mirrors, have delayed the construction of the final version of the trap to some extent. However, our investigation into the properties of the source has yielded the realization that very bright and highly collimated beams may be obtained by operating in the deeply hydrodynamic helium flow regime. Hydrodynamic beam sources of this type are now being used in a new experiment to search for the EDM of the electron in ThO, and may soon be employed in the ongoing BaF parity violation experiment in the DeMille group.

Our most recent work has focussed on finding ways to slow molecules from a hydrodynamic buffer gas source in order to load them into the microwave trap. To this end, we have devised a method for laser cooling species that exhibit highly diagonal Franck-Condon factors, allowing for quasi-cycling transitions to be established. In particular, we have conducted a series of experiments

on SrF, in which an average of ~ 150 photons have been scattered per molecule in order to produce measurable deflection of a hydrodynamic beam. As of this writing, all components are in place to extend the technique to perform transverse cooling. With the addition of one more vibrational repump laser, it should then be possible to implement chirped longitudinal deceleration, and thereby to reduce the forward velocity of the molecules to the Doppler limit. This corresponds to a forward kinetic energy of $\sim 200 \mu\text{K}$, which is not only sufficient to load the trap, but in fact significantly reduces the required microwave power (and corresponding heat dissipation) for effective confinement. Prospects for the demonstration of trap loading and evaporative cooling of SrF molecules in the near future thus seem very promising.

Appendix A

Drawings for HDL14 Cryostat

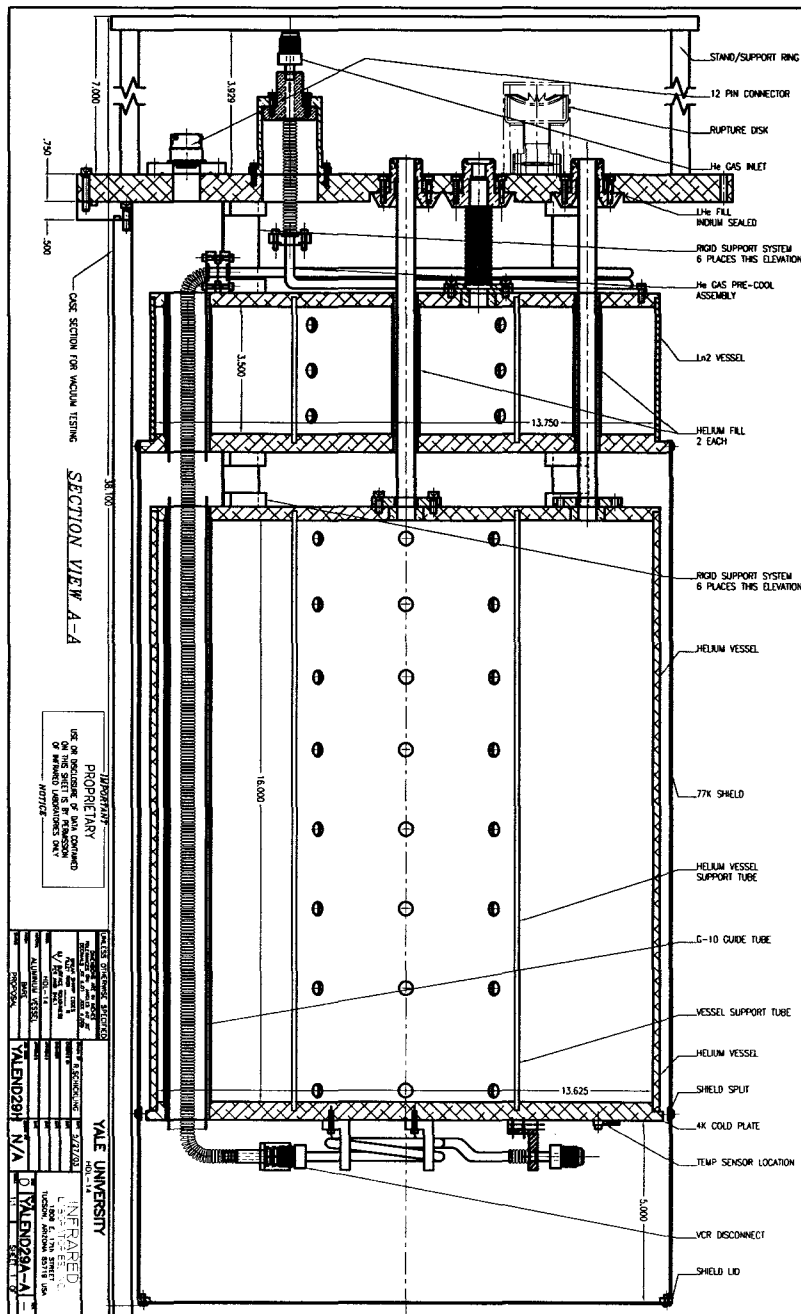


Figure A.1: Side section view of HDL14 cryostat.

Appendix B

FM Signal Size

We wish to calculate the FM absorption signal for the case of a probe beam with modulation depth $M \approx 1.4$, corresponding to a spectrum with approximately equal power in the fundamental and first-order sidebands. The electric field amplitude of the incident beam may be described approximately as

$$E_{in} = E_0[\beta_0 e^{i\omega_c t} + \beta_1 e^{i(\omega_c + \omega_m)t} - \beta_1 e^{i(\omega_c - \omega_m)t} + \beta_2 e^{i(\omega_c + 2\omega_m)t} + \beta_2 e^{i(\omega_c - 2\omega_m)t}] \quad (\text{B.1})$$

Here, ω_c and ω_m are the carrier (optical) frequency and the modulation (RF) frequency, respectively, and $\beta_k = J_k(M)$ are the sideband amplitude coefficients, which satisfy $\sum_k \beta_k^2 = 1$. For the particular case of $M = 1.4$ radians, they are found to be $\beta_0 = 0.567$, $\beta_1 = 0.542$, and $\beta_2 = 0.207$. The higher order sidebands account for less than 0.5% of the total power in the beam.

Now, assume that on passing through the molecular sample, the k^{th} -order sideband undergoes absorption $\delta_k = n \text{Re}\{\sigma(\omega_c + k\omega_m)\}L$ and dispersion $\phi_k = n \text{Im}\{\sigma(\omega_c + k\omega_m)\}L$. The electric field of the probe at the detector then takes the form

$$E_{out} = E_0[\beta_0 e^{(\delta_0 - i\phi_0)} e^{i\omega_c t} + \beta_1 e^{(\delta_1 - i\phi_1)} e^{i(\omega_c + \omega_m)t} - \beta_1 e^{(\delta_{-1} - i\phi_{-1})} e^{i(\omega_c - \omega_m)t} + \beta_2 e^{(\delta_2 - i\phi_2)} e^{i(\omega_c + 2\omega_m)t} + \beta_2 e^{(\delta_{-2} - i\phi_{-2})} e^{i(\omega_c - 2\omega_m)t}] \quad (\text{B.2})$$

The signal at the detector is then given by $I = EE^*$, which can be written explicitly as

$$\begin{aligned}
I = |E_0|^2 & [\beta_0^2 e^{-2\delta_0} + \beta_1^2 (e^{-2\delta_1} + e^{-2\delta_{-1}}) + \beta_2^2 (e^{-2\delta_2} + e^{-2\delta_{-2}})] \\
& + \beta_0 \beta_1 e^{-(\delta_0 + \delta_1)} e^{i(\phi_0 - \phi_1)} e^{-i\omega_m t} - \beta_0 \beta_1 e^{-(\delta_0 + \delta_{-1})} e^{i(\phi_0 - \phi_{-1})} e^{+i\omega_m t} \\
& + \beta_0 \beta_2 e^{-(\delta_0 + \delta_2)} e^{i(\phi_0 - \phi_2)} e^{-i2\omega_m t} + \beta_0 \beta_2 e^{-(\delta_0 + \delta_{-2})} e^{i(\phi_0 - \phi_{-2})} e^{+i2\omega_m t} \\
& + \beta_1 \beta_0 e^{-(\delta_1 + \delta_0)} e^{i(\phi_1 - \phi_0)} e^{+i\omega_m t} - \beta_1 \beta_1 e^{-(\delta_1 + \delta_{-1})} e^{i(\phi_1 - \phi_{-1})} e^{+i2\omega_m t} \\
& + \beta_1 \beta_2 e^{-(\delta_1 + \delta_2)} e^{i(\phi_1 - \phi_2)} e^{-i\omega_m t} + \beta_1 \beta_2 e^{-(\delta_1 + \delta_{-2})} e^{i(\phi_1 - \phi_{-2})} e^{+i3\omega_m t} \\
& - \beta_1 \beta_0 e^{-(\delta_{-1} + \delta_0)} e^{i(\phi_{-1} - \phi_0)} e^{-i\omega_m t} - \beta_1 \beta_1 e^{-(\delta_{-1} + \delta_{-1})} e^{i(\phi_{-1} - \phi_{-1})} e^{-i2\omega_m t} \\
& - \beta_1 \beta_2 e^{-(\delta_{-1} + \delta_2)} e^{i(\phi_{-1} - \phi_2)} e^{-i3\omega_m t} - \beta_1 \beta_2 e^{-(\delta_{-1} + \delta_{-2})} e^{i(\phi_{-1} - \phi_{-2})} e^{+i\omega_m t} \\
& + \beta_2 \beta_0 e^{-(\delta_2 + \delta_0)} e^{i(\phi_2 - \phi_0)} e^{+i2\omega_m t} + \beta_2 \beta_1 e^{-(\delta_2 + \delta_1)} e^{i(\phi_2 - \phi_1)} e^{+i\omega_m t} \\
& - \beta_2 \beta_1 e^{-(\delta_2 + \delta_{-1})} e^{i(\phi_2 - \phi_{-1})} e^{+i3\omega_m t} + \beta_2 \beta_2 e^{-(\delta_2 + \delta_{-2})} e^{i(\phi_2 - \phi_{-2})} e^{+i4\omega_m t} \\
& + \beta_2 \beta_0 e^{-(\delta_{-2} + \delta_0)} e^{i(\phi_{-2} - \phi_0)} e^{-i2\omega_m t} + \beta_2 \beta_1 e^{-(\delta_{-2} + \delta_1)} e^{i(\phi_{-2} - \phi_1)} e^{-i3\omega_m t} \\
& - \beta_2 \beta_1 e^{-(\delta_{-2} + \delta_{-1})} e^{i(\phi_{-2} - \phi_{-1})} e^{-i\omega_m t} + \beta_2 \beta_2 e^{-(\delta_{-2} + \delta_2)} e^{i(\phi_{-2} - \phi_2)} e^{-i4\omega_m t}]
\end{aligned} \tag{B.3}$$

The photodiode signal is passed through a bias-tee to separate the DC and RF components of the signal. In the limit of small absorption, $\delta_k \ll 1$, the zero frequency component gives $I_0 = |E_0|^2$. The RF part of the signal is mixed with the original modulation frequency ω_m and low-pass filtered, so that only the terms oscillating at $\pm\omega_m$ in the above expression need to be retained. Between the detector and the mixer, an amplifier and/or attenuator with total gain G are introduced to ensure that the signal level at the RF input port of the mixer is about 10dBm lower than the local oscillator. The filtered mixer output signal is then given by:

$$S_{out} = GI_0[\beta_0\beta_1e^{-(\delta_0+\delta_1)}e^{i(\phi_0-\phi_1)}e^{-i\omega_m t} - \beta_0\beta_1e^{-(\delta_0+\delta_{-1})}e^{i(\phi_0-\phi_{-1})}e^{+i\omega_m t} \quad (B.4)$$

$$\begin{aligned} & +\beta_1\beta_0e^{-(\delta_1+\delta_0)}e^{i(\phi_1-\phi_0)}e^{+i\omega_m t} + \beta_1\beta_2e^{-(\delta_1+\delta_2)}e^{i(\phi_1-\phi_2)}e^{-i\omega_m t} \\ & -\beta_1\beta_0e^{-(\delta_{-1}+\delta_0)}e^{i(\phi_{-1}-\phi_0)}e^{-i\omega_m t} - \beta_1\beta_2e^{-(\delta_{-1}+\delta_{-2})}e^{i(\phi_{-1}-\phi_{-2})}e^{+i\omega_m t} \\ & +\beta_2\beta_1e^{-(\delta_2+\delta_1)}e^{i(\phi_2-\phi_1)}e^{+i\omega_m t} - \beta_2\beta_1e^{-(\delta_{-2}+\delta_{-1})}e^{i(\phi_{-2}-\phi_{-1})}e^{-i\omega_m t}] \end{aligned}$$

$$\begin{aligned} = & GI_0[\beta_0\beta_1e^{-(\delta_0+\delta_1)}(e^{i(\phi_0-\phi_1-\omega_m t)} + e^{-i(\phi_0-\phi_1-\omega_m t)})] \\ & -\beta_0\beta_1e^{-(\delta_0+\delta_{-1})}(e^{i(\phi_0-\phi_{-1}+\omega_m t)} + e^{-i(\phi_0-\phi_{-1}+\omega_m t)}) \\ & +\beta_1\beta_2e^{-(\delta_1+\delta_2)}(e^{i(\phi_1-\phi_2-\omega_m t)} + e^{-i(\phi_1-\phi_2-\omega_m t)}) \\ & -\beta_1\beta_2e^{-(\delta_{-1}+\delta_{-2})}(e^{i(\phi_{-1}-\phi_{-2}+\omega_m t)} + e^{-i(\phi_{-1}-\phi_{-2}+\omega_m t)})] \end{aligned}$$

$$\begin{aligned} = & GI_0[2\beta_0\beta_1(e^{-(\delta_0+\delta_1)} \cos[(\phi_0 - \phi_1) - \omega_m t] - e^{-(\delta_0+\delta_{-1})} \cos[(\phi_0 - \phi_{-1}) + \omega_m t]) \\ & + 2\beta_1\beta_2(e^{-(\delta_1+\delta_2)} \cos[(\phi_1 - \phi_2) - \omega_m t] - e^{-(\delta_{-1}+\delta_{-2})} \cos[(\phi_{-1} - \phi_{-2}) + \omega_m t])] \end{aligned}$$

$$\begin{aligned} = & GI_0[\cos(\omega_m t)\{2\beta_0\beta_1(e^{-(\delta_0+\delta_1)} \cos(\phi_1 - \phi_0) - e^{-(\delta_0+\delta_{-1})} \cos(\phi_0 - \phi_{-1})) \\ & + 2\beta_1\beta_2(e^{-(\delta_1+\delta_2)} \cos(\phi_2 - \phi_1) - e^{-(\delta_{-1}+\delta_{-2})} \cos(\phi_{-1} - \phi_{-2}))\} \\ & - \sin(\omega_m t)\{2\beta_0\beta_1(e^{-(\delta_0+\delta_1)} \sin(\phi_1 - \phi_0) - e^{-(\delta_0+\delta_{-1})} \sin(\phi_0 - \phi_{-1})) \\ & + 2\beta_1\beta_2(e^{-(\delta_1+\delta_2)} \sin(\phi_2 - \phi_1) - e^{-(\delta_{-1}+\delta_{-2})} \sin(\phi_{-1} - \phi_{-2}))\}] \end{aligned}$$

Now consider the situation where the sideband at $+\omega_m$ is tuned to a molecular resonance and the other sidebands are not. The $\delta_1 = \delta$ and $\phi_1 = \phi$, and $\delta_k = \phi_k = 0$ for $k \neq 1$. Then the signal becomes

$$\begin{aligned} S_{out} = & GI_0[\cos(\omega_m t)\{2\beta_0\beta_1(e^{-\delta} \cos \phi - 1) + 2\beta_1\beta_2(e^{-\delta} \cos \phi - 1)\} \\ & - \sin(\omega_m t)\{2\beta_0\beta_1(e^{-\delta} \sin \phi) - 2\beta_1\beta_2(e^{-\delta} \sin \phi)\}] \quad (B.5) \end{aligned}$$

Finally, in the limit of small absorption $\delta \ll 1$, and dispersion $\phi \ll 1$, we find

$$S_{out} \approx GI_0[2\delta(\beta_0\beta_1 + \beta_1\beta_2) \cos(\omega_m t) + 2\phi(\beta_0\beta_1 - \beta_1\beta_2) \sin(\omega_m t)] \quad (\text{B.6})$$

The absorptive part of the signal can be selected by adjusting the phase of the local oscillator to match that of the cosine term in the above expression before sending it to the mixer. A similar (but algebraically simpler) calculation can be performed for the situation where the modulation depth M is smaller, such that only first-order sidebands are present ($\beta_0 > \beta_1$, $\beta_1 \gg \beta_k$ for $k > 2$), with the result

$$S_{out, M \leq 1} = 2I_0 G \beta_0 \beta_1 [\delta \cos(\omega_m t) + \phi \sin(\omega_m t)] \quad (\text{B.7})$$

A Note on Saturation and Bleaching:

Because the FM signal depends linearly on the intensity of the probe beam, we were initially somewhat confused about how it should behave at high intensities $I \gg I_{sat}$, where bleaching would occur for a normal absorption measurement. The following calculation shows that the FM signal should go to a constant value in this limit; since the shot noise in the probe increases as $N \propto \sqrt{I}$, the expected S/N ratio decreases with increasing power.

We begin with the expression for the FM output signal given on the third line of equation B.4.

$$\begin{aligned} S = & GI_0[2\beta_0\beta_1(e^{-(\delta_0+\delta_1)} \cos[(\phi_0 - \phi_1) - \omega_m t] - e^{-(\delta_0+\delta_{-1})} \cos[(\phi_0 - \phi_{-1}) + \omega_m t]) \\ & + 2\beta_1\beta_2(e^{-(\delta_1+\delta_2)} \cos[(\phi_1 - \phi_2) - \omega_m t] - e^{-(\delta_{-1}+\delta_{-2})} \cos[(\phi_{-1} - \phi_{-2}) + \omega_m t])] \end{aligned} \quad (\text{B.8})$$

For clarity, we take $G = 1$, and assume that the modulation depth used is sufficiently small to require that only the fundamental and first order sidebands to be considered. Furthermore, we consider the typical situation in our experiments, where $\phi_k = 0$ for all k , and only the first-order sideband is resonant, $\delta_1 = \delta$, $\delta_0 = \delta_{-1} = 0$. After mixing with the local oscillator to select the in-phase component of the signal, the output is

$$S = 2I_{tot}\beta_0\beta_1(e^{-\delta} - 1) \quad (\text{B.9})$$

Here, we have written I_{tot} for the total intensity of the probe beam. Comparing with the original expression for the intensity of the probe after transmission through the molecules (equation B.3), one finds that first term above can be related to the interference between the fundamental and the 1st-order sideband (which undergoes absorption δ), and the second term to the interference between the fundamental and the (-1)st-order sideband (which is not absorbed). The relative negative sign between them arises from the fact that the sidebands at $+\omega_m$ and $-\omega_m$ are out of phase by π . It is instructive rewrite equation B.9 with this in mind, using the notation $E_k = \beta_k \sqrt{I_{tot}}$. (Note that the E_k are strictly positive; the phase between the sidebands is already accounted for in the relative minus sign.) This gives

$$S = 2(E_0E_1e^{-\delta} - E_0E_{-1}) \quad (\text{B.10})$$

Now, in the case of intensities exceeding the saturation intensity of the sample being probed, the form of the transmitted electric field amplitude in the first sideband must be modified: $E_1e^{-\delta} \rightarrow E_1^{trans} = \sqrt{I_1^{in} - I_{sat}(1 - e^{-2\delta})}$, where $I_1^{in} = \beta_1^2 I_{tot}$. Furthermore, making the substitutions $E_0 = \beta_0 \sqrt{I_{tot}}$ and $E_{-1} = \beta_{-1} \sqrt{I_{tot}}$, we obtain

$$S = 2[\beta_0 \sqrt{I_{tot}} \sqrt{I_1^{in} - I_{sat}(1 - e^{-2\delta})} - \beta_0\beta_1 I_{tot}] \quad (\text{B.11})$$

Finally, define $\alpha = \frac{I_{sat}}{I_1^{in}} = \frac{I_{sat}}{\beta_1^2 I_{tot}}$. Then we have

$$S = 2[\beta_0\beta_1 I_{tot}(\sqrt{1 - \alpha(1 - e^{-2\delta})} - 1)] \quad (\text{B.12})$$

Now, in the limit of deep saturation, $\alpha = \frac{I_{sat}}{\beta_1^2 I_{tot}} \ll 1$, and series expansion in α gives

$$\begin{aligned} S &\approx 2[\beta_0\beta_1 I_{tot}(1 - \frac{1}{2}\alpha(1 - e^{-2\delta}) - 1)] = \alpha\beta_0\beta_1 I_{tot}(e^{-2\delta} - 1) \\ &= \alpha \frac{\beta_0}{\beta_1} I_{sat}(e^{-2\delta} - 1) \end{aligned} \quad (\text{B.13})$$

Thus, in the limit $I_{tot} \gg I_{sat}$, the signal goes to a constant value.

Appendix C

Noise in FM Spectroscopy

As described in Section 2.3.2, we have consistently observed higher than expected noise levels in the FM spectroscopy setup used for probing the spatial characteristics of the molecular beam. Noise properties were measured by digitizing the output from the FM detection circuit (or directly from the amplified photodiode, Thorlabs model PDA10A) using a National Instruments PCI-6024E digital-to-analog converter (DAC). Signals were first passed through a pre-amp (SRS model SR560) with a 30 kHz low-pass filter and a gain setting between 10^2 and 10^4 . The DAC was set to digitize at 60 kHz, the minimum sampling rate required to prevent aliasing. (A higher sampling rate would admit noise outside the pass band of the filter, and is therefore undesirable.) The dark-current noise of the photodiode used for detection was measured (with the detector covered by a lens cap) to be $1.9 \times 10^{-10} \text{ W}/\sqrt{\text{Hz}}$, several times higher than the specified value of $5.5 \times 10^{-11} \text{ W}/\sqrt{\text{Hz}}$. When the 786 nm probe beam was directed onto the detector with sidebands applied (at 100 MHz modulation frequency and ~ 1.4 radians modulation depth) and the FM homodyne detection circuit switched on, the noise at low frequencies (at a $1/e$ bandwidth of about 300 - 500 Hz) typically increased by a factor of ~ 3 - 30 times above the detector noise. (As expected, no increase in noise was observed in the FM output signal for an illuminated diode with detection circuit switched off or with no sidebands applied to the laser.)

Figure C.1 shows the beam geometry used for probing molecules with FM spectroscopy. This setup, when properly aligned, gave the best noise performance observed, typically $\sim 7 \times 10^{-10} \text{ W}/\sqrt{\text{Hz}}$ at low frequencies ($\lesssim 500 \text{ Hz}$) for $\sim 3 \text{ mW}$ of laser power. Light was delivered from a diode

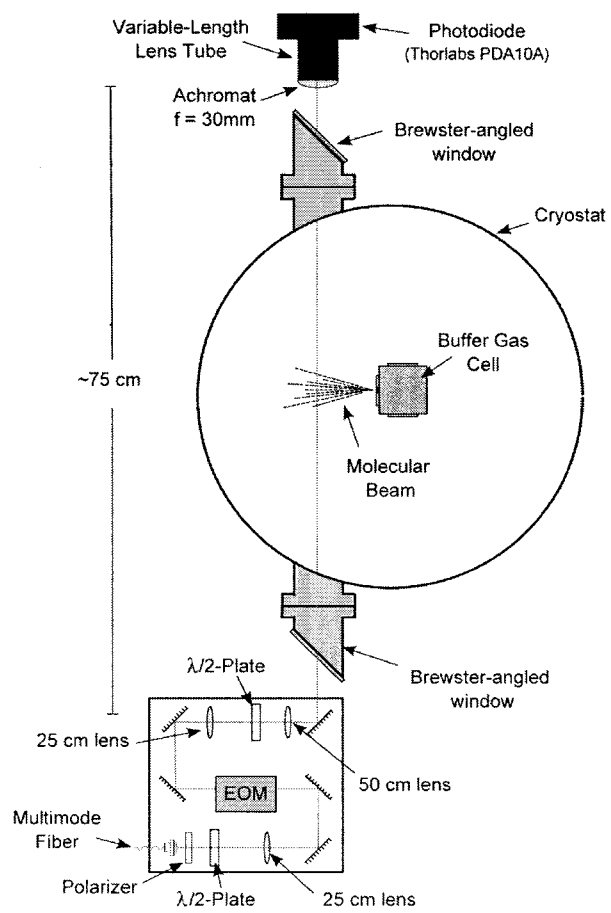


Figure C.1: Typical FM spectroscopy probe beam setup.

laser on the optical table¹ via a multi-mode fiber (Thorlabs M31L05, with Thorlabs CFC-11-B output coupler) to an optical breadboard that housed the EOM mounted next to the cryostat. A photograph of the EOM breadboard is displayed in Figure 2.3. The unpolarized output of the fiber was passed through a polarizer and half wave plate to align the optical polarization with the fast axis of the EOM crystal, then focussed through the EOM using a 1:1 telescope consisting of two lenses of focal length 25 cm. (This was sufficient to ensure that no clipping of the beam occurred at the apertures of the EOM case.) Another half wave plate was then used to align the outgoing polarization to minimize reflection from the two Brewster-angled windows by which the beam entered and exited the cryostat. An additional 50 cm lens (not shown in Figure 2.3) was sometimes introduced to improve the collimation of the outgoing light. The optical beam diameter in the plane intersecting the molecules was visually estimated to be on the order of ~2 - 3 mm, consistent with the nominal waist diameter of the fiber output coupler, although this was not measured quantitatively with a camera for the original SrO beam apparatus. Finally, the beam was tightly focussed onto the 0.8 mm² area of the detector using an achromatic doublet of 30 mm focal length mounted in an length-adjustable lens tube. Both the EOM breadboard and the detector were mounted on horizontal and vertical translation stages to allow for spatial distribution of the molecules to be probed.

Mechanical vibrations leading to small variations in the length of the beam path through the EOM crystal and/or clipping at the EOM input aperture were investigated as one possible source of increased noise; in particular, the fiber output coupler used to deliver light to the breadboard was known to be mechanically unstable and caused problems at times. (This was improved in the SrF beam setup by upgrading to a Thorlabs PAF-type collimator.) Moving the EOM to the optical table and delivering light to the cryostat by a single-mode, polarization-maintaining (PM) fiber (Thorlabs P3-780PM-FC5) did not improve the noise performance beyond the best levels observed with the setup in Figure C.1, however, and had the disadvantages of requiring more careful alignment at the fiber input port and reducing the total optical power that could be delivered to the experiment. It was also observed that maintaining low noise levels required careful alignment of the optical

¹Lasers used for FM spectroscopy included a distributed feedback (DFB) diode laser at 786 nm (Eagleyard Photonics EYP-DFB-0785-00150-1500-SOT02-0000), for probing the SrO X-A transition; an ECD in the Littman-Metcalf configuration (Sacher Lasertechnik TEC500) at 859 nm for probing the X-A transition in BaF; and a Littrow ECD (home-built) at 406 nm for probing the X-B transition in SrO. The EOM used in the first two cases had an anti-reflection coating designed for operating at red wavelengths (Thorlabs model EO-PM-R-C1); in the latter case a blue-wavelength AR-coated EOM was used (Thorlabs model EO-PM-R-C4). A home-built Littrow ECD at 663 nm was also used for FM spectroscopy of SrF (using the X-A transition) with the newer beam apparatus described in Section 4.3, using a setup very similar to that of Figure C.1

polarization relative to the EOM crystal axis², as any orthogonal polarization component does not undergo phase modulation and results in fluctuations in the power of the fundamental compared to the sidebands. Again, however, it was found that delivery of light to the EOM optics from the laser by PM-fiber did not improve significantly upon the setup shown, and resulted in a reduction of the available optical power. Finally, the polarization of the probe beam passing through the Brewster-angled windows was seen to have a small but noticeable effect on noise performance, presumably due to vibration-induced time-varying etalon effects in the cryostat windows if the beam was not perfectly p-polarized.

Assuming the correct polarization alignment, the parameter that had the greatest effect on the observed FM noise spectrum was the spatial alignment of the probe beam into the detector. Minor tweaking of the angle and/or position at which the probe impinged on the lens focussing onto the diode could change noise levels by as much as an order of magnitude. (As might be expected, the best performance was generally obtained with the beam impinging on the center of the lens and approximately normal to its surface.) It is not clear why this should be the case, unless there was some slight spatial separation of the various frequency components of the probe exiting the EOM that caused amplitude modulation at the 100 MHz beat frequency if the spot clipped the edge of the detector. This would be somewhat surprising, however, given that the expected minimum spot size after focussing the collimated ~ 3 mm diameter beam with a lens of 30 mm focal length is on the order of tens of μm , much smaller than the detector size, even allowing for misalignment and aberrations. In retrospect, it might have been interesting to test this hypothesis by eliminating the $\sim 75\text{cm}$ propagation length through the cryostat and sending the FM beam directly into the detector after exiting the EOM; this has not yet been attempted, however.

²This alignment can be performed by monitoring the EOM output on a scanning optical cavity and rotating the input polarization to maximize the sideband amplitude.

Appendix D

Electric Field in the Microwave Cavity

Following Jackson [121], the Q of the cavity can be written as

$$Q = 2\pi f \frac{U}{W_L} = 2\pi f \frac{\frac{\epsilon_0}{2} \int_V |E|^2 dV}{P_{in}} \quad (\text{D.1})$$

where U is the energy stored in the cavity and W_L is the rate of energy loss, which must equal P_{in} . The integral is over the volume of the cavity mode. Now, let's write down the amplitude of a $TEM_{0,0}$ Gaussian mode, normalized such that the peak field in the plane of the beam waist is E_0 :

$$E(r, z) = E_0 \frac{w_0}{w(z)} \exp\left(\frac{-r^2}{w(z)^2}\right) \sin\left(\frac{\pi q z}{L}\right) \quad (\text{D.2})$$

Here, the beam diameter in any given z-plane is given by $w(z) = w_0 \left[1 + \left(\frac{\lambda z}{\pi w_0^2}\right)^2\right]^{1/2}$, and $q = 2L/\lambda$ is the longitudinal mode number. ¹ Making the small approximation that the radial part goes to infinity (instead of the radius of the mirrors), the integral can be evaluated as follows:

¹Note that the expression for the field distribution in equation D.2 neglects the Gouy phase shift factor $\sin[\arctan\left(\frac{\lambda z}{\pi w_0^2}\right)]$. Numerical integration for our cavity parameters with this factor included changes the answer for the peak field by less than 1%.

$$\begin{aligned}
\int_V |E|^2 dV &= E_0^2 \int_0^L \left(\frac{w_0}{w(z)} \right)^2 \sin^2 \left(\frac{\pi qz}{L} \right) \left[\int_0^\infty r \exp \left[\frac{-2r^2}{w(z)^2} \right] dr \int_0^{2\pi} d\phi \right] dz \\
&= E_0^2 \int_0^L \left(\frac{w_0}{w(z)^2} \right)^2 \sin^2 \left(\frac{\pi qz}{L} \right) \left[\left(\frac{w(z)^2}{4} \right) 2\pi \right] dz \\
&= \frac{\pi}{4} E_0^2 w_0^2 L
\end{aligned} \tag{D.3}$$

Substituting back into (D.1):

$$Q = 2\pi f \frac{\frac{\epsilon_0}{2} \left[\frac{\pi}{4} E_0^2 w_0^2 L \right]}{P_{in}} \tag{D.4}$$

And solving for E_0 :

$$E_0 = \left[\frac{4QP_{in}}{\pi^2 f \epsilon_0 w_0^2 L} \right]^{1/2} \tag{D.5}$$

Finally, substituting the appropriate values for our cavity geometry and 2 kW of input power gives

$$E_0 = \left[\frac{2(4.5 \times 10^4)(4 \times 10^3 W)}{\pi^2 (18.1 \times 10^9 s^{-1})(8.85 \times 10^{-12} \frac{C^2}{Vm})(0.0305m)^2 (0.165m)} \right]^{1/2} = 12.2 kV/cm \tag{D.6}$$

Appendix E

Aperture Array Transmission

In order to estimate the scaling of the coupling through the microwave cavity input mirror, we will calculate the transmission of a plane wave through an infinite conducting screen, perforated with a regular (square) array of subwavelength apertures. The radius of each aperture is a , and the area density of apertures over the surface of the screen is $1/A$. We begin with a plane wave, $\vec{E} = E_0 e^{i(kz + \omega t)} \hat{x}$ impinging on the screen from $-\hat{z}$. Its associated magnetic field is $\vec{H} = \frac{E_0}{\eta_0} e^{i(kz + \omega t)} \hat{y}$, and its intensity is $I = \frac{c\epsilon_0}{2} |E_0|^2$. (Here, $\eta_0 = (c\epsilon_0)^{-1} \approx 377\Omega$ is the impedance of free space.)

According to Bethe [120], each hole in the screen will radiate as a magnetic dipole with moment $m_{eff} = \frac{8a^3}{3} \vec{H}_0$. (Also see Jackson [121], pg. 424.) Now we want to sum the radiation from the dipoles on the other side of the screen. Set up a coordinate system with the origin a distance L away from the screen. The transformation to cartesian coordinates for the location of any given hole relative to the test point P are as follows:

$$\begin{aligned} x &= R \cos \phi \sin \theta & x &= L \cos \phi \tan \theta \\ y &= R \sin \phi \sin \theta & y &= L \sin \phi \tan \theta \\ z &= L = R \cos \theta & R &= L \sec \theta \end{aligned} \tag{E.1}$$

From Jackson (pg. 411), the far-field patterns for an *electric* dipole are:

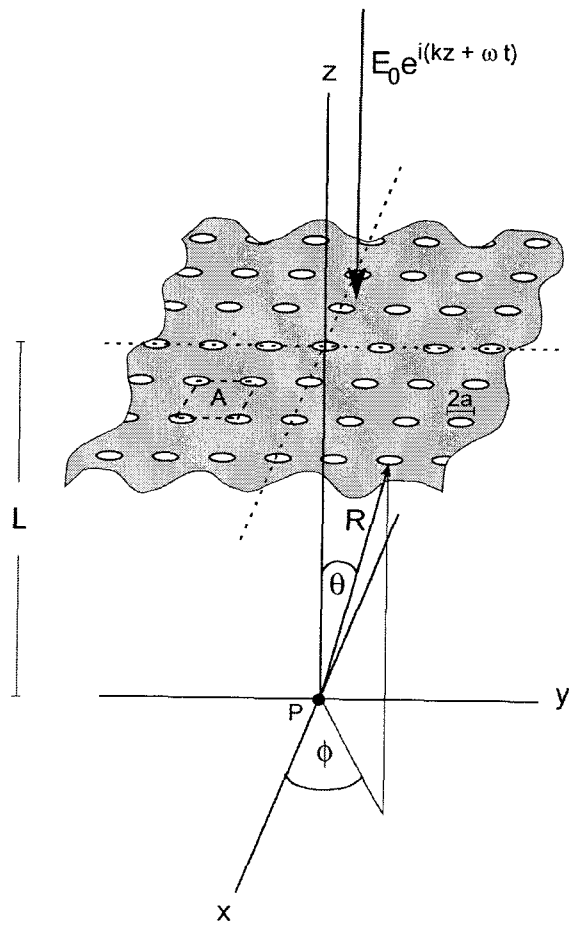


Figure E.1: Aperture array geometry.

$$\vec{H} = \frac{ck^2}{4\pi} (\hat{n} \times \vec{p}) \frac{e^{ikr}}{r}; \quad \vec{E} = \eta_0 \vec{H} \times \hat{n} \quad (\text{E.2})$$

Then, for a *magnetic* dipole, they must be:

$$\vec{E} = -\eta_0 \frac{ck^2}{4\pi} \left(\hat{n} \times \frac{\vec{m}}{c} \right) \frac{e^{ikr}}{r}; \quad \vec{H} = \frac{\vec{E}}{\eta_0} \times \hat{n} \quad (\text{E.3})$$

For our case, the excited magnetic dipoles must be in the \hat{y} -direction, $\vec{m} = m\hat{y}$. Thus, for the dipole located at (R, θ, ϕ) , we have $\vec{E} = -\eta_0 \frac{k^2 m}{4\pi} \frac{e^{ikR}}{R} (\hat{n} \times \hat{y})$.

$$\text{Now, } \hat{n} = \frac{\{-x, -y, L\}}{R} \Rightarrow \hat{n} \times \hat{y} = \frac{1}{R} \begin{vmatrix} \hat{x} & \hat{y} & \hat{z} \\ -x & -y & L \\ 0 & 1 & 0 \end{vmatrix} = \left\{ \frac{-L}{R}, 0, \frac{-x}{R} \right\} = \{-\cos \theta, 0, \cos \phi \sin \theta\}.$$

Hence, the dipole at (R, θ, ϕ) contributes $\vec{E} = -\eta_0 \frac{k^2 m}{4\pi} \frac{e^{ikR}}{R} \left(-\frac{L}{R} \hat{x} - \frac{x}{R} \hat{z} \right)$.

Recall that the array extends out infinitely in x and y , and has a dipole density of $1/A$. Then, the total electric field at the test point P will be:

$$\begin{aligned} \vec{E}_{tot} &= \eta_0 \frac{k^2 m}{4\pi} \frac{1}{A} \int_0^{\pi/2} d\theta \int_{-\pi}^{\pi} d\phi R^2 \sin \theta \frac{e^{ikR}}{R} (-\cos \theta \hat{x} - \cos \phi \sin \theta \hat{z}) \\ &= \frac{-\eta_0 \left(\frac{2\pi}{\lambda} \right)^2 m}{4\pi} \frac{1}{A} 2\pi \int_0^{\pi/2} d\theta R^2 \sin \theta \frac{e^{ikR}}{R} \left(-\frac{L}{R} \hat{x} \right) \\ &= \frac{\eta_0 m 2\pi^2 L}{\lambda^2 A} \int_0^{\pi/2} d\theta \sin \theta e^{ikL \sec \theta} \hat{x} \end{aligned} \quad (\text{E.4})$$

Integrating by the method of stationary phase gives $\int_0^{\pi/2} d\theta \sin \theta e^{i\alpha \sec \theta} \approx \frac{1}{\alpha} [\cos(\alpha + \pi/2) + i \cos \alpha]$, for $\alpha \gg 1$. Thus, far from the screen, (where $kL \gg 1$), we have

$$\begin{aligned} \vec{E}_{tot} &\approx \frac{2\pi^2 \eta_0 m}{\lambda^2 A} L \frac{1}{kL} [-\sin(kL) + i \cos(kL)] \hat{x} \\ &= \frac{\pi \eta_0 m}{\lambda A} [-\sin(kL) + i \cos(kL)] \hat{x} \end{aligned} \quad (\text{E.5})$$

The outgoing intensity is then $I_{out} = \frac{c\epsilon_0}{2} |E_{tot}^{\rightarrow}|^2 = \frac{c\epsilon_0}{2} \frac{\pi^2 \eta_0^2 m^2}{\lambda^2 A^2}$.

Assuming the dipoles are uncoupled (for A sufficiently large), we have from Bethe [120] that $m = \frac{8a^3}{3} H_0 = \frac{8a^3}{3} \frac{E_0}{\eta_0}$. Thus,

$$I_{out} = \frac{c\epsilon_0}{2} \frac{\pi^2 \eta_0^2}{\lambda^2 A^2} \left(\frac{8a^3}{3} \frac{E_0}{\eta_0} \right)^2 = \frac{c\epsilon_0}{2} \left(\frac{8\pi a^3 E_0}{3\lambda A} \right)^2 \quad (\text{E.6})$$

Finally, the transmission coefficient is given by

$$\alpha_{trans} = \frac{I_{out}}{I_{in}} = \frac{\frac{c\epsilon_0}{2} \left(\frac{8\pi a^3 E_0}{3\lambda A} \right)^2}{\frac{c\epsilon_0}{2} E_0^2} = \left(\frac{8\pi a^3}{3\lambda A} \right)^2 \quad (\text{E.7})$$

Bibliography

- [1] Metcalf, H. J. & van der Straten, P. *Laser Cooling and Trapping* (Springer, New York, USA, 1999).
- [2] Ye, J. & Cundiff, S. T. (eds.) *Femtosecond Optical Frequency Comb Technology: Principle, Operation and Application* (Springer, New York, 2004).
- [3] Boyd, M. M. *et al.* [sup 87]sr lattice clock with inaccuracy below 10[sup -15]. *Physical Review Letters* **98**, 083002 (2007).
- [4] Oskay, W. H. *et al.* Single-atom optical clock with high accuracy. *Physical Review Letters* **97**, 020801 (2006).
- [5] Shor, P. W. Polynomial-time algorithms for prime factorization and discrete logarithms on a quantum computer. *SIAM J. Comput.* **26**, 1484–1509 (1997).
- [6] Blatt, R. & Wineland, D. Entangled states of trapped atomic ions. *Nature* **453**, 1008–1015 (2008).
- [7] Hffner, H., Roos, C. & Blatt, R. Quantum computing with trapped ions. *Physics Reports* **469**, 155 – 203 (2008).
- [8] Isenhower, L. *et al.* Demonstration of a neutral atom controlled-NOT quantum gate. *ArXiv e-prints* (2009). 0907.5552.
- [9] Nelson, K. D., Li, X. & Weiss, D. S. Imaging single atoms in a three-dimensional array. *Nature Physics* **3**, 556–560 (2007).
- [10] Regan, B. C., Commins, E. D., Schmidt, C. J. & DeMille, D. New limit on the electron electric dipole moment. *Phys. Rev. Lett.* **88**, 071805 (2002).

- [11] Wood, C. S. *et al.* Measurement of Parity Nonconservation and an Anapole Moment in Cesium. *Science* **275**, 1759–1763 (1997).
- [12] Dimopoulos, S., Graham, P. W., Hogan, J. M. & Kasevich, M. A. Testing general relativity with atom interferometry. *Physical Review Letters* **98**, 111102 (2007).
- [13] Doyle, J., Friedrich, B., Krems, R. V. & Masnou-Seeuws, F. Editorial: Quo vadis, cold molecules? *European Physical Journal D* **31**, 149–164 (2004). arXiv:physics/0505201.
- [14] D. DeMille, D. G. & Petricka, J. Microwave traps for cold polar molecules. *The European Physical Journal D* **31**, 375–384 (2004).
- [15] Ertmer, W., Blatt, R., Hall, J. L. & Zhu, M. Laser manipulation of atomic beam velocities: Demonstration of stopped atoms and velocity reversal. *Phys. Rev. Lett.* **54**, 996–999 (1985).
- [16] Phillips, W. D. & Metcalf, H. Laser deceleration of an atomic beam. *Phys. Rev. Lett.* **48**, 596–599 (1982).
- [17] Chu, S., Hollberg, L., Bjorkholm, J. E., Cable, A. & Ashkin, A. Three-dimensional viscous confinement and cooling of atoms by resonance radiation pressure. *Phys. Rev. Lett.* **55**, 48–51 (1985).
- [18] Raab, E. L., Prentiss, M., Cable, A., Chu, S. & Pritchard, D. E. Trapping of neutral sodium atoms with radiation pressure. *Phys. Rev. Lett.* **59**, 2631–2634 (1987).
- [19] Ketterle, W. & van Druten, N. Evaporative Cooling of Trapped Atoms. In Bederson, B. & Walther, H. (eds.) *Advances in Atomic, Molecular, and Optical Physics*, vol. 37, 181–236 (1996).
- [20] Anderson, M. H., Ensher, J. R., Matthews, M. R., Wieman, C. E. & Cornell, E. A. Observation of Bose-Einstein Condensation in a Dilute Atomic Vapor. *Science* **269**, 198–201 (1995).
- [21] DeMarco, B. & Jin, D. S. Onset of Fermi Degeneracy in a Trapped Atomic Gas. *Science* **285**, 1703–1706 (1999).
- [22] Greiner, M., Mandel, O., Esslinger, T., Hänsch, T. W. & Bloch, I. Quantum phase transition from a superfluid to a mott insulator in a gas of ultracold atoms. *Nature* **415**, 39–44 (2002).
- [23] Bahns, J. T., Stwalley, W. C. & Gould, P. L. Laser cooling of molecules: A sequential scheme for rotation, translation, and vibration. *The Journal of Chemical Physics* **104**, 9689–9697 (1996).

- [24] Di Rosa, M. D. Laser-cooling molecules. *The European Physical Journal D - Atomic, Molecular, Optical and Plasma Physics* **31**, 395–402 (2004).
- [25] Viteau, M. *et al.* Optical Pumping and Vibrational Cooling of Molecules. *Science* **321**, 232–234 (2008).
- [26] Bohn, J. L. Inelastic collisions of ultracold polar molecules. *Phys. Rev. A* **63**, 052714 (2001).
- [27] Friedrich, B. & Doyle, J. Why are cold molecules so hot? *ChemPhysChem* **10**, 604–623 (2009).
- [28] Decarvalho, R. *et al.* Buffer-gas loaded magnetic traps for atoms and molecules: A primer. *European Physical Journal D* **7**, 289–309 (1999).
- [29] Bethlem, H. L., Berden, G. & Meijer, G. Decelerating neutral dipolar molecules. *Phys. Rev. Lett.* **83**, 1558–1561 (1999).
- [30] Motsch, M. *et al.* Collisional effects in the formation of cold guided beams of polar molecules. *New Journal of Physics* **11**, 055030–+ (2009). 0812.2850.
- [31] Campbell, W. C., Tsikata, E., Lu, H.-I., van Buuren, L. D. & Doyle, J. M. Magnetic trapping and zeeman relaxation of NH ($X^3\Sigma^-$). *Physical Review Letters* **98**, 213001 (2007).
- [32] Patterson, D., Rasmussen, J. & Doyle, J. M. Intense atomic and molecular beams via neon buffer-gas cooling. *New Journal of Physics* **11**, 055018+ (2009).
- [33] Hudson, E. R. *Experiments on Cold Molecules Produced via Stark Deceleration*. Ph.D. thesis, University of Colorado (2006).
- [34] Bethlem, H. L. *et al.* Alternating gradient focusing and deceleration of polar molecules. *Journal of Physics B: Atomic, Molecular and Optical Physics* **39**, R263–R291 (2006).
- [35] Rangwala, S. A., Junglen, T., Rieger, T., Pinkse, P. W. H. & Rempe, G. Continuous source of translationally cold dipolar molecules. *Phys. Rev. A* **67**, 043406 (2003).
- [36] van Buuren, L. D. *et al.* Electrostatic extraction of cold molecules from a cryogenic reservoir. *Physical Review Letters* **102**, 033001 (2009).
- [37] Kerman, A. J., Sage, J. M., Sainis, S., Bergeman, T. & DeMille, D. Production of ultracold, polar RbCs* molecules via photoassociation. *Phys. Rev. Lett.* **92**, 033004 (2004).

- [38] Ferlaino, F., Knoop, S. & Grimm, R. Ultracold feshbach molecules (2008).
- [39] Sage, J. M., Sainis, S., Bergeman, T. & DeMille, D. Optical production of ultracold polar molecules. *Phys. Rev. Lett.* **94**, 203001 (2005).
- [40] Ni, K.-K. *et al.* A High Phase-Space-Density Gas of Polar Molecules. *Science* **322**, 231–235 (2008).
- [41] Carr, L. D., DeMille, D., Krems, R. V. & Ye, J. Cold and ultracold molecules: science, technology and applications. *New Journal of Physics* **11**, 055049–+ (2009). 0904.3175.
- [42] Bloch, I. Exploring quantum matter with ultracold atoms in optical lattices. *Journal of Physics B Atomic Molecular Physics* **38**, 629–+ (2005).
- [43] Griesmaier, A., Werner, J., Hensler, S., Stuhler, J. & Pfau, T. Bose-einstein condensation of chromium. *Phys. Rev. Lett.* **94**, 160401 (2005).
- [44] Lahaye, T. *et al.* Strong dipolar effects in a quantum ferrofluid. *Nature* **448**, 672–675 (2007).
- [45] Góral, K., Santos, L. & Lewenstein, M. Quantum phases of dipolar bosons in optical lattices. *Phys. Rev. Lett.* **88**, 170406 (2002).
- [46] Menotti, C., Trefzger, C. & Lewenstein, M. Metastable states of a gas of dipolar bosons in a 2d optical lattice. *Physical Review Letters* **98**, 235301 (2007).
- [47] Capogrosso-Sansone, B., Trefzger, C., Lewenstein, M., Zoller, P. & Pupillo, G. Quantum Phases of Cold Polar Molecules in 2D Optical Lattices. *ArXiv e-prints* (2009). 0906.2009.
- [48] Barnett, R., Petrov, D., Lukin, M. & Demler, E. Quantum magnetism with multicomponent dipolar molecules in an optical lattice. *Physical Review Letters* **96**, 190401 (2006).
- [49] Büchler, H. P. *et al.* Strongly correlated 2d quantum phases with cold polar molecules: Controlling the shape of the interaction potential. *Physical Review Letters* **98**, 060404 (2007).
- [50] Rezayi, E. H., Read, N. & Cooper, N. R. Incompressible liquid state of rapidly rotating bosons at filling factor $3/2$. *Phys. Rev. Lett.* **95**, 160404 (2005).
- [51] Nielsen, M. A. & Chuang, I. L. *Quantum Computation and Quantum Information* (Cambridge University Press, New York, USA, 2000).

- [52] DeMille, D. Quantum computation with trapped polar molecules. *Phys. Rev. Lett.* **88**, 067901 (2002).
- [53] André, A. *et al.* A coherent all-electrical interface between polar molecules and mesoscopic superconducting resonators. *Nature Physics* **2**, 636–642 (2006).
- [54] Rabl, P. *et al.* Hybrid quantum processors: Molecular ensembles as quantum memory for solid state circuits. *Physical Review Letters* **97**, 033003 (2006).
- [55] DeMille, D. *et al.* Investigation of pbo as a system for measuring the electric dipole moment of the electron. *Phys. Rev. A* **61**, 052507 (2000).
- [56] Sauer, B. E., Ashworth, H. T., Hudson, J. J., Tarbutt, M. R. & Hinds, E. A. Probing the Electron EDM with Cold Molecules. In Roos, C., Haffner, H. & Blatt, R. (eds.) *Atomic Physics 20*, vol. 869 of *American Institute of Physics Conference Series*, 44–51 (2006).
- [57] Vutha, A. C. *et al.* Search for the electric dipole moment of the electron with thorium monoxide. *ArXiv e-prints* (2009). [0908.2412](https://arxiv.org/abs/0908.2412).
- [58] DeMille, D., Cahn, S. B., Murphree, D., Rahmlow, D. A. & Kozlov, M. G. Using molecules to measure nuclear spin-dependent parity violation. *Physical Review Letters* **100**, 023003 (2008).
- [59] DeMille, D. *et al.* Enhanced sensitivity to variation of m_e/m_p in molecular spectra. *Physical Review Letters* **100**, 043202 (2008).
- [60] Zelevinsky, T., Kotochigova, S. & Ye, J. Precision test of mass-ratio variations with lattice-confined ultracold molecules. *Physical Review Letters* **100**, 043201 (2008).
- [61] Sawyer, B. C., Stuhl, B. K., Wang, D., Yeo, M. & Ye, J. Molecular beam collisions with a magnetically trapped target. *Physical Review Letters* **101**, 203203 (2008).
- [62] Krems, R. V. Cold controlled chemistry. *Phys. Chem. Chem. Phys.* **10**, 4079–4092 (2008).
- [63] Bodo, E., Gianturco, F. A., Balakrishnan, N. & Dalgarno, A. Chemical reactions in the limit of zero kinetic energy: virtual states and ramsauer minima in $F + H_2 \rightarrow HF + H$. *Journal of Physics B: Atomic, Molecular and Optical Physics* **37**, 3641–3648 (2004).
- [64] Ticknor, C. & Bohn, J. L. Influence of magnetic fields on cold collisions of polar molecules. *Phys. Rev. A* **71**, 022709 (2005).

- [65] Avdeenkov, A. V. & Bohn, J. L. Linking ultracold polar molecules. *Phys. Rev. Lett.* **90**, 043006 (2003).
- [66] van Veldhoven, J., Bethlem, H. L. & Meijer, G. ac electric trap for ground-state molecules. *Phys. Rev. Lett.* **94**, 083001 (2005).
- [67] Weinstein, J. D., DeCarvalho, R., Guillet, T., Friedrich, B. & Doyle, J. M. Magnetic trapping of calcium monohydride molecules at millikelvin temperatures. *Nature* **395**, 148–150 (1998).
- [68] Egorov, D. *et al.* Buffer-gas cooling of NH via the beam loaded buffer-gas method. *The European Physical Journal D - Atomic, Molecular and Optical Physics* **31**, 307–311(5) (November 2004).
- [69] Petricka, J. A. *A New Cold Molecule Source: The Buffer Gas Cooled Molecular Beam*. Ph.D. thesis, Yale University (2008).
- [70] Campbell, W. C. *Magnetic Trapping of Imidogen Molecules*. Ph.D. thesis, Harvard University (2008).
- [71] Scoles, G. (ed.) *Atomic and Molecular Beam Methods* (Oxford University Press, New York, USA, 1988).
- [72] Hasted, J. *Physics of Atomic Collisions* (Elsevier Publishing Company, New York, USA, 1972), 2nd edn.
- [73] Lafferty, J. (ed.) *Foundations of Vacuum Science and Technology* (John Wiley & Sons, Inc., New York, USA, 1998).
- [74] Patterson, D. & Doyle, J. M. Bright, guided molecular beam with hydrodynamic enhancement. *The Journal of Chemical Physics* **126**, 154307–+ (2007).
- [75] Kerr, J. Strengths of chemical bonds. In *CRC Handbook of Chemistry and Physics* (CRC Press, 1996), 77 edn.
- [76] Luo, Y.-R. *Comprehensive Handbook of Chemical Bond Energies* (CRC Press, New York, 2007).
- [77] Basuchlicher, C. W., Partridge, H., Sodupe, M. & Langhoff, S. R. Theoretical study of the alkaline-earth metal superoxides BeO₂ through SrO₂. *J. Phys. Chem.* **96**, 9259–9264 (1992).
- [78] Darwent, B. Bond dissociation energies in simple molecules. Tech. Rep. (1970).

- [79] Weinstein, J. D. *et al.* Spectroscopy of buffer-gas cooled vanadium monoxide in a magnetic trapping field. *The Journal of Chemical Physics* **109**, 2656–2661 (1998).
- [80] Ekin, J. W. *Experimental Techniques for Low-Temperature Measurements* (Oxford University Press, New York, USA, 2006).
- [81] Sedgley, D., Tobin, A., Batzer, T. & Call, W. Characterization of charcoals for helium cryopumping in fusion devices. *Journal of Vacuum Science and Technology A: Vacuum, Surfaces, and Films* **5**, 2572–2576 (1987).
- [82] Demtroder, W. *Laser Spectroscopy* (Springer, Berlin, 1998).
- [83] Bjorklund, G. C. Frequency-modulation spectroscopy: a new method for measuring weak absorptions and dispersions. *Opt. Lett.* **5**, 15–17 (1980).
- [84] Budker, D., Kimball, D. F. & DeMille, D. P. *Atomic Physics: an exploration through problems and solutions* (Oxford University Press, New York, USA, 2004).
- [85] Li, H., Skelton, R., Focsa, C., Pinchemel, B. & Bernath, P. F. Fourier transform spectroscopy of chemiluminescence from the sro $A^1\Sigma^+ - X^1\Sigma^+$ transition. *Journal of Molecular Spectroscopy* **203**, 188 – 195 (2000).
- [86] Maxwell, S. E. *et al.* High-flux beam source for cold, slow atoms or molecules. *Phys. Rev. Lett.* **95**, 173201 (2005).
- [87] Gurevich, L., Petrovsky, V. & Pustovoit, A. Helium Cryopumping. *Plasma Devices and Operations* **1**, 97–102 (1990).
- [88] Omelyan, I. P., Mryglod, I. M. & Folk, R. Optimized forest-ruth- and suzuki-like algorithms for integration of motion in many-body systems. *Computer Physics Communications* **146**, 188 – 202 (2002).
- [89] Chu, S., Bjorkholm, J. E., Ashkin, A. & Cable, A. Experimental observation of optically trapped atoms. *Phys. Rev. Lett.* **57**, 314–317 (1986).
- [90] Barrett, M. D., Sauer, J. A. & Chapman, M. S. All-optical formation of an atomic bose-einstein condensate. *Phys. Rev. Lett.* **87**, 010404 (2001).

- [91] Tino Weber, M. M. H.-C. N., Jens Herbig & Grimm, R. Bose-einstein condensation of cesium. *Science* **299**, 232–235 (2003).
- [92] Bohn, J. L., Cavagnero, M. & Ticknor, C. Quasi-universal dipolar scattering in cold and ultracold gases. *New Journal of Physics* **11**, 055039 (18pp) (2009).
- [93] Kajita, M. Collisions between electrostatically confined linear polar molecules. *The European Physical Journal D* **20**, 55–59 (2002).
- [94] Amini, J. M. & Gould, H. High precision measurement of the static dipole polarizability of cesium. *Phys. Rev. Lett.* **91**, 153001 (2003).
- [95] Raimond, J. M., Brune, M. & Haroche, S. Manipulating quantum entanglement with atoms and photons in a cavity. *Rev. Mod. Phys.* **73**, 565–582 (2001).
- [96] Balshaw, N. *Practical Cryogenics: An introduction to laboratory cryogenics.* Oxford Instruments (UK) Ltd. (1996).
- [97] Siegman, A. E. *Lasers* (University Science Books, New Jersey, USA, 1986).
- [98] Yariv, A. *Quantum Electronics, 3rd ed.* (John Wiley and Sons, New York, USA, 1989).
- [99] Goldsmith, P. F. *Quasioptical Systems: Gaussian Beam Quasioptical Propagation and Applications* (IEEE Press, California, USA, 1998).
- [100] Fox, A. G. & Li, T. Resonant Modes in a Maser Interferometer. In Singer, J. R. (ed.) *Advances in Quantum Electronics*, 308 (1961).
- [101] Boyd, G. & Gordon, J. Confocal Multimode Resonator for Millimeter Through Optical Wavelength Masers. *Bell Systems Technical Journal* **40**, 489–508 (1961).
- [102] C. Cohen-Tannoudji, G. G., J. Dupont-Roc. *Atom Photon Interactions: Basic Processes and Applications* (John Wiley and Sons, New York, USA, 1992).
- [103] Zener, C. Non-Adiabatic Crossing of Energy Levels. *Royal Society of London Proceedings Series A* **137**, 696–702 (1932).
- [104] Joyce, W. B. & DeLoach, B. C. Millimetre-wave gaussian beam-mode optics and corrugated feed horns. *Appl. Opt.* **23**, 4187–4196 (1984).

- [105] Leurf, J. *Millimetre-Wave Optics, Devices and Systems* (Taylor and Francis, New York, 1990).
- [106] Degnan, J. J. The waveguide laser: A review. *Applied Physics* **11**, 1–33 (1976).
- [107] Wylde, R. J. Alignment of gaussian beams. *IEE Proceedings* **23**, 258–262 (1984).
- [108] Geyer, R. & Krupka, J. Microwave dielectric properties of anisotropic materials at cryogenic temperatures. *Instrumentation and Measurement, IEEE Transactions on* **44**, 329–331 (1995).
- [109] Murphy, J. A. Distortion of a simple Gaussian beam on reflection from off-axis ellipsoidal mirrors. *International Journal of Infrared and Millimeter Waves* **8**, 1165–1187 (1987).
- [110] Raguin, D. H. & Morris, G. M. Analysis of antireflection-structured surfaces with continuous one-dimensional surface profiles. *Appl. Opt.* **32**, 2582–2598 (1993).
- [111] van Vliet, A. H. F. & de Graauw, T. Quarter wave plates for submillimeter wavelengths. *International Journal of Infrared and Millimeter Waves* **2**, 465–477 (1981).
- [112] Grachev, L. P., Esakov, I. I., Malyk, S. G. & Khodataev, K. V. Two-Mirror Resonator for Studying High-Pressure Electrodeless Microwave Discharge. *Journal of Technical Physics* **46**, 709–717 (2001).
- [113] Slater, J. C. *Microwave Transmission* (McGraw-Hill, New York, USA, 1942).
- [114] Weinstein, L. *Open Resonators and Open Waveguides* (Golem Press, Boulder, Colorado, 1969).
- [115] Tsuji, M., Shigesawa, H. & Takiyama, K. Eigenvalues of a nonconfocal laser resonator with an output-coupling aperture. *Appl. Opt.* **18**, 1334–1340 (1979).
- [116] Levy, R. Improved single and multiaperature waveguide coupling theory, including explanation of mutual interactions. *Microwave Theory and Techniques, IEEE Transactions on* **28**, 331–338 (1980).
- [117] McDonald, N. Electric and magnetic coupling through small apertures in shield walls of any thickness. *Microwave Theory and Techniques, IEEE Transactions on* **20**, 689–695 (1972).
- [118] Becker, G. E. & Autler, S. H. Water vapor absorption of electromagnetic radiation in the centimeter wave-length range. *Phys. Rev.* **70**, 300–307 (1946).
- [119] Marcuvitz, N. (ed.) *Waveguide Handbook* (McGraw-Hill, New York, 1951).

- [120] Bethe, H. A. Theory of diffraction by small holes. *Phys. Rev.* **66**, 163–182 (1944).
- [121] Jackson, J. D. *Classical Electrodynamics, 3rd ed.* (John Wiley and Sons, New York, USA, 1999).
- [122] Eggimann, W. & Collin, R. Dynamic interaction fields in a two-dimensional lattice. *Microwave Theory and Techniques, IRE Transactions on* **9**, 110–115 (1961).
- [123] Chen, C.-C. Transmission through a conducting screen perforated periodically with apertures. *Microwave Theory and Techniques, IEEE Transactions on* **18**, 627–632 (1970).
- [124] Chen, C.-C. Diffraction of electromagnetic waves by a conducting screen perforated periodically with holes. *Microwave Theory and Techniques, IEEE Transactions on* **19**, 475–481 (1971).
- [125] Chen, C.-C. Transmission of microwave through perforated flat plates of finite thickness. *Microwave Theory and Techniques, IEEE Transactions on* **21**, 1–6 (1973).
- [126] Mittra, R., Chan, C. & Cwik, T. Techniques for analyzing frequency selective surfaces—a review. *Proceedings of the IEEE* **76**, 1593–1615 (1988).
- [127] University of Pavia Microwave Lab. URL <http://www-1.unipv.it/mwv/software/>.
- [128] Injectorall Electronics Corp. URL <http://www.injectorall.com/>.
- [129] Beruete, M., Sorolla, M., Campillo, I. & Dolado, J. Increase of the transmission in cut-off metallic hole arrays. *Microwave and Wireless Components Letters, IEEE* **15**, 116–118 (2005).
- [130] Beruete, M. *et al.* Enhanced millimeter wave transmission through quasioptical subwavelength perforated plates. *Antennas and Propagation, IEEE Transactions on* **53**, 1897–1903 (2005).
- [131] García de Abajo, F. J., Gómez-Medina, R. & Sáenz, J. J. Full transmission through perfect-conductor subwavelength hole arrays. *Phys. Rev. E* **72**, 016608 (2005).
- [132] Komiyama, B., Kiyokawa, M. & Matsui, T. Open resonator for precision dielectric measurements in the 100 GHz band. *Microwave Theory and Techniques, IEEE Transactions on* **39**, 1792–1796 (1991).
- [133] Pozar, D. M. *Microwave Engineering, 3rd ed.* (John Wiley and Sons, New York, USA, 2005).
- [134] Haberman, R. *Elementary and Applied Partial Differential Equations: With Fourier Series and Boundary Value Problems* (Prentice Hall, Upper Saddle River, NJ, 1998).

- [135] Sun, Y. & Driscoll, J. A new hybrid power technique utilizing a direct copper to ceramic bond. *Electron Devices, IEEE Transactions on* **23**, 961–967 (1976).
- [136] Burgess J. F., F. G., Neugebauer C. A. & R.E., M. The Direct Bonding of Metals to Ceramics and Application in Electronics. *ElectroComponent Science and Technology* **2**, 233–240 (1976).
- [137] Khounsary A.M., C. D. & L., A. Thermal contact resistance across a copper-silicon interface. *Technical Report, Argonne National Lab* (1997).
- [138] Lahmar, A. *et al.* Experimental investigation on the thermal contact resistance between gold coating and ceramic substrates. *Thin Solid Films* **389**, 167 – 172 (2001).
- [139] Elioff, M. S., Valentini, J. J. & Chandler, D. W. Subkelvin Cooling NO Molecules via "Billiard-like" Collisions with Argon. *Science* **302**, 1940–1943 (2003).
- [140] Hudson, E. R. Deceleration of continuous molecular beams. *Physical Review A (Atomic, Molecular, and Optical Physics)* **79**, 061407 (2009).
- [141] Stuhl, B. K., Sawyer, B. C., Wang, D. & Ye, J. Magneto-optical trap for polar molecules. *Physical Review Letters* **101**, 243002 (2008).
- [142] Bernard, A., Effantin, C., Andrianavalona, E., Vergès, J. & Barrow, R. F. Laser-induced fluorescence of BaF: Further results for six electronic states. *Journal of Molecular Spectroscopy* **152**, 174–178 (1992).
- [143] Dagdigian, P. J., Cruse, H. W. & Zare, R. N. Radiative lifetimes of the alkaline earth monohalides. *The Journal of Chemical Physics* **60**, 2330–2339 (1974).
- [144] Tellinghuisen, J. Fast, accurate RKR computations. *Journal of Molecular Spectroscopy* **44**, 194 – 196 (1972).
- [145] Herzberg, G. *Spectra of Diatomic Molecules, Volume 1: Molecular Spectra and Molecular Structure* (Krieger, New York, USA, 1950).
- [146] Steimle, T. C., Domaille, P. J. & Harris, D. O. Rotational analysis of the $A^2\Pi-X^2\Sigma$ system of SrF using a CW tunable dye laser. *Journal of Molecular Spectroscopy* **73**, 441–443 (1978).

- [147] Liu, X.-S., Liu, X.-Y., Zhou, Z.-Y., Ding, P.-Z. & Pan, S.-F. Numerical Solution of One-Dimensional Time-Independent Schrodinger Equation by Using Symplectic Schemes. *International Journal of Quantum Chemistry* **79**, 343–349 (2000).
- [148] Ryzlewicz, C., Schtze-Pahlmann, H. U., Hoefl, J. & Trring, T. Rotational spectrum and hyperfine structure of the $^2\Sigma$ radicals BaF and BaCl. *Chemical Physics* **71**, 389 – 399 (1982).
- [149] Childs, W. J., Goodman, L. S. & Renhorn, I. Radio-frequency optical double-resonance spectrum of SrF: The $X^2\Sigma^+$ state. *Journal of Molecular Spectroscopy* **87**, 522 – 533 (1981).
- [150] Sauer, B. E., Wang, J. & Hinds, E. A. Laser-rf double resonance spectroscopy of ^{174}YbF in the $X^2\Sigma^+$ state: Spin-rotation, hyperfine interactions, and the electric dipole moment. *The Journal of Chemical Physics* **105**, 7412–7420 (1996).
- [151] Childs, W. J., Goodman, G. L. & Goodman, L. S. Precise determination of the v and n dependence of the spin-rotation and hyperfine interactions in the CaF $X^2\Sigma_{1/2}$ ground state. *Journal of Molecular Spectroscopy* **86**, 365 – 392 (1981).
- [152] Steimle, T. C., Fletcher, D. A. & Scurlock, C. T. A Molecular Beam Study of the (0,0) $A^2\Pi$ - $X^2\Sigma^+$ Band System of SrF. *Journal of Molecular Spectroscopy* **158**, 487–488 (1993).
- [153] Janik, G., Nagourney, W. & Dehmelt, H. Doppler-free optical spectroscopy on the Ba^+ monion oscillator. *J. Opt. Soc. Am. B* **2**, 1251–1257 (1985).
- [154] Berkeland, D. J. & Boshier, M. G. Destabilization of dark states and optical spectroscopy in zeeman-degenerate atomic systems. *Phys. Rev. A* **65**, 033413 (2002).
- [155] Yale, C. G. Development of a buffer gas cooled molecular beam source. Senior Thesis, Yale University (2009).
- [156] Sesko, D. W., Fan, C. G. & Wieman, C. E. Production of a cold atomic vapor using diode-laser cooling. *Journal of the Optical Society of America B Optical Physics* **5**, 1225–1227 (1988).
- [157] Mok, C., Weel, M., Rotberg, E. & Kumarakrishnan, A. Design and construction of an efficient electro-optic modulator for laser spectroscopy. *Canadian Journal of Physics* **84**, 775–786 (2006).

- [158] Budker, D., Rochester, S. M. & Yashchuk, V. V. Obtaining frequency markers of variable separation with a spherical mirror Fabry-Perot interferometer. *Review of Scientific Instruments* **71**, 2984–2987 (2000).
- [159] Söding, J., Grimm, R., Ovchinnikov, Y. B., Bouyer, P. & Salomon, C. Short-distance atomic beam deceleration with a stimulated light force. *Phys. Rev. Lett.* **78**, 1420–1423 (1997).